FABRICATION AND MODIFICATION OF NANOCOMPOSITE MEMBRANES FOR ENHANCED WATER PURIFICATION

A Dissertation presented to
the Faculty of the Graduate School
at the University of Missouri

In Partial Fulfillment
of the Requirements for the Degree

Doctor of Philosophy

---

by

JUN YIN

Dr. Baolin Deng, Dissertation Supervisor

JULY 2014

The undersigned, appointed by the Dean of the Graduate School, have examined the dissertation entitled

FABRICATION AND MODIFICATION OF NANOCOMPOSITE MEMBRANES FOR ENHANCED WATER PURIFICATION

Presented by Jun Yin,

a candidate for the degree of Doctor of Philosophy,

and hereby certify that, in their opinion, it is worthy of acceptance.

Baolin Deng
Professor of Civil and Environmental Engineering

Matthew Bernards
Assistant professor of Chemical Engineering

Zhiqiang Hu
Associate professor of Civil and Environmental Engineering

Enos C. Inniss
Assistant professor of Civil and Environmental Engineering

Qingsong Yu
Associate professor of Mechanical and Aerospace Engineering

ACKNOWLEDGEMENTS

First of all, I would like to thank my supervisor, Professor Dr. Baolin Deng, for bringing me to this interesting and promising topic and his many inspiring and valuable discussions on this research and wonderful suggestions for my graduate work. Next, I would like to thank Dr. Matthew Bernards, Dr. Zhiqiang Hu, Dr. Enos Inniss and Dr. Qingsong Yu for serving in my dissertation committee and their precious time and valuable comments and suggestions. Especially, I would like to acknowledge Dr. Zhiqiang Hu for his critical revisions of Chapter Three and many constructive suggestions.

I would like to thank Dr. Eun-Sik Kim, Dr. Guocheng Zhu and Dr. Yu Yang for their support during the experiment. Special thanks go to our research groups, Peng Wan for the assist of membrane fabrication, Weiming Hu for the cooperation on the algae bioreactor study, Xiaofeng Wang for the antifouling study, and Zhe Yang, Chen Zhong, Zhibiao Li and other colleagues and friends.

Finally, I would like thank my parents for all of their concerns and supports, and would like to express my deepest gratitude to my wife, Guanghui Chen, and lovely daughter, Emma Yin.

TABLE OF CONTENTS

CHAPTER FOUR

Multi-walled carbon nanotubes (MWNTs)/polysulfone (PSU) nanocomposite hollow fiber membranes for enhanced water treatment

CHAPTER FIVE

Poly(vinylene fluoride) (PVDF)/nitrogen doped TiO_2 (N-TiO_2) nanocomposite hollow fiber membranes (HFMs) with advanced antifouling properties under visible light irradiation

LIST OF ABBREVIATIONS

AA	Atomic absorption spectroscopy
AFM	Atomic force microscopy
ATR	Attenuated total reflection
BET	Brunauer-Emmett-Teller
BPPO	Brominated polyphenylene oxide
BSA	Bovine serum albumin
CA	Cellulose acetate
CFU	Colony-forming units
CNTs	Carbon nanotubes
CTAB	Cetyltrimethylammonium
Da	Dalton
DI	Deionized
DMF	N,N-dimethylformamide
EDS	Energy-dispersive X-ray spectroscopy
FO	Forward osmosis
FT-IR	Fourier transform infrared spectroscopy
GO	Graphene oxide
HA	Humic acid
HFM	Hollow fiber membrane
iGO	Isocyanate-treated graphene oxide
IP	Interfacial polymerization
LB	Lysogeny broth
LED	Light-emitting diode
MBR	Membrane bioreactor
MF	Microfiltration
MMM	Mixed matrix membrane
MPD	m-phenylenediamine
M-TFN	Thin-film nanocomposite membrane containing MCM-41 nanoparticles
Mw	Molecular weight
MWCO	Molecular weight cutoff
MWNTs	Multi-walled carbon nanotubes
MO	Methyl orange
NF	Nanofiltration
NMP	1-methyl-2-pyrrolidinone
NPs	Nanoparticles
N-TiO_2	Nitrogen doped TiO_2
OMC	Ordered mesoporous carbon
OMWNTs	Oxidized multi-walled carbon nanotubes
PA	Polyamide

PAA	Poly(acrylic acid)
PAH	Poly(allylamine hydrochloride)
PAN	Polyacrylonitrile
PANI	Polyaniline
PBS	Phosphate buffered saline
PCL	Polycaprolactone
PEG	Polyethylene glycol
PEI	Polyetherimide
PEO	Poly(ethylene oxide)
PES	Polyethersulfone
PI	Phase inversion
PMA	Polymethylacrylate
PPESK	Poly(phthalazinoneether sulfone ketone)
PR	Procion red
PRO	Pressure-retarded osmosis
PSU	Polysulfone
PVDF	Poly(vinylidene fluoride)
PVA	Poly(vinyl alcohol)
PVB	Poly(vinyl butyral)
PVC	Polyvinyl chloride
PVDC	Poly(vinylidene chloride)
PVP	Polyvinylpyrrolidone
RMS	Root mean square
RO	Reverse osmosis
SEM	Scanning electron microscope
SPES	Sulfonated polyethersulfone
S-TFN	Thin-film nanocomposite membrane containing spherical silica nanoparticles
SWNTs	Single-walled carbon nanotubes
TEM	Transmission electron microscopy
TEOS	Tetraethyl orthosilicate
TFC	Thin-film composite
TFN	Thin-film nanocomposite
TFNC	Thin-film nanofibrous composite
TFN-SH	Thiol group terminated thin-film nanocomposite membrane
TFN-S-AgNPs	Thin-film nanocomposite membrane with surface grafted silver nanoparticles
TMC	Trimesoyl chloride
TMP	Trans-membrane pressure
TOC	Total organic carbon
TSP	Tangential streaming potential
UF	Ultrafiltration
UV	Ultraviolet
XRD	X-ray diffraction

LIST OF TABLES

LIST OF FIGURES

ABSTRACT

FABRICATION AND MODIFICATION OF NANOCOMPOSITE MEMBRANES FOR ENHANCED WATER PURIFICATION

By JUN YIN

Dr. Baolin Deng, Dissertation Supervisor

Developing cost-effective technologies to extend water resources and solve water pollution problems is critical to the sustainable development of human society. Membrane technology has been given much attention and already been widely used in many areas including drinking water treatment, brackish and seawater desalination, and wastewater treatment and reuse due to its simple operation, no involvement of phase change or chemical additives, and modular design for easy scale up. However, as the main type of membrane, polymeric membranes still have some challenges that need to be overcome, which include the trade-off between permeability and selectivity and fouling issues.

In this work, novel nanocomposite membranes with enhanced separation performance were developed for water and wastewater treatment. First, both flat-sheet and hollow fiber membrane fabrication systems were set up to provide capabilities for nanocomposite membrane preparation. Then, to improve membrane performance, nanomaterials with different components (inorganic or organic), structures (porous or nonporous), and functionalities (inert, antimicrobial activity, or photocatalytic activity)

were incorporated into polymeric membranes through phase inversion or interfacial polymerization process based on proposed applications. Novel nanomaterials, mesoporous silica, carbon nanotubes or graphene oxide, were applied to study their effects on membrane structure and other physicochemical properties. A biocidal nanomaterial, AgNPs, was used to improve membrane's anti-biofouling capability. Finally, a photocatalytic nanomaterial, nitrogen doped TiO_2 (N-TiO_2) with good visible light activity, was applied to improve the membrane antifouling properties.

The results showed that hydrophilic nanofillers could improve membrane surface hydrophilicity, leading to a membrane with enhanced water permeability and antifouling properties. Meanwhile, nanofillers containing internal pore structure could further improve water permeability by providing additional flow paths for facile water transport.

To control membrane biofouling, silver nanoparticles (AgNPs) were chemically attached onto the thin-film composite (TFC) membrane surfaces with cysteamine as a bridging agent. The modified membranes showed good stability for the immobilized AgNPs and excellent antibacterial properties, while maintained a good water flux and salt rejection.

Poly(vinylene fluoride) (PVDF)/N-TiO_2 nanocomposite hollow fiber membranes (HFMs) possessing visible light activity were first developed, which demonstrated an improved water permeability and superior antifouling properties due to the photodegradation of foulants and photoinduced hydrophilicity enhancement.

Based on these results, it was concluded that nanocomposite membranes were promising to mitigate or even overcome the intrinsic challenges of current polymeric

membranes on the market. The incorporation of nanomaterials with conventional membrane polymers could not only tune structure and physicochemical properties (e.g. hydrophilicity, porosity, charge density, thermal, and mechanical stability) of membranes, but also introduce unique functionalities (e.g. antibacterial property and photocatalytic capability) into the membranes. Overall, nanocomposite provides polymeric membrane design a new dimension, which could lead to the next generation of high performance membranes.

Introduction

Water is foundation of life. However, due to the rapid growth of world population, abuse of water resources, and water pollution, water shortage problem becomes more and more serious. Worldwide, around 780 million people still lack access to improved drinking water sources (WHO, 2012). Hence, cost-effective technologies must be developed to extend water resources and solve water pollution problems. Membrane technology is one of the most promising technologies that may provide a solution to challenging water problem. It has already been widely used in many areas including drinking water treatment, brackish and seawater desalination, and wastewater treatment and reuse, largely because it is simple in concept and operation, does not involve phase changes or chemical additives, can be made modular for easy scaleup.

Membrane, as the key part of membrane separation technology, can be defined as a thin and selective barrier which enables the transport or the retention of compounds between two media [1]. Membrane can be prepared by inorganic materials (such as ceramics) or organic materials (such as polymers). Inorganic materials including ceramics and metallics usually have better chemical/solvent resistance and could tolerate a wide range of temperature, pH, and pressure. However, they are also restricted by several disadvantages such as limited pore size availability and high operating and capital costs. Accordingly, current research on membranes mainly focuses on polymeric membranes due to the better control of pore forming mechanism, higher flexibility, smaller footprints required for installation, and lower costs compared to inorganic membranes [2].

Various polymer materials have been used to prepare polymeric membranes, such as cellulose acetate (CA), polysulfone (PSU), polyethylene (PE), polypropylene (PP), poly(vinylidene fluoride) (PVDF), polyethersulfone (PES), polycarbonates (PC) and polyacrylonitrile (PAN). Among them, PSU, PVDF and PES are the most commonly used materials because of their relatively low cost, decent thermal and chemical stabilities [3, 4].

Based on filtration class (separation capability), membrane can be classified as microfiltration (MF), ultrafiltration (UF), nanofiltration (NF), reverse osmosis (RO), and forward osmosis (FO) membrane. Their basic properties are summarized in Table 1.

Table 1. Membrane types based on filtration class*

Membrane type based on filtration class	Typical pore size	Typical targets removed	Typical operating pressure
MF	0.1-10 μm	Suspended solids, bacteria, protozoa	0.1-2 bar
UF	3-100 nm (1-100 kDa)	Colloidal or molecular particles, proteins, most bacteria, partially viruses	1-5 bar (cross-flow) 0.2-0.3 bar (dead-end and submerged)
NF	1-3 nm (250-400 Da)	Viruses, natural organic matter (NOM), divalent or multivalent ions	5 – 20 bar
RO	< 125 Da	Almost all impurities, including monovalent ions	10 – 100 bar
FO	< 125 Da	Almost all impurities, including monovalent ions	Osmotic pressure

* Modified from Membrane technologies for water applications, European Commission, 7th Framework programme, 2010 applications

Generally, the smaller the pore size, the smaller targets that can pass through the membrane. As the pores getting smaller, higher operating pressure is required, leading to a more energy-intensive filtration system.

Though polymeric membranes have unique properties which make them better materials for many applications, they also have met some challenges which need to be

overcome. The first is the trade-off relationship between permeability and selectivity (also called Robeson upper boundary) [5], which was first realized in gas separation membranes. Similarly in water treatment area, membranes with higher water permeability usually possess relatively lower solute rejection. It is the intrinsic property of polymer materials, so it seems not possible to solve the problem just based on the development of polymer material. The second challenge is membrane fouling, which is the accumulation of retained substances (such as colloidal and suspended particles, organic matter, inorganic matter, and biological foulants) on the membrane surface and/or within the membrane pores leading to the deterioration of membrane performance. Membrane fouling causes a number of problems including the increase in the operational pressure and the decline in the permeate quantity and quality of the membrane systems. The low mechanical strength of polymer materials is also a challenge, especially for a membrane which has a very thin structure. This is particularly critical to pressure driven filtration process, where a high transmembrane pressure (TMP) may be applied.

Nanocomposite (combine polymeric materials with nanomaterials) was first developed to improve the mechanical properties of polymeric materials. In membrane separation area, this concept was originally used and proved to be an efficient method to overcome the Robeson upper boundary in the field of gas separations [5, 6].

Recently, nanocomposite membrane has drawn a lot of attention and has been carried out for water treatment. Based on existing results (which will be illustrated in Chapter one), it seems to be a promising solution to above challenges of polymeric membranes. The incorporation of nanomaterials with conventional membrane polymers could not only tune structure and physicochemical properties (e.g. hydrophilicity,

porosity, charge density, thermal, and mechanical stability) of membranes, but also introduce unique functionalities (e.g. antibacterial property and photocatalytic capability) into the membranes.

Research Objective

The research objective of this study is to design suitable nanocomposite membranes with enhanced separation properties for water and wastewater treatment. It is expected that using the advanced high performance nanocomposite membranes will result in lower energy consumption in the membrane filtration systems. Since the membrane systems for water treatment are almost competitive of conventional water treatment process currently, the enhanced performance of nanocomposite membrane could be the tipping point that propels the membrane systems to much wider applications for water treatment, desalination, and wastewater reclamation.

Research Tasks

Task One: Set up membrane fabrication systems to prepare both flat-sheet and hollow fiber membranes.

With the capability of fabricating polymeric membranes, much more parameters (such as polymer types and concentration, solvent types, additive types and concentration, temperature) could be tuned to optimize the membrane structure and properties. These systems could be used to develop nanocomposite membranes through various fabrication methods such as phase inversion and interfacial polymerization.

Task Two: Incorporate novel nanomaterials with unique structures or properties into polymeric membrane to improve membrane performance in terms of permeability, selectivity, and fouling resistance.

Nanomaterials with different components (inorganic or organic), structures (porous or nonporous), functionalities (inert, antimicrobial activity, or photocatalytic activity) were incorporated into polymeric membranes based on the proposed applications to improve membrane performance. Inert nanomaterials were applied to study their effects on membrane structure and physicochemical properties. Biocidal nanomaterials were used to improve the membrane anti-biofouling properties. Photocatalytic nanomaterials were applied to improve the membrane antifouling properties.

Task Three: Explore the specific role of nanomaterials' internal pore structure in the nanocomposite membrane filtration process.

Silica NPs are chemically inert, thermally stable, inexpensive and easy to tune particle size and internal structure. In this study, tests were conducted using silica NPs with comparable chemical properties but with or without internal pores. By comparing the performance of nanocomposite membranes containing silica NPs with different internal structures, we evaluated the contribution of the internal pores to the water permeability and salt rejection. This fundamental understanding will help screen and develop new advanced thin-film nanocomposite membranes in general. In addition, fabrication parameters were fine-tuned to develop a high performance thin-film nanocomposite membrane.

References

[1] S.K. Burtrand Lee, Chemical Processing of Ceramics, Second Edition (Materials Engineering), CRC Press; second edition, 2005.

[2] L.Y. Ng, A.W. Mohammad, C.P. Leo, N. Hilal, Polymeric membranes incorporated with metal/metal oxide nanoparticles: A comprehensive review, Desalination, 308 (2013) 15-33.

[3] A.K. Ghosh, E.M.V. Hoek, Impacts of support membrane structure and chemistry on polyamide-polysulfone interfacial composite membranes, Journal of Membrane Science, 336 (2009) 140-148.

[4] L.Y. Yu, H.M. Shen, Z.L. Xu, PVDF-TiO_2 composite hollow fiber ultrafiltration membranes prepared by TiO_2 sol-gel method and blending method, Journal of Applied Polymer Science, 113 (2009) 1763-1772.

[5] L.M. Robeson, Correlation of separation factor versus permeability for polymeric membranes, Journal of Membrane Science, 62 (1991) 165-185.

[6] T.S. Chung, L.Y. Jiang, Y. Li, S. Kulprathipanja, Mixed matrix membranes (MMMs) comprising organic polymers with dispersed inorganic fillers for gas separation, Progress in Polymer Science (Oxford), 32 (2007) 483-507.

CHAPTER ONE

Literature review: Polymer-matrix nanocomposite membranes for water treatment

Polymer-matrix nanocomposite membranes are advanced membranes with nanomaterials dispersed in their polymer matrices. They could be used for gas-gas, liquid-liquid, and liquid-solid separations. The concept of making nanocomposite membranes was originally developed to overcome the Robeson upper boundary in the field of gas separation in 1990s [1, 2], where highly selective zeolites were incorporated into polymers to improve both permeability and selectivity [3, 4]. Besides gas separation [5-7], many other applications have been examined by using nanocomposite membranes, such as direct methanol fuel cells [8, 9], proton exchange membrane fuel cells (PEMFCs) [10], sensor applications [11, 12], lithium cell battery [13, 14], pervaporation (PV) [15-17], organic solvent nanofiltration (OSN) [18, 19], and water treatment. Due to its promise of overcoming the trade-off relationship between permeability and selectivity as well as mitigating membrane fouling problem during water treatment applications, it has gained increasing attention and is considered as the cutting edge of creating the next generation of high performance membranes.

The aim of this review is to summarize the recent scientific and technological advances in the development of nanocomposite membranes for water treatment. Challenges and future research directions will also be presented. Readers interested in gas separation should refer to two excellent reviews recently published on nanocomposite gas separation membranes [2, 5].

According to membrane structure and location of nanomaterials, nanocomposite membranes can be classified into four categories: (1) conventional nanocomposite; (2) thin-film nanocomposite (TFN); (3) thin-film composite (TFC) with nanocomposite substrate; and (4) surface located nanocomposite. The typical structures of these membranes are illustrated in Fig. 1.1. It is worth noting that the red spheres used in the figure not only stand for nanoparticles (NPs), but also could represent nanotubes, nanofibers or nanosheets. The publication numbers related to each type of the nanocompoite membranes for water treatment are also presented in Fig. 1.1, where the data are obtained based on searching and screening using the key words "nanocomposite and membrane" or "mixed matrix and membrane" in the database, Scopus.

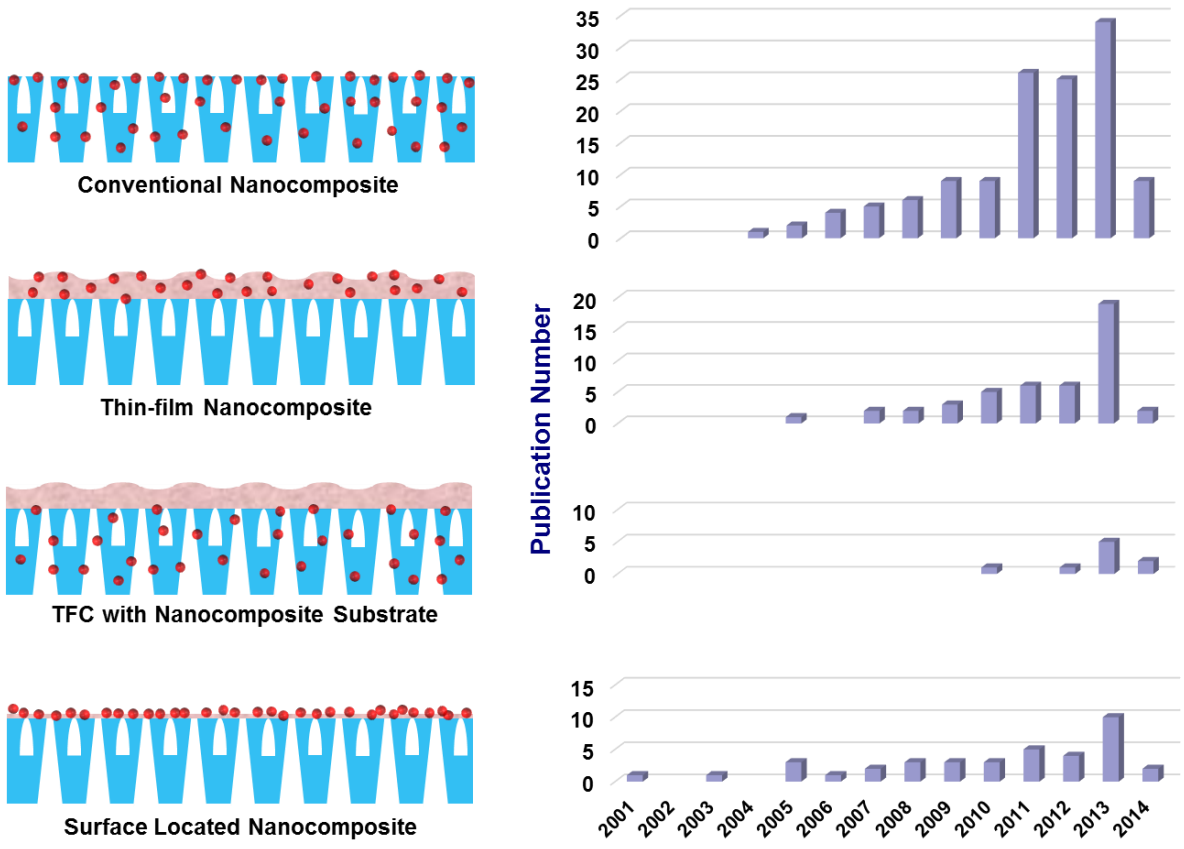

Fig. 1.1 Typical types of nanocomposite membranes and corresponding publication numbers related to water treatment applications.

1.1 Conventional Nanocomposite

In the conventional nanocomposite membranes, nanofillers fall into one of the four categories: 1) inorganic material; 2) organic material; 3) biomaterial, and 4) hybrid material with two or more material types. Fabrication of nanocomposite membranes is mostly based on phase inversion (PI) method in which nanofillers are dispersed in polymer solution prior to the PI process, and can be prepared in either flat sheet or hollow fiber configurations (Fig. 1.2).

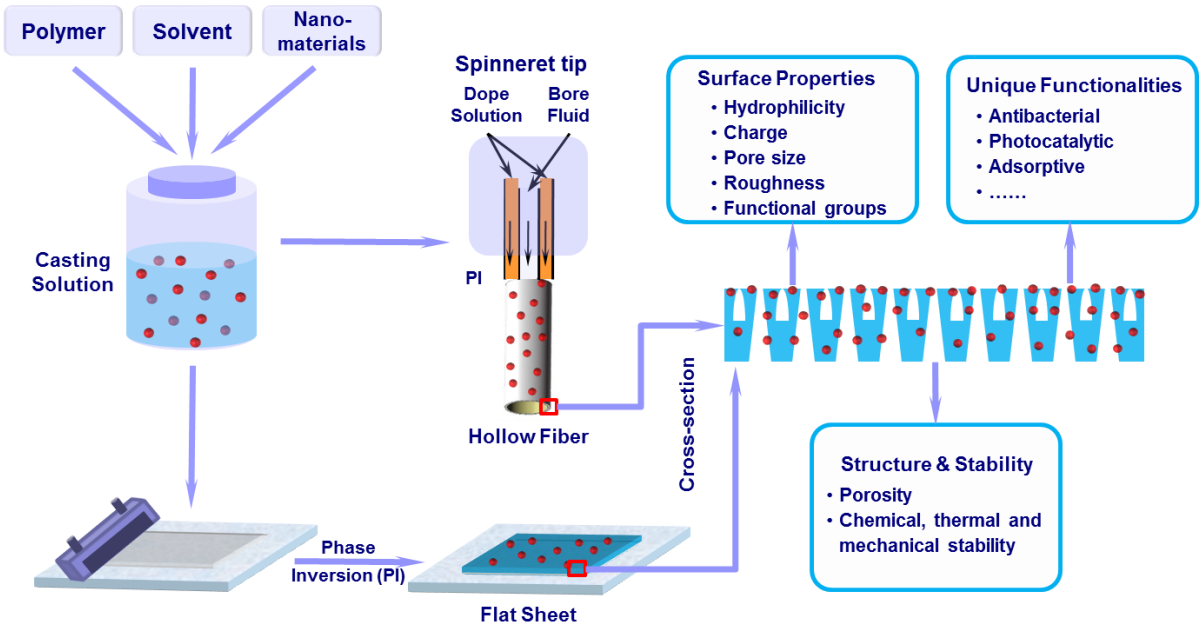

Fig. 1.2 Fabrication of conventional nanocomposite membranes through PI process and the main effects of nanofillers on final products

Representative publications on the development and use of nanocomposite membranes in each category are summarized in Table 1.1, along with filler and polymer types, fabrication methods, and main advantages of filler materials. These reported studies have demonstrated that the incorporation of nanomaterials into polymers could not only tune structure and physicochemical properties (hydrophilicity, porosity, charge

density, chemical, thermal and mechanical stability) of membranes, but can also introduce unique functionalities such as antibacterial and photocatalytic characteristics into the membranes. The effects of nanofiller on performance of nanocomposite membrane are summarized as follows.

.

Table 1.1 Summary of conventional nanocomposite membranes

Filler			Polymer	Fabrication Method	Main Advantages of filler	Reference
Inorganic material	Metal Oxide	TiO_2	PAI; PVDF; PSU; PAN; PPESK; PVB; PES; CA; PVDF/SPES; PU	Blending + PI	Hydrophilicity	[20-52]
		TiO_2 with photoreaction	PES; PVDF	Blending + PI	Hydrophilicity; Photocatalytic functionality	[32, 53-55]
		SiO_2	PES; PSU; Nafion	PI; Casting and drying	Hydrophilicity	[56-64]
		Al_2O_3	PVDF; PES	Blending + PI	Hydrophilicity	[22, 65-68]
		Fe_3O_4	PVA; PES; PVC	Blending + PI	Magnetic property; Core for shell coating; Hydrophilicity	[69-73]
		ZrO_2	PES	Blending + PI	Hydrophilicity	[22, 68]
		Hydrous MnO_2	PES	Blending + PI	Heavy metal adsorption; Hydrophilicity	[74, 75]
		ZnO	PSU	Blending + PI	Hydrophilicity	[76]
	Metal	Ag	CA; PI; PSU; PES; PVDF; PAN; PLA; PU	Blending + PI; Electrospinning	Antimicrobial functionality	[57, 77-90]
		Cu	PSU; PLA; PES	Blending + PI; Electrospinning	Antimicrobial functionality	[57, 82, 86, 91]
		Se	PES	Blending + PI	Antimicrobial functionality	[91]
	Zeolite		PU; Ultem; PAN; PVDF; PSU	Solvent evaporation; Blending + PI	Molecular sieving; Hydrophilicity; Cross-link property	[57, 81, 92-96]
	Clay		PSU; Nylon 6; PES; PVDF	Blending + PI	Mechanical property; Hydrophilicity	[97-105]
	Boehmite; Acrylate-alumoxane		PES	Blending + PI	Hydrophilicity; Provide polymerization initiation sites	[106, 107]
	CNTs		PVDF; BPPO; PEI; PA; PVA; PES; PAN	Blending + PI; Cross-linking	Electrical conductivity; Potential water channel; Mechanical property; Hydrophilicity after modification	[46, 108-124]
	GO		PSU; PES	Blending + PI	Hydrophilicity; Negative charge; High surface area support	[64, 125-128]
	C60		PSU; Poly(phenylene isophtalamide)	Blending + PI	Model hydrophobic filler; Interlocking property	[129, 130]
Organic material	Cyclodextrin		PSU	Blending + PI	Special molecule with an inner cavity of several Å	[131-134]
	PANI		PSU; PAN-co-PMA; PES	Blending/In site blending + PI	Hydrophilicity	[135-140]
	Polypyrrole		PSU	Blending + PI	Hydrophilicity	[141]
	Chitosan beads		Ethylene vinyl alcohol (EVAL)	Blending + PI	Adsorption of Cu^{2+}	[142]
	Polyhedral oligomeric silsesquioxane		CA	Blending + PI	Special structure; Anti-compaction	[143]
	Semi-interpenetrating network polymeric NPs		PES	Spin coating + PI	Hydrophilicity; Suppress the protein adsorption	[144]
Biomaterial	Aquaporin		$PMOXA_m$-$PDMS_n$-$PMOXA_m$ (ABA)	Film rehydration method	Water-channel membrane proteins	[145]
	Lignin		Cellulose triacetate	Vapor-induced phase separation	Reinforcement effect	[146]
Hybrid material	TiO_2/MWNTs; Au/xGnPs; Fe/Mn; SiO_2/GO		PES; PSU	Blending + PI	Synergistic effect	[46, 64, 127, 147]

PI: Phase inversion

1.1.1 Effects on membrane structure and physicochemical properties

As the barrier of the separation process, a functional membrane should have the right structure (e.g. pore size and porosity) and physicochemical properties (e.g. surface hydrophilicity and roughness, chemical, thermal and mechanical stability) suitable for the proposed applications. Generally, surface pore size and membrane porosity will determine the permeability and rejection, especially those for MF and UF applications. Surface hydrophilicity and roughness largely control the membrane fouling characteristics, while chemical, thermal and mechanical stability determine the membrane durability under various environments.

Incorporation of various nanoflllers into polymer matrices is known to affect membrane structure and properties. Most studies found the membrane surface hydrophilicity is enhanced by incorporating hydrophilic nanomaterials that are partially exposed to the surface. For example, when preparing polyaniline (PANI)/PSU nanocomposite membranes, Fan et al. [135] found the hydrophilic PANI nanofibers migrated from polymer matrix to the surface during the membrane formation, leading to the formation of membranes with higher hydrophilicity, porosity and pore connectivity. Similarly, Zhao et al. [137] found hydrophilic PANI nanofibers would migrate toward water bath or the polymer-poor phase of the casting film during the PI process to reduce interfacial energy. The existence of PANI nanofibers near the membrane surface will improve membrane hydrophilicity. When preparing hyperbranched poly(amine-ester) functionalized MWNTs ($MWNT_{HPAE}$)/PVDF nanocomposite membranes, Zhao et al. [115] observed a significantly improved surface hydrophilicity, which could be attributed to the increased surface coverage of hydrophilic -OH groups from the nanofillers. In

general, increasing the surface hydrophilicity of a membrane decreases membrane fouling because the hydrogen bonding formation between the surface hydrophilic groups and water molecules creates a water layer on membrane surface that could prevent foulant adsorption [115]. This applies for inorganic fillers as well, for example, when hydrophilic metal-oxide NPs were embedded into polymer matrix, the membrane fouling resistance was enhanced [22].

Incorporation of nanomaterials can also change the porosity and pore size of membranes, and subsequently, change their water permeability and solute rejection. Yu et al. [30] found that for the TiO_2/PVDF hollow fiber membranes (HFMs), the surface pore size increased with increasing TiO_2 concentration initially, but decreased with further increase in TiO_2 loading. This is similar to what we have observed on the impact of oxidized MWNTs on the membrane structure [120], where the incorporation of the oxidized MWNTs into polysulfone (PSU) polymer matrix led to an increase in the surface pore size initially, but then a decrease, with increasing the MWNTs concentration. This trend was consistent with the water flux results that showed a convex profile with increasing nanofiller concentration. Generally, the addition of hydrophilic substance in the dope solution leads to an accelerated solvent and non-solvent exchange (caused by thermodynamic immiscibility) and thus encourages formation of a more porous structure [148]. With a further increase in the filler loading, however, the viscosity of the dope solution would increase, leading to a diffusion delay. Under this delayed demixing condition, the top layer will be dense and thick with low porosity and low degree of pore interconnectivity due to the high concentration of the polymer solution at the onset of demixing [149].

In another study, Mansourpanah et al. [112] introduced polycaprolactone (PCL) modified MWNTs into PES matrix and studied its effects on membrane morphology and performance. With an increasing filler concentration, the skin layer thickness decreased and sub-layer structure changed to finger-like macrovoids, leading to a higher porosity and enhanced permeability.

Membrane surface charge density could also be affected by the incorporation of nanofillers due to their surface functional groups. To illustrate, Zhao et al. [126] incorporated isocyanate-treated GO (iGO) into the PSU ultrafiltration membrane, creating a nanocomposite membrane with an enhanced hydrophilicity and fouling resistance. In addition to the contribution of the hydrophilic surface that prevents protein adsorption and membrane fouling, the negative surface charge induced by the nanofillers has also led to a situation that foulants with a negative charge would be repelled [150].

Membranes need to be robust or mechanically strong for many applications. After evaluating the strengths of nanocomposite membranes containing various nanofillers (Ag, Cu, silica, and zeolite), Hoek et al. [57] found most of these membranes showed enhanced mechanical stabilities since there were good compatibility between fillers and polymer and favorable changes in the membrane structure such as substitution of finger-like structure by sponge-like macrovoids. Liao et al. [81] also found zeolite/PVDF nanocomposite membranes possessed enhanced mechanical stability in terms of tensile strength and break elongation. And they attributed this phenomenon to the good interaction between zeolite and PVDF matrix, where zeolite NPs could act as a crosslinking agent for the polymeric chains and increase membrane rigidity. The cross-linking phenomenon was first emphasized by Ciobanu et al. [92], and could be attributed

to the hydrogen bonds between polymer chains and hydroxyl groups T-OH (T=Si, Al, P) on zeolite surface. As a common reinforce material for polymeric nanocomposites, clay minerals (modified or not) have been used to improve mechanical and thermal properties of nanocomposite membranes [97, 98].

One-dimensional nanomaterials such as PANI nanofiber and MWNTs showed positive effects on the mechanical strength of nanocomposite membranes. For example, PANI/PSU membrane had higher breaking strength than the PSU membrane [137, 138]. MWNTs/PA membrane showed enhanced mechanical properties in terms of Young's modulus, toughness, and tensile strength [111]. By loading 2 wt% MWNTs, the tensile strength of MWNTs/PAN membranes was increased over 97% due to the combined effects of sufficient bonding (CH-π interactions) between nanotubes and the matrix and the decreased membrane porosity [114].

The changes of membrane structure and property due to the presence of nanomaterials rely on the good dispersion of nanomaterials in casting solution and hence polymer matrix. Many effects were devoted to improve the dispersion of nanofillers either through modifying nanomaterial surface or applying surfactant, especially for those materials that are inherent hydrophobic such as carbon nanotubes (CNTs). A common strategy to improve the dispersion of CNTs is through oxidation to generate hydroxyl and carboxyl functional groups on their surface with acid treatment [120]. Other strategies include surface grafting as in the preparation of hyperbranched poly(amine-ester) HPAE-MWNTs [115] or PAA-MWNTs [117] and use of surfactants [110].

1.1.2 New functionalities introduced by nanomaterials

Functional membranes are those not only capable of filtering solute and particles from water, but also adsorbing, degrading, and/or deactivating them. Functional membranes are normally designed and optimized with specific applications in mind.

1.1.2.1 Adsorption

It is common to incorporate NPs inside the polymer matrix to make functional membranes with specific capability to adsorb heavy metals from water. For example, Daraei and et al. [70] incorporated PANI/Fe_3O_4 NPs inside PES matrix through PI method to remove Cu (II) from aqueous solution. The efficient dispersion of NPs was observed at relatively low loading (0.1%), providing more accessible active sites for sorption of copper ions. Regeneration of this membrane by EDTA is possible for reuse. In another study, Tetala and Stamatialis [142] developed a copper removal membrane by incorporating chitosan beads (20-40 μm) inside ethylene vinyl alcohol (EVAL) matrix. While the particle size is significantly larger than the nanoscale, almost the same strategy was used for the membrane fabrication, resulting in a membrane with fast adsorption kinetics and high adsorption capacity (225.7 mg/g) of Cu^{2+} ions.

In a similar way, hydrous manganese dioxide (HMO) [74] and Fe_3O_4 NPs (60 nm) [71] were embedded into the PES and PVC matrices, respectively, to remove lead from aqueous solution. In another study [147], Fe-Mn binary oxide (FMBO) was used to prepare PES nanocomposite membrane for As (III) removal.

These studies all confirmed the possibility of preparing nanocomposite membranes containing certain adsorbents for adsorptive removal of contaminants from water.

However, the relatively short contact time (high water permeability) and limited adsorption capacity may hinder their practical applications.

1.1.2.2 Photocatalysis

TiO_2 has been widely used for water splitting, water treatment, air purification and self-cleaning of surfaces because of its unique photocatalytic properties (such as photodegradation and photoinduced superhydrophilicity), stability, commercial availability, and ease of preparation [151, 152]. In the nanocomposite membrane research area, TiO_2 has also been incorporated into various membrane matrices to provide membrane with photocatalytic activities.

Rahimpour et al. [53] studied the effects of UV irradiation on the performance of TiO_2/PES nanocomposite membranes, and found UV-irradiated TiO_2/PES membranes had higher flux and enhanced fouling resistance when compared to corresponding nanocomposites. They attributed this enhancement to the photocatalysis and superhydrophilicity of TiO_2 under the UV irradiation. Similarly, after applying TiO_2 into PVDF membrane matrix and providing UV irradiation, Damodar et al. [54] obtained a superior membrane with enhanced permeability and fouling resistance, as well as high antibacterial capability. In another study, UV-cleaning process was carried out by Ngang et al. [55] on their TiO_2/PVDF nanocomposite membranes, allowing the recovery of water flux after filtration process.

1.1.2.3 Antimicrobial activity

Membrane biofouling due to the microbial growth and biofilm formation is one of the most challenging issues in membrane separation for water and wastewater treatment [153]. It decreases membrane permeability, reduces permeate quality, and increases

energy costs of the separation process. Developing antimicrobial membranes will likely increase membrane efficiency and application duration significantly. In addition, use of antimicrobial membrane helps to provide pathogen-free clean water.

Silver (Ag) is the most widely explored antimicrobial agent in nanocomposite membrane due to its excellent biocidal properties and successful applications in many areas such as antimicrobial plastics, coatings, and wound and burn dressing [154]. For example, Chou et al. [77] introduced AgNPs into cellulose acetate matrix for anti-bacterial applications. Zodrow et al. [79] impregnated AgNPs into polysulfone (PSU) matrix to improve biofouling resistance and virus removal. Zhang et al. [87] incorporated biogenic AgNPs into PES membrane and evaluated its anti-biofouling capability in a MBR system.

Many methods were developed to improve the dispersion and stability of AgNPs inside polymer matrix. For example, polyvinylpyrrolidone (PVP) or 2,4,6-triamino pyrimidine (TAP) [80, 83] was used as dispersant or compatibilizer in polymer casting solution to facilitate the dispersion of AgNPs so to improve antibacterial properties. In another study [85], pretreatment of AgNPs with amphiphilic polymer was carried out to improve the dispersion and compatibility of AgNPs with polymer matrix.

One challenge with the AgNPs inside the bulk matrices is its weak resistance to washing, as the AgNPs can be released either as NPs or in the dissolved form of Ag^{+} ions, so the antimicrobial ability of membranes would disappear with time. Accordingly, many efforts have been devoted to developing durable antimicrobial membranes by immobilizing AgNPs into the membrane's dense barrier layer (e.g., thin-film layer of TFC membrane, refer to Section 1.2.3) or graft them onto membrane surface through

stronger bonding (e.g., electrostatic attraction or chemical bonding, refer to Section 1.4). Other nanomaterials such as copper [82, 86, 91] and selenium [91] have also be explored for their potential applications to make antimicrobial membranes.

1.1.2.4 Platform sites for polymerization initiation

Nanomaterials with specific functional groups could be incorporated into membrane matrix to provide polymerization initiation sites for further surface modification. For instance, Daraei et al. [107] prepared PES nanocomposite membranes containing acrylate-alumoxane nanofillers and then grafted PAA on its surface to further improve dye removal rate and fouling resistance. Results showed that PAA grafting rate was improved due to the presence of carbon-carbon reactive double bonds on membrane surface as an active site for PAA chain growth.

1.1.3 Multiple effects introduced by hybrid materials

The effects of embedding TiO_2 coated MWNTs into the PES matrix on membrane morphology, properties and anti-biofouling were studied by Vatanpour et al. [46]. The resulting membrane showed enhanced hydrophilicity and pure water flux. During whey solution filtration, membrane exhibited improved fouling resistance, which could be attributed to the lower surface roughness and synergistic photocatalytic activity. The existence of carbon nanotubes was believed to reduce the electron/hole recombination and improve the photon efficiency. Crock et al. [127] designed a multifunctional membrane by incorporating AuNPs/exfoliated graphite nano-platelets into PSU membrane (Fig. 1.3). Their membranes showed enhanced compaction resistance and permeability as well as superior catalytic property on the reduction of 4-nitrophenol to 4-aminophenol by $NaBH_4$, where AuNPs served as the catalyst. Furthermore, the structure

and catalytic activity of such membranes could be controlled separately by changing the relative contents of corresponding components in the nanofiller hierarchy.

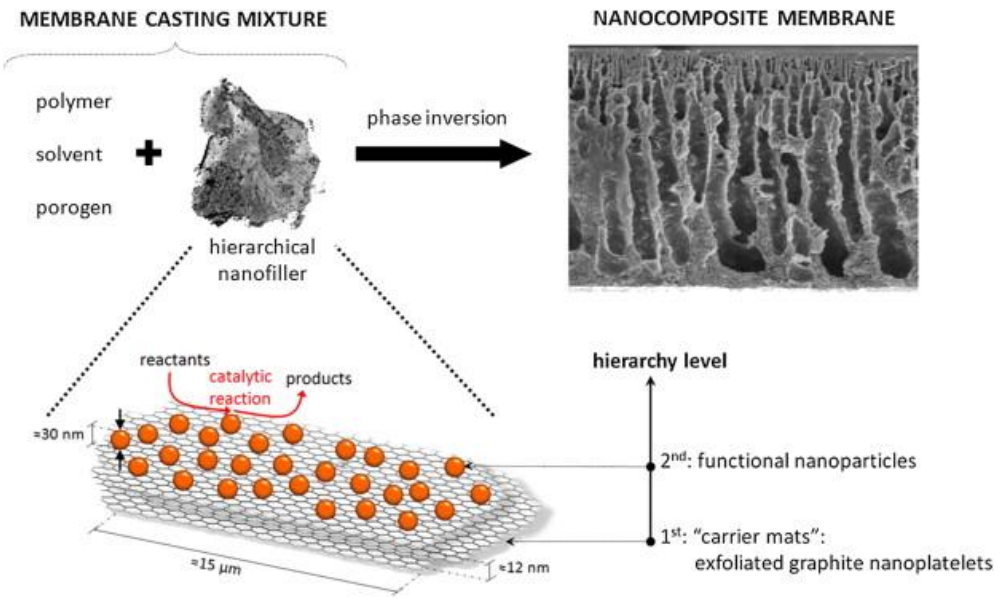

Fig. 1.3 Conceptual illustration of hierarchical nanofillers as building blocks for multifunctional nanocomposite membranes. Adapted with permission from [127].

In another study [64], nanocomposite membranes containing SiO_2/GO hybrid material were found to exhibit much better permeability, protein rejection, and fouling resistance than the SiO_2/PSU and GO/PSU membranes. The synergistic effect of SiO_2/GO could be attributed to its high hydrophilicity as well as special sandwiched structure that facilitated its dispersion in the PSU matrix.

1.2 Thin-film Nanocomposite (TFN)

Thin film composite (TFC) membrane consists of an ultra-thin barrier layer (commonly made of polyamide (PA)) atop a more porous supporting layer. It has been the major type of RO/NF membrane since being first developed by Cadotte in the 1970s [155], and widely used to desalinate seawater/brackish water or remove heavy metals, hardness, organic micropollutants such as pesticides, disinfection by-products (DBPs), endocrine disrupting compounds (EDCs), and pharmaceutically active compounds. Recently, the development of forward osmosis (FO)/ pressure-retarded osmosis (PRO) processes has further stimulated the development of TFC membrane, as there is a potential for further energy saving or even energy generation during the seawater/brackish water desalination.

Many efforts have been devoted to improve water flux, solute rejection and antifouling properties of TFC membranes in the past 30 years. One focus is to select or modify the supporting layer so the adhesion between the barrier layer and the supporting layer could be enhanced; the other is to optimize the barrier layer by varying the interfacial polymerization (IP) conditions, changing monomers, applying physical coating, or by chemical modification.

With the advent of nanocomposite, a new concept has been proposed based on dispersing nanomaterials into the ultra-thin barrier to improve membrane performance for water filtration [156]. By now, nanomaterials used in the past for conventional nanocomposite membrane preparation have also been explored to fabricate TFN membranes, including zeolites, CNTs, silica, Ag, TiO_2. Common fabrication process is through the *in-situ* IP process between aqueous m-phenylenediamine (MPD) and

trimesoyl chloride (TMC) organic solution as presented in Fig. 1.4. The nanofillers can be dispersed either in aqueous or in organic phase.

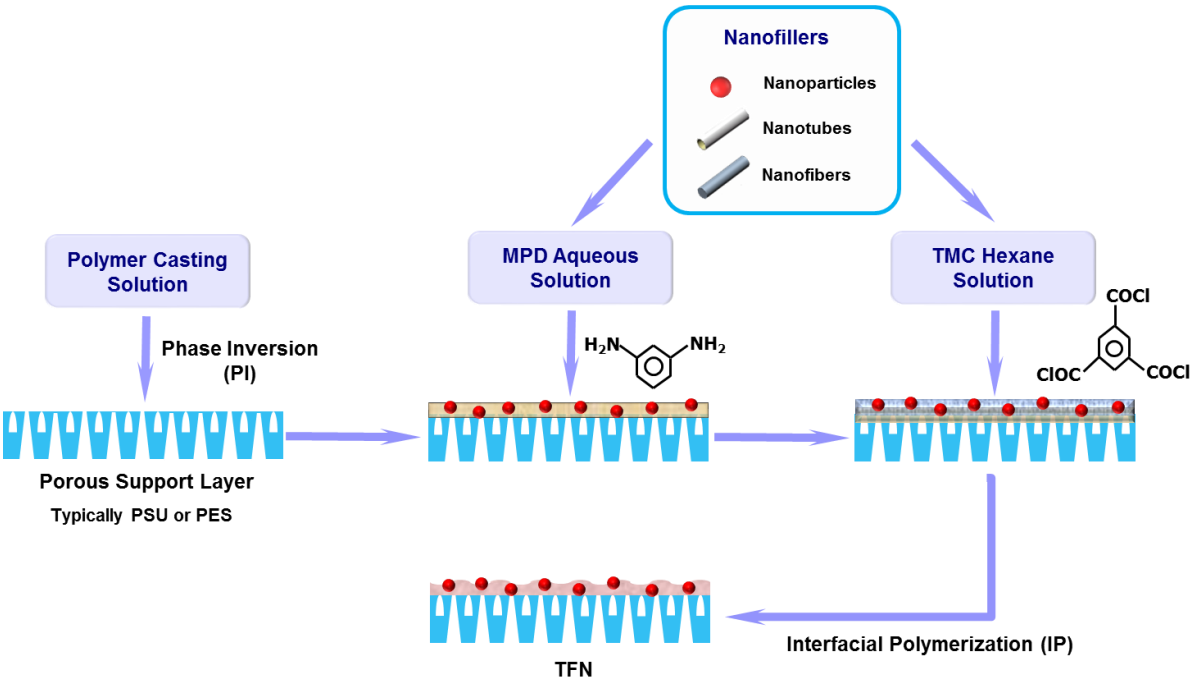

Fig. 1.4 Fabrication of TFN membranes through IP process

Table 1.2 lists, in a chronological order, the TFN membrane-related research publications. In the following sections, the effects of nanofillers on TFN membrane performance, such as trade-off relationship between permeability and selectivity, antifouling property, antimicrobial activity, chlorine resistance, and thermal stability are summarized.

Table 1.2 Summary of thin-film nanocomposite membranes

TFN		Particle Size	Loading wt% (Best performance)	Fabrication Method	Application	Performance	Published year and reference
Filler	**Polymer**						
Oxidized MWNTs	Pebax 1074 or PVA	OD = 20-40 nm L = 5-15 μm	0-20% of polymer (10% of PVA)	Coating + Solvent evaporation	Water/oil emulsion separation	Under 100 psi, optimal water flux is 330 L/m^{2}h, organic solute rejection is 99.8%; Fouling resistance ↑	2005 [157]
Zeolite (NaA)	PA	50-150 nm	0.004-0.4% (w/v) in organic phase	IP	RO	Surface hydrophilicity ↑; P_w ↑; Salt rejection no change New concept: TFN	2007 [156]
Ag NPs	PA	50-100 nm	10% of polymer in organic phase	IP	NF	Water flux and salt rejection no change Good antibiofouling property	2007 [158]
TiO_2 (P25)	PA	30 nm	1.0-9.0% (5.0%) Organic phase	IP	NF	Under 87 psi, optimal water flux is 9.1 L/m^{2}h, $MgSO_4$ rejection (95%, 2000 mg/L)	2008 [159]
Silica (LUDOX® HS-40)	PA	~ 13.2 nm	5-28% of PA	IP	Dioxane solution filtration	P_w ↑; Solute rejection ↓	2008 [160]
Zeolite (NaA and AgA)	PA	50-250 nm	0.4% (w/v) in organic phase	IP	RO	P_w ↑; Salt rejection no change; AgA-TFN membranes exhibited more hydrophilic and smooth surfaces.	2009 [161]
Zeolite	PA	97, 212, and 286 nm	0.2% (w/v) in organic phase	IP	RO	Smaller NPs produced higher permeability enhancements, but larger NPs produced more surface properties change	2009 [162]
Silica	PA	3 and 16 nm	0-0.4% (3nm) and 0-0.5% (16nm) in aqueous phase	IP	RO	P_w ↑; NaCl rejection ↗↘ Thermal stability ↑	2009 [163]
Oxidized MWNTs or Cellulose Nanofibers	PVA	OD = 8-15 nm L = 10-50 μm OD = ~ 5 nm L < 10 μm	10% of PVA 0.25% and 1.25% of PVA	Coating + Cross-linking	UF of oil/water emulsion	P_w ↑; Solute rejection slightly decreased Suggested the presence of directional water channels through the interface between filler and PVA matrix	2010 [164]
Carboxylic MWNTs	Polyester	OD < 8 nm L = 10-30 μm	0.05% (w/v) in aqueous phase	Modified IP O/A/O	NF	P_w ↑; Na_2SO_4 rejection ↑ Immerse support layer into organic phase before conventional IP process improved TFN performance	2010 [165]
MWNTs	PA	OD = 9-12 nm L = 10-15 μm	0.1, 0.5, 1, 5% (w/v) in aqueous phase	IP	RO	Surfactant (Triton X-100) was used to facilitate the dispersion of MWNTs; Chlorine resistance ↑	2010 [166]
Zeolite (LTA)	PA	~ 250 nm	0.2% in organic phase	IP	Seawater RO	Under 800 psi, optimal permeate flux is around 42 L/m^{2}h, NaCl rejection (99.4%, 32000 mg/L) Defects and molecular-sieving largely govern transport through zeolite-TFN membranes	2010 [167]
Functionalized Silica	PA	-	0.04, 0.4% in aqueous phase	IP	RO PV	Small-angle neutron scattering (SANS) was used to study the dispersion of silica NPs in thin-film layer Thermal stability ↑; P_w ↑; NaCl rejection ↓	2010 [168]
Functionalized MWNTs	PA	OD = ~ 30 nm L_1 = 10-30 μm L_2= 0.5-2.0 μm	0.01-0.06% in aqueous or organic phase	IP	NF	P_w ↑; Solute rejection no change Nanogaps around the external surface of fillers provide a low resistance solvent pathway	2011 [169]
Oxidized MWNTs	PA	-	0-0.2% (w/v) in aqueous phase	IP	RO	Surface hydrophilicity ↑; P_w ↑; NaCl rejection ↓	2011 [170]
Metal alkoxide (TTIP, BTESE, PhTES)	PA	-	0-5% in organic phase	IP	NF/RO	Pore size ↑; P_w ↑ With PhTES, P_w ↑, NaCl rejection no change	2011 [171]
Zeolite (NaX)	PA	40-150 nm	0.004, 0.01, 0.04, 0.2% (w/v) in organic phase (0.2%)	IP	RO	Thermal stability ↑; Hydrophilicity ↑; P_w ↑; NaCl rejection no change	2011 [172]

Hydrophilized ordered mesoporous carbon (OMC)	PA	-	0-10% in aqueous phase (5%)	IP	NF	Hydrophilicity ↑; Protein adsorption ↓ P_w ↑; NaCl rejection ↓; Na_2SO_4 rejection slightly ↓	2011 [173]
Hydrophilic macromolecules + Ag^+	PA	11000 Da	0.25% of (MDI+PEG) in organic phase 0.25% of AgNO3 in aqueous phase	IP	Seawater RO	Good seawater desalination performance Fouling resistance ↑; Biofouling resistance ↑	2011 [174]
Ag NPs	PA	Several nanometers	Dispersed in aqueous phase Finally, 10% in PA	IP	NF	Surface hydrophilicity ↑; P_w ↑; Salt rejection no change Biofouling resistance ↑	2012 [175]
Mesoporous silica (MCM-41) and nonporous silica	PA	~ 100 nm ~ 100 nm	0-0.1% in organic phase (0.05%)	IP	RO	Surface hydrophilicity ↑; P_w ↑; Salt rejection no change Under 300 psi, optimal permeate flux is 46.6 L/m^{2}h, NaCl rejection (97.9, 2000 mg/L) Porous structures of filler contributed significantly to the water flux enhancement	2012 [176]
Proteoliposome with aquaporin	PA	< 150 nm	10 mg/ml in aqueous phase	IP	RO	P_w ↑; Salt rejection no change Under 72.5 psi, water flux is 20 L/m^{2}h, NaCl rejection (~97%, 584.4 mg/L)	2012 [177]
Aluminosilicate SWNTs	PVA	OD = 2.7 nm L > 200 nm	0-20% (v/v) in PVA solution	Coating + Cross-linking	NF	Surface hydrophilicity ↑; Roughness ↓ P_w ↑; Salt rejection ↑	2012 [178]
Zeolite (NaY)	PA	40-150 nm	0-0.4% (w/v) in organic phase (0.1%)	IP	FO	P_w ↗↘; NaCl rejection ↘↗ Surface roughness ↗↘	2012 [179]
Alumina NPs	PA	~ 14 nm	1% in organic phase	IP	NF	Surface hydrophilicity ↑; P_w ↑; Salt rejection no change	2012 [180]
Oxidized MWNTs	PA	OD = 5-10 nm L = 10-30 μm	5% of PA	IP	Oil sand process-affected water treatment	Water flux ↑; Organic fraction rejection ↑ Fouling resistance ↑	2013 [122]
Zwitterion functionalized CNTs	PA	OD = 1.5 nm L = 1 μm	0, 9, 20% of PA (20%)	Deposition + IP	RO	Water flux and salt rejection ↑ Under 530 psi, optimal water flux is 48.8 L/m^{2}h, NaCl rejection (98.6%, 2542 mg/L)	2013 [181]
Carboxylic MWNTs	PA	OD < 8 nm L = 10-30 μm	3 mg per membrane sample	Deposition + IP	RO	High electrical conductivity (~400 S/m), NaCl rejection (>95%, 1000 mg/L), high water flux Biofouling resistance ↑ under electric potential	2013 [182]
Oxidized MWNTs	PVA	OD = 10-30 nm L = 0.5-2 μm	0, 5, 10, 15% of PVA	Electrospinning+ Cross-linking	UF	Water flux ↑; Organic fraction rejection (99.5%) Good mechanical properties	2013 [183]
PMMA modified MWNTs	PA	OD = 20-30 nm L < 50 μm	0-5.4 g/L in organic phase (0.67 g/L)	IP	NF	P_w and selectivity ↑	2013 [184]
PMMA modified MWNTs	PA	OD = 20-30 nm L < 10 μm	0.67, 1.33, 2.0 g/L in organic phase (0.67)	IP	NF	Under 145 psi, optimal water flux is 69.7 L/m^{2}h, Na_2SO_4 rejection (99.0%, 2000 mg/L)	2013 [185]
Carboxylic MWNTs	PA	OD < 8 nm L = 10-30 μm	0-2.0 mg/ml in aqueous phase (0.5)	Modified IP O/A/O	NF	P_w ↗↘; Hydrophilicity ↗↘ Under 87 psi, optimal water flux is 21.2 L/m^{2}h, Na_2SO_4 rejection (>70%, 5 mmol/L)	2013 [186]
Amine functionalized MWNTs	PA	OD = ~ 5 nm L = ~ 50 μm	0.01, 0.05, 0.1% in aqueous phase	IP	FO	Hydrophilicity ↑; S value ↓ P_w and salt rejection ↑ in both AL-FS and AL-DS modes	2013 [187]
Zeolite (Silicalite-1)	PA	-	0-0.2% in organic phase	IP	RO	P_w, hydrophilicity, and acid stability ↑ Silicalite-1 is superior to NaA in fabricating TFN	2013 [188]
Zeolite (NaA)	PA	-	0-0.2%(w/v) in organic phase	IP	RO	Water flux and salt rejection ↑	2013 [189]

Aminated Zeolite	PA	≤ 100 nm	0.02% in aqueous solution	IP	RO	P_w ↑; Chlorine resistance ↑ Under 800 psi, water flux is 37.8 L/m^{2}h, NaCl rejection is 98.8% (32000 mg/L)	2013 [190]
Zeolite A	PA	250 nm	0.2% in organic phase	IP	RO	P_w and salt rejection ↑ Resistance to physical compaction ↑	2013 [191]
Modified mesoporous silica	PA	~ 100 nm	0-0.07% in aqueous phase (0.03%)	IP	NF	Under 87 psi, optimal water flux is 32.4 L/m^{2}h, Na_2SO_4 rejection (> 80%, 5 mmol/L)	2013 [192]
Mesoporous silica	PA	~ 164 nm	0-0.1% (w/v) in organic phase (0.1)	IP	RO	P_w and hydrophilicity ↑ Under 232 psi, optimal water flux is 53 L/m^{2}h, NaCl rejection (>96%, 2000 mg/L)	2013 [193]
Aminated hyper branched silica	PA	~ 7 nm	0.02% in aqueous solution	IP	RO	P_w ↑; Chlorine resistance ↑ Under 800 psi, water flux is 34.5 L/m^{2}h, NaCl rejection is 97.7% (32000 mg/L)	2013 [194]
Silica	Fluoropolyamide	-	0-1.0% (w/v) in aqueous phase (0.1)	IP	NF	P_w ↑; Na2SO4 rejection ↗↘ Under 87 psi, optimal water flux is 15.2 L/m^{2}h, Na_2SO_4 rejection (85.0%, 2000 mg/L)	2013 [195]
Aluminosilicate SWNT	PA	OD = ~ 2.7 nm L = 150 nm	0.05, 0.1, 0.2% (w/v) in organic phase	IP (single pass flow)	Low pressure RO	P_w and salt rejection ↑	2013 [196]
Aminosilanized TiO_2	PA	~ 21 nm	0.005, 0.05, 0.1% in aqueous solution (0.005%)	IP	NF	P_w and selectivity ↑; Thermal stability ↑ Under 110 psi, optimal water flux is 12.3 L/m^{2}h, NaCl rejection is 54% (2000 mg/L)	2013 [197]
Organoclay (Cloisite 15A and 30B)	Chitosan	-	0.5, 1, 2% in casting solution	Coating on PVDF substrate	NF for dye removal	Dye removal ↑ Adsoption is the dominating removal mechanism	2013 [198]
Proteoliposome containing Aquaporin Z	PEI	~ 107.8 nm	0, 50, 200, 400 in Lipid-to-protein ratio (200)	PEI crosslinking	NF	Under 14.5 psi, optimal water flux is 36.6 L/m^{2}h $MgCl_2$ rejection (95%, 100 mg/L)	2014 [199]
Carboxylic MWNTs	PA	OD = 20-40 nm L = 1-5 μm	0-0.1% in MPD solution	IP	RO	Hydrophilicity ↑; Water flux ↑ Solute rejection no change Better antifouling and antioxidative properties	2014 [200]

IP: Interfacial polymerization
PA: Polyamide
PV: Pervaporation
P_w: Water permeability

1.2.1 Effects on the trade-off relationship between permeability and selectivity

As the barrier of TFC membrane, PA thin-film layer largely controls the membrane performance in terms of permeability, selectivity, and fouling resistance. The incorporation of nanomaterials into the PA layer could modify the physicochemical properties of the membrane such as hydrophilicity, charge density, porosity, and cross-linking or even provide special water channels that may overcome the permeability/ selectivity trade-off relationship.

Based on the solution-diffusion theory widely used to describe the mass transport in the PA TFC membrane [201, 202], an increase in hydrophilicity of membranes could facilitate water solubilization and diffusion through the membrane, thus improve water permeability [203].

So far, almost all of the studies using hydrophilic nanofillers resulted in a TFN membrane with decreased contact angle, indicating an enhanced surface hydrophilicity. For example, the contact angle of zeolite-PA TFN membrane decreased from around 70 ° to 40 °with increasing zeolite loading from 0 to 0.4%(w/v) in the organic phase [156]. The contact angle for the oxidized MWNTs-PA TFN membranes decreased from around 70 °to 25 °with increasing MWNTs loading from 0 to 0.2%(w/v) in the aqueous phase [204]. For the mesoporous silica-PA TFN membranes, the contact angle was decreased from around 57 °to 28 °with increasing silica loading from 0 to 0.1%(w/w) in the organic phase [205]. Accordingly, all these studies exhibited an enhanced water permeability with an increasing nanofiller loading.

The decrease of contact angle in the presence of embedded NPs could be caused by two reasons. First, the NPs may hydrate and release heat when contacting with the MPD

aqueous solution [162]. This process may affect the IP reaction between MPD and TMC, and subsequently the chemical structure of the PA thin-film. If more number of the acyl chloride groups in TMC remained on the surface without reacting with amine groups, the hydrolysis of acyl chloride could generate carboxylic acid functional groups; thus, surface hydrophilicity would increase [206]. Second, the embedded hydrophilic nanomaterials can be exposed on the membrane surface, providing more hydrophilic functional groups to membrane surface. This mechanism is similar to the one in the conventional nanocomposite membrane that improved surface hydrophilicity.

Besides the hydrophilicity, the cross-linking condition and thickness of thin-film layer are also important factors controlling the water permeability and salt rejection [207]. In general, lower degree of cross-linking and thinner thickness of thin-film layer result in higher water permeability. Embedding nanofillers in the PA matrix could reduce the cross-linking (or integrating) in the thin-film layer by disturbing the reaction between amine groups and acyl chloride groups or even forming nanovoids around the interfaces between nanofiller and PA matrix.

Based on the FTIR and XPS results, Lind et al. [167] pointed out that all TFN membranes prepared in their study were less cross-linked than the corresponding TFC membrane; however, the cross-linking extent didn't show a strong correlation with water or salt permeability, which suggested that defects or molecular-sieving effect might have played a major role in the membrane separation performance. In another study examining the effects of MWNTs on TFN membrane performance, Roy et al. [169] showed that the nanogaps between the external surfaces of MWNTs and the polymer matrix could provide a very low resistance pathway for solvent leading to the permeability

enhancement. Meanwhile, the PA matrix was still the main contributor to the solute rejection.

In addition to causing changes for the polymer cross-linking, the incorporation of nanofiller may also provide additional channels for facile transport of water but not solutes. Jeong et al. [156] introduced the zeolite-A NPs into TFN membrane, resulting in a higher water flux with constant salt rejection. After blocking the pores inside the zeolite, they found the permeability enhancement obviously decreased, although the permeability was still higher than that of conventional TFC membrane. This hydrophilic molecular-sieving NPs may provide preferential flow paths for water molecules. Yin et al. [176] compared the effects of two silica NPs with similar outside diameter (~100 nm) while different internal structures on the TFN membrane performance. When compared to the nonporous silica NPs, mesoporous silica NPs (MCM-41) containing highly ordered hexagonal pores exhibited significantly higher impact on water permeability. With the non-porous silica NPs, the reduction in polymer cross-linking could still occur but there will be no water permeation through internal structures of NPs; therefore, while the observed water flux in the membrane containing non-porous silica is higher than the conventional TFC, it is less than that in the membrane containing mesoporous silica. This result indicated that the internal pores of nanofiller contributed significantly to water permeability enhancement. In another study [199], proteoliposome containing aquaporin, a typical water channel protein, was fully encapsulated into the thin-film layer through crosslinking of poly(ethyleneimine) (PEI). This novel TFN membrane showed a significantly enhanced water permeability and typical NF rejection to $MgCl_2$.

In order to overcome the permeability/selectivity trade-off relationship observed for polymeric membranes, solute rejection should remain near the same when the water permeability is improved. Based on the open literature, the high solute rejection seemed to be maintained by a combination of steric and Donnan exclusion [208]. So the goal of breaking the trade-off relationship mainly rely on one or more factors including a moderate reduction on cross-linking, an enhanced membrane surface charge density, an appropriate nanovoids, and additional water channels. For example, zeolite could provide molecular-sieving channels and enhanced charge density; mesoporous silica could provide large water channels combined with enhanced charge density; while aquaporin could provide exclusive water channels.

To fully exploit the favorable properties of nanomateirals, we need to introduce the nanofillers with appropriate size, internal structure, and surface properties, and ensure suitable interfacial interactions with polymer matrices. Considering a typical thickness of the thin-film layer approximates several hundred nanometers [163, 207], the nanofiller particle should not be too large to ruin the barrier. The effects of crystal size of zeolite in the TFN membrane were investigated [162], and small sized NPs (~97 nm) were found to best match the thin-film thickness and provided permeability enhancement. To improve the dispersion of nanofillers and the interaction between nanofillers and polymer matrix, it is common to modify nanofillers surface prior the embedding process. Using CNTs as an example, the most common modification is to treat CNTs by concentrated acid to generate oxygen-containing functional groups so an adequate dispersion could be achieved for the membrane fabrication. It is also needed to provide good interactions

between CNTs and polymer matrices. This is consistent with the strategy used in the conventional nanocomposite membrane preparation (Section 1.1.1).

1.2.2 Effects on antifouling properties

As mentioned above (section 1.2.1), the introduction of hydrophilic nanofillers into the PA structure will increase the surface hydrophilicity and generally help mitigate surface fouling. Kim et al., [173] demonstrated that after incorporating hydrophilized ordered mesoporous carbons (H-OMCs) into PA thin-film layer, membranes showed an enhanced surface hydrophilicity (surface contact angle was decreased from around 79 °to 46 °). With increasing H-OMCs loading, the adsorption of bovine serum albumin (BSA) was clearly decreased, indicating that the antifouling capability to organic protein materials was enhanced by H-OMCs. Another study showed that after incorporating in-situ hydrophilic surface modifying macromolecules (iLSMM) [174], the TFN membrane surface exhibited significantly improved hydrophilicity. Their long term (200 h) fouling tests with sodium humate, silica particles, and chloroform showed the TFN membranes had a much lower flux reduction when compared to the conventional TFC membranes. The reduced flux reduction was also observed by Zhao et al [200] when using TFN membrane prepared by MWNTs to treat feed solution containing foulants $Ca(HCO_3)_2$ or BSA.

1.2.3 Effects on antibacterial properties

Built on the successful applications of biocidal materials in conventional nanocomposite membrane, it is reasonable to expect that the antimicrobial materials could also be applied for TFN membrane applications. In one study, Lee et al. [158] incorporated AgNPs into the PA structure during the IP process, where AgNPs were

homogenously dispersed in the organic phase. The membrane demonstrated a dramatic anti-biofouling capability on *Pseudomonas* with a good stability of the incorporated AgNPs. Rana et al. [174] incorporated iLSMM containing silver salts (such as silver citrate hydrate (SCH), silver lactate (SL), and silver nitrate (SN)) into the PA structure. The disk test results showed that the antimicrobial capability came in the order of SN > SL > SCH. In another study, AgNPs was dispersed in MPD aqueous solution [175] and the prepared membrane showed clear antibacterial properties. However, in these studies, there was no long time filtration test conducted with feed stream containing bacteria.

Considering the dense structure and good ion rejection property of PA barrier, most of the embedded AgNPs (released as silver ions) inside the PA matrix is unlikely to be exposed to the interface between membrane and feed stream containing bacteria to act as biocidal material. Although this kind of membrane may show a relatively slow leaching rate, it can't guarantee a long-term antimicrobial activity. Accordingly, an attempt was made to prepare an anti-biofouling membrane by incorporating zeolite nanocrystals in the silver form (AgA) by Lind et al., [161]. Due to the significant bactericidal activity of AgA nanocrystals, it was expected that antimicrobial property of TFN membrane would be improved. However, besides exhibiting a higher water permeability and comparable salt rejection, the membrane didn't show the strong biocidal activity as expected.

1.2.4 Effects on chlorine resistance

The amide linkage in PA TFC membranes is susceptible to attack by chlorine, leading to the undesired degradation that could essentially ruin the membrane. Therefore, much attention must be paid to prevent the membrane from being exposed to strong oxidants especially chlorine [209]. Solutions proposed include coating PA surface with

chlorine resistant materials [210] and introducing specific functional groups to the amide structure [211].

Introducing nanomaterials into PA structure provides a new dimension to design chlorine resistant membranes. When MWNTs were incorporated into PA thin-film layer at a loading of 0.1-1 wt%, for example, the membrane showed a much improved chlorine resistance [166]. It was believed that the interactions between the carboxylic group of modified MWNTs and the amide bond made the membrane more stable against chlorine. Similarly, Zhao et al. [200] found the MWNTs embedded TFN membrane had a better chlorine resistance and attributed this phenomenon to the protection of amide linkage by electron-rich MWNTs.

Because amide bonds are the main target of chlorine attack, introduction of additional amide bonds or amino groups to the membrane seems to be a reasonable strategy to protect the PA cross-linking structure. Hence, Kim et al. incorporated aminated zeolite [190] or hyper-branched polyamide modified silica NPs [194] into the PA thin-film layers. The results demonstrated that these two TFN membranes had an enhanced chlorine resistance. This enhanced resistance could result from: 1) the intermolecular hydrogen bonding between aminated NPs and PA structure, which mitigates the replacement of hydrogen by chlorine, and 2) the additional amide bonds or amino groups introduced by aminated NPs that renders the membrane more resistant to the chlorine attack.

1.2.5 Effects on thermal stability

Jadav et al. [163, 168] found that after incorporating silica NPs into the PA thin-film layer, the thermal stability of the TFN membranes was increased. This phenomenon could be attributed to the stronger electrostatic and steric interactions between silica and PA in the modified polymer network structures. The incorporation of zeolite (NaX) [172] inside the PA structure also led to an TFN membrane with a higher thermal stability and an enhanced filtration performance. However, no significant change in the thermal decomposition temperature was observed in these studies, suggesting that there was no strong interaction between the nanofillers and polymer backbone chains. To improve the interaction between nanofiller and PA structure for further improvement of thermal stability, TiO_2 was aminosilanized prior to IP process [197], resulting in a membrane that indeed had an better thermal stability, in addition to an improved permeability and selectivity.

1.3 TFC with nanocomposite substrate

This class of membranes was first developed to investigate the effects of nanofiller on membrane compaction behavior, which is listed along with other studies in Table 1.3. In that study by Pendergast et al. [212], silica or zeolite NPs were embedded into the PSU substrate, which was then used in the IP process to prepare TFC membranes for RO. The prepared membranes showed a higher initial permeability and experienced less flux decline during the compaction when compared with the original TFC membrane. The existence of nanomaterials was believed to have provided necessary mechanical support to mitigate the collapse of porous structure and thickness reduction upon compaction. Further study found that membranes with nanocomposite substrate undergone far less physical compaction and played an important role in maintaining high water permeability [191], as illustrated in Fig. 1.5.

Table 1.3 Summary of TFC membranes with nanocomposite substrate

TFC with Nanocomposite Substrate		Particle Size	Loading wt.% (Best performance)	Fabrication Method	Application	Performance	Published year and reference
Filler	Polymer						
SiO_2	PSU	34-130 nm	-	PI + IP	RO	Minimize the deleterious effects of physical compaction	2010 [212]
Zeolite		250-300 nm	-				
MWNTs	PSU	Diameter = 5-10 nm Length = 10-30 μm	0-5 (5)	PI + IP	NF/RO	Hydrophilicity of substrate ↑; P_w ↑	2012 [175]
SiO_2	PAN	< 10 nm	6	Electrospinning + Dip-coating + Cross-linking	PRO	Mechanical strength of substrate ↑ Intrinsic P_w (A) ↑; S ↓	2013 [213]
Zeolite A	PSU	250 nm	20% of PSU	PI + IP	RO	P_w and rejection of substrate ↑ P_w and salt rejection ↑ Resistance to physical compaction ↑	2013 [191]
Zeolite (NaY)	PSU	40-150 nm	0, 0.5, 1.0 (0.5)	PI + IP	FO	P_w and hydrophilicity of substrate ↑; S ↓; ICP ↓	2013 [214]
MWNTs	PES	Diameter = 10-20 nm Length = 1-5 μm	0-2.5	PI + IP	FO	Tensile strength of substrate ↑ P_w and salt rejection ↑; S ↓ and ICP ↓	2013 [215]
TiO_2 (P25)	PSU	~ 21 nm	0.5	PI + IP	FO	P_w, hydrophilicity, and porosity of substrate ↑ P_w ↑, S ↓ and ICP ↓	2013 [216]
TiO_2 (P25)	PSU	~ 21 nm	0-1.0 (0.5)	PI + IP	FO	P_w, hydrophilicity, and porosity of substrate ↑ P_w ↑, S ↓ and ICP ↓	2014 [217]
TiO_2 (P25)	PSU	~ 21 nm	0-0.9 (0.6)	PI + IP	FO	P_w, hydrophilicity, and porosity of substrate ↑ P_w ↑, S ↓ and ICP ↓	2014 [218]

PI: Phase inversion
IP: Interfacial polymerization
P_w: Water permeability
S: Structural parameter

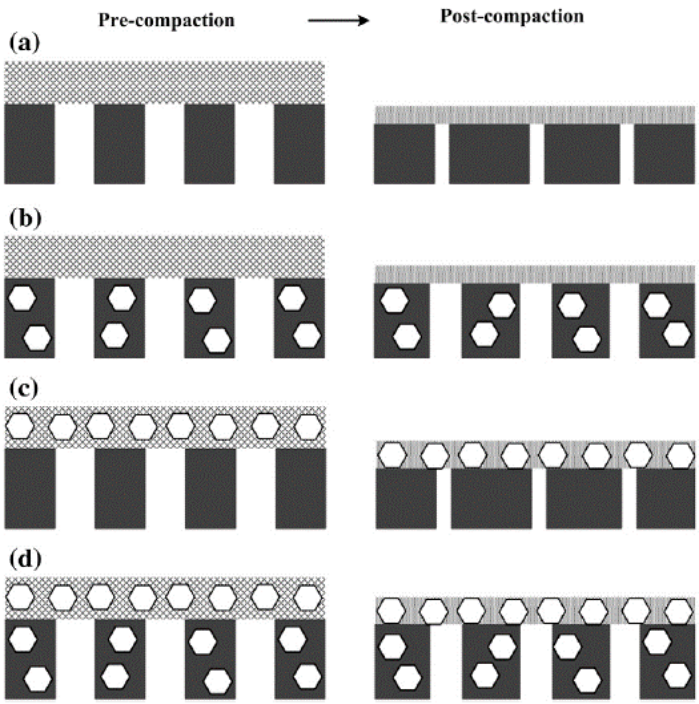

Fig. 1.5 Schematic drawings showing the proposed physical changes to support and thin film structure during compaction in (a) TFC, (b) TFC with nanocomposite substrate, (c) TFN, and (d) TFN with nanocomposite substrate. Adapted with permission from [191].

Recently, this concept was mainly implemented to mitigate internal concentration polarization (ICP, occurring inside the porous support layer), which may negatively impact the FO and PRO processes because it can significantly reduce the available osmotic driving force and hence lower the water flux [219]. The nanocomposite substrate may have an enhanced hydrophilicity and a reduced structural parameter (S) controlled by thickness (l), tortuosity (τ) and porosity (ε). Generally, a large S value inevitably leads to severe ICP. The relationship between S and those membrane parameters (l, τ, ε) is as follow [220]:

$$S = \frac{l \cdot \tau}{\varepsilon} \quad (1)$$

Ma and et al. [214] incorporated zeolite into PSU substrate, resulting in a significant reduction of S from 0.96 mm to 0.34 mm and a higher water flux under either Al-DS (active layer facing draw solution) or AL-FS (active layer facing feed solution) condition. They attributed this phenomenon to an improved porosity, better hydrophilicity and additional water pathways through porous NPs. This is the first study that demonstrated the possibility to use porous NPs and nanocomposite substrate to control ICP in FO operation. Subsequent studies used MWNTs [215] and TiO_2 [216-218] to mitigate ICP problem in the nanocomposite substrate for FO process. The resulting membranes all showed an enhanced FO performance with a reduced S. For example, the S value of the membrane containing MWNTs decreased from 3.939 mm to 2.042 mm. Furthermore, the same substrate also showed an enhanced tensile strength, another desirable property change for practical FO application.

1.4 Surface located nanocomposite

In addition to membrane structure, porosity and thickness, membrane surface properties such as hydrophilicity, pore size, charge density, and roughness have a major impact on the membrane performance in terms of separation and antifouling characteristics. Modification of surface properties, therefore, could significantly improve the efficiency of membrane water treatment, as for surface-located nanocomposite membranes listed in Table 1.4. The process of preparing this type of membranes has minimal effects on the membrane's intrinsic structures, so there is a good potential of implementing such an approach on commercially available membranes.

Surface located nanocomposite membranes could be prepared based on methods such as self-assembly, coating/deposition, and chemical grafting (Table 1.4). Those

fabrication methods can be implemented individually or be involved simultaneously, for example, during the layer-by-layer assembly process, the electrostatic attraction is a common assembly force. Those methods are listed here based on their most unique properties such as bonding force and bonding process.

Table 1.4 Summary of surface located nanocomposite membranes

Fabrication Method	Nanomaterial	Application	Performance	Reference
Self-assembly	TiO_2	RO; UF; NF; PMR	Hydrophilic; Fouling resistance ↑; Antimicrobial activity under UV	[221-229]
Coating/Deposition	TiO_2	UF	Hydrophilic; Fouling resistance ↑	[21, 53, 230, 231]
	PANI	UF	Hydrophilic; Fouling resistance ↑	[135]
	GO	NF	High water flux, good dye rejection	[232]
	GO/TiO_2	UF	High flux and photodegradation activity	[233]
	CNTs	Viral and bacterial pathogens removal; Drinking water treatment	Significant antimicrobial activity	[234, 235]
Adsorption-reduction	Ag	RO; UF	Antimicrobial activity	[153, 236-238]
Electrostatic attraction	Ag	UF	Antimicrobial activity	[239]
	Silica	FO	Hydrophilic; Good organic fouling resistance	[240]
	Cu	RO	Antimicrobial activity	[241]
Layer-by-layer assembly	CNTs	RO	Thermal stability ↑; Chlorine resistance ↑	[242]
	GO	NF; PV; RO	Used as rejection layer ; Chlorine resistance ↑	[243-245]
	Ag	NF; FO	Antimicrobial activity	[246]
	Aquaporin	NF	P_w ↑; $MgCl_2$ rejection ↑	[247]
Chemical grafting	TiO_2	NF	Fouling resistance ↑	[248]
	CNTs	RO	Antimicrobial activity	[249]
	Ag/CNTs	Water disinfection	Antimicrobial activity	[250]
	Ag	RO; UF	Antimicrobial activity	[251, 252]
Cross-linking	Cellulose nanofiber	UF	Hydrophilic; Fouling resistance ↑	[253]
Colloidal precipitation	TiO_2	UF	P_w ↑; HA rejection ↑	[254]
Low temperature hydrothermal process	TiO_2	Membrane distillation	Fouling resistance ↑	[255]

1.4.1 Self-assembly

Self-assembly is the main process used to attach TiO_2 NPs onto specific membrane surfaces containing -COOH, $-SO^{3-}H^{+}$, and sulfone groups through coordination and H-bonding interactions (Fig. 1.6) [222, 224]. Membrane surfaces without these functional

groups could be pretreated to introduce such groups prior to the self-assembly process. For example, sulfonated PES [223, 225], polyimide (PI) blended PES [227], poly(styrene-alt-maleic anhydride)(SMA) blended PVDF [228], and poly(acrylic acid) (PAA) modified polypropylene membranes [229] were all successfully used to carried out the TiO_2 self-assembly process. During these studies, the incorporation of TiO_2 NPs on membrane surface not only increased membrane hydrophilicity but also provided membrane with photocatalytic properties.

Bae and et al. [223, 225] introduced TiO_2 self-assembled nanocomposite membranes into membrane bioreactor (MBR) and found the membrane fouling was significantly reduced due to the increased hydrophilicity of the membrane surface. Their studies also proved that nanocomposite membrane showed lower extent of cake layer formation and irreversible fouling.

Under UV light irradiation, TiO_2 self-assembled membranes showed clear antimicrobial activities [221, 222], self-cleaning [226] and organic material decomposition capabilities [229], all attributable to the photocatalytic property of TiO_2.

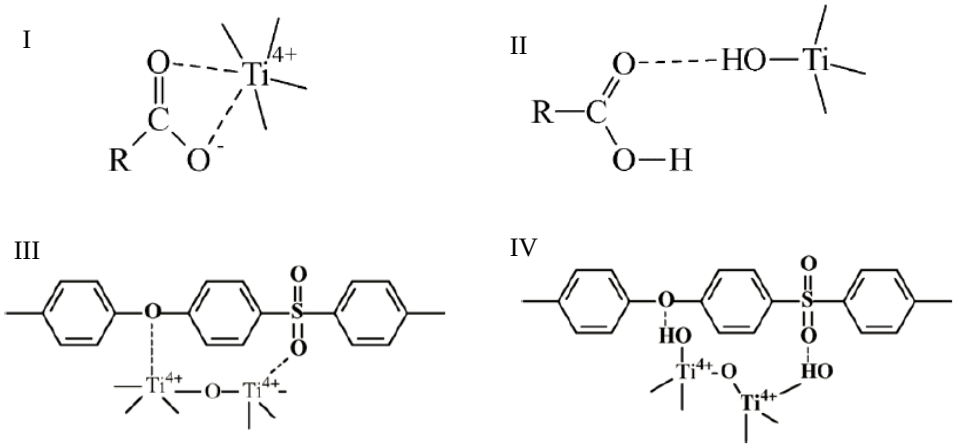

Fig. 1.6 Mechanism of self-assembly of TiO_2 NPs onto specific membrane surface (Adapted with permission from [222, 224]). I. A bidendate coordination of carboxylate to Ti^{4+}; II. A H-bond between carbonyl group and hydroxyl group of TiO_2. III. A coordination of sulfone group and ether bond to Ti^{4+}; IV. A H-bond between sulfone group and ether bond and hydroxyl group of TiO_2.

1.4.2 Coating/Deposition

Coating/Deposition is another widely used process to prepare surface located nanocomposite in which straight forward dip-coating or filtration-deposition are applied to place nanomaterials onto membrane surface. For instance, Bae and Tak [21] deposited TiO_2 NPs onto different polymeric membrane (PSU, PVDF and PAN) surfaces and compared their performance with TiO_2 entrapped membranes in a MBR system. They found TiO_2 deposited membranes showed a greater fouling mitigation effect because of a large amount of TiO_2 located on membrane surface. Han et al. [232] deposited an ultrathin (22-53 nm thick) GO barrier onto a MF membrane surface and demonstrated that the prepared membrane had a much higher water flux and good rejection for organic dyes. However, one shortage of coating/deposition method is the potential loss of deposited nanomaterials with time due to the weak interactions between nanomaterials

and membrane surface. This may seriously hinder its applications, particularly in cross-flow systems.

1.4.3 Electrostatic attraction

Electrostatic attraction has been explored to attach positively charged PEI encapsulated AgNPs [239] or CuNPs [241] and ($-N(CH_3)_3^+$) modified silica NPs [240] onto negatively charged membrane surfaces to enhance membrane's antimicrobial and antifouling properties. The results indicated that membranes covered with AgNPs and CuNPs showed a clear antimicrobial activity, while superhydrophilic silica covered membrane showed enhanced antifouling capability due to the lower adhesion force between organic foulant and membrane surface. However, one challenge here is the quick release of silver or copper ions leading to a fast depletion of antimicrobial capability. Using CuNPs covered membrane as an example, over 30% of the loaded copper will detach from the membrane surface into water either as Cu^{2+} or as NPs during the first two days. The detachment rate is expected to increase when the membrane is utilized under the cross-flow configuration, especially with a feed solution of low pH, high ionic strength, and high concentrations of chelating agents or organic ligands. To maintain a sufficient antimicrobial activity, frequent recharge of those nanoparticles is necessary.

1.4.4 Adsorption-reduction

Silver NPs could also be attached onto membrane surfaces through an adsorption-reduction mechanism, where silver ions were first adsorbed by the membrane surface, and then reduced by chemical agents such as formaldehyde [236], vitamin C (VC) [237], and ascorbic acid [153] or under light irradiation [238]. Using this approach, Zhu et al. [153] prepared chitosan based membranes immobilized with ionic or metallic silver and

then compared their anti-biofouling performances by using two typical bacteria (*E. coli* and *Pseudomonas sp.*). Although both membranes showed effective anti-bacterial and anti-biofouling activities, the membrane with metallic silver possessed more stable and better overall anti-biofouling performance.

1.4.5 Layer-by-layer assembly

During the lay-by-lay assembly, electrostatic attraction, hydrogen bonding, and/or chemical bonding could all be involved in the attachment of multiple layers of nanomaterials onto the membrane surface. However, the electrostatic attraction is the most common force exploited, notable between polycation and polyanion species. For instance, Park et al. [242] used PAH as polycation and PAA containing carboxylated MWNTs as polyanion to do the assembly on the negatively charged PSU membrane surface. After thermal cross-linking, the membrane showed an enhanced thermal stability and chlorine resistance. Wang et al. [243] used PEI modified GO as polycation and PAA as polyanion to prepare PAN-based NF membranes, which exhibited improved mechanical and thermal properties. Liu et al. [246] used PAH as polycation and Poly(sodium 4-styrene-sulfonate) (PSS) as polyanion for the surface assembly, and during the process, AgNPs were introduced by being suspended either in the PAH solution or the PSS solution. After cross-linking, the silver nanocomposite membranes showed a good NF and FO performance and exhibited excellent antibacterial properties against both Gram-positive and Gram-negative bacteria. In another study [245], new materials such as GO and aminated-GO were used as polyanion and polycation, respectively, to form an chlorine barrier on the PA TFC membrane surface to improve chlorine resistance.

Chemical bonding could also be used in the lay-by-lay assembly. Hu and Mi [244] prepared a novel membrane via layer-by-layer deposition of GO nanosheets onto a polydopamine coated PSU membrane, where TMC was used as a cross-linking agent (Fig. 1.7). The resulting membrane showed a very high water permeability and good rejection to Rhodamine-WT dye.

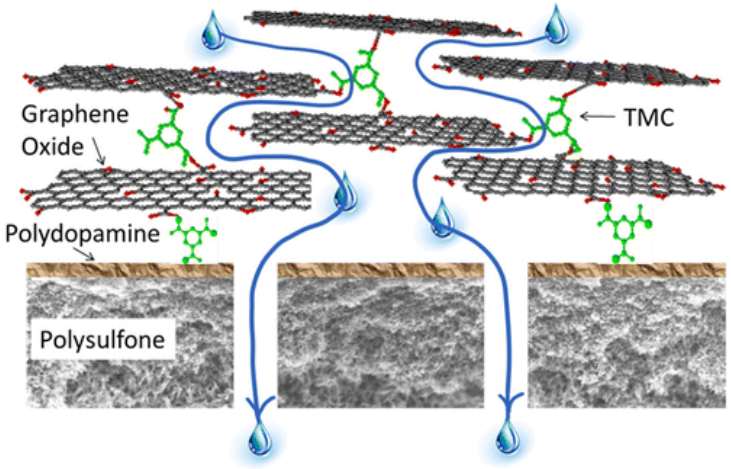

Fig. 1.7 The conceptual digram of layer-by-layer assemblied GO membrane. Adapted with permission from [244]. Copyright 2014 American Chemical Society.

1.4.6 Chemical grafting

One concern of the surface located nanocomposite membrane is the depletion of the deposited nanomaterials during the filtration process, especially for those attached onto the membrane surface through weak van der Waals and electrostatic forces. The loss of nanomaterials will gradually deplete the desired functionality of the nanocomposite membranes and may also release nanomaterials to water which may have potential risks to humans.

As a result, stronger attachments through processes such as chemical bonding have been actively explored to extend the desirable functionality of nanocomposite membranes. For example, Gunawan et al. [250] used polyethylene glycol-grafted

MWNTs as a bridging structure between AgNPs and hollow fiber membrane surface. In their study, AgNPs were firstly coated onto MWNTs to prepare Ag/MWNTs, and then Ag/MWNTs were covalently bonded to the external surface of a chemically modified PAN membrane. Yin et al [251] effectively attached AgNPs onto the surface of PA TFC membrane through chemical bonding (Ag-S) by using cysteamine (H_2N-$(CH_2)_2$-SH) as a bridging agent, as illustrated in Fig. 1.8. The prepared membrane showed good stability of the immobilized AgNPs and excellent antibacterial properties, while the water flux and salt rejection were maintained. Lately, Park et al. [252] attached the AgNPs onto thiolated PVDF UF membrane surface, resulting in a stable antimicrobial membrane.

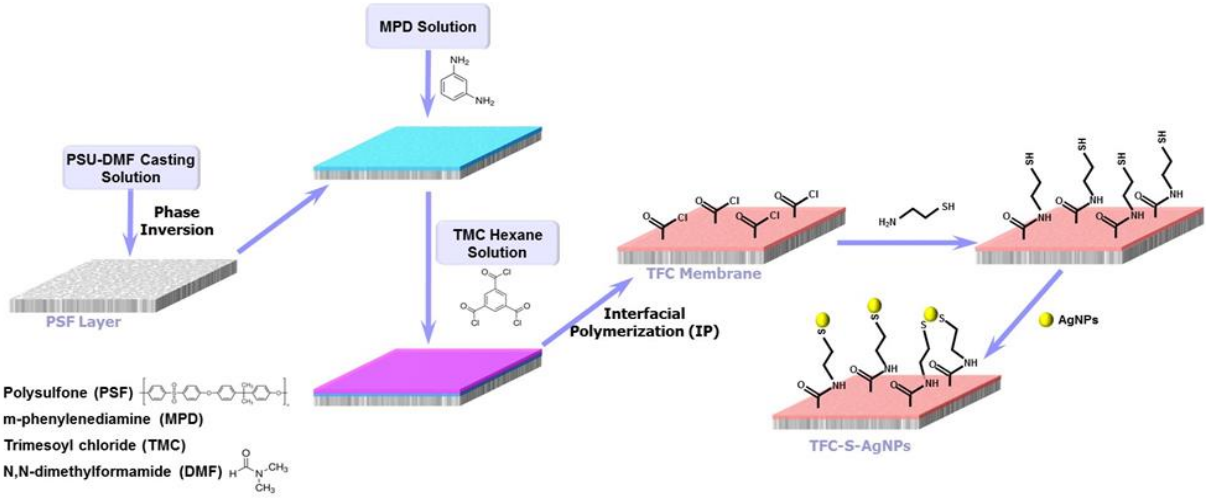

Fig. 1.8 Schematic diagram of immobilization of AgNPs onto the surface of PA TFC membrane. Adapted with permission from [251].

1.4.7 Other fabrication methods

Other fabrication methods such as cross-linking, colloidal precipitation and hydrothermal process have been successfully used to prepare surface located nanocomposite membranes. In the cross-linking process, an additional polymer was

needed to form the cross-linked matrix to wrap up nanomaterials for their incorporation onto the membrane surface. For example, Wang et al. [253] attached cellulose nanofiber onto nanofibrous UF membrane surface by using cross-linked PEG, resulting in a superior membrane with an improved water permeability and fouling resistance.

1.5 Conclusions and Perspectives

Progress in the development of polymer-matrix nanocomposite membranes for water treatment has been tremendous in recent years. Besides tuning the physicochemical properties of membranes (hydrophilicity, porosity, charge density, thermal, and mechanical stability), the incorporation of nanomaterials can provide membranes with some unique properties of nanomaterials and also possibly induce new characteristics and functions based on their synergetic effects. It provides a new dimension to design the next generation of polymeric membranes with high performance and antifouling properties. The potential applications of nanocomposite membranes could cover the whole filtration spectrum including MF, UF, NF, RO, and FO.

Several challenges still need to be addressed to optimize the design of the nanocomposite membranes for industrial applications at a large scale. First, no fundamental understandings were developed to systematically reflect the effects of nanomaterials on membrane structures and correlate them to the membrane performance changes. Specific contributions of surface hydrophilicity, pore size, charge density and membrane porosity to the membrane performance are still unclear.

Second, approaches for better dispersion of nanomaterials needs to be further explored. Aggregation is a common problem that may prevent nanomaterials from being homogeneously dispersed inside polymer matrices. Improved dispersion of nanofillers

could be achieved by modifying nanofiller surfaces or optimizing the embedding process, and the specific process will depend on polymer chemistry involved for membrane fabrications.

Third, it is important to ensure the compatibility of nanofillers with polymers. The compatibility will determine both the optimal membrane performance and the stability of nanofillers within the host polymer. They are critical to optimize the loading concentration and durability of nanocomposite membranes. Considering the potential effects of leached nanomaterials to the environment, nanomaterial leakage and its environmental toxicity also need to be systematically evaluated.

Finally, the industrial application of nanocomposite membranes for water treatment is still in its infancy. There are many laboratory based studies on the application of nanocomposite membranes, but very few reports exist on the large scale production and industrial application. More work is needed to evaluate the cost-effectiveness of large scale membrane fabrication including the supplies of nanomaterials, and monitor the long-term stability of membranes under practical application conditions. These studies should be implemented on a case by case basis with a full consideration of the source water quality and application environments. Using antimicrobial membrane as an example, it is attractive due to its demonstrated resistance to membrane biofouling. However, for long-term application, the loss of antimicrobial activity due to the depletion of biocidal agents or insufficient contact between bacteria and biocide caused by other foulant necessitates frequent recharging and cleaning of the membranes. How to effectively attach biocidal agents onto membrane and control their release should be

further examined. For commercial applications, there is a need to consider cost-effectively attaching biocidal agents onto the membrane and recharging them as needed.

Acknowledgments

Financial support of this research was partially provided by the United States Geological Survey through Missouri Water Resources Research Center (MWRRC).

References

[1] L.M. Robeson, Correlation of separation factor versus permeability for polymeric membranes, Journal of Membrane Science, 62 (1991) 165-185.

[2] T.S. Chung, L.Y. Jiang, Y. Li, S. Kulprathipanja, Mixed matrix membranes (MMMs) comprising organic polymers with dispersed inorganic fillers for gas separation, Progress in Polymer Science (Oxford), 32 (2007) 483-507.

[3] M. Jia, K.V. Peinemann, R.D. Behling, Molecular sieving effect of the zeolite-filled silicone rubber membranes in gas permeation, Journal of Membrane Science, 57 (1991) 289-296.

[4] J.M. Duval, B. Folkers, M.H.V. Mulder, G. Desgrandchamps, C.A. Smolders, Adsorbent filled membranes for gas separation. Part 1. Improvement of the gas separation properties of polymeric membranes by incorporation of microporous adsorbents, Journal of Membrane Science, 80 (1993) 189-198.

[5] H. Cong, M. Radosz, B.F. Towler, Y. Shen, Polymer-inorganic nanocomposite membranes for gas separation, Separation and Purification Technology, 55 (2007) 281-291.

[6] G. Choudalakis, A.D. Gotsis, Permeability of polymer/clay nanocomposites: A review, European Polymer Journal, 45 (2009) 967-984.

[7] D. Gomes, S.P. Nunes, K.V. Peinemann, Membranes for gas separation based on poly(1-trimethylsilyl-1-propyne)- silica nanocomposites, Journal of Membrane Science, 246 (2005) 13-25.

[8] Z. Chen, B. Holmberg, W. Li, X. Wang, W. Deng, R. Munoz, Y. Yan, Nafion/zeolite nanocomposite membrane by in situ crystallization for a direct methanol fuel cell, Chemistry of Materials, 18 (2006) 5669-5675.

[9] D.H. Jung, S.Y. Cho, D.H. Peck, D.R. Shin, J.S. Kim, Preparation and performance of a Nafion®/montmorillonite nanocomposite membrane for direct methanol fuel cell, Journal of Power Sources, 118 (2003) 205-211.

[10] N.H. Jalani, K. Dunn, R. Datta, Synthesis and characterization of Nafion®-MO_2 (M = Zr, Si, Ti) nanocomposite membranes for higher temperature PEM fuel cells, Electrochimica Acta, 51 (2005) 553-560.

[11] C. Jiang, S. Markutsya, Y. Pikus, V.V. Tsukruk, Freely suspended nanocomposite membranes as highly sensitive sensors, Nature Materials, 3 (2004) 721-728.

[12] J. Lu, L.T. Drzal, R.M. Worden, I. Lee, Simple fabrication of a highly sensitive glucose biosensor using enzymes immobilized in exfoliated graphite nanoplatelets nafion membrane, Chemistry of Materials, 19 (2007) 6240-6246.

[13] F. Croce, G.B. Appetecchi, L. Persi, B. Scrosati, Nanocomposite polymer electrolytes for lithium batteries, Nature, 394 (1998) 456-458.

[14] Z.H. Li, H.P. Zhang, P. Zhang, G.C. Li, Y.P. Wu, X.D. Zhou, Effects of the porous structure on conductivity of nanocomposite polymer electrolyte for lithium ion batteries, Journal of Membrane Science, 322 (2008) 416-422.

[15] Y.C. Wang, S.C. Fan, K.R. Lee, C.L. Li, S.H. Huang, H.A. Tsai, J.Y. Lai, Polyamide/SDS-clay hybrid nanocomposite membrane application to water-ethanol mixture pervaporation separation, Journal of Membrane Science, 239 (2004) 219-226.

[16] F. Peng, F. Pan, H. Sun, L. Lu, Z. Jiang, Novel nanocomposite pervaporation membranes composed of poly(vinyl alcohol) and chitosan-wrapped carbon nanotube, Journal of Membrane Science, 300 (2007) 13-19.

[17] D. Yang, J. Li, Z. Jiang, L. Lu, X. Chen, Chitosan/TiO_2 nanocomposite pervaporation membranes for ethanol dehydration, Chemical Engineering Science, 64 (2009) 3130-3137.

[18] I. Soroko, A. Livingston, Impact of TiO_2 nanoparticles on morphology and performance of crosslinked polyimide organic solvent nanofiltration (OSN) membranes, Journal of Membrane Science, 343 (2009) 189-198.

[19] S. Sorribas, P. Gorgojo, C. Tellez, J. Coronas, A.G. Livingston, High flux thin film nanocomposite membranes based on metal-organic frameworks for organic solvent nanofiltration, Journal of the American Chemical Society, 135 (2013) 15201-15208.

[20] K. Ebert, D. Fritsch, J. Koll, C. Tjahjawiguna, Influence of inorganic fillers on the compaction behaviour of porous polymer based membranes, Journal of Membrane Science, 233 (2004) 71-78.

[21] T.H. Bae, T.M. Tak, Effect of TiO_2 nanoparticles on fouling mitigation of ultrafiltration membranes for activated sludge filtration, Journal of Membrane Science, 249 (2005) 1-8.

[22] J. Marí a Arsuaga, A. Sotto, G. del Rosario, A. Martínez, S. Molina, S.B. Teli, J. de Abajo, Influence of the type, size, and distribution of metal oxide particles on the properties of nanocomposite ultrafiltration membranes, Journal of Membrane Science, 428 (2013) 131-141.

[23] Y. Yang, P. Wang, Q. Zheng, Preparation and properties of polysulfone/TiO_2 composite ultrafiltration membranes, Journal of Polymer Science, Part B: Polymer Physics, 44 (2006) 879-887.

[24] X. Cao, J. Ma, X. Shi, Z. Ren, Effect of TiO_2 nanoparticle size on the performance of PVDF membrane, Applied Surface Science, 253 (2006) 2003-2010.

[25] Y. Xiao, K. Yu Wang, T.S. Chung, J. Tan, Evolution of nano-particle distribution during the fabrication of mixed matrix TiO_2-polyimide hollow fiber membranes, Chemical Engineering Science, 61 (2006) 6228-6233.

[26] J.B. Li, J.W. Zhu, M.S. Zheng, Morphologies and properties of poly(phthalazinone ether sulfone ketone) matrix ultrafiltration membranes with entrapped TiO_2 nanoparticles, Journal of Applied Polymer Science, 103 (2007) 3623-3629.

[27] Y. Yang, H. Zhang, P. Wang, Q. Zheng, J. Li, The influence of nano-sized TiO_2 fillers on the morphologies and properties of PSF UF membrane, Journal of Membrane Science, 288 (2007) 231-238.

[28] X. Fu, H. Matsuyama, H. Nagai, Structure control of asymmetric poly(vinyl butyral)-TiO_2 composite membrane prepared by nonsolvent induced phase separation, Journal of Applied Polymer Science, 108 (2008) 713-723.

[29] G. Wu, S. Gan, L. Cui, Y. Xu, Preparation and characterization of PES/TiO_2 composite membranes, Applied Surface Science, 254 (2008) 7080-7086.

[30] L.Y. Yu, H.M. Shen, Z.L. Xu, PVDF-TiO_2 composite hollow fiber ultrafiltration membranes prepared by TiO2 sol-gel method and blending method, Journal of Applied Polymer Science, 113 (2009) 1763-1772.

[31] J.F. Li, Z.L. Xu, H. Yang, L.Y. Yu, M. Liu, Effect of TiO_2 nanoparticles on the surface morphology and performance of microporous PES membrane, Applied Surface Science, 255 (2009) 4725-4732.

[32] S.J. Oh, N. Kim, Y.T. Lee, Preparation and characterization of PVDF/TiO_2 organic-inorganic composite membranes for fouling resistance improvement, Journal of Membrane Science, 345 (2009) 13-20.

[33] A. Razmjou, J. Mansouri, V. Chen, The effects of mechanical and chemical modification of TiO_2 nanoparticles on the surface chemistry, structure and fouling performance of PES ultrafiltration membranes, Journal of Membrane Science, 378 (2011) 73-84.

[34] S.S. Madaeni, S. Zinadini, V. Vatanpour, A new approach to improve antifouling property of PVDF membrane using in situ polymerization of PAA functionalized TiO_2 nanoparticles, Journal of Membrane Science, 380 (2011) 155-162.

[35] A. Sotto, A. Boromand, S. Balta, J. Kim, B. Van Der Bruggen, Doping of polyethersulfone nanofiltration membranes: Antifouling effect observed at ultralow concentrations of TiO_2 nanoparticles, Journal of Materials Chemistry, 21 (2011) 10311-10320.

[36] N.A.A. Hamid, A.F. Ismail, T. Matsuura, A.W. Zularisam, W.J. Lau, E. Yuliwati, M.S. Abdullah, Morphological and separation performance study of polysulfone/titanium dioxide (PSF/TiO_2) ultrafiltration membranes for humic acid removal, Desalination, 273 (2011) 85-92.

[37] R. Abedini, S.M. Mousavi, R. Aminzadeh, A novel cellulose acetate (CA) membrane using TiO_2 nanoparticles: Preparation, characterization and permeation study, Desalination, 277 (2011) 40-45.

[38] E. Yuliwati, A.F. Ismail, Effect of additives concentration on the surface properties and performance of PVDF ultrafiltration membranes for refinery produced wastewater treatment, Desalination, 273 (2011) 226-234.

[39] A. Rahimpour, M. Jahanshahi, B. Rajaeian, M. Rahimnejad, TiO_2 entrapped nano-composite PVDF/SPES membranes: Preparation, characterization, antifouling and antibacterial properties, Desalination, 278 (2011) 343-353.

[40] A. Sotto, A. Boromand, R. Zhang, P. Luis, J.M. Arsuaga, J. Kim, B. Van der Bruggen, Effect of nanoparticle aggregation at low concentrations of TiO_2 on the hydrophilicity, morphology, and fouling resistance of PES-TiO_2 membranes, Journal of Colloid and Interface Science, 363 (2011) 540-550.

[41] V. Vatanpour, S.S. Madaeni, A.R. Khataee, E. Salehi, S. Zinadini, H.A. Monfared, TiO_2 embedded mixed matrix PES nanocomposite membranes: Influence of different sizes and types of nanoparticles on antifouling and performance, Desalination, 292 (2012) 19-29.

[42] A. Razmjou, A. Resosudarmo, R.L. Holmes, H. Li, J. Mansouri, V. Chen, The effect of modified TiO_2 nanoparticles on the polyethersulfone ultrafiltration hollow fiber membranes, Desalination, 287 (2012) 271-280.

[43] S.S. Homaeigohar, H. Mahdavi, M. Elbahri, Extraordinarily water permeable sol-gel formed nanocomposite nanofibrous membranes, Journal of Colloid and Interface Science, 366 (2012) 51-56.

[44] S. Zhao, P. Wang, C. Wang, X. Sun, L. Zhang, Thermostable PPESK/TiO_2 nanocomposite ultrafiltration membrane for high temperature condensed water treatment, Desalination, 299 (2012) 35-43.

[45] R. Abedini, S.M. Mousavi, R. Aminzadeh, Effect of sonochemical synthesized TiO_2 nanoparticles and coagulation bath temperature on morphology, thermal stability and pure water flux of asymmetric cellulose acetate nanocomposite membranes prepared via phase inversion method, Chemical Industry and Chemical Engineering Quarterly, 18 (2012) 385-398.

[46] V. Vatanpour, S.S. Madaeni, R. Moradian, S. Zinadini, B. Astinchap, Novel antibifouling nanofiltration polyethersulfone membrane fabricated from embedding TiO_2 coated multiwalled carbon nanotubes, Separation and Purification Technology, 90 (2012) 69-82.

[47] H.P. Ngang, A.L. Ahmad, S.C. Low, B.S. Ooi, Preparation of mixed-matrix membranes for micellar enhanced ultrafiltration based on response surface methodology, Desalination, 293 (2012) 7-20.

[48] G. Zhang, S. Lu, L. Zhang, Q. Meng, C. Shen, J. Zhang, Novel polysulfone hybrid ultrafiltration membrane prepared with TiO_2-g-HEMA and its antifouling characteristics, Journal of Membrane Science, 436 (2013) 163-173.

[49] F. Zhang, W. Zhang, Y. Yu, B. Deng, J. Li, J. Jin, Sol-gel preparation of PAA-g-PVDF/TiO_2 nanocomposite hollow fiber membranes with extremely high water flux and improved antifouling property, Journal of Membrane Science, 432 (2013) 25-32.

[50] S.B. Teli, S. Molina, A. Sotto, E.G. Calvo, J. De Abajo, Fouling resistant polysulfone-PANI/TiO_2 ultrafiltration nanocomposite membranes, Industrial and Engineering Chemistry Research, 52 (2013) 9470-9479.

[51] Y.H. Teow, A.L. Ahmad, J.K. Lim, B.S. Ooi, Studies on the surface properties of mixed-matrix membrane and its antifouling properties for humic acid removal, Journal of Applied Polymer Science, 128 (2013) 3184-3192.

[52] H. Joo Kim, H. Raj Pant, J. Hee Kim, N. Jung Choi, C. Sang Kim, Fabrication of multifunctional TiO_2-fly ash/polyurethane nanocomposite membrane via electrospinning, Ceramics International, 40 (2014) 3023-3029.

[53] A. Rahimpour, S.S. Madaeni, A.H. Taheri, Y. Mansourpanah, Coupling TiO_2 nanoparticles with UV irradiation for modification of polyethersulfone ultrafiltration membranes, Journal of Membrane Science, 313 (2008) 158-169.

[54] R.A. Damodar, S.J. You, H.H. Chou, Study the self cleaning, antibacterial and photocatalytic properties of TiO_2 entrapped PVDF membranes, Journal of Hazardous Materials, 172 (2009) 1321-1328.

[55] H.P. Ngang, B.S. Ooi, A.L. Ahmad, S.O. Lai, Preparation of PVDF-TiO_2 mixed-matrix membrane and its evaluation on dye adsorption and UV-cleaning properties, Chemical Engineering Journal, 197 (2012) 359-367.

[56] M. Sun, Y. Su, C. Mu, Z. Jiang, Improved antifouling property of PES ultrafiltration membranes using additive of silica-PVP nanocomposite, Industrial and Engineering Chemistry Research, 49 (2010) 790-796.

[57] E.M.V. Hoek, A.K. Ghosh, X. Huang, M. Liong, J.I. Zink, Physical-chemical properties, separation performance, and fouling resistance of mixed-matrix ultrafiltration membranes, Desalination, 283 (2011) 89-99.

[58] A. Jomekian, S.A.A. Mansoori, N. Monirimanesh, Synthesis and characterization of novel PEO-MCM-41/PVDC nanocomposite membrane, Desalination, 276 (2011) 239-245.

[59] C. Klaysom, S.H. Moon, B.P. Ladewig, G.Q.M. Lu, L. Wang, The influence of inorganic filler particle size on composite ion-exchange membranes for desalination, Journal of Physical Chemistry C, 115 (2011) 15124-15132.

[60] J.N. Shen, H.M. Ruan, L.G. Wu, C.J. Gao, Preparation and characterization of PES-SiO_2 organic-inorganic composite ultrafiltration membrane for raw water pretreatment, Chemical Engineering Journal, 168 (2011) 1272-1278.

[61] B. Muriithi, D.A. Loy, Processing, morphology, and water uptake of nafion/Ex situ stöber silica nanocomposite membranes as a function of particle size, ACS Applied Materials and Interfaces, 4 (2012) 6766-6773.

[62] J. Huang, K. Zhang, K. Wang, Z. Xie, B. Ladewig, H. Wang, Fabrication of polyethersulfone-mesoporous silica nanocomposite ultrafiltration membranes with antifouling properties, Journal of Membrane Science, 423-424 (2012) 362-370.

[63] M. Pakizeh, A.N. Moghadam, M.R. Omidkhah, M. Namvar-Mahboub, Preparation and characterization of dimethyldichlorosilane modified SiO_2/PSf nanocomposite membrane, Korean Journal of Chemical Engineering, 30 (2013) 751-760.

[64] H. Wu, B. Tang, P. Wu, Development of novel SiO_2-GO nanohybrid/polysulfone membrane with enhanced performance, Journal of Membrane Science, 451 (2014) 94-102.

[65] L. Yan, S. Hong, M.L. Li, Y.S. Li, Application of the Al_2O_3-PVDF nanocomposite tubular ultrafiltration (UF) membrane for oily wastewater treatment and its antifouling research, Separation and Purification Technology, 66 (2009) 347-352.

[66] N. Maximous, G. Nakhla, W. Wan, K. Wong, Preparation, characterization and performance of Al_2O_3/PES membrane for wastewater filtration, Journal of Membrane Science, 341 (2009) 67-75.

[67] N. Maximous, G. Nakhla, K. Wong, W. Wan, Optimization of Al_2O_3/PES membranes for wastewater filtration, Separation and Purification Technology, 73 (2010) 294-301.

[68] N. Maximous, G. Nakhla, W. Wan, K. Wong, Effect of the metal oxide particle distributions on modified PES membranes characteristics and performance, Journal of Membrane Science, 361 (2010) 213-222.

[69] I. Csetneki, G. Filipcsei, M. Zr ńyi, Smart nanocomposite polymer membranes with on/off switching control, Macromolecules, 39 (2006) 1939-1942.

[70] P. Daraei, S.S. Madaeni, N. Ghaemi, E. Salehi, M.A. Khadivi, R. Moradian, B. Astinchap, Novel polyethersulfone nanocomposite membrane prepared by PANI/Fe_3O_4 nanoparticles with enhanced performance for Cu(II) removal from water, Journal of Membrane Science, 415-416 (2012) 250-259.

[71] A. Gholami, A.R. Moghadassi, S.M. Hosseini, S. Shabani, F. Gholami, Preparation and characterization of polyvinyl chloride based nanocomposite nanofiltration-membrane modified by

iron oxide nanoparticles for lead removal from water, Journal of Industrial and Engineering Chemistry, (2013).

[72] J. Alam, L.A. Dass, M. Ghasemi, M. Alhoshan, Synthesis and optimization of PES-Fe_3O_4 mixed matrix nanocomposite membrane: Application studies in water purification, Polymer Composites, 34 (2013) 1870-1877.

[73] P. Daraei, S.S. Madaeni, N. Ghaemi, M.A. Khadivi, B. Astinchap, R. Moradian, Fouling resistant mixed matrix polyethersulfone membranes blended with magnetic nanoparticles: Study of magnetic field induced casting, Separation and Purification Technology, 109 (2013) 111-121.

[74] R. Jamshidi Gohari, W.J. Lau, T. Matsuura, E. Halakoo, A.F. Ismail, Adsorptive removal of Pb(II) from aqueous solution by novel PES/HMO ultrafiltration mixed matrix membrane, Separation and Purification Technology, 120 (2013) 59-68.

[75] R. Jamshidi Gohari, E. Halakoo, N.A.M. Nazri, W.J. Lau, T. Matsuura, A.F. Ismail, Improving performance and antifouling capability of PES UF membranes via blending with highly hydrophilic hydrous manganese dioxide nanoparticles, Desalination, 335 (2014) 87-95.

[76] M. Alhoshan, J. Alam, L.A. Dass, N. Al-Homaidi, Fabrication of polysulfone/ZnO membrane: Influence of ZnO nanoparticles on membrane characteristics, Advances in Polymer Technology, 32 (2013).

[77] W.L. Chou, D.G. Yu, M.C. Yang, The preparation and characterization of silver-loading cellulose acetate hollow fiber membrane for water treatment, Polymers for Advanced Technologies, 16 (2005) 600-607.

[78] Y. Deng, G. Dang, H. Zhou, X. Rao, C. Chen, Preparation and characterization of polyimide membranes containing Ag nanoparticles in pores distributing on one side, Materials Letters, 62 (2008) 1143-1146.

[79] K. Zodrow, L. Brunet, S. Mahendra, D. Li, A. Zhang, Q. Li, P.J.J. Alvarez, Polysulfone ultrafiltration membranes impregnated with silver nanoparticles show improved biofouling resistance and virus removal, Water Research, 43 (2009) 715-723.

[80] H. Basri, A.F. Ismail, M. Aziz, K. Nagai, T. Matsuura, M.S. Abdullah, B.C. Ng, Silver-filled polyethersulfone membranes for antibacterial applications - effect of PVP and TAP addition on silver dispersion, Desalination, 261 (2010) 264-271.

[81] C. Liao, P. Yu, J. Zhao, L. Wang, Y. Luo, Preparation and characterization of NaY/PVDF hybrid ultrafiltration membranes containing silver ions as antibacterial materials, Desalination, 272 (2011) 59-65.

[82] S. Kar, M. Subramanian, A.K. Ghosh, R.C. Bindal, S. Prabhakar, J. Nuwad, C.G.S. Pillai, S. Chattopadhyay, P.K. Tewaria, Potential of nanoparticles for water purification: A case study on anti-biofouling behaviour of metal based polymeric nanocomposite membrane, Desalination and Water Treatment, 27 (2011) 224-230.

[83] H. Basri, A.F. Ismail, M. Aziz, Polyethersulfone (PES)-silver composite UF membrane: Effect of silver loading and PVP molecular weight on membrane morphology and antibacterial activity, Desalination, 273 (2011) 72-80.

[84] H. Basri, A.F. Ismail, M. Aziz, Polyethersulfone (PES) ultrafiltration (UF) membranes loaded with silver nitrate for bacteria removal, Membrane Water Treatment, 2 (2011).

[85] S.K. Jewrajka, S. Haldar, Amphiphilic poly(acrylonitrile-co-acrylic acid)/silver nanocomposite additives for the preparation of antibiofouling membranes with improved properties, Polymer Composites, 32 (2011) 1851-1861.

[86] A. Dasari, J. Quirós, B. Herrero, K. Boltes, E. García-Calvo, R. Rosal, Antifouling membranes prepared by electrospinning polylactic acid containing biocidal nanoparticles, Journal of Membrane Science, 405-406 (2012) 134-140.

[87] M. Zhang, K. Zhang, B. De Gusseme, W. Verstraete, Biogenic silver nanoparticles (bio-Ag 0) decrease biofouling of bio-Ag 0/PES nanocomposite membranes, Water Research, 46 (2012) 2077-2087.

[88] Y. Liu, E. Rosenfield, M. Hu, B. Mi, Direct observation of bacterial deposition on and detachment from nanocomposite membranes embedded with silver nanoparticles, Water Research, 47 (2013) 2949-2958.

[89] A. Alpatova, E.S. Kim, X. Sun, G. Hwang, Y. Liu, M. Gamal El-Din, Fabrication of porous polymeric nanocomposite membranes with enhanced anti-fouling properties: Effect of casting composition, Journal of Membrane Science, 444 (2013) 449-460.

[90] H.R. Pant, H.J. Kim, M.K. Joshi, B. Pant, C.H. Park, J.I. Kim, K.S. Hui, C.S. Kim, One-step fabrication of multifunctional composite polyurethane spider-web-like nanofibrous membrane for water purification, Journal of Hazardous Materials, 264 (2014) 25-33.

[91] N. Akar, B. Asar, N. Dizge, I. Koyuncu, Investigation of characterization and biofouling properties of PES membrane containing selenium and copper nanoparticles, Journal of Membrane Science, 437 (2013) 216-226.

[92] G. Ciobanu, G. Carja, O. Ciobanu, Preparation and characterization of polymer-zeolite nanocomposite membranes, Materials Science and Engineering C, 27 (2007) 1138-1140.

[93] S. Husain, W.J. Koros, Macrovoids in hybrid organic/inorganic hollow fiber membranes, Industrial and Engineering Chemistry Research, 48 (2009) 2372-2379.

[94] M.U.M. Junaidi, C.P. Leo, S.N.M. Kamal, A.L. Ahmad, Fouling mitigation in humic acid ultrafiltration using polysulfone/SAPO-34 mixed matrix membrane, Water Science and Technology, 67 (2013) 2102-2109.

[95] C.P. Leo, N.H. Ahmad Kamil, M.U.M. Junaidi, S.N.M. Kamal, A.L. Ahmad, The potential of SAPO-44 zeolite filler in fouling mitigation of polysulfone ultrafiltration membrane, Separation and Purification Technology, 103 (2013) 84-91.

[96] F. Liu, B.R. Ma, D. Zhou, Y.H. Xiang, L.X. Xue, Breaking through tradeoff of Polysulfone ultrafiltration membranes by zeolite 4A, Microporous and Mesoporous Materials, 186 (2014) 113-120.

[97] O. Monticelli, A. Bottino, I. Scandale, G. Capannelli, S. Russo, Preparation and properties of polysulfone-clay composite membranes, Journal of Applied Polymer Science, 103 (2007) 3637-3644.

[98] A.M.D. Leite, L.F. Maia, E.M. Araujo, H.L. Lira, Nylon 6/Brazilian clay membranes prepared by phase inversion, Journal of Applied Polymer Science, 113 (2009) 1488-1493.

[99] P. Anadão, L.F. Sato, H. Wiebeck, F.R. Valenzuela-Díaz, Montmorillonite as a component of polysulfone nanocomposite membranes, Applied Clay Science, 48 (2010) 127-132.

[100] C.Y. Lai, A. Groth, S. Gray, M. Duke, Investigation of the dispersion of nanoclays into PVDF for enhancement of physical membrane properties, Desalination and Water Treatment, 34 (2011) 251-256.

[101] N. Ghaemi, S.S. Madaeni, A. Alizadeh, H. Rajabi, P. Daraei, Preparation, characterization and performance of polyethersulfone/organically modified montmorillonite nanocomposite membranes in removal of pesticides, Journal of Membrane Science, 382 (2011) 135-147.

[102] Y. Ma, F. Shi, W. Zhao, M. Wu, J. Zhang, J. Ma, C. Gao, Preparation and characterization of PSf/clay nanocomposite membranes with LiCl as a pore forming additive, Desalination, 303 (2012) 39-47.

[103] P. Wang, J. Ma, Z. Wang, F. Shi, Q. Liu, Enhanced separation performance of PVDF/PVP-g-MMT nanocomposite ultrafiltration membrane based on the NVP-grafted polymerization modification of montmorillonite (MMT), Langmuir, 28 (2012) 4776-4786.

[104] P. Anad ão, R.R. Montes, N.M. Larocca, L.A. Pessan, Influence of the clay content and the polysulfone molar mass on nanocomposite membrane properties, Applied Surface Science, 275 (2013) 110-120.

[105] C.Y. Lai, A. Groth, S. Gray, M. Duke, Enhanced abrasion resistant PVDF/nanoclay hollow fibre composite membranes for water treatment, Journal of Membrane Science, 449 (2013) 146-157.

[106] V. Vatanpour, S.S. Madaeni, L. Rajabi, S. Zinadini, A.A. Derakhshan, Boehmite nanoparticles as a new nanofiller for preparation of antifouling mixed matrix membranes, Journal of Membrane Science, 401-402 (2012) 132-143.

[107] P. Daraei, S.S. Madaeni, N. Ghaemi, M.A. Khadivi, L. Rajabi, A.A. Derakhshan, F. Seyedpour, PAA grafting onto new acrylate-alumoxane/PES mixed matrix nano-enhanced membrane: Preparation, characterization and performance in dye removal, Chemical Engineering Journal, 221 (2013) 111-123.

[108] G. Mago, D.M. Kalyon, F.T. Fisher, Membranes of polyvinylidene fluoride and PVDF nanocomposites with carbon nanotubes via immersion precipitation, Journal of Nanomaterials, 2008 (2008).

[109] H. Wu, B. Tang, P. Wu, Novel ultrafiltration membranes prepared from a multi-walled carbon nanotubes/polymer composite, Journal of Membrane Science, 362 (2010) 374-383.

[110] P.S. Goh, B.C. Ng, A.F. Ismail, M. Aziz, S.M. Sanip, Surfactant dispersed multi-walled carbon nanotube/polyetherimide nanocomposite membrane, Solid State Sciences, 12 (2010) 2155-2162.

[111] H.A. Shawky, S.R. Chae, S. Lin, M.R. Wiesner, Synthesis and characterization of a carbon nanotube/polymer nanocomposite membrane for water treatment, Desalination, 272 (2011) 46-50.

[112] Y. Mansourpanah, S.S. Madaeni, A. Rahimpour, M. Adeli, M.Y. Hashemi, M.R. Moradian, Fabrication new PES-based mixed matrix nanocomposite membranes using polycaprolactone modified carbon nanotubes as the additive: Property changes and morphological studies, Desalination, 277 (2011) 171-177.

[113] V. Vatanpour, S.S. Madaeni, R. Moradian, S. Zinadini, B. Astinchap, Fabrication and characterization of novel antifouling nanofiltration membrane prepared from oxidized multiwalled carbon nanotube/polyethersulfone nanocomposite, Journal of Membrane Science, 375 (2011) 284-294.

[114] S. Majeed, D. Fierro, K. Buhr, J. Wind, B. Du, A. Boschetti-de-Fierro, V. Abetz, Multi-walled carbon nanotubes (MWCNTs) mixed polyacrylonitrile (PAN) ultrafiltration membranes, Journal of Membrane Science, 403-404 (2012) 101-109.

[115] X. Zhao, J. Ma, Z. Wang, G. Wen, J. Jiang, F. Shi, L. Sheng, Hyperbranched-polymer functionalized multi-walled carbon nanotubes for poly (vinylidene fluoride) membranes: From dispersion to blended fouling-control membrane, Desalination, 303 (2012) 29-38.

[116] C.F. de Lannoy, D. Jassby, D.D. Davis, M.R. Wiesner, A highly electrically conductive polymer-multiwalled carbon nanotube nanocomposite membrane, Journal of Membrane Science, 415-416 (2012) 718-724.

[117] P. Daraei, S.S. Madaeni, N. Ghaemi, H. Ahmadi Monfared, M.A. Khadivi, Fabrication of PES nanofiltration membrane by simultaneous use of multi-walled carbon nanotube and surface graft polymerization method: Comparison of MWCNT and PAA modified MWCNT, Separation and Purification Technology, 104 (2013) 32-44.

[118] P. Daraei, S.S. Madaeni, N. Ghaemi, M.A. Khadivi, B. Astinchap, R. Moradian, Enhancing antifouling capability of PES membrane via mixing with various types of polymer modified multi-walled carbon nanotube, Journal of Membrane Science, 444 (2013) 184-191.

[119] C.F. De Lannoy, E. Soyer, M.R. Wiesner, Optimizing carbon nanotube-reinforced polysulfone ultrafiltration membranes through carboxylic acid functionalization, Journal of Membrane Science, 447 (2013) 395-402.

[120] J. Yin, G. Zhu, B. Deng, Multi-walled carbon nanotubes (MWNTs)/polysulfone (PSU) mixed matrix hollow fiber membranes for enhanced water treatment, Journal of Membrane Science, 437 (2013) 237-248.

[121] N. Phao, E.N. Nxumalo, B.B. Mamba, S.D. Mhlanga, A nitrogen-doped carbon nanotube enhanced polyethersulfone membrane system for water treatment, Physics and Chemistry of the Earth, 66 (2013) 148-156.

[122] E.S. Kim, Y. Liu, M. Gamal El-Din, An in-situ integrated system of carbon nanotubes nanocomposite membrane for oil sands process-affected water treatment, Journal of Membrane Science, 429 (2013) 418-417.

[123] A. Zirehpour, A. Rahimpour, M. Jahanshahi, M. Peyravi, Mixed matrix membrane application for olive oil wastewater treatment: Process optimization based on Taguchi design method, Journal of Environmental Management, 132 (2014) 113-120.

[124] R. Saranya, G. Arthanareeswaran, D.D. Dionysiou, Treatment of paper mill effluent using Polyethersulfone/functionalised multiwalled carbon nanotubes based nanocomposite membranes, Chemical Engineering Journal, 236 (2014) 369-377.

[125] B.M. Ganesh, A.M. Isloor, A.F. Ismail, Enhanced hydrophilicity and salt rejection study of graphene oxide-polysulfone mixed matrix membrane, Desalination, 313 (2013) 199-207.

[126] H. Zhao, L. Wu, Z. Zhou, L. Zhang, H. Chen, Improving the antifouling property of polysulfone ultrafiltration membrane by incorporation of isocyanate-treated graphene oxide, Physical Chemistry Chemical Physics, 15 (2013) 9084-9092.

[127] C.A. Crock, A.R. Rogensues, W. Shan, V.V. Tarabara, Polymer nanocomposites with graphene-based hierarchical fillers as materials for multifunctional water treatment membranes, Water Research, 47 (2013) 3984-3996.

[128] S. Zinadini, A.A. Zinatizadeh, M. Rahimi, V. Vatanpour, H. Zangeneh, Preparation of a novel antifouling mixed matrix PES membrane by embedding graphene oxide nanoplates, Journal of Membrane Science, 453 (2014) 292-301.

[129] J.S. Taurozzi, C.A. Crock, V.V. Tarabara, C60-polysulfone nanocomposite membranes: Entropic and enthalpic determinants of C60 aggregation and its effects on membrane properties, Desalination, 269 (2011) 111-119.

[130] N.N. Sudareva, A.V. Penkova, T.A. Kostereva, A.E. Polotskii, G.A. Polotskaya, Properties of casting solutions and ultrafiltration membranes based on fullerene-polyamide nanocomposites, Express Polymer Letters, 6 (2012) 178-188.

[131] F.V. Adams, E.N. Nxumalo, R.W.M. Krause, E.M.V. Hoek, B.B. Mamba, Preparation and characterization of polysulfone/β-cyclodextrin polyurethane composite nanofiltration membranes, Journal of Membrane Science, 405-406 (2012) 291-299.

[132] F.V. Adams, D.S. Dlamini, E.N. Nxumalo, R.W.M. Krause, E.M.V. Hoek, B.B. Mamba, Solute transport and structural properties of polysulfone/B-cyclodextrin polyurethane mixed-matrix membranes, Journal of Membrane Science, 429 (2013) 58-65.

[133] F.V. Adams, E.N. Nxumalo, R.W.M. Krause, E.M.V. Hoek, B.B. Mamba, The influence of solvent properties on the performance of polysulfone/β-cyclodextrin polyurethane mixed-matrix membranes, Journal of Applied Polymer Science, 130 (2013) 2005-2014.

[134] F.V. Adams, E.N. Nxumalo, R.W.M. Krause, E.M.V. Hoek, B.B. Mamba, Application of polysulfone/cyclodextrin mixed-matrix membranes in the removal of natural organic matter from water, Physics and Chemistry of the Earth, (2013).

[135] Z. Fan, Z. Wang, N. Sun, J. Wang, S. Wang, Performance improvement of polysulfone ultrafiltration membrane by blending with polyaniline nanofibers, Journal of Membrane Science, 320 (2008) 363-371.

[136] M. Sankir, S. Bozkir, B. Aran, Preparation and performance analysis of novel nanocomposite copolymer membranes for Cr(VI) removal from aqueous solutions, Desalination, 251 (2010).

[137] S. Zhao, Z. Wang, X. Wei, X. Tian, J. Wang, S. Yang, S. Wang, Comparison study of the effect of PVP and PANI nanofibers additives on membrane formation mechanism, structure and performance, Journal of Membrane Science, 385-386 (2011) 110-122.

[138] S. Zhao, Z. Wang, J. Wang, S. Yang, S. Wang, PSf/PANI nanocomposite membrane prepared by in situ blending of PSf and PANI/NMP, Journal of Membrane Science, 376 (2011) 83-95.

[139] S.B. Teli, S. Molina, E.G. Calvo, A.E. Lozano, J. de Abajo, Preparation, characterization and antifouling property of polyethersulfone-PANI/PMA ultrafiltration membranes, Desalination, 299 (2012) 113-122.

[140] S. Zhao, Z. Wang, X. Wei, B. Zhao, J. Wang, S. Yang, S. Wang, Performance improvement of polysulfone ultrafiltration membrane using well-dispersed polyaniline-poly(vinylpyrrolidone) nanocomposite as the additive, Industrial and Engineering Chemistry Research, 51 (2012) 4661-4672.

[141] Y. Liao, X. Wang, W. Qian, Y. Li, X. Li, D.G. Yu, Bulk synthesis, optimization, and characterization of highly dispersible polypyrrole nanoparticles toward protein separation using nanocomposite membranes, Journal of Colloid and Interface Science, 386 (2012) 148-157.

[142] K.K.R. Tetala, D.F. Stamatialis, Mixed matrix membranes for efficient adsorption of copper ions from aqueous solutions, Separation and Purification Technology, 104 (2013) 214-220.

[143] C.H. Worthley, K.T. Constantopoulos, M. Ginic-Markovic, E. Markovic, S. Clarke, A study into the effect of POSS nanoparticles on cellulose acetate membranes, Journal of Membrane Science, 431 (2013) 62-71.

[144] W. Zhao, J. Huang, B. Fang, S. Nie, N. Yi, B. Su, H. Li, C. Zhao, Modification of polyethersulfone membrane by blending semi-interpenetrating network polymeric nanoparticles, Journal of Membrane Science, 369 (2011) 258-266.

[145] M. Kumar, M. Grzelakowski, J. Zilles, M. Clark, W. Meier, Highly permeable polymeric membranes based on the incorporation of the functional water channel protein Aquaporin Z, Proceedings of the National Academy of Sciences of the United States of America, 104 (2007) 20719-20724.

[146] L. Manjarrez Nevárez, L. Ballinas Casarrubias, O.S. Canto, A. Celzard, V. Fierro, R. Ibarra Gómez, G. González Sánchez, Biopolymers-based nanocomposites: Membranes from propionated lignin and cellulose for water purification, Carbohydrate Polymers, 86 (2011) 732-741.

[147] R. Jamshidi Gohari, W.J. Lau, T. Matsuura, A.F. Ismail, Fabrication and characterization of novel PES/Fe-Mn binary oxide UF mixed matrix membrane for adsorptive removal of As(III) from contaminated water solution, Separation and Purification Technology, 118 (2013) 64-72.

[148] M. Mulder, Basic Principles of Membrane Technology, Kluwer Academic Publishers, Dordrecht, 1991.

[149] P. Van De Witte, P.J. Dijkstra, J.W.A. Van Den Berg, J. Feijen, Phase separation processes in polymer solutions in relation to membrane formation, Journal of Membrane Science, 117 (1996) 1-31.

[150] D. Rana, T. Matsuura, Surface modifications for antifouling membranes, Chemical Reviews, 110 (2010) 2448-2471.

[151] A. Mills, S. Le Hunte, An overview of semiconductor photocatalysis, Journal of Photochemistry and Photobiology A: Chemistry, 108 (1997) 1-35.

[152] Y. Paz, Application of TiO_2 photocatalysis for air treatment: Patents' overview, Applied Catalysis B: Environmental, 99 (2010) 448-460.

[153] X. Zhu, R. Bai, K.H. Wee, C. Liu, S.L. Tang, Membrane surfaces immobilized with ionic or reduced silver and their anti-biofouling performances, Journal of Membrane Science, 363 (2010) 278-286.

[154] Y. Liu, X. Wang, F. Yang, X. Yang, Excellent antimicrobial properties of mesoporous anatase TiO_2 and Ag/TiO_2 composite films, Microporous and Mesoporous Materials, 114 (2008) 431-439.

[155] J.E. Cadotte, Interfacially synthesized reverse osmosis membrane, in, 1981.

[156] B.-H. Jeong, E.M.V. Hoek, Y. Yan, A. Subramani, X. Huang, G. Hurwitz, A.K. Ghosh, A. Jawor, Interfacial polymerization of thin film nanocomposites: A new concept for reverse osmosis membranes, Journal of Membrane Science, 294 (2007) 1-7.

[157] X. Wang, X. Chen, K. Yoon, D. Fang, B.S. Hsiao, B. Chu, High flux filtration medium based on nanofibrous substrate with hydrophilic nanocomposite coating, Environmental Science and Technology, 39 (2005) 7684-7691.

[158] S.Y. Lee, H.J. Kim, R. Patel, S.J. Im, J.H. Kim, B.R. Min, Silver nanoparticles immobilized on thin film composite polyamide membrane: Characterization, nanofiltration, antifouling properties, Polymers for Advanced Technologies, 18 (2007) 562-568.

[159] H.P. Rønningsen, B. Bjørndal, A.B. Hansen, W.B. Pedersen, Wax precipitation from North Sea crude oils. 1. Crystallization and dissolution temperatures, and Newtonian and non-Newtonian flow properties, Energy and Fuels, 5 (1991) 895-908.

[160] P.S. Singh, V.K. Aswal, Characterization of physical structure of silica nanoparticles encapsulated in polymeric structure of polyamide films, Journal of Colloid and Interface Science, 326 (2008) 176-185.

[161] M.L. Lind, B.H. Jeong, A. Subramani, X. Huang, E.M.V. Hoek, Effect of mobile cation on zeolite-polyamide thin film nanocomposite membranes, Journal of Materials Research, 24 (2009) 1624-1631.

[162] M.L. Lind, A.K. Ghosh, A. Jawor, X. Huang, W. Hou, Y. Yang, E.M.V. Hoek, Influence of zeolite crystal size on zeolite-polyamide thin film nanocomposite membranes, Langmuir, 25 (2009) 10139-10145.

[163] G.L. Jadav, P.S. Singh, Synthesis of novel silica-polyamide nanocomposite membrane with enhanced properties, Journal of Membrane Science, 328 (2009) 257-267.

[164] H. Ma, K. Yoon, L. Rong, M. Shokralla, A. Kopot, X. Wang, D. Fang, B.S. Hsiao, B. Chu, Thin-film nanofibrous composite ultrafiltration membranes based on polyvinyl alcohol barrier layer containing directional water channels, Industrial and Engineering Chemistry Research, 49 (2010) 11978-11984.

[165] H. Wu, B. Tang, P. Wu, MWNTs/polyester thin film nanocomposite membrane: An approach to overcome the trade-off effect between permeability and selectivity, Journal of Physical Chemistry C, 114 (2010) 16395-16400.

[166] J. Park, W. Choi, S.H. Kim, B.H. Chun, J. Bang, K.B. Lee, Enhancement of chlorine resistance in carbon nanotube-based nanocomposite reverse osmosis membranes, Desalination and Water Treatment, 15 (2010) 198-204.

[167] M.L. Lind, D.E. Suk, T.V. Nguyen, E.M.V. Hoek, Tailoring the structure of thin film nanocomposite membranes to achieve seawater RO membrane performance, Environmental Science and Technology, 44 (2010) 8230-8235.

[168] G.L. Jadav, V.K. Aswal, P.S. Singh, SANS study to probe nanoparticle dispersion in nanocomposite membranes of aromatic polyamide and functionalized silica nanoparticles, Journal of Colloid and Interface Science, 351 (2010) 304-314.

[169] S. Roy, S.A. Ntim, S. Mitra, K.K. Sirkar, Facile fabrication of superior nanofiltration membranes from interfacially polymerized CNT-polymer composites, Journal of Membrane Science, 375 (2011) 81-87.

[170] L. Zhanga, G.Z. Shia, S. Qiua, L.H. Cheng, H.L. Chen, Preparation of high-flux thin film nanocomposite reverse osmosis membranes by incorporating functionalized multi-walled carbon nanotubes, Desalination and Water Treatment, 34 (2011) 19-24.

[171] C. Kong, A. koushima, T. Kamada, T. Shintani, M. Kanezashi, T. Yoshioka, T. Tsuru, Enhanced performance of inorganic-polyamide nanocomposite membranes prepared by metal-alkoxide-assisted interfacial polymerization, Journal of Membrane Science, 366 (2011) 382-388.

[172] M. Fathizadeh, A. Aroujalian, A. Raisi, Effect of added NaX nano-zeolite into polyamide as a top thin layer of membrane on water flux and salt rejection in a reverse osmosis process, Journal of Membrane Science, 375 (2011) 88-95.

[173] E.-S. Kim, B. Deng, Fabrication of polyamide thin-film nano-composite (PA-TFN) membrane with hydrophilized ordered mesoporous carbon (H-OMC) for water purifications, Journal of Membrane Science, 375 (2011) 46-54.

[174] D. Rana, Y. Kim, T. Matsuura, H.A. Arafat, Development of antifouling thin-film-composite membranes for seawater desalination, Journal of Membrane Science, 367 (2011) 110-118.

[175] E.S. Kim, G. Hwang, M. Gamal El-Din, Y. Liu, Development of nanosilver and multi-walled carbon nanotubes thin-film nanocomposite membrane for enhanced water treatment, Journal of Membrane Science, 394-395 (2012) 37-48.

[176] J. Yin, E.S. Kim, J. Yang, B. Deng, Fabrication of a novel thin-film nanocomposite (TFN) membrane containing MCM-41 silica nanoparticles (NPs) for water purification, Journal of Membrane Science, 423-424 (2012) 238-246.

[177] Y. Zhao, C. Qiu, X. Li, A. Vararattanavech, W. Shen, J. Torres, C. Hélix-Nielsen, R. Wang, X. Hu, A.G. Fane, C.Y. Tang, Synthesis of robust and high-performance aquaporin-based biomimetic membranes by interfacial polymerization-membrane preparation and RO performance characterization, Journal of Membrane Science, 423-424 (2012) 422-428.

[178] G.N.B. Baroña, M. Choi, B. Jung, High permeate flux of PVA/PSf thin film composite nanofiltration membrane with aluminosilicate single-walled nanotubes, Journal of Colloid and Interface Science, 386 (2012) 189-197.

[179] N. Ma, J. Wei, R. Liao, C.Y. Tang, Zeolite-polyamide thin film nanocomposite membranes: Towards enhanced performance for forward osmosis, Journal of Membrane Science, 405-406 (2012) 149-157.

[180] T.A. Saleh, V.K. Gupta, Synthesis and characterization of alumina nano-particles polyamide membrane with enhanced flux rejection performance, Separation and Purification Technology, 89 (2012) 245-251.

[181] W.F. Chan, H.Y. Chen, A. Surapathi, M.G. Taylor, X. Shao, E. Marand, J.K. Johnson, Zwitterion functionalized carbon nanotube/polyamide nanocomposite membranes for water desalination, ACS Nano, 7 (2013) 5308-5319.

[182] C.F. De Lannoy, D. Jassby, K. Gloe, A.D. Gordon, M.R. Wiesner, Aquatic biofouling prevention by electrically charged nanocomposite polymer thin film membranes, Environmental Science and Technology, 47 (2013) 2760-2768.

[183] H. You, X. Li, Y. Yang, B. Wang, Z. Li, X. Wang, M. Zhu, B.S. Hsiao, High flux low pressure thin film nanocomposite ultrafiltration membranes based on nanofibrous substrates, Separation and Purification Technology, 108 (2013) 143-151.

[184] J.N. Shen, C.C. Yu, H.M. Ruan, C.J. Gao, B. Van der Bruggen, Preparation and characterization of thin-film nanocomposite membranes embedded with poly(methyl methacrylate) hydrophobic modified multiwalled carbon nanotubes by interfacial polymerization, Journal of Membrane Science, 442 (2013) 18-26.

[185] C.C. Yu, H.W. Yu, Y.X. Chu, H.M. Ruan, J.N. Shen, Preparation thin film nanocomposite membrane incorporating PMMA modified MWNT for nanofiltration, in, 2013, pp. 882-886.

[186] H. Wu, B. Tang, P. Wu, Optimization, characterization and nanofiltration properties test of MWNTs/polyester thin film nanocomposite membrane, Journal of Membrane Science, 428 (2013) 425-433.

[187] M. Amini, M. Jahanshahi, A. Rahimpour, Synthesis of novel thin film nanocomposite (TFN) forward osmosis membranes using functionalized multi-walled carbon nanotubes, Journal of Membrane Science, 435 (2013) 233-241.

[188] H. Huang, X. Qu, X. Ji, X. Gao, L. Zhang, H. Chen, L. Hou, Acid and multivalent ion resistance of thin film nanocomposite RO membranes loaded with silicalite-1 nanozeolites, Journal of Materials Chemistry A, 1 (2013) 11343-11349.

[189] H. Huang, X. Qu, H. Dong, L. Zhang, H. Chen, Role of NaA zeolites in the interfacial polymerization process towards a polyamide nanocomposite reverse osmosis membrane, RSC Advances, 3 (2013) 8203-8207.

[190] S.G. Kim, D.H. Hyeon, J.H. Chun, B.H. Chun, S.H. Kim, Nanocomposite poly(arylene ether sulfone) reverse osmosis membrane containing functional zeolite nanoparticles for seawater desalination, Journal of Membrane Science, 443 (2013) 10-18.

[191] M.M. Pendergast, A.K. Ghosh, E.M.V. Hoek, Separation performance and interfacial properties of nanocomposite reverse osmosis membranes, Desalination, 308 (2013) 180-185.

[192] H. Wu, B. Tang, P. Wu, Optimizing polyamide thin film composite membrane covalently bonded with modified mesoporous silica nanoparticles, Journal of Membrane Science, 428 (2013) 341-348.

[193] M. Bao, G. Zhu, L. Wang, M. Wang, C. Gao, Preparation of monodispersed spherical mesoporous nanosilica-polyamide thin film composite reverse osmosis membranes via interfacial polymerization, Desalination, 309 (2013) 261-266.

[194] S.G. Kim, J.H. Chun, B.H. Chun, S.H. Kim, Preparation, characterization and performance of poly(aylene ether sulfone)/modified silica nanocomposite reverse osmosis membrane for seawater desalination, Desalination, 325 (2013) 76-83.

[195] D. Hu, Z.L. Xu, Y.M. Wei, A high performance silica-fluoropolyamide nanofiltration membrane prepared by interfacial polymerization, Separation and Purification Technology, 110 (2013) 31-38.

[196] G.N.B. Baroña, J. Lim, M. Choi, B. Jung, Interfacial polymerization of polyamide-aluminosilicate SWNT nanocomposite membranes for reverse osmosis, Desalination, 325 (2013) 138-147.

[197] B. Rajaeian, A. Rahimpour, M.O. Tade, S. Liu, Fabrication and characterization of polyamide thin film nanocomposite (TFN) nanofiltration membrane impregnated with TiO_2 nanoparticles, Desalination, 313 (2013) 176-188.

[198] P. Daraei, S.S. Madaeni, E. Salehi, N. Ghaemi, H.S. Ghari, M.A. Khadivi, E. Rostami, Novel thin film composite membrane fabricated by mixed matrix nanoclay/chitosan on PVDF microfiltration support: Preparation, characterization and performance in dye removal, Journal of Membrane Science, 436 (2013) 97-108.

[199] X. Li, R. Wang, F. Wicaksana, C. Tang, J. Torres, A.G. Fane, Preparation of high performance nanofiltration (NF) membranes incorporated with aquaporin Z, Journal of Membrane Science, 450 (2014) 181-188.

[200] H. Zhao, S. Qiu, L. Wu, L. Zhang, H. Chen, C. Gao, Improving the performance of polyamide reverse osmosis membrane by incorporation of modified multi-walled carbon nanotubes, Journal of Membrane Science, 450 (2014) 249-256.

[201] D. Li, H. Wang, Recent developments in reverse osmosis desalination membranes, Journal of Materials Chemistry, 20 (2010) 4551-4566.

[202] C. Bellona, J.E. Drewes, P. Xu, G. Amy, Factors affecting the rejection of organic solutes during NF/RO treatment - A literature review, Water Research, 38 (2004) 2795-2809.

[203] I.J. Roh, A.R. Greenberg, V.P. Khare, Synthesis and characterization of interfacially polymerized polyamide thin films, Desalination, 191 (2006) 279-290.

[204] L. Zhang, G.Z. Shi, S. Qiu, L.H. Cheng, H.L. Chen, Preparation of high-flux thin film nanocomposite reverse osmosis membranes by incorporating functionalized multi-walled carbon nanotubes, Desalination and Water Treatment, 34 (2011) 19-24.

[205] J. Yin, E.-S. Kim, J. Yang, B. Deng, Fabrication of a novel thin-film nanocomposite (TFN) membrane containing MCM-41 silica nanoparticles (NPs) for water purification, Journal of Membrane Science, 423–424 (2012) 238-246.

[206] C.K. Kim, J.H. Kim, I.J. Roh, J.J. Kim, The changes of membrane performance with polyamide molecular structure in the reverse osmosis process, Journal of Membrane Science, 165 (2000) 189-199.

[207] A.K. Ghosh, B.H. Jeong, X. Huang, E.M.V. Hoek, Impacts of reaction and curing conditions on polyamide composite reverse osmosis membrane properties, Journal of Membrane Science, 311 (2008) 34-45.

[208] H. Saitua, R. Gil, A.P. Padilla, Experimental investigation on arsenic removal with a nanofiltration pilot plant from naturally contaminated groundwater, Desalination, 274 (2011) 1-6.

[209] J. Glater, S.k. Hong, M. Elimelech, The search for a chlorine-resistant reverse osmosis membrane, Desalination, 95 (1994) 325-345.

[210] Y.N. Kwon, S. Hong, H. Choi, T. Tak, Surface modification of a polyamide reverse osmosis membrane for chlorine resistance improvement, Journal of Membrane Science, 415-416 (2012) 192-198.

[211] T. Shintani, H. Matsuyama, N. Kurata, Development of a chlorine-resistant polyamide reverse osmosis membrane, Desalination, 207 (2007) 340-348.

[212] M.T.M. Pendergast, J.M. Nygaard, A.K. Ghosh, E.M.V. Hoek, Using nanocomposite materials technology to understand and control reverse osmosis membrane compaction, Desalination, 261 (2010) 255-263.

[213] X. Song, Z. Liu, D.D. Sun, Energy recovery from concentrated seawater brine by thin-film nanofiber composite pressure retarded osmosis membranes with high power density, Energy and Environmental Science, 6 (2013) 1199-1210.

[214] N. Ma, J. Wei, S. Qi, Y. Zhao, Y. Gao, C.Y. Tang, Nanocomposite substrates for controlling internal concentration polarization in forward osmosis membranes, Journal of Membrane Science, 441 (2013) 54-62.

[215] Y. Wang, R. Ou, Q. Ge, H. Wang, T. Xu, Preparation of polyethersulfone/carbon nanotube substrate for high-performance forward osmosis membrane, Desalination, 330 (2013) 70-78.

[216] D. Emadzadeh, W.J. Lau, A.F. Ismail, Synthesis of thin film nanocomposite forward osmosis membrane with enhancement in water flux without sacrificing salt rejection, Desalination, 330 (2013) 90-99.

[217] D. Emadzadeh, W.J. Lau, T. Matsuura, M. Rahbari-Sisakht, A.F. Ismail, A novel thin film composite forward osmosis membrane prepared from PSf-TiO_2 nanocomposite substrate for water desalination, Chemical Engineering Journal, 237 (2014) 70-80.

[218] D. Emadzadeh, W.J. Lau, T. Matsuura, A.F. Ismail, M. Rahbari-Sisakht, Synthesis and characterization of thin film nanocomposite forward osmosis membrane with hydrophilic nanocomposite support to reduce internal concentration polarization, Journal of Membrane Science, 449 (2014) 74-85.

[219] J.R. McCutcheon, M. Elimelech, Influence of concentrative and dilutive internal concentration polarization on flux behavior in forward osmosis, Journal of Membrane Science, 284 (2006) 237-247.

[220] J. Wei, C. Qiu, C.Y. Tang, R. Wang, A.G. Fane, Synthesis and characterization of flat-sheet thin film composite forward osmosis membranes, Journal of Membrane Science, 372 (2011) 292-302.

[221] S.Y. Kwak, S.H. Kim, S.S. Kim, Hybrid organic/inorganic reverse osmosis (RO) membrane for bactericidal anti-fouling. 1. Preparation and characterization of TiO_2 nanoparticle self-assembled aromatic polyamide thin-film-composite (TFC) membrane, Environmental Science and Technology, 35 (2001) 2388-2394.

[222] S.H. Kim, S.Y. Kwak, B.H. Sohn, T.H. Park, Design of TiO_2 nanoparticle self-assembled aromatic polyamide thin-film-composite (TFC) membrane as an approach to solve biofouling problem, Journal of Membrane Science, 211 (2003) 157-165.

[223] T.H. Bae, T.M. Tak, Preparation of TiO_2 self-assembled polymeric nanocomposite membranes and examination of their fouling mitigation effects in a membrane bioreactor system, Journal of Membrane Science, 266 (2005) 1-5.

[224] M.L. Luo, J.Q. Zhao, W. Tang, C.S. Pu, Hydrophilic modification of poly(ether sulfone) ultrafiltration membrane surface by self-assembly of TiO_2 nanoparticles, Applied Surface Science, 249 (2005) 76-84.

[225] T.H. Bae, I.C. Kim, T.M. Tak, Preparation and characterization of fouling-resistant TiO_2 self-assembled nanocomposite membranes, Journal of Membrane Science, 275 (2006) 1-5.

[226] S.S. Madaeni, N. Ghaemi, Characterization of self-cleaning RO membranes coated with TiO2 particles under UV irradiation, Journal of Membrane Science, 303 (2007) 221-233.

[227] Y. Mansourpanah, S.S. Madaeni, A. Rahimpour, A. Farhadian, A.H. Taheri, Formation of appropriate sites on nanofiltration membrane surface for binding TiO_2 photo-catalyst: Performance, characterization and fouling-resistant capability, Journal of Membrane Science, 330 (2009) 297-306.

[228] J.H. Li, Y.Y. Xu, L.P. Zhu, J.H. Wang, C.H. Du, Fabrication and characterization of a novel TiO_2 nanoparticle self-assembly membrane with improved fouling resistance, Journal of Membrane Science, 326 (2009) 659-666.

[229] S. Yang, J.S. Gu, H.Y. Yu, J. Zhou, S.F. Li, X.M. Wu, L. Wang, Polypropylene membrane surface modification by RAFT grafting polymerization and TiO_2 photocatalysts immobilization for phenol decomposition in a photocatalytic membrane reactor, Separation and Purification Technology, 83 (2011) 157-165.

[230] Z. Fan, Z. Wang, M. Duan, J. Wang, S. Wang, Preparation and characterization of polyaniline/polysulfone nanocomposite ultrafiltration membrane, Journal of Membrane Science, 310 (2008) 402-408.

[231] S.S. Madaeni, N. Ghaemi, A. Alizadeh, M. Joshaghani, Influence of photo-induced superhydrophilicity of titanium dioxide nanoparticles on the anti-fouling performance of ultrafiltration membranes, Applied Surface Science, 257 (2011) 6175-6180.

[232] Y. Han, Z. Xu, C. Gao, Ultrathin graphene nanofiltration membrane for water purification, Advanced Functional Materials, 23 (2013) 3693-3700.

[233] P. Gao, Z. Liu, M. Tai, D.D. Sun, W. Ng, Multifunctional graphene oxide-TiO_2 microsphere hierarchical membrane for clean water production, Applied Catalysis B: Environmental, 138-139 (2013) 17-25.

[234] A.S. Brady-Estévez, S. Kang, M. Elimelech, A single-walled-carbon-nanotube filter for removal of viral and bacterial pathogens, Small, 4 (2008) 481-484.

[235] F. Ahmed, C.M. Santos, J. Mangadlao, R. Advincula, D.F. Rodrigues, Antimicrobial PVK: SWNT nanocomposite coated membrane for water purification: Performance and toxicity testing, Water Research, 47 (2013) 3966-3975.

[236] H.L. Yang, J.C.T. Lin, C. Huang, Application of nanosilver surface modification to RO membrane and spacer for mitigating biofouling in seawater desalination, Water Research, 43 (2009) 3777-3786.

[237] X. Cao, M. Tang, F. Liu, Y. Nie, C. Zhao, Immobilization of silver nanoparticles onto sulfonated polyethersulfone membranes as antibacterial materials, Colloids and Surfaces B: Biointerfaces, 81 (2010) 555-562.

[238] S. Zhang, G. Qiu, Y.P. Ting, T.S. Chung, Silver-PEGylated dendrimer nanocomposite coating for anti-fouling thin film composite membranes for water treatment, Colloids and Surfaces A: Physicochemical and Engineering Aspects, 436 (2013) 207-214.

[239] M.S. Mauter, Y. Wang, K.C. Okemgbo, C.O. Osuji, E.P. Giannelis, M. Elimelech, Antifouling ultrafiltration membranes via post-fabrication grafting of biocidal nanomaterials, ACS Applied Materials and Interfaces, 3 (2011) 2861-2868.

[240] A. Tiraferri, Y. Kang, E.P. Giannelis, M. Elimelech, Superhydrophilic thin-film composite forward osmosis membranes for organic fouling control: Fouling behavior and antifouling mechanisms, Environmental Science and Technology, 46 (2012) 11135-11144.

[241] M. Ben-Sasson, K.R. Zodrow, Q. Genggeng, Y. Kang, E.P. Giannelis, M. Elimelech, Surface functionalization of thin-film composite membranes with copper nanoparticles for antimicrobial surface properties, Environmental Science and Technology, 48 (2014) 384-393.

[242] J. Park, W. Choi, J. Cho, B.H. Chun, S.H. Kim, K.B. Lee, J. Bang, Carbon nanotube-based nanocomposite desalination membranes from layer-by-layer assembly, Desalination and Water Treatment, 15 (2010) 76-83.

[243] N. Wang, S. Ji, G. Zhang, J. Li, L. Wang, Self-assembly of graphene oxide and polyelectrolyte complex nanohybrid membranes for nanofiltration and pervaporation, Chemical Engineering Journal, 213 (2012) 318-329.

[244] M. Hu, B. Mi, Enabling graphene oxide nanosheets as water separation membranes, Environmental Science and Technology, 47 (2013) 3715-3723.

[245] W. Choi, J. Choi, J. Bang, J.H. Lee, Layer-by-layer assembly of graphene oxide nanosheets on polyamide membranes for durable reverse-osmosis applications, ACS Applied Materials and Interfaces, 5 (2013) 12510-12519.

[246] X. Liu, S. Qi, Y. Li, L. Yang, B. Cao, C.Y. Tang, Synthesis and characterization of novel antibacterial silver nanocomposite nanofiltration and forward osmosis membranes based on layer-by-layer assembly, Water Research, 47 (2013) 3081-3092.

[247] G. Sun, T.S. Chung, K. Jeyaseelan, A. Armugam, A layer-by-layer self-assembly approach to developing an aquaporin-embedded mixed matrix membrane, RSC Advances, 3 (2013) 473-481.

[248] J. Mo, S.H. Son, J. Jegal, J. Kim, Y.H. Lee, Preparation and characterization of polyamide nanofiltration composite membranes with TiO_2 layers chemically connected to the membrane surface, Journal of Applied Polymer Science, 105 (2007) 1267-1274.

[249] A. Tiraferri, C.D. Vecitis, M. Elimelech, Covalent binding of single-walled carbon nanotubes to polyamide membranes for antimicrobial surface properties, ACS Applied Materials and Interfaces, 3 (2011) 2869-2877.

[250] P. Gunawan, C. Guan, X. Song, Q. Zhang, S.S.J. Leong, C. Tang, Y. Chen, M.B. Chan-Park, M.W. Chang, K. Wang, R. Xu, Hollow fiber membrane decorated with Ag/MWNTs: Toward effective water disinfection and biofouling control, ACS Nano, 5 (2011) 10033-10040.

[251] J. Yin, Y. Yang, Z. Hu, B. Deng, Attachment of silver nanoparticles (AgNPs) onto thin-film composite (TFC) membranes through covalent bonding to reduce membrane biofouling, Journal of Membrane Science, 441 (2013) 73-82.

[252] S.Y. Park, J.W. Chung, Y.K. Chae, S.Y. Kwak, Amphiphilic thiol functional linker mediated sustainable anti-biofouling ultrafiltration nanocomposite comprising a silver nanoparticles and poly(vinylidene fluoride) membrane, ACS Applied Materials and Interfaces, 5 (2013) 10705-10714.

[253] Z. Wang, H. Ma, B.S. Hsiao, B. Chu, Nanofibrous ultrafiltration membranes containing cross-linked poly(ethylene glycol) and cellulose nanofiber composite barrier layer, Polymer (United Kingdom), 55 (2014) 366-372.

[254] Y.H. Teow, A.L. Ahmad, J.K. Lim, B.S. Ooi, Preparation and characterization of PVDF/TiO_2 mixed matrix membrane via in situ colloidal precipitation method, Desalination, 295 (2012) 61-69.

[255] A. Razmjou, E. Arifin, G. Dong, J. Mansouri, V. Chen, Superhydrophobic modification of TiO_2 nanocomposite PVDF membranes for applications in membrane distillation, Journal of Membrane Science, 415-416 (2012) 850-863.

CHAPTER TWO

Fabrication of a novel thin-film nanocomposite (TFN) membrane containing MCM-41 silica nanoparticles (NPs) for water purification

Abstract

A thin-film nanocomposite (TFN) membrane containing porous MCM-41 silica nanoparticles (NPs) was prepared by the in situ interfacial polymerization (IP) process. Aqueous *m*-phenylenediamine (MPD) and organic trimesoyl chloride (TMC)-NPs mixture solutions were used in the IP process. Porous MCM-41 (~100 nm) and non-porous spherical silica NPs (~100 nm) were synthesized and used as the fillers to fabricate the TFN membrane at concentrations ranging from 0 to 0.1 wt%. The membranes were characterized by scanning electron microscopy (SEM), transmission electron microscopy (TEM), atomic force microscopy (AFM) and attenuated total reflection Fourier transform infrared (ATR FT-IR) spectroscopy, and their performances were evaluated based on the water permeability and salt rejection. Results indicated that the MCM-41 NPs dispersed well in polyamide (PA) thin-film layer and improved membrane performances under optimal concentrations. By increasing concentration of MCM-41 NPs, hydrophilicity, roughness and zeta potential of TFN membranes all increased. Notably, the permeate water flux increased from 28.5 ± 1.0 L/m^{2}h to 46.6 ± 1.1 L/m^{2}h with the incorporation of MCM-41 NPs, while maintaining high rejections of NaCl and Na_2SO_4 (97.9 ± 0.3 % and 98.5 ± 0.2 %, respectively). A comparison between the membranes with non-porous silica NPs (S-TFN) and with the porous MCM-41 NPs (M-TFN) suggested that the internal pores of MCM-41 NPs contributed significantly to the increase of water permeability.

Keywords: MCM-41 nanoparticles; Polyamide; Thin-film nanocomposite; Interfacial polymerization; Desalination

2.1 Introduction

Reverse osmosis (RO) and nanofiltration (NF) membranes have been widely used for water reclamation, desalination, and other separation processes [1-3]. The thin-film composite (TFC) membrane is a major type of RO and NF membranes, which consists of a thin-film layer supported on a porous substrate (support layer) [4]. High water flux, high solute rejection, minimum membrane fouling, and excellent mechanical durability are major attributes of a good TFC membrane [5]. Many efforts have been devoted to modify polymer materials, develop new membranes, and implement proper pre-treatments in order to improve the membrane performance. Because of the multilayer structure of TFC membranes, replacing or modifying the support layer is one way to improve their performance. Polysulfone (PSU) is a dominant material used for the support layer, which shows good thermal and chemical stabilities with low cost [1, 6]. Optimizing its structure through modified fabrication process [1], or replacing it with other polymer such as the plasma-treated polyvinylidene fluoride (PVDF) [7] have been reported to improve the TFC membrane performance. The other approach is to change properties of the thin-film layer. Uses of different interfacial polymerization (IP) conditions [8], monomers [9], and physical coating or chemical modifications [10, 11] could be explored to optimize the membrane performances.

Recently, the thin-film nanocomposite (TFN) membrane is under active development in which nanomaterials are embedded in the thin-film layer to improve the membrane physicochemical properties and performance. Jeong et al. [12] introduced the Zeolite-A nanoparticles (NPs) into TFN membrane, resulting in higher water flux with constant salt rejection. The hydrophilic and negatively charged Zeolite-A NPs provided

the preferential flow paths for water molecules and the combination of steric and Donnan exclusion maintained high salt rejection. The effects of crystal size of zeolite in the TFN membrane were investigated [13], and small sized NPs (~100nm) were found to best match the thin-film thickness and provided permeability enhancement. Silica (SiO_2) NPs improved membrane thermal stability and performance [14], TiO_2 increased surface hydrophilicity and enhanced water flux [15], and silver (Ag) NPs promoted the anti-biofouling properties [16]. These results suggested a great potential of TFN membranes to out-perform those conventional thin-film composites currently available on the market. However, the mechanism of water permeability enhancement of TFN membrane is still unclear. Changes in surface hydrophilicity, porous structures of filler, and cross-linking of polymers in the thin-film layer could all contribute to this performance improvement. Therefore, it is necessary to explore the specific contributions of these possible factors. And this fundamental understanding will help screen good filler candidates with desirable properties for a new generation of high performance TFN membranes.

The primary objective of this study was to illustrate if the internal pore structures of fillers could influence the performance of TFN membranes, and then develop a high performance TFN membrane. Silica is chemically inert, thermally stable, and inexpensive [17], so two silica-based fillers with similar size but different internal structures were synthesized as model filler materials. Ordered mesoporous material, MCM-41 NPs, which possesses a two-dimensional (2D) hexagonal ordered structure, tunable size and controllable morphology [18-20] was used to represent a porous filler, while spherical silica NPs without internal pores was used as a non-porous filler. To be compatible with the typical thickness of thin-film layer which is about several hundred nanometers [8,

14], the size of filler was controlled at around 100 nm. These two kinds of fillers were incorporated into the polyamide (PA) thin-film layer during the IP process, thus creating the TFN membranes. The physicochemical properties of the NPs and TFN membranes were evaluated by scanning electron microscopy (SEM), transmission electron microscopy (TEM), atomic force microscopy (AFM), attenuated total reflection Fourier transform infrared (ATR FT-IR) spectroscopy, contact angle and streaming potential measurements. The membrane performances were examined by water permeability and solute rejection based on different loadings of NPs. The effect of filler's internal pores was explored by comparing the performance of different TFN membranes embedded with specific fillers.

2.2 Materials and methods

2.2.1 Materials

Cetyltrimethylammonium bromide (CTAB, 95%, Aldrich) and tetraethyl orthosilicate (TEOS, 98%, Sigma-Aldrich) were used as surfactant and silica source, respectively, for the synthesis of MCM-41. TEOS and aqueous ammonia solution (catalyst, 20–22%, Fisher Scientific) were used for the synthesis of spherical silica NPs. PSU (Mw = 35,000, Aldrich) pellets dissolved in *N*, *N*-dimethylformamide (DMF, 99.8%, Aldrich) were used as the casting solution to make the support layer. *m*-phenylenediamine (MPD, >99%, Aldrich) and trimesoyl chloride (TMC, >98.5%, Aldrich) were monomers used in the IP process. All chemicals were ACS reagents grade. Deionized (DI) water produced by Millipore DI system (Synergy 185, 18.2 MΩ·cm) was used for solution preparation and filtration study.

2.2.2 Synthesis and characterization of MCM-41 NPs and spherical silica NPs

MCM-41 NPs were synthesized by a procedure reported in the literature [20]. A 3.5 mL of 2 M sodium hydroxide solution (NaOH, Aldrich) and 480 mL of DI water were mixed for 10 min, and 1.0 g of CTAB was added to mixture with stirring at 353 K for 30 min. Then, a 5 mL of TEOS was added drop-wise to the prepared solution. After 2 h of stirring, a white slurry mixture formed was centrifuged at 10,000 rpm for 10 min (5810R, Eppendorf Corp., Hamburg, Germany) and washed twice with DI water. The products were dried at ambient temperature and calcinated in air at 823K for 4 h.

The hydrolysis of TEOS in ethanol with ammonia as a catalyst was used to synthesize the spherical silica NPs [21]. A 14 g of ammonia aqueous solution was mixed with 190 mL ethanol, and then 22.3 mL TEOS was added. After 4 h of stirring at room temperature (23 ± 1 ℃), the mixture was centrifuged at 10,000 rpm for 10 min. The product was washed twice with ethanol, dried and calcinated in air at 723K for 3 h. The final products (i.e., MCM-41 NPs and spherical silica NPs) were stored in a desiccator.

The crystalline structures of synthesized NPs were analyzed by an X-ray powder diffractometer (XRD, Ultima IV, Rigaku Americas Corp., The Woodlands, TX). The samples were scanned from 0.8° to 10° (2θ) with a step size of 0.02° and a count time of 1 s at each point. N_2 adsorption onto and desorption from the NPs were carried out on QUADRASORB™ SI (Quantachrome Instruments, Boynton Beach, FL) at 77 K. The specific surface areas and pore size distributions were calculated by Brunauer-Emmett-Teller (BET) method and density functional theory (DFT) method, respectively. Morphology and internal structure of NPs were examined by SEM (Quanta FEG 600, FEI Company, Hillsboro, OR) and TEM (JEM 1400, JEOL Ltd., Peabody, MA). SEM

specimen was prepared by dropping NPs-ethanol mixture solution onto a silicon wafer. After complete drying at room temperature, the specimen was coated with platinum by a sputter coater (K575x, Emitech Ltd., Kent, England) at 20 mA for 1 min to increase conductivity. TEM samples of NPs were prepared by dropping NPs-ethanol mixture solution onto carbon coated copper grid and drying at the room temperature.

2.2.3 Preparation of PSU support layer and TFN membrane

The PSU support layer was fabricated by the phase inversion method (presented in SI Fig. 2.1s) using 15 wt% PSU-DMF casting solution. The casting solution was stirred at 50 ℃ for 6 h, and kept overnight for degassing. The clear solution was spread on a glass plate and casted by casting knife (EQ-Se-KTQ-150, MTI Corp., Richmond, CA) to approximately 100 μm of film thickness. Then, glass plate was immediately immersed into a DI water bath (25 ℃). The precipitated PSU support membrane was washed and stored in DI water at least 24 h until use.

For TFN membrane fabrication (presented in SI Fig. 2.2s), the prepared PSU support layer was immersed in a 2.0 wt% MPD-water solution for 3 min. Excess solution on the surface was removed by a rubber roller. Next, the MPD saturated PSU support layer was soaked in a 0.15 wt% of TMC-hexane solution for 2 min, resulting in the formation of a PA thin-film layer. The amounts of NPs (MCM-41 or spherical silica NPs) dispersed in the TMC-hexane solution varied from 0 to 0.1 wt%. A complete mixing of NPs in the TFC-hexane solution was achieved by ultrasonication for 1 h. The TFN membranes were rinsed with pure hexane and cured at 80 ℃ in an oven for 5 min, and then stored in DI water at 5 ℃. The final products were named as M-TFN-x or S-TFN-x, where x denoted the concentration of filler in TMC solution during the IP process. For

example, TFN membrane prepared by 0.05 wt% MCM-41 NPs was named as M-TFN-0.05.

2.2.4 TFN membrane characterization and performance assessment

SEM analysis of membrane surface was conducted using a piece of membrane dried at room temperature. The operational condition was identical with NPs analysis described in the section of 2.2.2. To obtain the TEM cross-section, the membranes were embedded in Epon resin (Eponate 12, Ted Pella, Inc., Redding, CA) and cut by Reichert-Jung Ultracut E ultramicrotome (Reichert, Inc. Depew, NY). The images were taken under 80 kV by using JEM 1400. Hydrophilicity of membrane was assessed based on the measurement of pure water contact angles. The video contact angle system (VCA-2500 XE, AST products, Billerica, MA) was employed to perform the sessile drop method. At least six stabilized contact angles from different sites of each sample were obtained to calculate average contact angle and standard deviation. The functional groups of membrane surface were identified by attenuated total reflection Fourier transform infrared (ATR FT-IR) spectroscopy. Nicolet 4700 FT-IR (Thermo Electron Corporation, Waltham, MA) equipped with multi-reflection Smart Performer® ATR accessory was used for this analysis. All spectra included the wave numbers from 500 to 4000 cm^{-1} with 128 scans at a resolution of 2.0 cm^{-1}. Quantitative surface roughness of the membrane was analyzed by atomic force microscopy (AFM5500, Agilent Technologies, Inc. Santa Clara, CA) with tapping mode in air. A 100 μm^2 of surface area was tested and the root mean square (RMS) roughness was recorded. Tangential streaming potential was measured to calculate surface zeta (ζ) potential with 0.01 M potassium chloride (KCl, Fisher) used as an electrolyte solution. All measurements were carried out at room

temperature (23 ±1 ℃) and the solution pH was controlled at 5.8 ±0.2. The zeta potential was obtained by the classic Helmholtz-Smoluchowski (H-S) equation:

$$\zeta = \frac{E_S}{\Delta P}\frac{\eta\kappa}{\varepsilon_r\varepsilon_0} \tag{1}$$

where E_s is the tangential streaming potential, ΔP is the pressure gradient, κ is the conductance of electrolyte solution, η is the liquid viscosity, ε_0 is the vacuum permittivity, and ε_r is the relative dielectric constant.

A high pressure cross-flow filtration system (pressure range: 50–500 psi) was used to evaluate water flux and solute rejection. A schematic diagram of the filtration system is shown in Fig. 2.1.

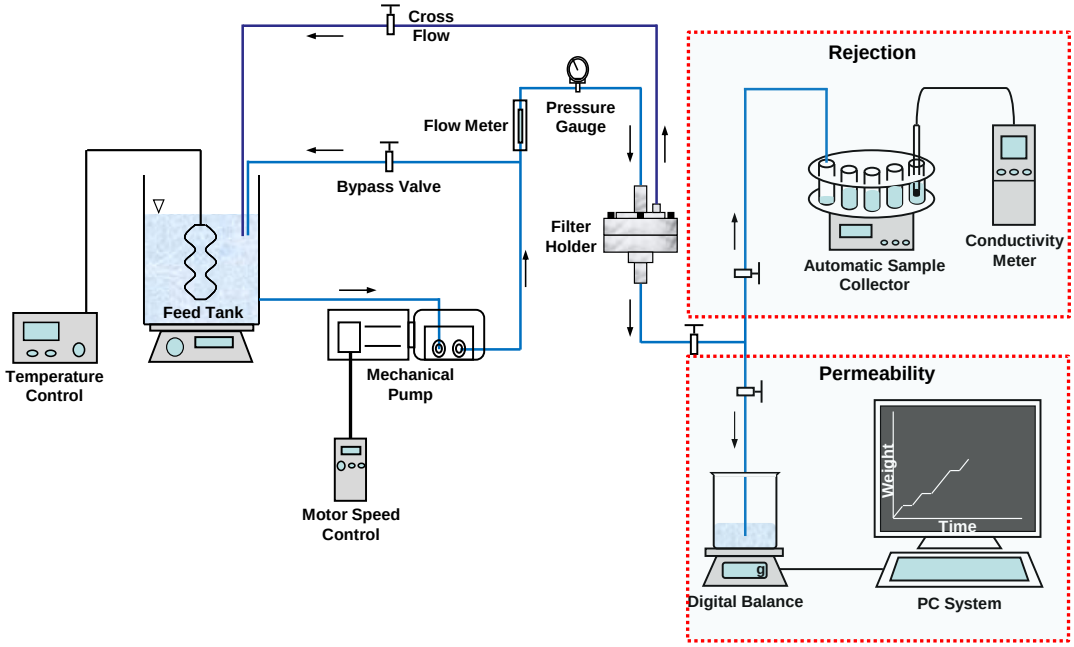

Fig. 2.1 The schematic diagram of a high pressure cross-flow filtration system.

The filter holder (Model: XX4504700, stainless steel, Millipore Corp., Billerica, MA) in the test apparatus had an effective membrane area of 9.6 cm^2. Prior to test, each membrane was compressed by DI water at 300 psi for 5 h. Water flux was measured by

the weight of the permeate water at a constant transmembrane pressure (TMP). The weight of the permeate water was recorded by a LabVIEW automated system (National Instruments LabVIEW 8.2 with Ohaus digital balance). After pure water flux test, salt solution (final concentration of 2,000 ppm of NaCl or Na_2SO_4) was added and the conductivity of feed and permeate solutions was measured by a conductivity/TDS meter (HACH Company, Loveland, CO). The measurement was conducted at 25 ± 1 ℃, which was controlled by a water circulator (Isotemp 6200 R20F, Fisher Scientific, Inc., Pittsburgh, PA). The flux and rejection was calculated with equation (2) and equation (3), respectively.

$$J = \frac{V_p}{A \cdot t} \tag{2}$$

$$R = \left(1 - \frac{C_p}{C_f}\right) \times 100 \tag{3}$$

where J is the water flux (L/m^{2}h), V_p is the permeate volume (L), A is the membrane area (m^2) and t is the treatment time (hr). R is the rejection ratio and C_p and C_f are the conductivities of permeate and feed solution, respectively.

2.3 Results and discussion

2.3.1 Characterization of synthesized NPs

The small-angle XRD patterns of spherical silica and MCM-41 NPs are presented in Fig. 2.2. MCM-41 NPs showed four well-resolved peaks at 2θ of 2.1°, 3.8°, 4.4° and 5.8°. These peaks were indexed as (100), (110), (200) and (210), respectively, consistent with the hexagonal lattice symmetry of MCM-41 structure [19-20]. The repeat distance (a_0) between two pore centers in MCM-41 NPs can be calculated (hexagonal a_0 =

2d100/√3) [20]. From the result of XRD, d_{100} for this sample is 4.203 nm, so a_0 is about 4.85 nm. After subtracting pore wall thickness which is approximately 1 nm [22], the pore diameter of synthesized MCM-41NPs is about 3.85 nm. The BET analysis showed that MCM-41 NPs had a much large surface area (949.4 m^2/g) when compared to spherical silica NPs (72.7 m^2/g). The pore size inside MCM-41 is around 3.03 nm while there is no internal pore inside the spherical silica NPs, which is consistent with the result of XRD.

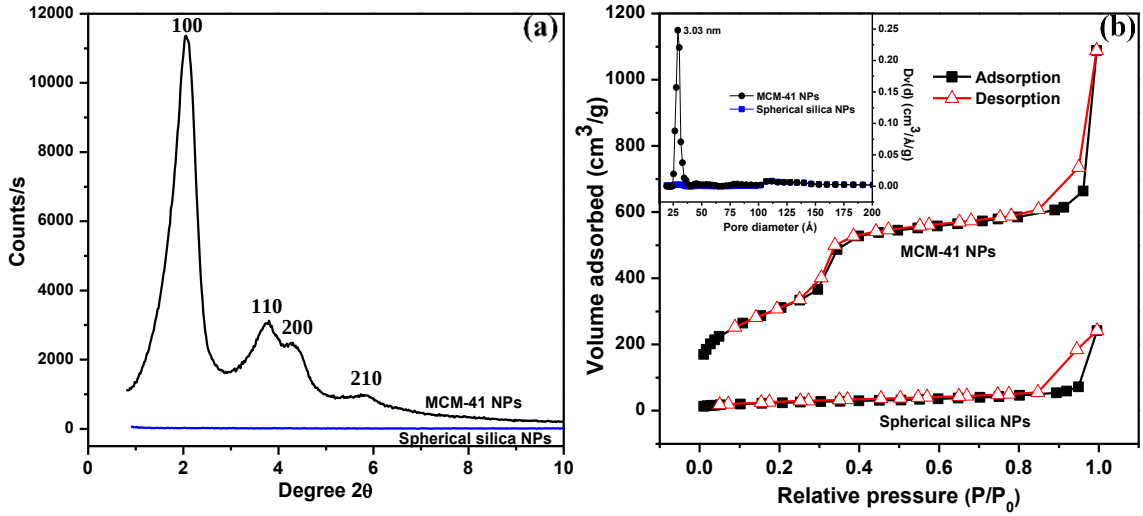

Fig. 2.2 XRD patterns (a) and N_2 adsorption/desorption isotherm & pore size distribution (b) of NPs.

Both SEM (Fig. 2.3a) and TEM (Fig. 2.3b) micrographs demonstrated that MCM-41 NPs had near spherical shape. The size of particle was about 100 nm. Highly ordered hexagonal array and streak structure were detected inside particles. TEM image of spherical silica NPs (Fig. 2.3c) also showed a uniform spherical shape with an average particle size around 100 nm, but without internal pores. This was also consistent with the small-angle XRD pattern of spherical silica NPs that showed no peaks in the range from 0.8 °to 10 ℃f 2θ (Fig. 2.2a).

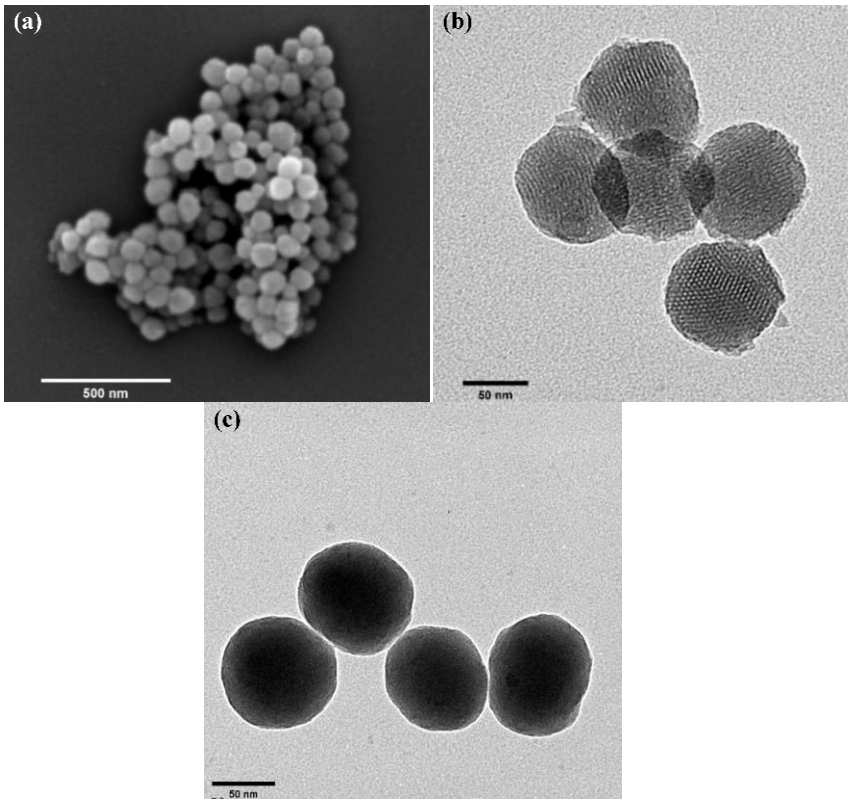

Fig. 2.3 Microscopic images of nanofillers: (a) SEM image and (b) TEM image of porous MCM-41NPs; and (c) TEM image of non-porous spherical silica NPs.

2.3.2 Characterization of TFN membranes

The ATR FT-IR spectra of PSU support layer, TFC and M-TFN membranes are shown in Fig. 2.4. For the PSU support layer (Fig. 2.4a), peaks at 1590 $cm^{-1}$and 1488 cm^{-1} could be assigned to aromatic C-C stretching, 1325 cm^{-1} and 1298 cm^{-1} to the doublet from the asymmetric O=S=O stretching of sulfone group, 1245 cm^{-1} to the asymmetric C-O-C stretching of aryl ether group and 1150 cm^{-1} to the symmetric O=S=O stretching of sulfone group, all existing in the PSU cross-linking polymerization [23, 24]. PA thin-film layer was coated on the PSU support layer following the IP process, and several new peaks appeared on the spectrum (Fig. 2.4b). Peaks at 1660 cm^{-1} (amide I, C=O stretching vibrations of amide), 1547 cm^{-1} (amide II, in-plane N-H bending and C-N stretching

vibrations), 1610 cm^{-1} (N-H stretching of amide) and 1450 cm^{-1} (C=O stretching and O-H bending of carboxylic acid) were originated from the PA polymerization and consisted with amide functionalities [15, 24, 25]. Besides these peaks from PA thin-film layer, the peak between 1040 and 1080 cm^{-1} derived from the asymmetric vibration of Si-O-Si [14] increased with increasing concentrations of MCM-41 NPs from 0.05 wt% to 0.1 wt%. To further explore the spectral change due to the NPs, we prepared a membrane with a relatively high loading (0.5 wt%) and its spectrum is presented as Fig. 2.4e. Except for the obvious peak located around 1040-1080 cm^{-1}, a small peak around 950 cm^{-1} appeared, which could be attributed to the stretching vibration of Si-OH [26]. This result verified the existence of MCM-41 NPs in the membrane after the interfacial polymerization process. No other new peaks were observed after this increase in NPs loading, suggesting that there is no strong chemical bonding between the NPs and polymer functional groups.

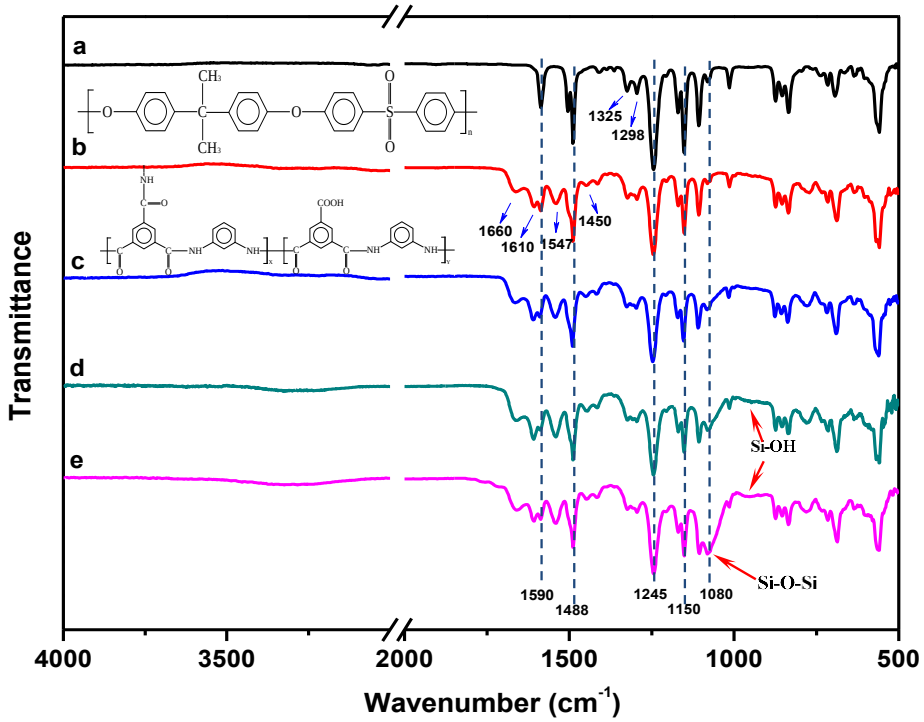

Fig. 2.4 ATR FT-IR spectra of (a) PSU support layer; (b) TFC (without NPs); (c) M-TFN-0.05; (d) M-TFN-0.1; and (e) M-TFN-0.5 membrane.

The SEM surface morphologies of the PSU support layer, TFC, M-TFN-0.01 and M-TFN-0.05 membranes are shown in Fig. 2.5. The PSU support layer was porous with a pore size of 23.2 ± 8.4 nm, based on the calculation by the software ImageJ from a total of 1438 pore counts. After the IP process, PA thin-film layer coated on the PSU support layer by the reaction between MPD and TMC and resulted a leaf-like morphology (Fig. 2.5b-d). The impregnation of MCM-41 NPs did not affect the overall morphology of thin-film layer in the tested concentration range, but partial aggregation of MCM-41 NPs was observed in samples with higher concentrations (indicated by white circle in Fig. 2.5d).

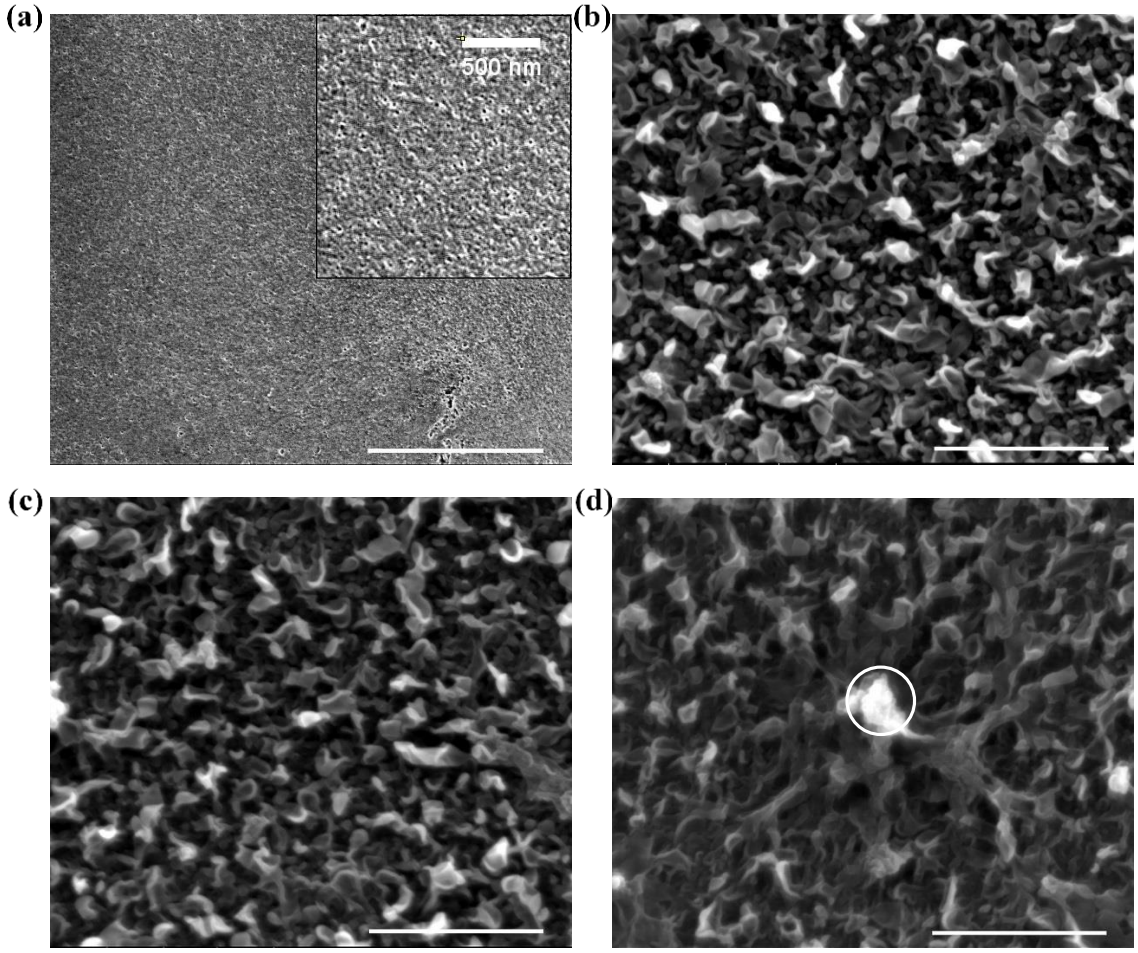

Fig. 2.5 SEM images of membrane surface morphologies: (a) PSU support layer; (b) TFC; (c) M-TFN-0.01; and (d) M-TFN-0.05. All scales were represented in 2 μm.

TEM images of the cross-sections of TFC and M-TFN-0.05 membranes (Fig. 2.6) indicated that the PA thin-film layer in both membranes had a thickness between 300 and 500 nm. The leaf-like structure of PA thin-film layer was consistent with the SEM observation (Fig. 2.5). The dark spots appeared in the PA thin-film layer of M-TFN membrane (Fig. 2.6b) indicated the presence of MCM-41 NPs. And aggregation of the MCM-41 NPs could be detected on the surface of thin-film layer in the TEM cross-sectional image.

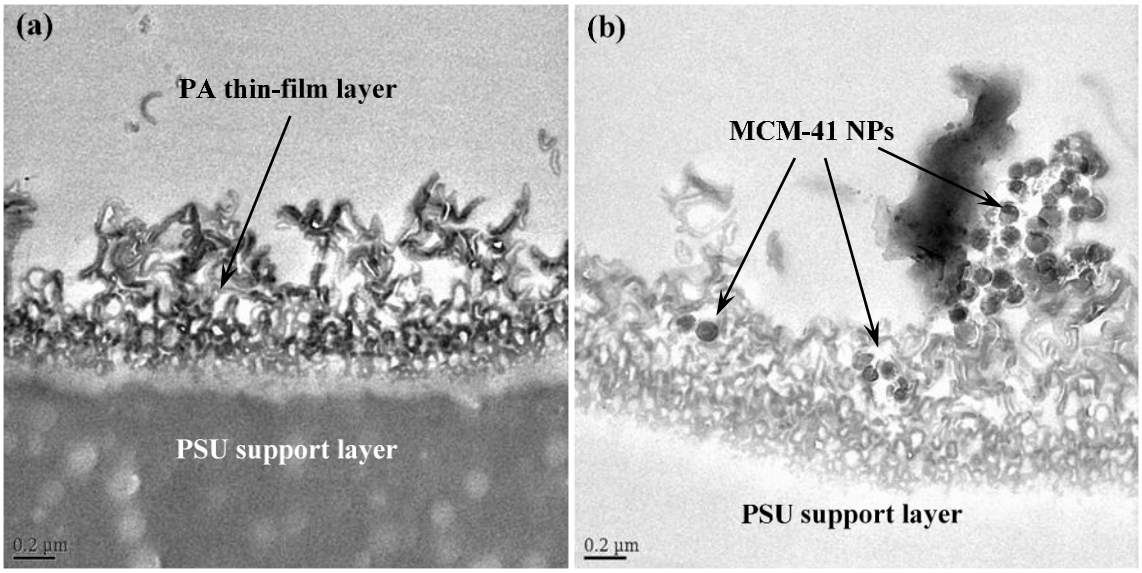

Fig. 2.6 TEM images of the cross-section of (a) TFC membrane; and (b) M-TFN-0.05 membrane.

As presented in Fig. 2.7a, the contact angle of M-TFN membranes decreased from 57.1 ± 2.7 ° to 27.9 ± 1.3 °, while contact angle of S-TFN membranes decreased from 57.1 ± 2.7 ° to 30.6 ± 1.4 ° with increasing NPs concentrations from 0 to 0.1 wt%. The contact angle was decreased to 28.8 ± 1.6 ° when the concentration of MCM-41 NPs was increased to 0.05 wt%, then leveled off with further increases of the NPs concentration.

The decrease of the contact angles in the presence of the embedded NPs could be caused by two reasons. First, the NPs may hydrate and release heat when contacting with MPD aqueous solution [13]. This process may affect the IP reaction between MPD and TMC, and subsequently the chemical structure of the PA thin-film. If more number of the acyl chloride groups in TMC remained on the surface without reaction with amine groups, the hydrolysis of acyl chloride could generate carboxylic acid functional groups; thus, surface hydrophilicity increased [9]. Second, the embedded spherical silica or MCM-41 NPs can be exposed on the membrane surface. Therefore, the membrane surface hydrophilicity may increase because of the hydrophilic properties of these two NPs. Embedding with porous MCM-41 NPs, the membrane surface could even become more hydrophilic due to the capability of the hydrophilic pores to imbibe water via capillary effects [27]. This is consistent with the result by Jeong et al. [12], who observed that the contact angle of membrane surface decreased with increasing Zeolite concentration and attributed this to the super-hydrophilic property of Zeolite.

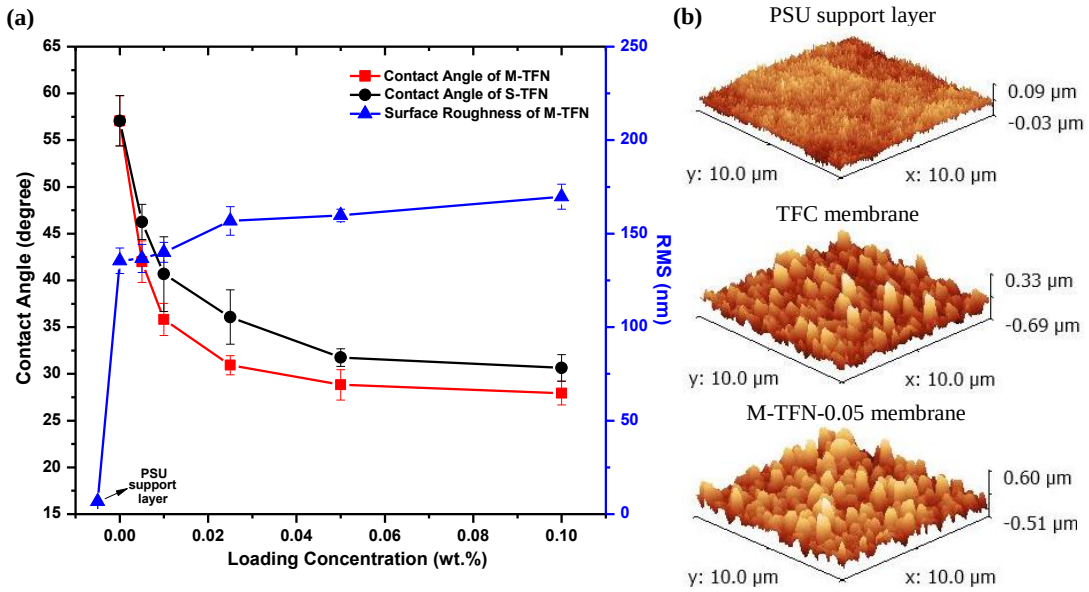

Fig. 2.7 (a) Pure water contact angles (M-TFN and S-TFN) and RMS roughness of M-TFN membranes; and (b) 3D AFM images of PSU support layer, TFC and M-TFN-0.05 membrane.

AFM was used to further analyze the morphology of membrane surface. As shown in Fig. 2.7b, the original PSU support layer was relatively smooth with RMS roughness of 6.8 ± 0.1 nm. The TFC membrane showed much higher surface roughness (135.5 ± 6.8 nm) due to the leaf-like shape of the PA thin-film layer, consistent with the SEM observation (Fig. 2.5). The RMS value increased to 159.8 ± 3.3 nm in the M-TFN-0.05 membrane, which could be caused by the aggregation of MCM-41 NPs on the membrane surface.

The ζ potentials of membrane surfaces were calculated from the tangential steaming potential measurements and presented in Fig. 2.8. The ζ potential of PA TFC membrane (0 wt% loading concentration) is -5.7 ± 0.4 mV. This is similar to the results of other researchers, where the number is -2.5 mV at pH 5.8 [12] and -8.77 mV at pH 6.0 [28]. With increasing MCM-41 NPs concentration from 0 to 0.1 wt%, the ζ potential decreased to -9.54 ± 0.68 mV. According to the isoelectric point (IEP, pH 3.6 ± 0.18) of MCM-41 NPs [29], MCM-41 NPs carried negative charge at pH 5.8. And some embedded NPs may be exposed to the membrane surface as discussed above (Fig. 2.5 and 2.6). The surface NPs in direct contact with the electrolyte may exert additional negative charge on the surface.

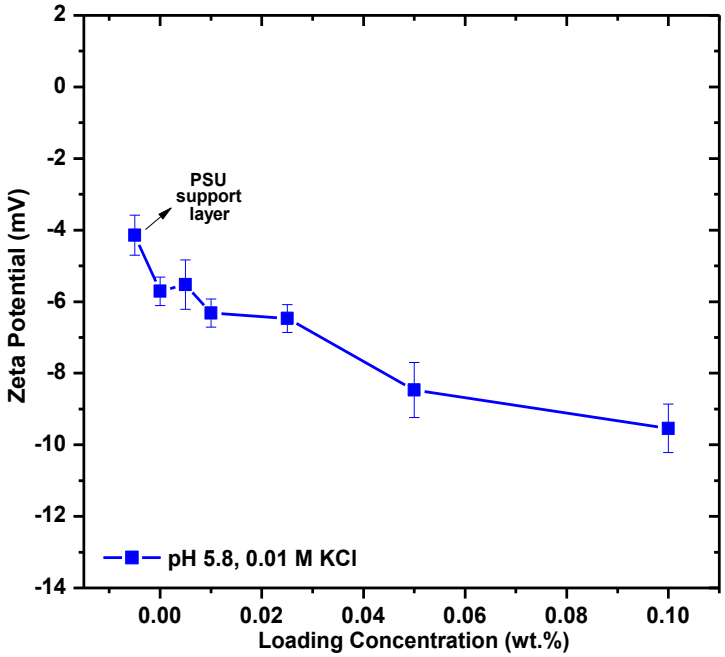

Fig. 2.8 ζ potential of PSU support layer, TFC and M-TFN membranes.

2.3.3 Membrane permeability and salt rejection

Permeate flux from 2000 mg/L NaCl solution and salt rejections of the TFC and TFN membranes were measured at 300 psi of TMP (Fig. 2.9). TFC membrane rejected NaCl and Na_2SO_4 of 98.1 ± 0.5% and 98.6 ± 0.3%, respectively, which was greatly higher than the salt rejections of the PSU support layer (less than 2%, data not shown). Apparently the nano-porous structure of PSU support layer did not allow significant salt rejection. Following the IP process, these nano-pores were covered by a PA thin-film layer, which acted as a dense barrier to reject salt ions.

For the M-TFN membranes, the permeate flux increased from 28.5 ± 1.0 L/m^{2}h to 46.6 ± 1.1 L/m^{2}h (a 63.5% increase) with increasing MCM-41NPs concentration from 0 to 0.1 wt%. It can be caused by the increase of membrane hydrophilicity since the high hydrophilicity facilitates the solubilization and diffusion of water molecules into the

membrane. Additionally, the NPs embedded in PA thin-film layer can change the cross-linking condition of the polymer matrix through creating microporous defects between inorganic NPs and polymer interface or enhancing the miscibility of the aqueous and organic phases by releasing heat during the polymerization process to increase water permeability [12, 13]. Moreover, the internal pores of MCM-41 NPs could enhance the water permeability by providing short flow paths for water molecules.

Clearly, the membrane prepared by using 0.05 wt% of MCM-41 NPs was considered optimal, because the water flux increased up to this point and then leveled off with further concentration increases. The leveling-off effect might be caused by the aggregation of MCM-41 NPs, which could occur more easily at a higher concentration. The aggregation could disturb the dispersion of NPs in the thin-film layer, similar to what was observed with ordered mesoporous carbon (OMC) [30], where the aggregation of filler, less water uptakes and permeable fluxes were detected with higher loadings of filler in thin-film layer.

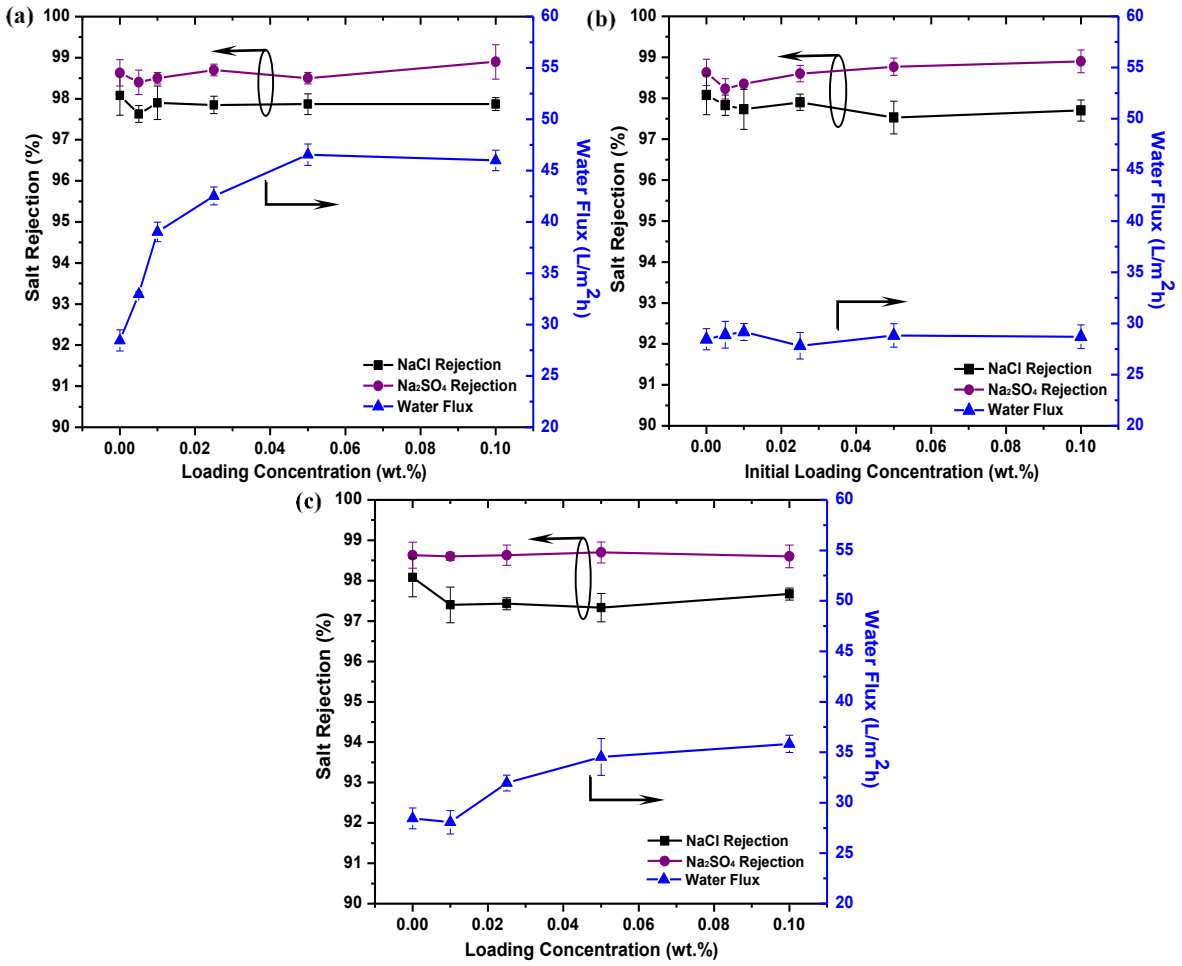

Fig. 2.9 Membrane water flux and salt rejection of (a) M-TFN; (b) Ṁ-TFN (NPs were removed before the IP reaction); and (c) S-TFN. The experiments were performed on 300 psi of TMP at 25 ℃.

To explore the origin of increased water flux in the TFN membranes, membranes in which MCM-41 NPs were removed from the TMC-hexane solution before the IP process were fabricated and evaluated. The separation of NPs from hexane solution was accomplished by settling for 30 mins and filtration through 0.1 μm Nylon syringe filter (Whatman). The results, as presented in Fig. 2.9b, showed that the high water flux observed in the M-TFN membranes disappeared when the MCM-41 NPs were prevented from entering the thin-film layer. The constant water fluxes and salt rejections on

different conditions eliminate our concern about the potential effects of MCM-41 NPs on the chemical nature of TMC in the hexane solution, and indicated that the chemical nature of TMC monomer was not changed to affect the water flux. Therefore, the MCM-41 NPs must be the critical component of the M-TFN membranes that contributed to the enhanced water flux.

To further investigate the contribution of internal pores of filler, the TFN membrane fabricated with spherical silica NPs without internal pores (S-TFN) was prepared and evaluated. As shown in Fig. 2.9c, the permeate water flux of S-TFN membranes increased with increasing NPs concentration (28.5 $\pm$1.0 L/m^{2}h to 35.8 $\pm$0.9 L/m^{2}h); however, the increased ratio (25.6%) was lower than that of M-TFN membranes (63.5%). M-TFN and S-TFN membranes had the similar NPs chemical property, loading and hydrophilicity; therefore, the flux differences between these two membranes elucidate the important role of internal pores to the increase of water flux, probably by providing short flow paths for water molecules during the filtration process.

The salt rejections of M-TFN and S-TFN membranes changed little with the increase NPs concentrations (Fig. 2.9). The salt rejections of M-TFN were all above 97.5% for NaCl and 98.5% for Na_2SO_4, while those of S-TFN were maintained above 97% and 98.5% for NaCl and Na_2SO_4, respectively. Na_2SO_4 was better rejected than NaCl, which is likely due to the combined actions of electrostatic repulsion and size sieving processes [31]. Negatively charged membranes have a stronger repulsive force to the divalent SO_4^{2-} than to the monovalent Cl^-, and tested membranes were negatively charged under the applied pH of 5.8. Furthermore, the radius of hydrated SO_4^{2-} ions (3.00

Å) is larger than that of hydrated Cl^- ions (1.95 Å) [32]. Therefore, SO_4^{2-} ions face more resistance than Cl^- ions when penetrating through the membrane.

2.3.4 Mechanisms for the enhanced water flux in M-TFN membranes

A conceptual representation of the proposed mechanisms for the enhanced water flux in the M-TFN membranes are shown in Fig. 2.10. In this model, layer (a) denotes the porous PSU support layer, layer (b) shows the ridge-valley structure of the PA thin-film with MCM-41 NPs inside it, and layer (c) stands for the feed solution containing electrolytes such as NaCl.

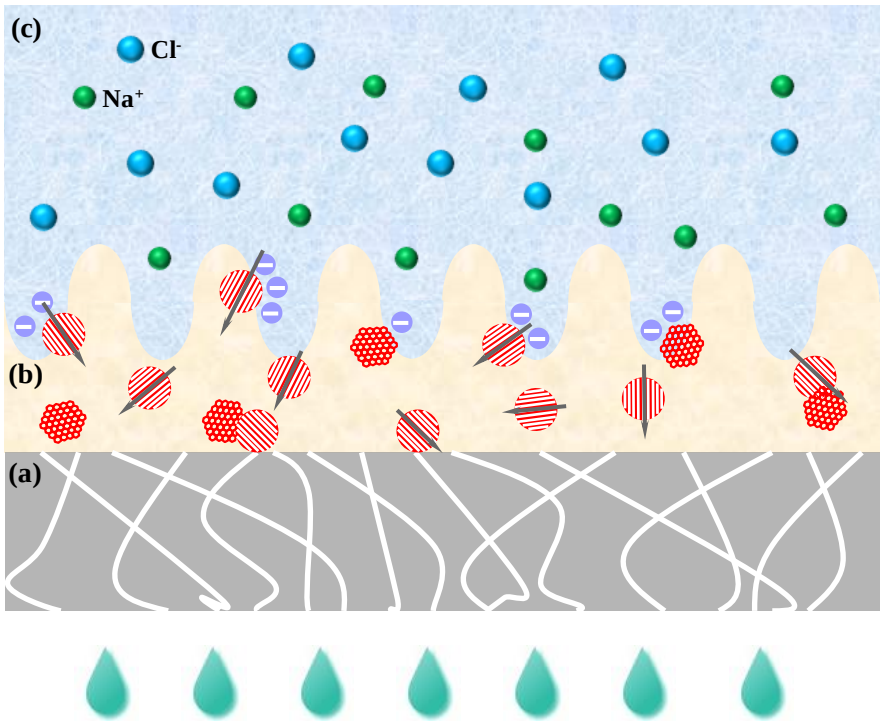

Fig. 2.10 Schematic illustration of hypothesized mechanism of MCM-41 NPs enhanced TFN membrane.

Based on the solution-diffusion theory which was widely used to explain the mass transport in the PA TFC membrane [5, 33], an increase in hydrophilicity of the M-TFN membranes could facilitate water solubilization and diffusion through the membrane,

thus improve water permeability [34]. Besides the hydrophilicity, the cross-linking condition and thickness of thin-film layer are also important factors controlling the water permeability and salt rejection [8]. In general, lower degree of cross-linking and thinner thickness of thin-film layer result in higher water permeability. Embedding the inorganic MCM-41 NPs in the PA polymer could simultaneously reduce the cross-linking in the thin-film layer and provide additional short paths for water flow through the hydrophilic ordered porous structure; therefore, water can penetrate the thin-film layer more quickly. With the non-porous silica NPs, the reduction in polymer cross-linking could still occur but there will be no water permeation through internal structures of NPs; therefore, while the observed water flux in the S-TFN is higher than the conventional thin-film composite, it is less than that in the M-TFN.

It should be noted that the enhancement of water flux observed in M-TFN membranes does not compromise the membrane's ability for salt rejection. Apparently should the introduced NPs have reduced the polymer cross-linking, the degree of the effect had not ruined the integrity of the PA thin-film layer. An alternative explanation is that the increased negative charge of M-TFN membrane caused by MCM-41 NPs (Fig. 8) has contributed to salt rejection by the electrical repulsion or Donnan exclusion [35]; thus, the level of salt rejection can be maintained.

2.4 Conclusions

A novel MCM-41 NPs enhanced TFN membrane was prepared in the present study by an in situ IP process using aqueous MPD and organic TMC-NPs mixture solutions. The NPs loadings were varied from 0 to 0.1 wt. %. A good dispersion of MCM-41 NPs occurred in the PA thin-film layer, as indicated by the TEM and ATR FT-IR results. With

an increasing concentration of MCM-41 NPs, hydrophilicity, roughness and zeta potential of the M-TFN membranes all increased. The resultant increase in the permeate water flux was from 28.5 ± 1.0 L/m^{2}h to 46.6 ± 1.1 L/m^{2}h while the salt rejections were maintained essentially the same (97.9 ± 0.3 % for NaCl and 98.5 ± 0.2 % for Na_2SO_4). Compared with S-TFN membranes, M-TFN membranes showed enhanced permeability, suggesting that the short flow paths through the hydrophilic porous structure of MCM-41 NPs had played a role in water permeation. It is expected that the high hydrophilicity and negative charge of M-TFN membrane introduced by MCM-41 NPs could improve the membrane's resistance to fouling, although additional work is needed to verify this point. Overall, MCM-41 silica NPs, with tunable mesopores, is a good filler to make the high performance mixed matrix PA TFN membrane. Optimizing conditions further for the M-TFN membrane preparation could result in membranes with significantly higher water permeability and high salt rejection.

Acknowledgments

We gratefully acknowledge Ms. Cheryl Jensen from Electron Microscopy Core (EMC) at University of Missouri for preparing the TEM cross-sectional membrane samples. We also thank Professor Qingsong Yu in the Department of Mechanical & Aerospace Engineering at MU for providing us access to the video contact angle measurement system.

References

[1] A.K. Ghosh, E.M.V. Hoek, Impacts of support membrane structure and chemistry on polyamide-polysulfone interfacial composite membranes, Journal of Membrane Science, 336 (2009) 140-148.
[2] Y. Yoon, R.M. Lueptow, Removal of organic contaminants by RO and NF membranes, Journal of Membrane Science, 261 (2005) 76-86.
[3] A.A. Hussain, A.E. Al-Rawajfeh, Recent patents of nanofiltration applications in oil processing, desalination, wastewater and food industries, Recent Patents on Chemical Engineering, 2 (2009) 51-66.
[4] J.E. Cadotte, Interfacially synthesized reverse osmosis membrane, in, 1981.
[5] D. Li, H. Wang, Recent developments in reverse osmosis desalination membranes, Journal of Materials Chemistry, 20 (2010) 4551-4566.
[6] A.L. Ahmad, M. Sarif, S. Ismail, Development of an integrally skinned ultrafiltration membrane for wastewater treatment: effect of different formulations of PSf/NMP/PVP on flux and rejection, Desalination, 179 (2005) 257-263.
[7] E.S. Kim, Y.J. Kim, Q. Yu, B. Deng, Preparation and characterization of polyamide thin-film composite (TFC) membranes on plasma-modified polyvinylidene fluoride (PVDF), Journal of Membrane Science, 344 (2009) 71-81.
[8] A.K. Ghosh, B.H. Jeong, X. Huang, E.M.V. Hoek, Impacts of reaction and curing conditions on polyamide composite reverse osmosis membrane properties, Journal of Membrane Science, 311 (2008) 34-45.
[9] C.K. Kim, J.H. Kim, I.J. Roh, J.J. Kim, The changes of membrane performance with polyamide molecular structure in the reverse osmosis process, Journal of Membrane Science, 165 (2000) 189-199.
[10] Y. Zhou, S. Yu, C. Gao, X. Feng, Surface modification of thin film composite polyamide membranes by electrostatic self deposition of polycations for improved fouling resistance, Separation and Purification Technology, 66 (2009) 287-294.
[11] J.S. Louie, I. Pinnau, I. Ciobanu, K.P. Ishida, A. Ng, M. Reinhard, Effects of polyether-polyamide block copolymer coating on performance and fouling of reverse osmosis membranes, Journal of Membrane Science, 280 (2006) 762-770.
[12] B.-H. Jeong, E.M.V. Hoek, Y. Yan, A. Subramani, X. Huang, G. Hurwitz, A.K. Ghosh, A. Jawor, Interfacial polymerization of thin film nanocomposites: A new concept for reverse osmosis membranes, Journal of Membrane Science, 294 (2007) 1-7.
[13] M.L. Lind, A.K. Ghosh, A. Jawor, X. Huang, W. Hou, Y. Yang, E.M.V. Hoek, Influence of zeolite crystal size on zeolite-polyamide thin film nanocomposite membranes, Langmuir, 25 (2009) 10139-10145.
[14] G.L. Jadav, P.S. Singh, Synthesis of novel silica-polyamide nanocomposite membrane with enhanced properties, Journal of Membrane Science, 328 (2009) 257-267.
[15] H.S. Lee, S.J. Im, J.H. Kim, H.J. Kim, J.P. Kim, B.R. Min, Polyamide thin-film nanofiltration membranes containing TiO2 nanoparticles, Desalination, 219 (2008) 48-56.

[16] S.Y. Lee, H.J. Kim, R. Patel, S.J. Im, J.H. Kim, B.R. Min, Silver nanoparticles immobilized on thin film composite polyamide membrane: Characterization, nanofiltration, antifouling properties, Polymers for Advanced Technologies, 18 (2007) 562-568.
[17] A.B.D. Nandiyanto, S.-G. Kim, F. Iskandar, K. Okuyama, Synthesis of spherical mesoporous silica nanoparticles with nanometer-size controllable pores and outer diameters, Microporous and Mesoporous Materials, 120 (2009) 447-453.
[18] J.S. Beck, J.C. Vartuli, W.J. Roth, M.E. Leonowicz, C.T. Kresge, K.D. Schmitt, C.T.W. Chu, D.H. Olson, E.W. Sheppard, S.B. McCullen, J.B. Higgins, J.L. Schlenker, A new family of mesoporous molecular sieves prepared with liquid crystal templates, Journal of the American Chemical Society, 114 (1992) 10834-10843.
[19] C.T. Kresge, M.E. Leonowicz, W.J. Roth, J.C. Vartuli, J.S. Beck, Ordered mesoporous molecular sieves synthesized by a liquid-crystal template mechanism, Nature, 359 (1992) 710-712.
[20] Q. Cai, Z.S. Luo, W.Q. Pang, Y.W. Fan, X.H. Chen, F.Z. Cui, Dilute solution routes to various controllable morphologies of MCM-41 silica with a basic medium, Chemistry of Materials, 13 (2001) 258-263.
[21] W. Stöber, A. Fink, E. Bohn, Controlled growth of monodisperse silica spheres in the micron size range, Journal of Colloid and Interface Science, 26 (1968) 62-69.
[22] C.-Y. Chen, S.L. Burkett, H.-X. Li, M.E. Davis, Studies on mesoporous materials II. Synthesis mechanism of MCM-41, Microporous Materials, 2 (1993) 27-34.
[23] H. Deng, Y. Xu, Q. Chen, X. Wei, B. Zhu, High flux positively charged nanofiltration membranes prepared by UV-initiated graft polymerization of methacrylatoethyl trimethyl ammonium chloride (DMC) onto polysulfone membranes, Journal of Membrane Science, 366 (2011) 363-372.
[24] B.J.A. Tarboush, D. Rana, T. Matsuura, H.A. Arafat, R.M. Narbaitz, Preparation of thin-film-composite polyamide membranes for desalination using novel hydrophilic surface modifying macromolecules, Journal of Membrane Science, 325 (2008) 166-175.
[25] H.A. Shawky, S.-R. Chae, S. Lin, M.R. Wiesner, Synthesis and characterization of a carbon nanotube/polymer nanocomposite membrane for water treatment, Desalination, 272 (2011) 46-50.
[26] N. Viart, D. Niznansky, J.L. Rehspringer, Structural Evolution of a Formamide Modified Sol - Spectroscopic Study, Journal of Sol-Gel Science and Technology, 8 (1997) 183-187.
[27] J.H. Li, Y.Y. Xu, L.P. Zhu, J.H. Wang, C.H. Du, Fabrication and characterization of a novel TiO2 nanoparticle self-assembly membrane with improved fouling resistance, Journal of Membrane Science, 326 (2009) 659-666.
[28] C. Park, Y.H. Lee, S. Lee, S. Hong, Effect of cake layer structure on colloidal fouling in reverse osmosis membranes, Desalination, 220 (2008) 335-344.
[29] J. Deere, E. Magner, J.G. Wall, B.K. Hodnett, Mechanistic and structural features of protein adsorption onto mesoporous silicates, Journal of Physical Chemistry B, 106 (2002) 7340-7347.
[30] E.-S. Kim, B. Deng, Fabrication of polyamide thin-film nano-composite (PA-TFN) membrane with hydrophilized ordered mesoporous carbon (H-OMC) for water purifications, Journal of Membrane Science, 375 (2011) 46-54.

[31] A. Santafé-Moros, J.M. Gozálvez-Zafrilla, J. Lora-García, Performance of commercial nanofiltration membranes in the removal of nitrate ions, Desalination, 185 (2005) 281-287.
[32] M.Y. Kiriukhin, K.D. Collins, Dynamic hydration numbers for biologically important ions, Biophysical Chemistry, 99 (2002) 155-168.
[33] C. Bellona, J.E. Drewes, P. Xu, G. Amy, Factors affecting the rejection of organic solutes during NF/RO treatment - A literature review, Water Research, 38 (2004) 2795-2809.
[34] I.J. Roh, A.R. Greenberg, V.P. Khare, Synthesis and characterization of interfacially polymerized polyamide thin films, Desalination, 191 (2006) 279-290.
[35] H. Saitua, R. Gil, A.P. Padilla, Experimental investigation on arsenic removal with a nanofiltration pilot plant from naturally contaminated groundwater, Desalination, 274 (2011) 1-6.

Support Information

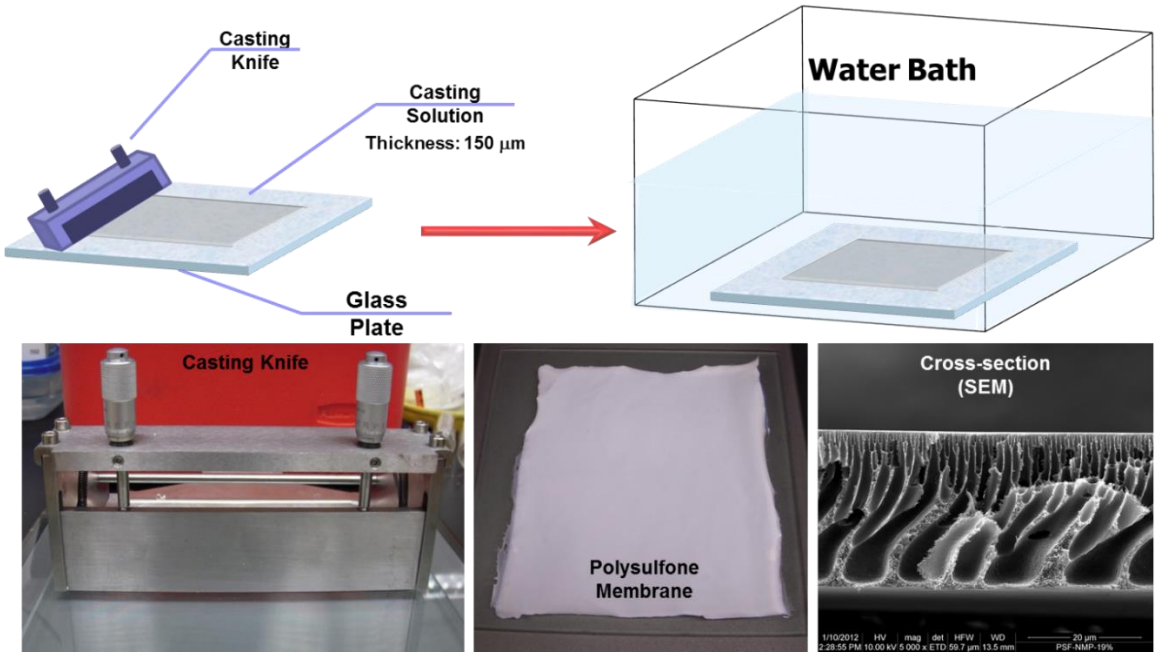

Fig. 2.1s Phase inversion process for support layer fabrication

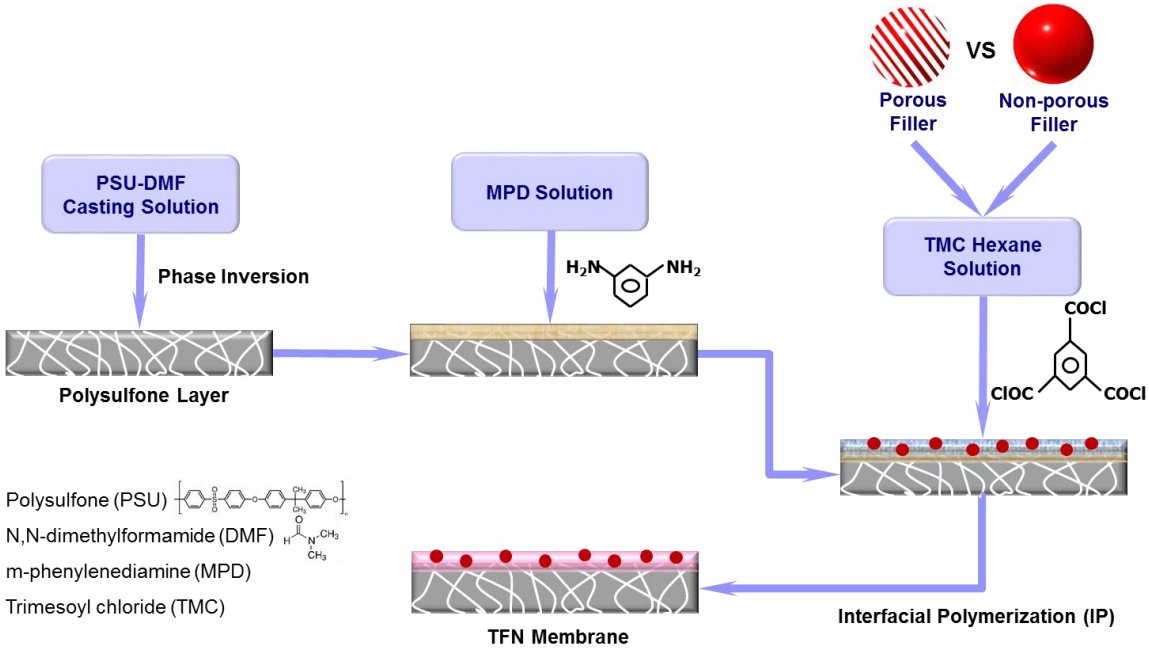

Fig. 2.2s Interfacial polymerization process for TFN membrane fabrication

CHAPTER THREE

Attachment of silver nanoparticles (AgNPs) onto thin-film composite (TFC) membranes through covalent bonding to reduce membrane biofouling

Abstract

Membrane biofouling has a negative impact on the membrane treatment performance. Silver nanoparticles (AgNPs) are well-known antimicrobial agent. Herein, AgNPs with approximately 15 nm in diameter were effectively attached to the surface of polyamide (PA) thin-film composite (TFC) membrane via covalent bonding, with cysteamine as a bridging agent. Scanning electron microscopy (SEM), energy dispersive X-ray spectroscopy (EDS) and cross-sectional transmission electron microscopy (TEM) studies all showed the immobilization of AgNPs. Compared with the pristine TFC membrane, thiol-terminated membrane (TFC-SH) and AgNPs grafted membrane (TFC-S-AgNPs) both showed a higher water flux with slightly lower salt rejection. At a constant transmenbrane pressure of 300 psi, the water permeability of TFC-SH, TFC-S-AgNPs, and control TFC membranes was 70.6 $\pm$0.5, 69.4 $\pm$0.3, and 49.8 $\pm$1.7 L/m^{2}h, respectively, while NaCl rejection was 93.4 $\pm$0.1%, 93.6 $\pm$0.2%, and 95.9 $\pm$0.6%, respectively. TFC-S-AgNPs had an improved antibacterial ability to inhibit *E. coli* growth. The silver leaching from the TFC-S-AgNPs membrane surfaces was minimal, as tested by both batch and flow-through methods. The result successfully demonstrated that AgNPs could be grafted onto TFC via chemical bonding, leading towards the development of an advanced functional TFC membrane with anti-biofouling properties.

Keywords: Silver nanoparticles; Thiol group; Polyamide; Thin-film composite; Covalent bonding; Anti-biofouling

3.1 Introduction

Membrane biofouling due to the microbial growth and biofilm formation is one of the most challenging issues in membrane separation processes [1]. Even when treated with disinfectants such as chlorine, some bacteria could still survive and migrate to the membrane surface and multiply [1, 2]. Besides, the use of chlorine may result in formation of harmful disinfection byproducts and chlorine itself could accelerate degradation of polyamide TFC membranes [3, 4]. In addition to biofouling that could decrease the membrane efficiency, the demand for pathogen-free clean water [5] is another driving force for the development of membranes with antimicrobial properties.

Silver ions and silver-based compounds have excellent biocidal properties and are widely used to prepare antimicrobial plastics, coatings, and wound and burn dressings, etc. [6, 7]. To improve polymeric membrane's anti-biofouling property, many researchers introduced silver into membrane matrix. For example, Zodrow et al. [8] impregnated AgNPs into polysulfone (PSU) matrix to improve biofouling resistance and virus removal, and Chou et al. [9] introduced AgNPs into cellulose acetate matrix for anti-bacterial applications. However, the AgNPs inside the bulk matrixes have weak resistance to washing and can be easily released in the form of Ag^{+} ions, so the membranes quickly lost their antimicrobial function [8-10].

Recently, efforts have been devoted to developing more effective methods to immobilize AgNPs into the membrane's barrier layer or graft them onto membrane surface through covalent bond formation. Lee et al. [3] and Kim et al. [11] immobilized AgNPs into the polyamide (PA) thin-film layer to improve antifouling properties of TFC membrane. Cao et al. [12] introduced AgNPs on the surface of sulfonated

polyethersulfone membrane by using vitamin C as a reducing agent. Gunawan et al. [5] used polyethylene glycol-grafted multiwalled carbon naotubes (MWNTs) as a connecting structure between AgNPs and hollow fiber membrane surface. In their study, AgNPs were firstly coated with MWNTs to prepare Ag/MWNTs, and then Ag/MWNTs were covalently bonded to the external surface of a chemically modified PAN hollow fiber membrane. In another study [13], AgNPs coated with positively charged polyethyleneimine (PEI) were immobilized in an oxygen plasma-modified PSU ultrafiltration (UF) membrane. These findings suggest that it is important to have the AgNPs located at the feed interface of membrane to allow a direct contact between silver and bacterial cells for best antimicrobial performance. To improve the durability of silver-containing membrane and simultaneously reduce the potential risks of releasing AgNPs and Ag^{+} ions at high load to the environment [14, 15], one approach is to chemically immobilize AgNPs on the membrane surface with slow silver release and long anti-biofouling characteristics.

In this study, the surface of freshly fabricated TFC membrane was first thiol-derivatized by reacting with NH_2-$(CH_2)_2$-SH in ethanol solution, and then the freshly synthesized AgNPs were attached onto the membrane surface via the Ag-S chemical bonding. The membrane surface and cross-sectional characteristics were examined by scanning electron microscopy (SEM) and transmission electron microscopy (TEM), and surface chemistry was investigated using energy dispersive X-ray spectroscopy (EDS), attenuated total reflectance Fourier transform infrared (ATR FT-IR) spectroscopy, and Raman spectroscopy. We also assessed the membrane performance including water flux and salt rejection, Ag^{+} ion release in both batch and flow-through dissolution tests, and

antibacterial properties of the membranes by using Gram-negative bacteria, *E. Coli* as a model organism.

3.2 Materials and methods

3.2.1 Materials

All chemicals were of ACS reagent grades, obtained from Sigma-Aldrich (silver nitrate ($AgNO_3$), sodium borohydride ($NaBH_4$), polyvinylpyrrolidone (PVP40), polysulfone (MW = 35,000), N, N-dimethylformamide (DMF, 99.8%), m-phenylenediamine (MPD, >99%), trimesoyl chloride (TMC, >98.5%), and cysteamine (H_2N-$(CH_2)_2$-SH, ≥98.0%)). Deionized (DI) water, obtained from a Milli-Q ultrapure water purification system (Synergy 185, 18.2 MΩ·cm, EMD Millipore Corp., Billerica, MA), was used for solution preparation and filtration study.

3.2.2 Synthesis and characterization of AgNPs

To synthesize AgNPs, a method modified from our previous work was applied here [16]. An aliquot (50 ml) of 14 mM sodium borohydride ($NaBH_4$) solution was mixed with 900 ml of 0.06 wt% PVP40 water solution, and then 50 ml of 14 mM silver nitrate ($AgNO_3$) solution was rapidly injected into the vigorously stirred solution (500 rpm) at room temperature (22 ℃). TEM (JEOL 1400, JEOL Ltd., Peabody, MA) coupled with a submicron particle size analyzer (Delsa^{TM} Nano HC, Beckman Coulter, Inc., Brea, CA) was used to determine the morphology and size distribution of the freshly synthesized AgNPs. TEM samples of AgNPs were prepared by dropping the AgNPs solution onto carbon coated copper grid and drying at the room temperature.

3.2.3 Preparation of TFC and TFC-S-AgNPs membrane

The PSU support layer was fabricated by the phase inversion method using a 15 wt% PSU-DMF casting solution. The casting solution was stirred at 50 ℃ for 6 h, and kept overnight for degassing. The clear solution was spread on a glass plate and casted by casting knife (EQ-Se-KTQ-150, MTI Corp., Richmond, CA) to approximately 100 μm of film thickness. Then, glass plate was immediately immersed into a water bath (25 ℃). The precipitated PSU support membrane was washed and stored in DI water for at least 24 h before use. For TFC membrane fabrication, the prepared PSU support layer was attached to a small glass plate with tape around the edge, and then immersed in a 2.0 wt% MPD-water solution for 3 min. Excess solution on the surface was removed by a rubber roller. Next, the MPD saturated PSU support layer was soaked in a 0.15 wt% of TMC-hexane solution for 30 seconds, resulting in the formation of a polyamide (PA) thin-film layer. The TFC membranes were rinsed with pure hexane and then ethanol before the surface grafting.

To prevent hydrolysis of acyl chlorides, a newly fabricated TFC membrane sample (10 cm^2) was immediately immersed in a H_2N-$(CH_2)_2$-SH ethanol solution (20 mM, 50 ml) for various time durations (3, 6, 24 h). And then the membrane sample (labeled as TFC-SH) was moved out from the ethanol solution, rinsed with pure ethanol and DI water, and incubated with the PA active layer in contact with an AgNPs suspension (0.1 mM, 50 ml) for 12 h. Finally, the membrane sample (labeled as TFC-S-AgNPs) was rinsed with DI water and stored in DI water at 4 ℃ before use.

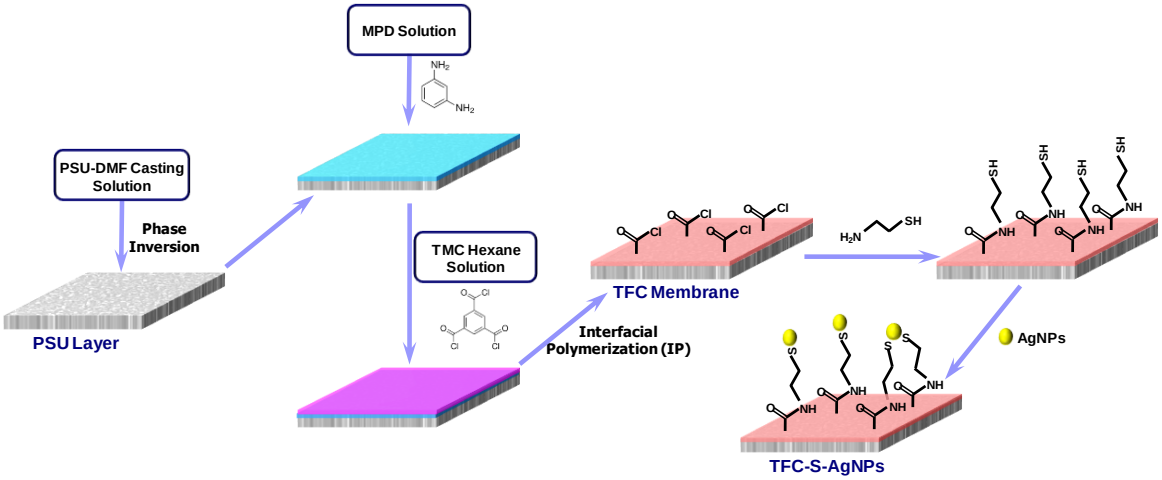

Fig. 3.1 Schematic diagram of immobilization of AgNPs onto the surface of PA TFC membrane.

3.2.4 Membrane characterization and performance assessment

SEM and EDS analysis of membrane surface was conducted using a piece of membrane dried at room temperature. To obtain the TEM cross-section, the membranes were embedded in Epon resin (Eponate 12, Ted Pella, Inc., Redding, CA) and cut by Reichert-Jung Ultracut E ultramicrotome (Reichert, Inc. Depew, NY). The images were taken under 80 kV by using JEM 1400. Hydrophilicity of membrane surface was assessed according to the pure water contact angle, which was measured by the sessile drop method on a video contact angle system (VCA-2500 XE, AST products, Billerica, MA). At least six stabilized contact angles from different locations of each sample were obtained to calculate an averaged value of contact angles. The functional groups of membrane surface were identified by ATR FT-IR spectroscopy, which was conducted on the Nicolet 4700 FT-IR (Thermo Electron Corp., Waltham, MA) equipped with multi-reflection Smart Performer® ATR accessory. All spectra included the wave numbers from 500 to 4000 cm^{-1} with 128 scans at a resolution of 1.0 cm^{-1}. An Invia Renishaw spectrometer system (RM1000 series, Gloucestershire, UK) equipped with a Leica

DMLB microscope (Wetzlar, Germany) and 514.5 nm laser line was used to detect the thiol group on membrane surface.

A high pressure cross-flow filtration system was used to evaluate pure water flux and solute rejection, as described in our previous work [17]. Prior to test, each membrane (9.6 cm^2 of effective area) was compressed by DI water at 300 psi for 3 h. Pure water flux was measured by the weight of permeate water at a constant transmembrane pressure (TMP). The weight of the permeate water was recorded by a LabVIEW automated system (National Instruments LabVIEW 8.2 with Ohaus digital balance). After the flux test, NaCl salt solution of 2,000 mg/L was added and the conductivity of feed and permeate solutions was measured by a conductivity/TDS meter (HACH Company, Loveland, CO). The test was conducted at 25 $\pm$1 ℃, controlled by a water circulator (Isotemp 6200 R20F, Fisher Scientific, Inc., Pittsburgh, PA). The flux and rejection was calculated with Equation (1) and Equation (2), respectively.

$$J = \frac{V_p}{A \cdot t} \tag{1}$$

$$R = \left(1 - \frac{C_p}{C_f}\right) \times 100 \tag{2}$$

where J is the water flux (L/m^2h), V_p the permeate volume (L), A the membrane area (m^2), t the treatment time (h), R the rejection ratio, and C_p and C_f the conductivities of permeate and feed solution, respectively.

Releases of silver ions from the functionalized membranes were assessed via both batch and flow-through experiments. In the batch test, membrane samples were incubated

in DI water (the ratio is 1 cm^2 membrane sample : 20 ml DI water) placed on an orbital shaker (4516, Forma Scientific, Inc., Marietta, OH) under 100 rpm and the water was replaced every 24 h. All water samples were collected and acidified by 1% HNO_3 and analyzed by an atomic absorption spectrophotometer (AA, model 210 VGP + 220 GF, Buck Scientific, Inc., East Norwalk, CT). The silver release rate under the flow-through condition was assessed by driving DI water through the membrane at a constant TMP of 300 psi, and permeate was collected as a function of time and analyzed for the released silver concentration by AA.

3.2.5 Antibacterial Assessment

E. coli MG1655 (ATCC 47076) was inoculated into liquid culture of Lysogeny broth (LB, 20g/L) and incubated in an Isotemp incubator (Fisher Scientific, Inc., Pittsburgh, PA) with shaking at 150 rpm overnight under 37 ˚C. This culture was then centrifuged for 10 min at 2700 rpm. After decanting the supernatant, the pellet was resuspended in LB solution. The resulting bacterial culture was centrifuged again, followed by resuspension of the pellet in LB solution. The resulting cell suspension served as a bacterial stock solution, which was further diluted to approximately 10^5 colony-forming units (CFU)/ml before use. Studies of the antibacterial properties of membrane samples, disk experiment, SEM investigation and biofilm growth test were carried out as detailed below.

In the disk experiment, aliquots (50 μL) of *E. coli* working solutions were spread, in triplicate, onto plates of nutrient agar. Membrane samples (diameter 1 cm and 3.7 cm) were then placed onto the nutrient agar plate with the active layer in contact with the agar

surface. After incubation at 37 ℃ for 24 h, the colony forming cells under the membrane samples were examined.

During SEM investigation, membrane samples with size of 5 cm^2 were immersed in 25 mL of *E. coli* suspension (1.0×10^5 CFU/mL) with shaking at 150 rpm for 5 h at room temperature. Then, the bacteria were fixed in 3 vol.% glutaraldehyde PBS solution for 5 h at 4 ℃ and rinsed with PBS solution several times to remove any remaining glutaraldehyde on the surface. After fixation, the samples were dehydrated with an ethanol series (25, 50, 75 and 100%), air-dried, and coated with platinum (20 mA, 30 s) using sputter coater for SEM observation.

Furthermore, a biofilm growth test was carried out to examine the anti-biofouling properties of membranes on a drip flow biofilm reactor (DFR110, Biosurface Technologies Co., Bozeman, MT). First, membrane samples (2.5 cm × 6.0 cm) were attached on a glass plate with active layer facing up and immerged into 25 mL of *E. coli* suspension (1.0×10^5 CFU/mL) for 5 h. Then the membrane samples were moved from the suspension and gently rinsed with PBS solution for three times. The membranes were transferred into different test chambers and feed with LB solution (5 g/L) at 1.0 ml/min for 7 days. Finally, the growth of biofilm on membrane surface was examined.

3.3 Results and discussion

3.3.1 AgNPs Characteristics

As shown by the TEM image in Fig. 3.2a, AgNPs were well dispersed and of spherical morphology. The average diameter was 14.8 nm based on the calculation by the software ImageJ from a total of 171 particles. The absorption spectra of the AgNPs solution (Fig. 3.2b) showed a well-defined plasmon band at about 400 nm, characteristic of nanosized silver [18]. And the intensity of this peak increased proportionally with increasing AgNPs concentration. The particle size distribution was given in the upper right corner of Fig. 3.2b, and the average diameter of 15.3 ± 4.8 nm was consistent with that from the TEM analysis.

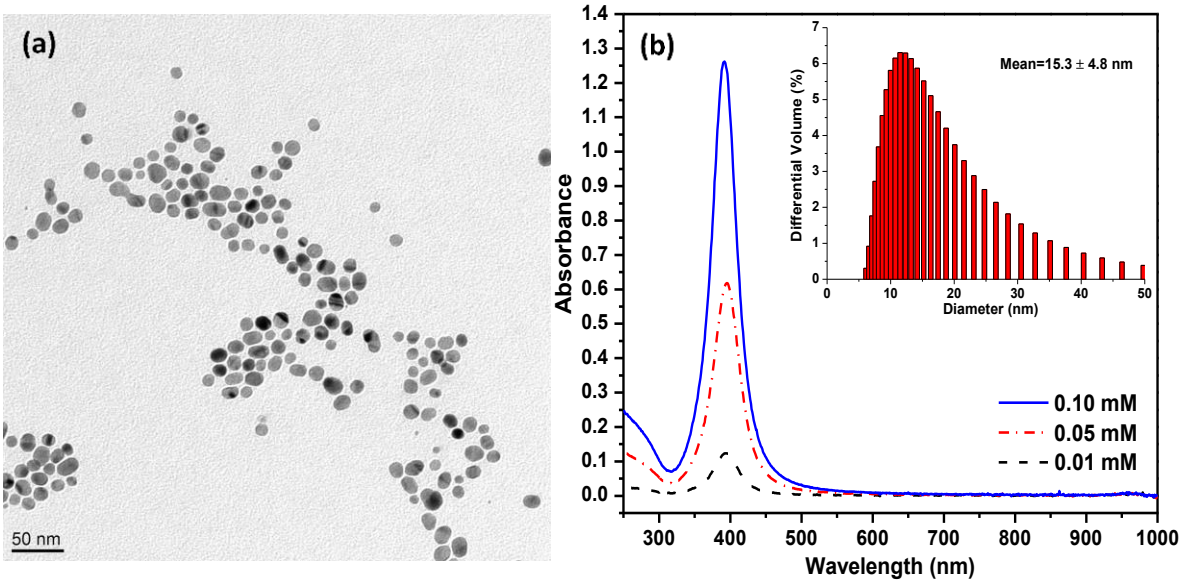

Fig. 3.2 TEM image of AgNPs (a) and UV-vis absorption spectrum & size distribution of AgNPs suspension (b).

3.3.2 Membrane properties

The photos of original, thiol modified and silver immobilized TFC membranes are showed in Fig. 3.3a. After reaction with AgNPs suspension, the originally white-colored thiol-modified TFC membrane became yellowish, indicating the immobilization of AgNPs on the membrane surface. Based on the SEM images as shown in Fig. 3.3(b-e), all of these membrane surfaces had a "ridge and valley" structure characteristic of the PA thin-film layer [19, 20]. There were no obvious differences among these membranes. Fig. 3.3f showed the SEM morphology of TFC-S-AgNPs membrane after it was used in filtration for 72 h under 300 psi. The "ridge and valley" structure was apparently flattened, which could be attributed to the compaction under the pressure.

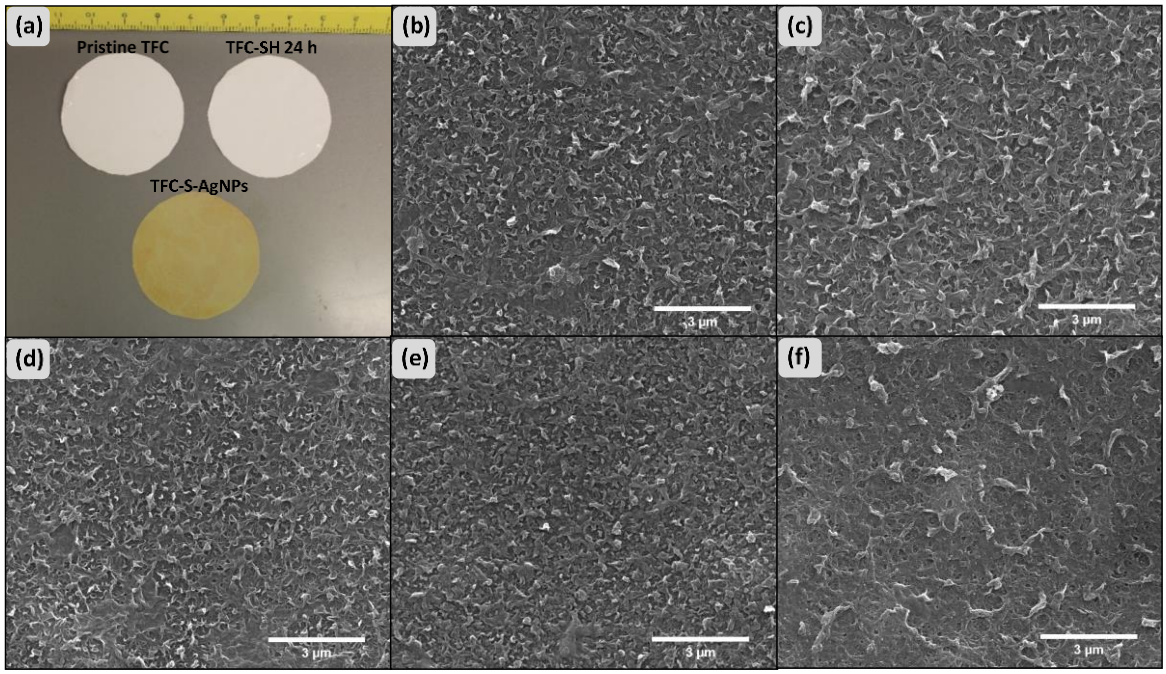

Fig. 3.3 Picture of membrane samples (a) and surface morphologies of pristine TFC (b), TFC-SH 6 h (c), TFC-SH 24 h (d), TFC-S-AgNPs (e) and TFC-S-AgNPs (after 72 h filtration) membrane (f). The scale bar in each SEM image is 3 µm.

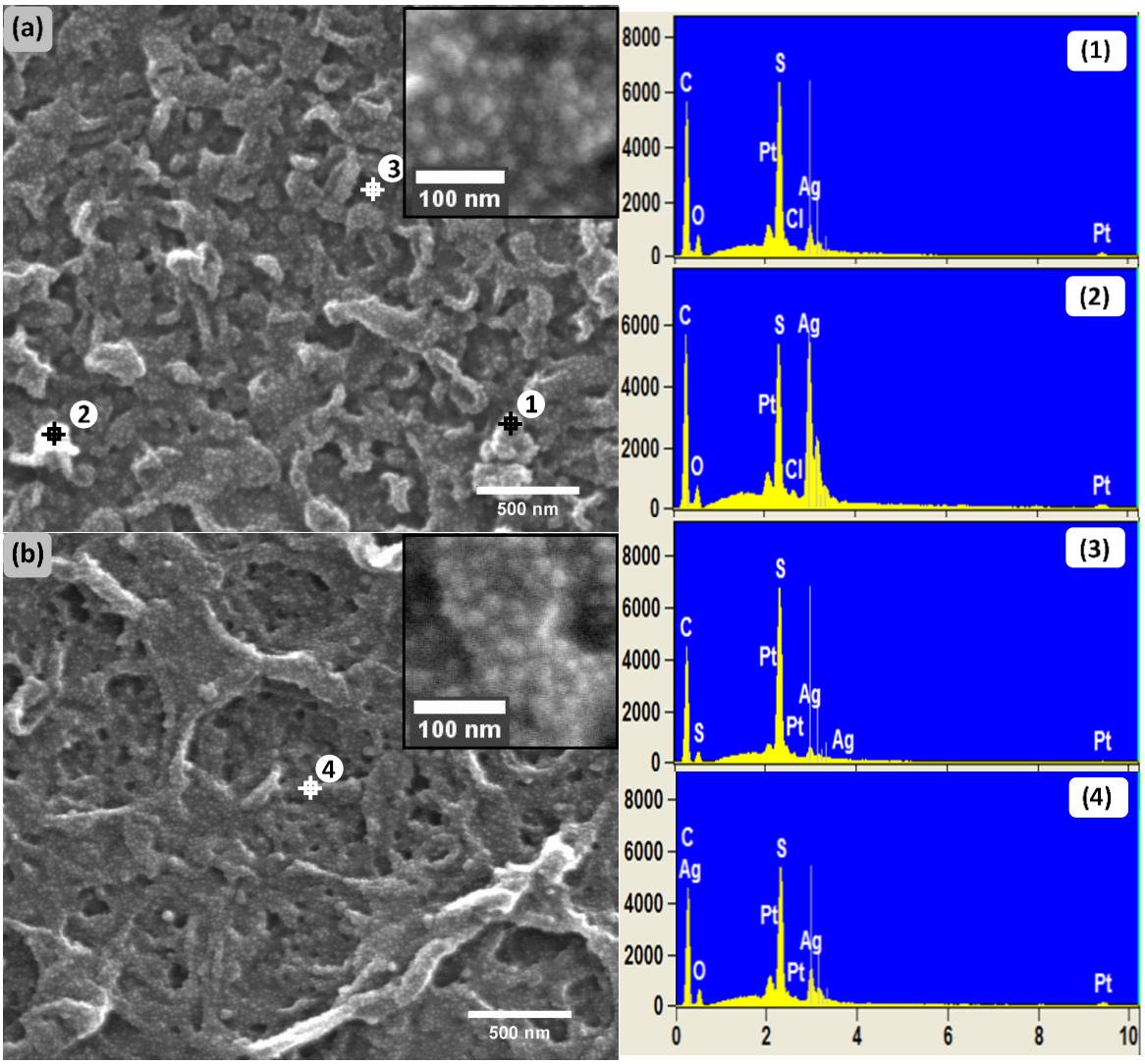

Fig. 3.4 High magnification SEM image and EDS spectra of TFC-S-AgNPs surface before filtration (a) and after 72 h filtration (b). Four spots were randomly chosen and labeled by numbers. The scale bar in each SEM image is 500 nm. Two higher magnification images were inserted in the upper right corner of the original images.

The high resolution SEM images showed spherical particles located on the membrane surface, both before (Fig. 3.4a) and after (Fig. 3.4b) the filtration test. The particles ranged from 10 to 20 nm in diameter, about the same size with that of AgNPs. Furthermore, the EDS spectra of four spots located on membrane surface (Fig. 3.4) showed the presence of silver, confirming the attachment of AgNPs on the membrane

surface. The weight percentage of silver at those four spots is 5.12%, 24.78%, 4.15% and 8.47%, respectively. The amount of AgNPs attached to the TFC-S-AgNPs surface was further measured through acid leaching and AA analysis. The leaching test showed that there was 15.5 ± 2.6 μg of AgNPs that could be leached out on every square centimeter of membrane surface, corresponding to approximately 0.7% of the total mass of a membrane sample. Clearly this value is lower than the result from the EDS analysis. Considering the limited penetration depth of primary electrons in EDS (in the order of 2 μm for a carbon sample at an acceleration voltage of 20 kV [21]) and accumulation of AgNPs that occurred primarily on the membrane surface, it was reasonable to observe a higher amount of silver in EDS analysis than that by the leaching test.

Cross-sectional TEM images provided more detailed information about the distribution of AgNPs on membrane surfaces (Fig. 3.5). The images clearly delineated the 'ridge and valley' structure of the PA thin-film layer of a thickness between 100 to 200 nm, located on the porous PSU support layer. A comparison between TFC and TFC-S-AgNPs indicated the presence of AgNPs on the surface of PA thin-film layer as dark spots, consistent with the SEM image and EDS data for the TFC-S-AgNPs membrane. It appeared that the amount of AgNPs remained the same on the TFC-S-AgNPs surface after 72 h of filtration test (Fig. 3.5e and 3.5f), suggesting a strong attachment of the AgNPs on the membrane surface. Similar to the SEM results, the TEM images showed a denser and smoother surface after the membrane was used for filtration due to compaction.

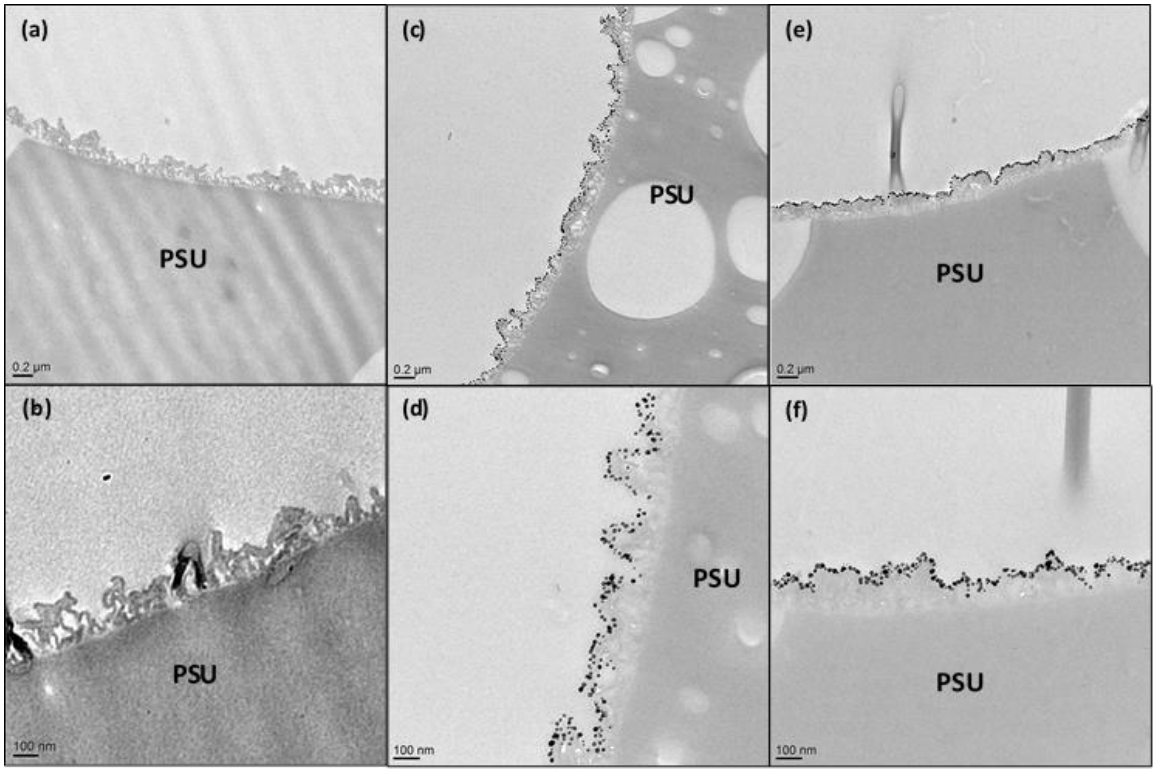

Fig. 3.5 TEM images of the cross-sections of (a,b) TFC membrane; (c,d) TFC-S-AgNPs membrane; (e,f) TFC-S-AgNPs membrane after 72 h filtration. Dark spots located on functionalized membrane surface are AgNPs.

FT-IR spectra of various membrane surfaces are shown in Fig. 3.6. Peaks originated from the PA polymerization included 1660 cm^{-1} (amide I, C=O stretching vibrations of amide), 1547 cm^{-1} (amide II, in-plane N-H bending and C-N stretching vibrations), 1610 cm^{-1} (N-H stretching of amide), and 1450 cm^{-1} (C=O stretching and O-H bending of carboxylic acid) [22-24]. The peak at 768 cm^{-1} could be due to the C-Cl stretching [25]. After reaction between C-Cl and H_2N-$(CH_2)_2$-SH, the intensity of this peak decreased. However, the characteristic peak of S-H stretching located near 2540-2560 cm^{-1} [26-28] didn't show up. This could be caused by two reasons: i) the low sensitivity of thiol group

in FT-IR due to the high polarizability of sulphur [27]; and ii) the small amounts of thiol group on membrane surface.

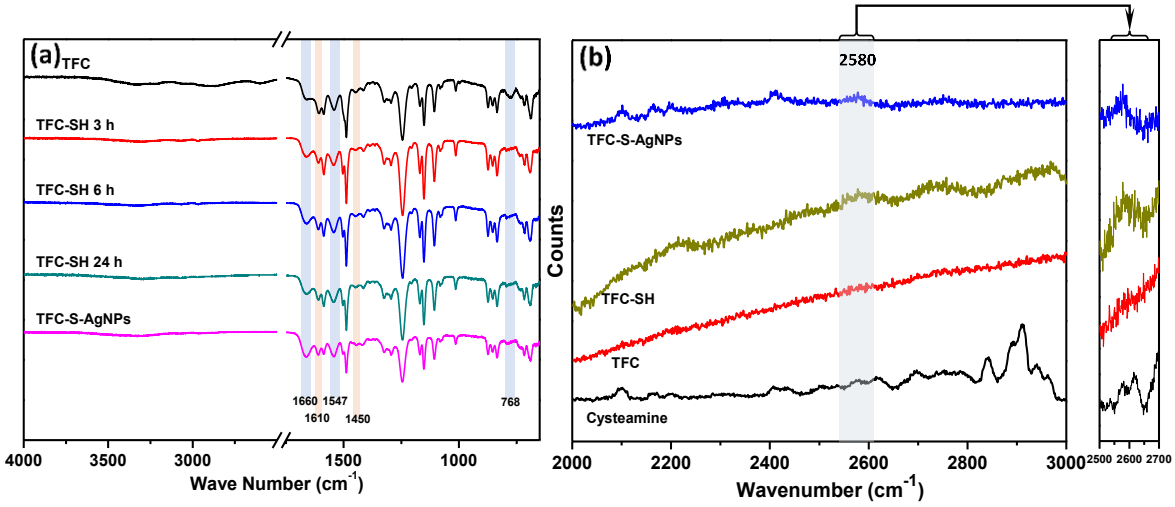

Fig. 3.6 Spectrum analysis of membrane surface: (a) ATR FT-IR; (b) Raman.

Thiol group is highly polarizable and could produce a stronger Raman spectral activity than the infrared spectrum [29], so we explored to detect the thiol group on the membrane surface by Raman spectroscopy. As shown in Fig. 3.6b, both TFC-SH and TFC-S-AgNPs had a peak around 2580 cm^{-1} but not for the original TFC membrane, suggesting the existence of thiol group on the membrane surface [30].

In comparison with the original TFC membrane with a water contact angle of 56.7 ± 2.2 °, the contact angles of membrane with grafted NH_2-$(CH_2)_2$-SH were essentially the same (Fig. 3.7), suggesting the existence of thiol groups on membrane surface did not significantly change the surface hydrophilicity. After grafting AgNPs, however, the contact angle decreased to 32.9 ± 0.7 °(before filtration) and 32.2 ± 2.4 °(after filtration). The decrease in contact angle by the grafted AgNPs, although it was somewhat more significant, is generally consistent with the reports in the literature [8, 11, 31]. AgNPs

were accumulated on the membrane surface in this study, which could have a more direct effect on the surface hydrophilicity.

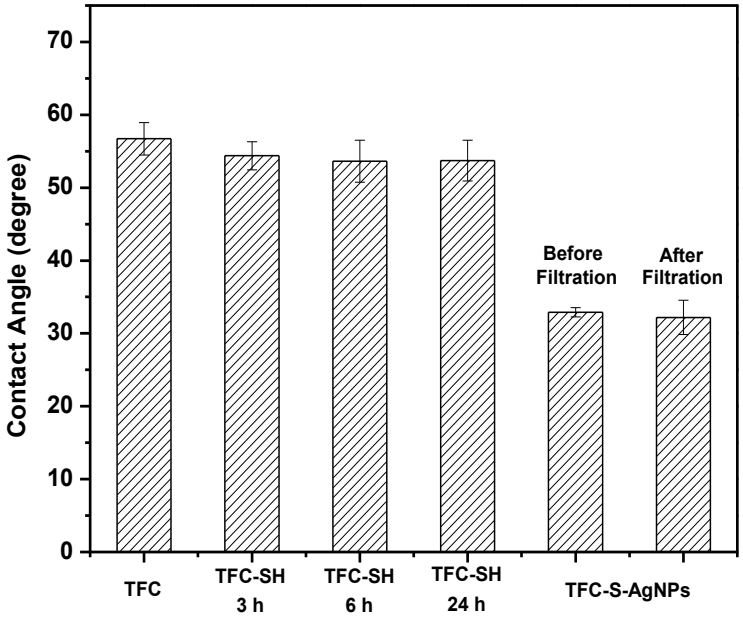

Fig. 3.7 Water contact angles of membrane surfaces

3.3.3 Performance of membranes for water filtration

The pure water flux, salt rejection and permeate flux of membranes are presented in Fig. 3.8. At a constant TMP of 300 psi, the pure water flux increased from 67.1 L/m^{2}h (original TFC) to 90.6 L/m^{2}h (TFC-SH, 24 h) and 88.7 L/m^{2}h (TFC-S-AgNPs). When feeding with a 2000 mg/L NaCl solution, the permeate flux of the original TFC, TFC-SH (24 h), and TFC-S-AgNPs membranes were 49.8 $\pm$1.7, 70.6 $\pm$0.5, and 69.4 $\pm$0.3 L/m^{2}h, respectively, and NaCl rejection was 95.9 $\pm$0.6%, 93.4 $\pm$0.1%, and 93.6 $\pm$0.2%, respectively.

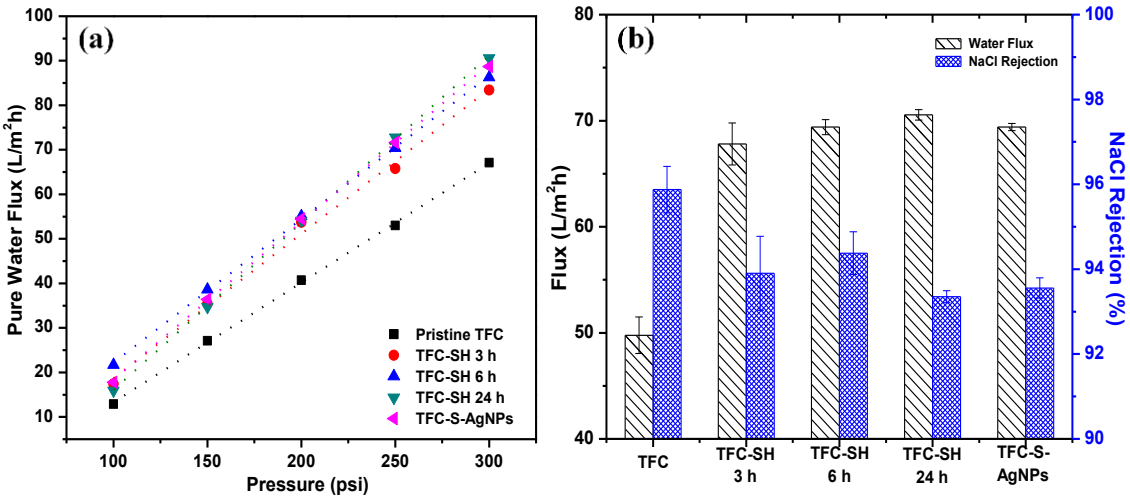

Fig. 3.8 Performance of membrane samples: (a) pure water flux; (b) NaCl rejection and solution flux (2,000 mg/L NaCl solution was fed under 300 psi of TMP).

The higher water flux and slightly lower salt rejection for the TFC-SH and TFC-S-AgNPs membranes could be due to the effects of ethanol solution used in the grafting process. Kulkarni et al [32] also suggested that a mild solvent such as ethanol could increase the water flux of TFC membranes with no loss in rejection. Ethanol could result in membrane swelling and removal of small molecular fragments, so a more loose structure can be produced but still not enough to significantly decrease salt rejection.

3.3.4 Stability of AgNPs-containing membranes

The release rate of silver ions from the AgNPs grafted membrane would control the duration of the effectiveness of grafted AgNPs, so we examined the silver release in both batch and flow-through experiments. As presented in Fig. 3.9a, the initial silver ion release from the TFC-S-AgNPs membrane was around 0.37 $\mu g \cdot cm^{-2} day^{-1}$ and then declined steadily with time. After 7 days, the release rate leveled off to a level below 0.1 $\mu g \cdot cm^{-2} day^{-1}$. Based on the total amount of AgNPs on membrane surface (which was 15.5

± 2.6 μg/cm^2), the amount leached out during 14 days of batch test accounted for only 12% of the total amount of silver on the membrane. Considering the relatively low release rate of around 0.1 μg·cm^{-2}day^{-1} at the steady state, the membrane is expected to be effective for months for its anti-bacterial properties due to the strong covalent bonding between the thiol groups and AgNPs.

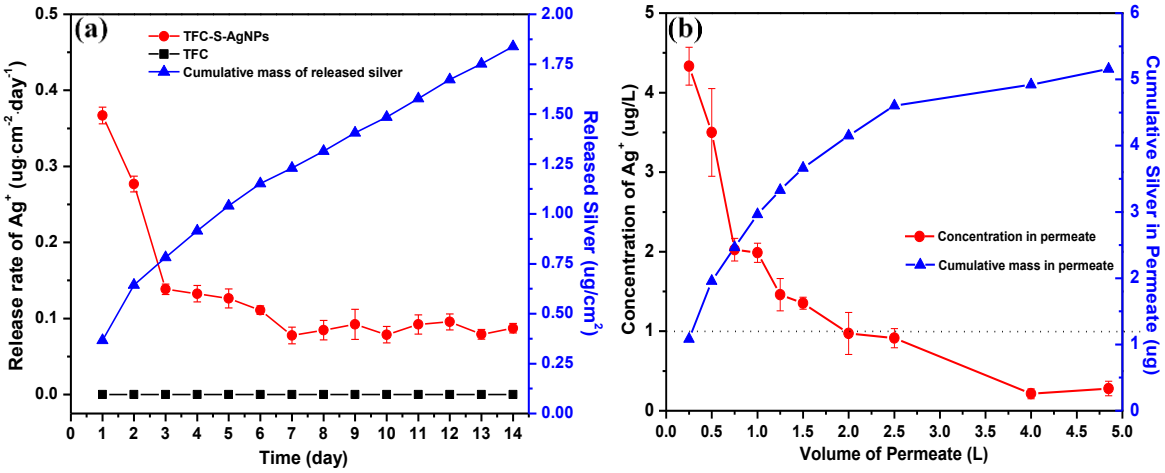

Fig. 3.9 Silver ion release from the batch (a) and flow-through (b) tests. During the batch test, membrane samples were incubated in 20 ml DI water under 100 rpm and the water was replaced every 24 h. During the flow-through test, DI water was driven through the membrane at a constant TMP of 300 psi.

In the flow-through experiment (Fig. 3.9b), silver ion concentration in the permeate side is very low, less than 5 μg/L in the initial 0.25 L of permeate and further decreased to less than 1 μg/L (detection limit) after about 2.0 L water permeating through the membrane. Although the last several data points were already below the detection limit and may not be that accurate, we still gave out the calculated number based on the calibration curve to show the trend of concentration change. The National Secondary Drinking Water Regulations for silver is 100 μg/L, so the amount of silver released from the membrane, if there is any, is of no health concern. The cumulative amount of Ag^+

ions in the 4.85 liter of permeate (5.16 μg) accounted for only 3.5 % of the total amount of silver in the membrane samples (9.6 cm^2 × 15.5 μg/cm^2 = 148.8 μg), again suggesting that the antimicrobial effect of AgNPs could exist for a long time.

3.3.5 Antibacterial properties of membrane surface

As illustrated by the disk tests with and without various membranes (Fig. 3.10), the original TFC and TFC-SH samples (b and c) had no significant effect on the growth of *E. coli*, while TFC-S-AgNPs (d and e) showed a clear LB surface with no evidence of bacterial growth.

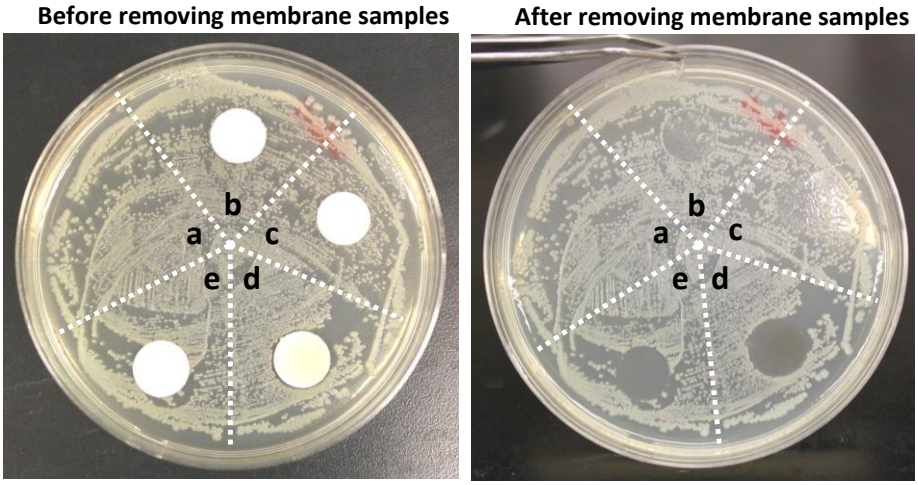

Fig. 3.10 Disk experiments for membranes of (a) control (without membrane sample); (b) TFC; (c) TFC-SH 24 h; (d) TFC-S-AgNPs and (e) TFC-S-AgNPs after 14-day batch release test. OD of membrane sample is 1.0 cm. Membranes were peeled from the nutrient agar after 24 h incubation.

An inhibition zone (0.5 mm) around the sample d was also observed. Similarly, many researchers [12, 33] also found the appearance of inhibition zone around the substrate containing AgNPs due to the antibacterial function of AgNPs [34, 35]. AgNPs could inhibit the growth of microbes through multiple pathways. Firstly, AgNPs can release Ag^+ ions, which interact with disulfide or thiol groups of enzymes or DNA and

then disrupt metabolic processes, generate reactive oxygen species or interrupt replication of DNA [36-38]. All these processes could lead to the damage or even the death of bacterial cells. Secondly, AgNPs can also be attached to the surface of the cell membrane and disturb its proper function [35, 39, 40]. These results also showed that nano-Ag could destabilize the outer membrane, collapse the plasma membrane potential and deplete the levels of intracellular ATP. Thirdly, AgNPs with smaller particle size (1-10 nm) are able to penetrate inside the bacteria and cause further damage by possibly interacting with sulfur- and phosphorus-containing compounds such as DNA [41]. However, due to the bigger size (15.3 ± 4.8 nm) and strong bonding between AgNPs and TFC-SH membrane surface, the third pathway may not be so significant in this study.

Notably, after 14-day silver release test, TFC-S-AgNPs membrane still showed good inhibition capability towards *E. coli*, which further confirmed the good stability of AgNPs on membrane surface.

Further disk experiment was carried out using real size membrane samples (OD = 3.7 cm, using for filtration test, Fig. 3.11). Similar to the observation in Fig. 3.10, after removing the membrane samples, growth of bacteria was observed under the pristine TFC membrane, while clear LB surface was observed under the TFC-S-AgNPs membrane. After checking the membrane surface contacted with bacteria, it is clear that spot-like *E. coli* colonies were clearly observed on the TFC membrane surface, whereas the TFC-S-AgNPs membrane showed a clear and smooth surface. The easy attachment of *E. coli* on pristine TFC membrane surface suggests that PA TFC membrane surface is prone to biofouling and further demonstrates the necessity of surface anti-bacterial modification.

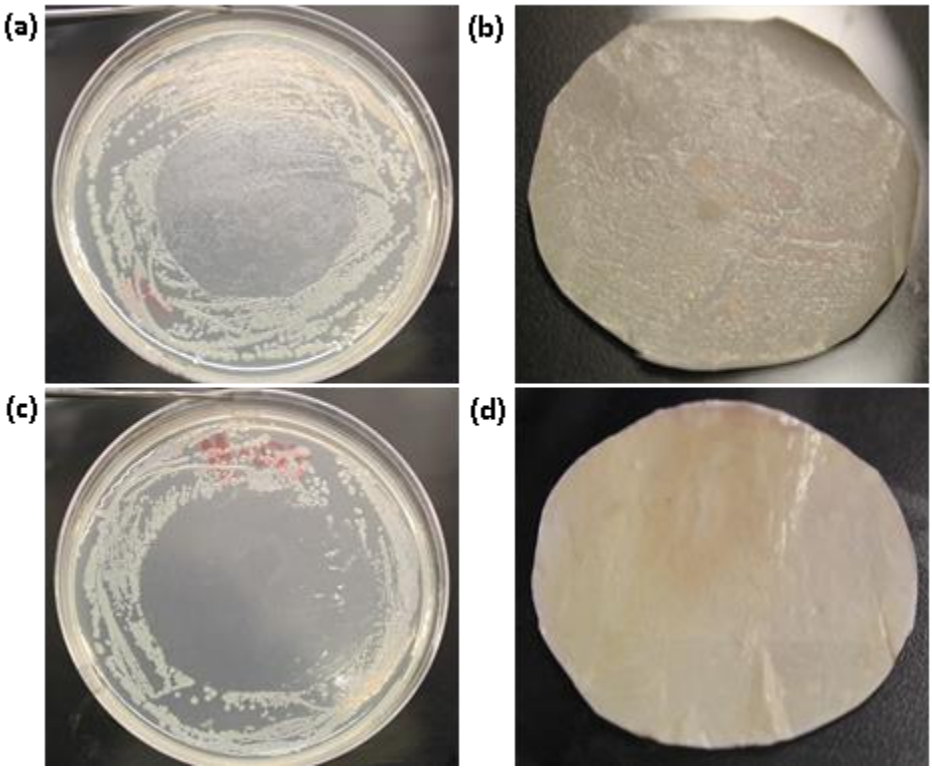

Fig. 3.11 Disk experiments: (a) area contacted with TFC; (b) TFC surface; (c) area contacted with TFC-S-AgNPs and (d) TFC-S-AgNPs surface. OD of membrane sample is 3.7 cm. Membranes were peeled from the nutrient agar after 24 h incubation.

SEM images (Fig. 3.12) were obtained after removing membrane samples from the bacterial suspension. It was clear that rod-shaped *E. coli* bacteria with approximately 0.8 μm in diameter and 2.0 μm in length attached on TFC membrane surface (indicated by white arrow in Fig. 3.12a) after 5 h contact. On the contrary, TFC-S-AgNPs membrane surface (Fig. 3.12b) was relatively clean and the attached cell was disrupted (magnified image in Fig. 3.12b) when compared with normal cell (magnified image in Fig. 3.12a). Gunawan et al. [5] also found the appearance of disrupted cells when they tested their Ag/MWNTs modified hollow fiber membrane using *E. coli*-containing feedwater, and attributed this phenomenon to the direct contact between the cells and AgNPs. So this

result suggested again that TFC-S-AgNPs membrane possessed excellent anti-bacterial properties.

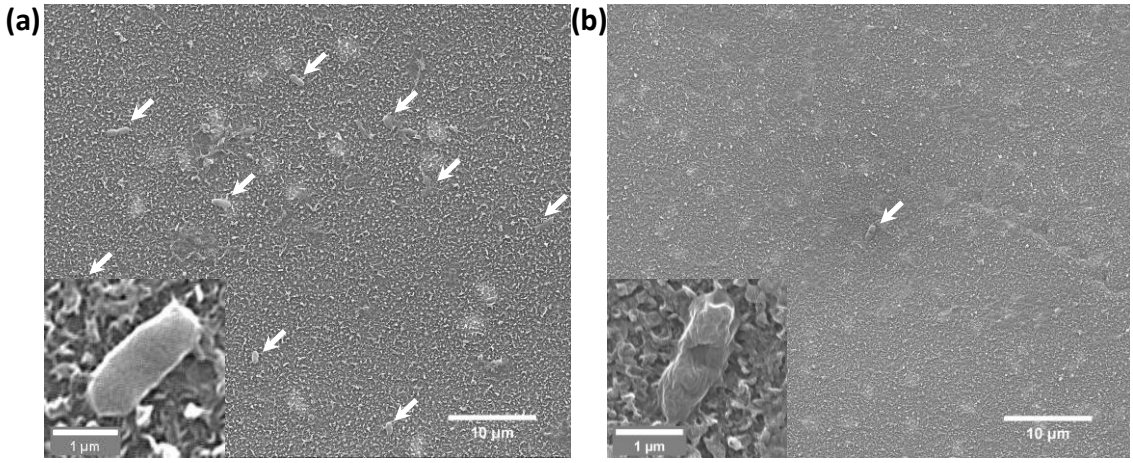

Fig. 3.12 SEM images of membrane surfaces submerged in an aqueous suspension of *E. coli* for 5h: (a) TFC, (b) TFC-S-AgNPs.

Furthermore, after 7-day biofilm growth test (Fig. 3.13), biofilm formation was observed (indicated by black arrow) on the TFC membrane surface, while the TFC-S-AgNPs membrane surface was relatively clean and free of biofilm growth. All these results demonstrated that AgNPs-grafted membrane possessed excellent antibacterial function, which could reduce biofouling [42].

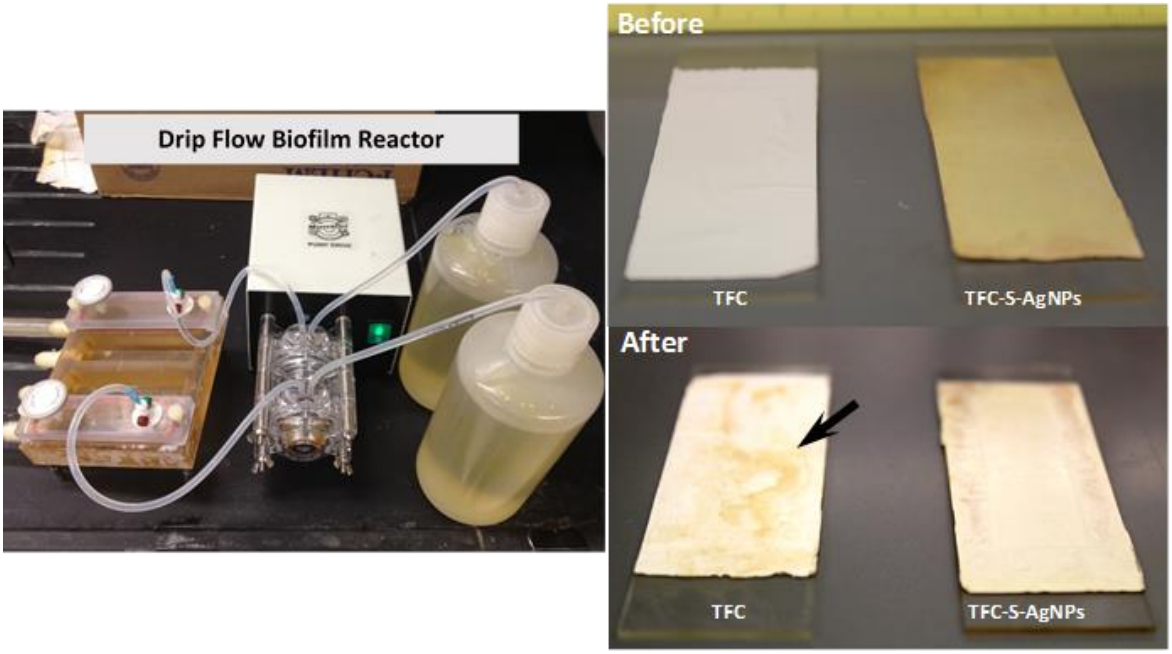

Fig. 3.13 Difference in *E. coli* biofilm growth on TFC membrane and TFC-S-AgNPs membrane in a drip flow biofilm reactor fed with a LB solution (5 g/L) at 1.0 ml/min for 7 days at 25 ˚C.

3.4 Conclusions

A covalent bonding method was developed to attach silver nanoparticles (AgNPs) onto the surface of polyamide (PA) thin-film composite (TFC) membrane with cysteamine as a bridging agent. The TFC-S-AgNPs membranes showed good stability of immobilized AgNPs and excellent antibacterial properties, while maintaining good water flux and salt rejection. The results demonstrated that chemically immobilizing AgNPs onto membrane surface could be an effective approach to reduce membrane biofouling. Further research is needed to optimize the dose of AgNPs to be grafted onto the TFC membrane and determine its long-term performance under continuous filtration conditions.

Acknowledgments

We gratefully acknowledge Professor Qingsong Yu in the Department of Mechanical & Aerospace Engineering at MU for providing us access to the video contact angle measurement system.

References

[1] X. Zhu, R. Bai, K.H. Wee, C. Liu, S.L. Tang, Membrane surfaces immobilized with ionic or reduced silver and their anti-biofouling performances, Journal of Membrane Science, 363 (2010) 278-286.

[2] J.S. Baker, L.Y. Dudley, Biofouling in membrane systems — A review, Desalination, 118 (1998) 81-89.

[3] S.Y. Lee, H.J. Kim, R. Patel, S.J. Im, J.H. Kim, B.R. Min, Silver nanoparticles immobilized on thin film composite polyamide membrane: Characterization, nanofiltration, antifouling properties, Polymers for Advanced Technologies, 18 (2007) 562-568.

[4] W.J. Lau, A.F. Ismail, N. Misdan, M.A. Kassim, A recent progress in thin film composite membrane: A review, Desalination, 287 (2012) 190-199.

[5] P. Gunawan, C. Guan, X. Song, Q. Zhang, S.S.J. Leong, C. Tang, Y. Chen, M.B. Chan-Park, M.W. Chang, K. Wang, R. Xu, Hollow fiber membrane decorated with Ag/MWNTs: Toward effective water disinfection and biofouling control, ACS Nano, 5 (2011) 10033-10040.

[6] Y. Liu, X. Wang, F. Yang, X. Yang, Excellent antimicrobial properties of mesoporous anatase TiO2 and Ag/TiO2 composite films, Microporous and Mesoporous Materials, 114 (2008) 431-439.

[7] H.J. Klasen, A historical review of the use of silver in the treatment of burns. II. Renewed interest for silver, Burns, 26 (2000) 131-138.

[8] K. Zodrow, L. Brunet, S. Mahendra, D. Li, A. Zhang, Q. Li, P.J.J. Alvarez, Polysulfone ultrafiltration membranes impregnated with silver nanoparticles show improved biofouling resistance and virus removal, Water Research, 43 (2009) 715-723.

[9] W.L. Chou, D.G. Yu, M.C. Yang, The preparation and characterization of silver-loading cellulose acetate hollow fiber membrane for water treatment, Polymers for Advanced Technologies, 16 (2005) 600-607.

[10] Y.L. Wang, Y.Z. Wan, X.H. Dong, G.X. Cheng, H.M. Tao, T.Y. Wen, Preparation and characterization of antibacterial viscose-based activated carbon fiber supporting silver, Carbon, 36 (1998) 1567-1571.

[11] E.S. Kim, G. Hwang, M. Gamal El-Din, Y. Liu, Development of nanosilver and multi-walled carbon nanotubes thin-film nanocomposite membrane for enhanced water treatment, Journal of Membrane Science, 394-395 (2012) 37-48.

[12] X. Cao, M. Tang, F. Liu, Y. Nie, C. Zhao, Immobilization of silver nanoparticles onto sulfonated polyethersulfone membranes as antibacterial materials, Colloids and Surfaces B: Biointerfaces, 81 (2010) 555-562.

[13] M.S. Mauter, Y. Wang, K.C. Okemgbo, C.O. Osuji, E.P. Giannelis, M. Elimelech, Antifouling ultrafiltration membranes via post-fabrication grafting of biocidal nanomaterials, ACS Applied Materials and Interfaces, 3 (2011) 2861-2868.

[14] S.W.P. Wijnhoven, W.J.G.M. Peijnenburg, C.A. Herberts, W.I. Hagens, A.G. Oomen, E.H.W. Heugens, B. Roszek, J. Bisschops, I. Gosens, D. Van De Meent, S. Dekkers, W.H. De Jong, M. Van Zijverden, A.J.A.M. Sips, R.E. Geertsma, Nano-silver - A review of available data and knowledge gaps in human and environmental risk assessment, Nanotoxicology, 3 (2009) 109-138.

[15] P. Gajjar, B. Pettee, D.W. Britt, W. Huang, W.P. Johnson, A.J. Anderson, Antimicrobial activities of commercial nanoparticles against an environmental soil microbe, Pseudomonas putida KT2440, Journal of Biological Engineering, 3 (2009).

[16] Y. Yang, Q. Chen, J.D. Wall, Z. Hu, Potential nanosilver impact on anaerobic digestion at moderate silver concentrations, Water Research, 46 (2012) 1176-1184.

[17] J. Yin, E.-S. Kim, J. Yang, B. Deng, Fabrication of a novel thin-film nanocomposite (TFN) membrane containing MCM-41 silica nanoparticles (NPs) for water purification, Journal of Membrane Science, 423–424 (2012) 238-246.

[18] J.S. Kim, E. Kuk, K.N. Yu, J.H. Kim, S.J. Park, H.J. Lee, S.H. Kim, Y.K. Park, Y.H. Park, C.Y. Hwang, Y.K. Kim, Y.S. Lee, D.H. Jeong, M.H. Cho, Antimicrobial effects of silver nanoparticles, Nanomedicine: Nanotechnology, Biology, and Medicine, 3 (2007) 95-101.

[19] E.M.V. Hoek, S. Bhattacharjee, M. Elimelech, Effect of membrane surface roughness on colloid-membrane DLVO interactions, Langmuir, 19 (2003) 4836-4847.

[20] R.J. Petersen, Composite reverse osmosis and nanofiltration membranes, Journal of Membrane Science, 83 (1993) 81-150.

[21] M.P. Seah, W.A. Dench, Quantitative electron spectroscopy of surfaces: a standard data base for electron inelastic mean free paths in solids, Surface and Interface Analysis, 1 (1979) 2-11.

[22] H.S. Lee, S.J. Im, J.H. Kim, H.J. Kim, J.P. Kim, B.R. Min, Polyamide thin-film nanofiltration membranes containing TiO2 nanoparticles, Desalination, 219 (2008) 48-56.

[23] B.J.A. Tarboush, D. Rana, T. Matsuura, H.A. Arafat, R.M. Narbaitz, Preparation of thin-film-composite polyamide membranes for desalination using novel hydrophilic surface modifying macromolecules, Journal of Membrane Science, 325 (2008) 166-175.

[24] H.A. Shawky, S.-R. Chae, S. Lin, M.R. Wiesner, Synthesis and characterization of a carbon nanotube/polymer nanocomposite membrane for water treatment, Desalination, 272 (2011) 46-50.

[25] M.A. Parada, A. de Almeida, P.N. Volpe, C. Muntele, D. Ila, Damage effects of 1 MeV proton bombardment in PVDC polymeric film, Surface and Coatings Technology, 201 (2007) 8052-8054.

[26] J.-M. Yeh, K.-Y. Huang, S.-Y. Lin, Y.-Y. Wu, C.-C. Huang, S.-J. Liou, Noncovalent Interaction between Gold Nanoparticles and Multiwalled Carbon Nanotubes via an Intermediatory, Journal of Nanotechnology, 2009 (2009).

[27] C.W. Wharton, Review article: Infra-red and Raman spectroscopic studies of enzyme structure and function, Biochemical Journal, 233 (1986) 25-36.

[28] T.G. Carter, W. Yantasee, T. Sangvanich, G.E. Fryxell, D.W. Johnson, R.S. Addleman, New functional materials for heavy metal sorption: " Supramolecular" attachment of thiols to mesoporous silica substrates, Chemical Communications, (2008) 5583-5585.

[29] A. El Harrak, G. Carrot, J. Oberdisse, J. Jestin, F. Bou é, Atom transfer radical polymerization from silica nanoparticles using the 'grafting from' method and structural study via small-angle neutron scattering, Polymer, 46 (2005) 1095-1104.

[30] L. Barrientos, P. Allende, C. Orellana, P. Jara, Ordered arrangements of metal nanoparticles on alpha-cyclodextrin inclusion complexes by magnetron sputtering, Inorganica Chimica Acta, 380 (2012) 372-377.

[31] V. Prabhawathi, P.M. Sivakumar, M. Doble, Green synthesis of protein stabilized silver nanoparticles using Pseudomonas fluorescens, a marine bacterium, and its biomedical applications when coated on polycaprolactam, Industrial and Engineering Chemistry Research, 51 (2012) 5230-5239.

[32] A. Kulkarni, D. Mukherjee, W.N. Gill, Flux enhancement by hydrophilization of thin film composite reverse osmosis membranes, Journal of Membrane Science, 114 (1996) 39-50.

[33] R.R. Khaydarov, R.A. Khaydarov, Y. Estrin, S. Evgrafova, T. Scheper, C. Endres, S.Y. Cho, Silver Nanoparticles Nanomaterials: Risks and Benefits, in: I. Linkov, J. Steevens (Eds.), Springer Netherlands, 2009, pp. 287-297.

[34] J.P. Ruparelia, A.K. Chatterjee, S.P. Duttagupta, S. Mukherji, Strain specificity in antimicrobial activity of silver and copper nanoparticles, Acta Biomaterialia, 4 (2008) 707-716.

[35] I. Sondi, B. Salopek-Sondi, Silver nanoparticles as antimicrobial agent: A case study on E. coli as a model for Gram-negative bacteria, Journal of Colloid and Interface Science, 275 (2004) 177-182.

[36] Q.L. Feng, J. Wu, G.Q. Chen, F.Z. Cui, T.N. Kim, J.O. Kim, A mechanistic study of the antibacterial effect of silver ions on Escherichia coli and Staphylococcus aureus, Journal of Biomedical Materials Research, 52 (2000) 662-668.

[37] Y. Matsumura, K. Yoshikata, S.I. Kunisaki, T. Tsuchido, Mode of bactericidal action of silver zeolite and its comparison with that of silver nitrate, Applied and Environmental Microbiology, 69 (2003) 4278-4281.

[38] A.D. Russell, W.B. Hugo, Antimicrobial Activity and Action of Silver, Progress in medicinal chemistry, 31 (1994) 351-370.

[39] O. Choi, K.K. Deng, N.J. Kim, L. Ross Jr, R.Y. Surampalli, Z. Hu, The inhibitory effects of silver nanoparticles, silver ions, and silver chloride colloids on microbial growth, Water Research, 42 (2008) 3066-3074.

[40] C.N. Lok, C.M. Ho, R. Chen, Q.Y. He, W.Y. Yu, H. Sun, P.K.H. Tam, J.F. Chiu, C.M. Che, Proteomic analysis of the mode of antibacterial action of silver nanoparticles, Journal of Proteome Research, 5 (2006) 916-924.

[41] J.R. Morones, J.L. Elechiguerra, A. Camacho, K. Holt, J.B. Kouri, J.T. Ram ŕez, M.J. Yacaman, The bactericidal effect of silver nanoparticles, Nanotechnology, 16 (2005) 2346-2353.

[42] C. Liao, P. Yu, J. Zhao, L. Wang, Y. Luo, Preparation and characterization of NaY/PVDF hybrid ultrafiltration membranes containing silver ions as antibacterial materials, Desalination, 272 (2011) 59-65.

CHAPTER FOUR

Multi-walled carbon nanotubes (MWNTs)/polysulfone (PSU) nanocomposite hollow fiber membranes for enhanced water treatment

Abstract

Due to the carbon nanotubes' unique one-dimensional tubular structure and superior mechanical and chemical properties, it has been used as fillers to prepare high performance flat sheet membranes. In this study, we explored if the incorporation of oxidized multi-walled carbon nanotubes (MWNTs) into polysulfone (PSU) hollow fiber membranes could enhance the membrane performance. Polyvinylpyrrolidone (PVP) was used as porogen and 1-methyl-2-pyrrolidinone (NMP) as the solvent in the phase inversion spinning process, and deionized water was used as bore fluid and coagulant. Purified and oxidized MWNTs in the mixed acid solution (H_2SO_4/HNO_3 = 3/1 in volume) was used as filler at concentrations ranging from 0 to 1 wt%. Results indicated that at three different PSU concentrations (15, 18, 20 wt%), pure water flux of all membranes increased first and then gradually decreased with increasing nanotube concentrations. The optimized nanocomposite membranes showed a significant increase in pure water flux (60% to 100%) while maintaining a similar capability for solute rejection, and also an improved resistance to protein fouling. The water contact angle of the membrane decreased with increasing filler concentrations, suggesting an increase in the membrane surface hydrophilicity that might have contributed to the improved membrane performance.

Keywords: Multi-walled carbon nanotubes; Nanocomposite membrane; Hollow fiber membrane; Phase inversion; Molecular weight cut off (MWCO); Membrane fouling

4.1 Introduction

Since its discovery by Iijima in 1991 [1], carbon nanotube (CNT) has attracted much attention in the scientific community due to its unique one-dimensional tubular structure and excellent mechanical, chemical, and electronic properties. CNTs have been explored for many applications including nanocomposites [1, 2], energy storage [3], electronic devices [4, 5], nanoprobes and sensors [6], and biomedicine [7, 8].

Recently, Gerhard and co-workers [9] reported the osmotically driven transport of water molecules through CNTs, suggesting an exciting opportunity of using nanotube networks and assemblies for high efficiency water filtration. Subsequently, many studies have been carried out to incorporate CNTs into polymers to make composite membrane for water purification. For example, Ma et al. [10] developed a new class of high flux thin-film nanofibrous composite (TFNC) membranes which contained oxidized MWNTs inside the cross-linked polyvinyl alcohol (PVA) barrier layer. They attributed the enhanced water flux to the formation of directional water channels through the interface between fillers and barrier layer matrix and the interconnections among the fine nanofiber network. Tiraferri et al. [11] conferred antimicrobial properties to polyamide thin-film composite (TFC) membranes by covalently binding cytotoxic single-walled carbon nanotubes (SWNTs) to their active surfaces. Their results suggested the potential of these membranes to delay the onset of biofouling in membrane-based separation applications. Zhang et al. [12] incorporated acid-treated MWNTs into polyamide layer of the thin-film nanocomposite (TFN) reverse osmosis (RO) membranes resulting in enhanced water permeability. Qiu and co-workers [13] introduced MWNTs functionalized with isocyanate and isophthaloyl chloride groups into PSU matrix, and found that a proper

amount of modified MWNTs could enhance the water flux of membrane through influencing the surface mean pore size and membrane porosity.

The current researches revealed that achieving homogenous dispersion of CNTs in the polymer matrix through strong interfacial interactions is crucial to the successful development of CNT/polymer nanocomposite [14]. As a result, various chemical or physical modifications were applied to CNTs to improve its dispersion and compatibility with polymer matrix. Among these approaches acid treatment was considered most convenient [15], in which hydroxyl and carboxyl groups generated would concentrate on the ends of the CNT and at defect sites, making them more reactive and thus better dispersed [16, 17].

Previous researches on the incorporation of functionalized CNTs into composite membranes were mostly carried out on flat sheet membranes. Hollow fiber membranes (HFM), however, may have more advantages in applications because of the large membrane surface areas that could be packed per unit volume. Fabrication of HFM with CNTs could be more complex than that of flat sheet membranes because it involves rapid phase inversion kinetics and interfacial mass transfer [18], and there are more parameters to control [19] such as the dimensions of the spinneret (inner diameter, outside diameter), dope composition and flow rate, bore fluid composition and flow rate, length of the air gap, fiber take-up speed, and coupling effect of the polymer-solvent-nonsolvent system. Considering the potential influences of CNTs on the physicochemical properties of dope solution (e.g., composition and rheological behavior) [20] and change of membrane formation route originated from various additives [21], it is necessary to study the effects of CNTs on the morphology and performance of HFM and to explore the potential

applications of CNTs in HFM for water treatment.

The primary objective of this study was to evaluate the effects of oxidized CNTs on the physicochemical properties of PSU HFM, and hence, the membrane performance. The CNTs was first oxidized by concentrated acid solution (H_2SO_4/HNO_3 = 3/1 in volume), and then incorporated into the PSU matrix through the phase inversion method. The concentration of nanotubes in the polymer matrix was controlled from 0 to 1.0 wt%. The physicochemical properties of nanocomposite HFM were evaluated by scanning electron microscopy (SEM), attenuated total reflection Fourier transform infrared (ATR FT-IR) spectroscopy, and contact angle measurements. The membrane performances were assessed by water permeability and solute rejection. The fouling resistance of the membrane to protein was also evaluated using bovine serum albumin (BSA) as a model fouling agent.

4.2 Materials and methods

4.2.1 Materials

Polysulfone (PSU) with a molecular weight of 35,000 Da was obtained in the form of transparent pellets from Sigma-Aldrich and dried for 3 h at 120 °C before usage. 1-Methyl-2-pyrrolidinone (NMP, 99.5%, Aldrich) was selected as solvent due to its low toxicity [22] and strong interaction with polymer and miscibility with water [23, 24]. All other chemicals were obtained from Sigma-Aldrich and were of ACS reagent grade. Multi-walled carbon nanotubes (MWNTs, diameter 10-20 nm, length 5-15 μm and purity of 95%) were manufactured by Shenzhen Nanotech Port Co. Ltd., China. Deionized water (DI) produced by Millipore DI system (Synergy 185, 18.2 MΩ·cm) was used for

solution preparation and filtration study.

4.2.2 Preparation and characterization of oxidized MWNTs

A mixed acid solution (H_2SO_4/HNO_3 = 3/1 in volume) was first prepared, then MWNTs was added at a ratio of 1 g per 100 mL acid solution and refluxed at 80 °C for 3 h. After dilution by DI water, the MWNTs were collected by membrane filtration (PSU membrane with MWCO around 50,000 Da, fabricated in our lab) and multiple washing with Milli-Q water until the pH of water reached near neutral. The final products were dried at 80 °C for 24 h under vacuum and were labeled as OMWNTs.

Morphology and internal structure of nanotubes were examined by SEM (Quanta FEG 600, FEI Company, Hillsboro, OR) and TEM (JEOL 1400, JEOL Ltd., Peabody, MA). SEM specimen was prepared by dropping nanotubes-ethanol mixture solution onto a silicon wafer. After complete drying at room temperature, the specimen was coated with platinum by a sputter coater (K575x, Emitech Ltd., Kent, England) at 20 mA for 60 s. TEM samples were prepared by dropping nanotubes-ethanol mixture solution onto carbon coated copper grid and drying at the room temperature. The functional groups of nanotube surface were identified by Fourier transform infrared (FT-IR) spectroscopy on Nicolet 4700 FT-IR (Thermo Electron Corp., Waltham, MA). All spectra included the wave numbers from 650 to 4000 cm^{-1} with 128 scans at a resolution of 2.0 cm^{-1}. For the Raman scattering analysis, an Invia Renishaw spectrometer (RM1000 series, Gloucestershire, UK) equipped with a Leica DMLB microscope (Wetzlar, Germany) and a 785 nm near-infrared diode laser source was used.

4.2.3 Spinning of hollow fiber membranes

The OMWNTs/PSU nanocomposite HFMs were fabricated by the phase inversion method on a custom-designed single-head spinning machine presented in SI Fig. 4.1s. To make dope solution, a certain amount of OMWNTs was dispersed in NMP solvent and sonicated for 10 min to achieve dispersion. PSU and PVP were then added into the mixture and stirred for 6 h at 50 °C to form dope solution. The dope solution was kept overnight for degassing prior to use.

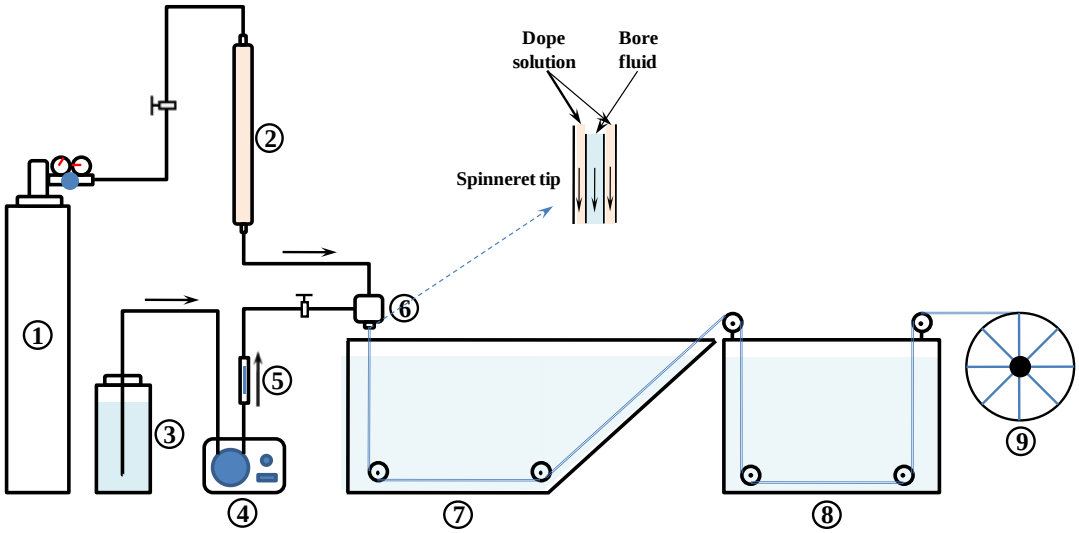

Fig. 4.1 Schematic diagram of the custom-designed single-head spinning system: (1) high purity nitrogen, (2) dope solution, (3) bore fluid, (4) gear pump, (5) flow meter, (6) spinneret, (7) coagulation bath, (8) washing bath, (9) collecting drum.

As shown in Fig. 4.1 illustrating the spinning process, the dope solution was fed into the annulus of the spinneret under certain pressure provided by the high purity nitrogen. DI water was used as bore fluid and pumped into the inner tube of the spinneret. Once the dope and bore fluid met at the tip of the spinneret, they entered the coagulation bath. The precipitated PSU fiber was prewashed in washing bath and collected by the collecting drum. Finally, the collected fibers were rinsed in the tap water at room temperature for at

least 24 h to remove the residual solvent, and then immersed in a 25 wt% glycerol aqueous solution for another 24 h before drying in the ambient environment. Experimental parameters of spinning process were listed in Table 4.1. The membranes containing 15, 18 or 20 wt% of PSU were labeled as HFM15-x, HFM18-x or HFM20-x, respectively, where x stands for the concentration of nanotubes. For example, if a membrane sample possessed 18 wt% PSU and the amount of filler took up 1.0 wt% of PSU, this membrane was named HFM18-1.0%.

Table 4.1 Spinning conditions of PSU hollow fiber membranes

Parameter	Condition
Spinneret OD/ID	1.0 mm/0.6 mm
Spinneret temperature (℃)	25
Dope solution	PSU/PVP/NMP
Concentration (wt%)	15/5/80; 18/5/77; 20/5/75
Dope solution flow rate (mL/min)	1.2
Bore fluid composition	DI water
Bore fluid flow rate (mL/min)	1.8
Range of air-gap distance (cm)	0
Coagulant	Tap water
Coagulant temperature (℃)	25
Washing bath	Tap water
Washing bath temperature (℃)	25
Take-up speed (cm/min)	450

4.2.4 Membrane characterization and performance assessment

Membrane surface and cross-section were characterized by SEM on Quanta FEG 600. The sample of membrane surface was obtained by drying a piece of membrane at room temperature, while the cross-section was obtained by freeze-fracturing of the membranes in the liquid nitrogen. These specimens were coated with platinum at 20 mA

for 60 s prior to imaging. To understand the dispersion of MWNT in the membrane, we collected the cross-sectional TEM images following the reported procedures in the literature [25, 26]. Briefly, the membranes were embedded in Epon resin and cut by Reichert– Jung Ultracut E ultramicrotome (Reichert, Inc. Depew, NY). The images were taken under 80 kV by using JEM 1400. Furthermore, Raman spectra were collected at four locations randomly selected on membrane sample surface to verify the dispersion of OMWNTs on the membrane outside surface. The spectra were collected with a 5 μm spot size and 4.1 mW at a 60 s exposure time. The wavelength of the laser source is 785 nm. The viscosities of the polymer solutions were measured using a Brookfield Digital Rheometer (DV-II, Brookfield Engineering Laboratories, Inc., Middleboro, MA) with a shear rate of 13.2 sec^{-1} at 25 °C.

Hydrophilicity of membrane was determined by measuring the pure water contact angle based on the sessile drop method. A video contact angle system (VCA-2500 XE, AST products, Billerica, MA) was employed to perform the test. At least eight stabilized contact angles from different sites of each sample were obtained to calculate the average contact angle and standard deviation. Functional groups of membrane surface were identified by ATR FT-IR on the Nicolet 4700 equipped with multi-reflection Smart Performer® ATR accessory. The condition was the same as that used in the FT-IR analysis of nanotubes.

A low pressure cross-flow filtration system (pressure range: 0 - 50 psi) was used to evaluate pure water flux, solute rejection, molecular weight cut off (MWCO), and fouling resistance of the membranes. The membrane module was sealed by epoxy resin, with an effective membrane area of around 50 cm^2. A schematic diagram of the filtration system is

shown in Fig. 4.2.

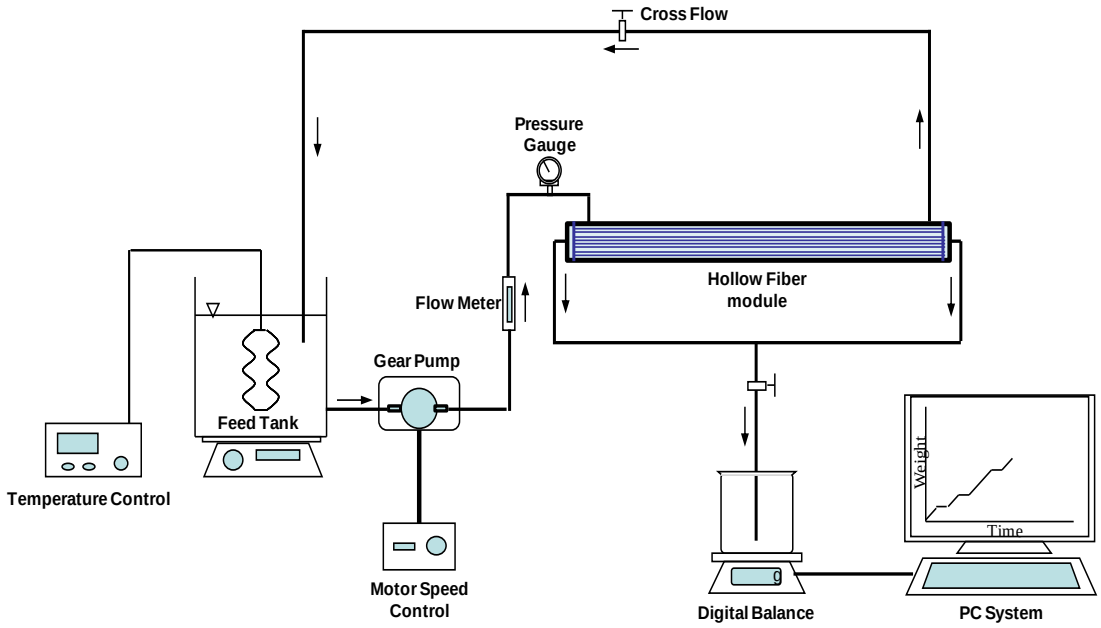

Fig. 4.2 Schematic diagram of the hollow fiber membrane filtration system

Prior to test, each membrane was compressed by DI water at a constant trans-membrane pressure (TMP) of 15 psi for 3 h. Pure water flux was measured by weighing the permeate water as a function of time at 10 psi, and recorded by a LabVIEW automated system (National Instruments LabVIEW 8.2 with Ohaus digital balance). After the flux test, feed solution containing 50 mg/L of humic acid (HA, prefiltered with a 0.45 μm filter, Aldrich) or Procion Red (PR, MX-5B, Aldrich) was filtrated and solute concentrations of feed and permeate solutions were measured using a UV-visible spectrophotometer (Lambda 25, PerkinElmer, Waltham, MA) at a wavelength of 254 and 538 nm, respectively. The measurement was conducted at 25 ± 1 °C, which was controlled by a water circulator (Isotemp 6200 R20F, Fisher Scientific, Inc., Pittsburgh, PA). The flux and rejection was calculated with Equation (1) and Equation (2), respectively:

$$J = \frac{V_p}{A \cdot t} \quad (1)$$

$$R = \left(1 - \frac{C_p}{C_f}\right) \times 100 \quad (2)$$

where, J is the water flux (L/m^{2}h), V_p the permeate volume (L), A the membrane area (m^2) and t the treatment time (h). R is the rejection ratio and C_p and C_f are the concentrations of permeate and feed solution, respectively.

MWCO values of membranes were evaluated by determining the rejections of polyethylene glycol (PEG, 3350 Da), PVP (10,000 and 40,000 Da) or BSA (67,000 Da) under a solution concentration of 1000 mg/L. The MWCO of a particular membrane was defined as the molecular weight of the solute which had a 90% rejection. The concentrations of PEG and PVP were measured by a TOC analyzer (TOC-5000, Shimadzu Corp., Japan), while the concentrations of BSA were determined on a UV-visible spectrophotometer at 280 nm.

To evaluate the fouling resistance of the nanocomposite membranes, a 1000 mg/L BSA phosphate-buffered saline solution (pH~7.4) was forced to permeate through the membranes at a constant pressure of 10 psi for 5 h. Membranes were compressed by DI water at 15 psi for 3 h prior to the fouling tests.

4.3 Results and discussion

4.3.1 Characteristics of MWNTs before and after oxidation

As shown by the SEM images, raw MWNTs (Fig. 4.3a) contained bulk material that could be metal catalysts and impurities. After the acid treatment, the metal catalysts and impurities largely disappeared in OMWNT (Fig. 4.3b). The TEM images (Fig. 4.3c and 4.3d) are consistent with the SEM results, showing the tubular structures of raw and oxidized MWNTs, and the removal of the dark spots after acid treatment.

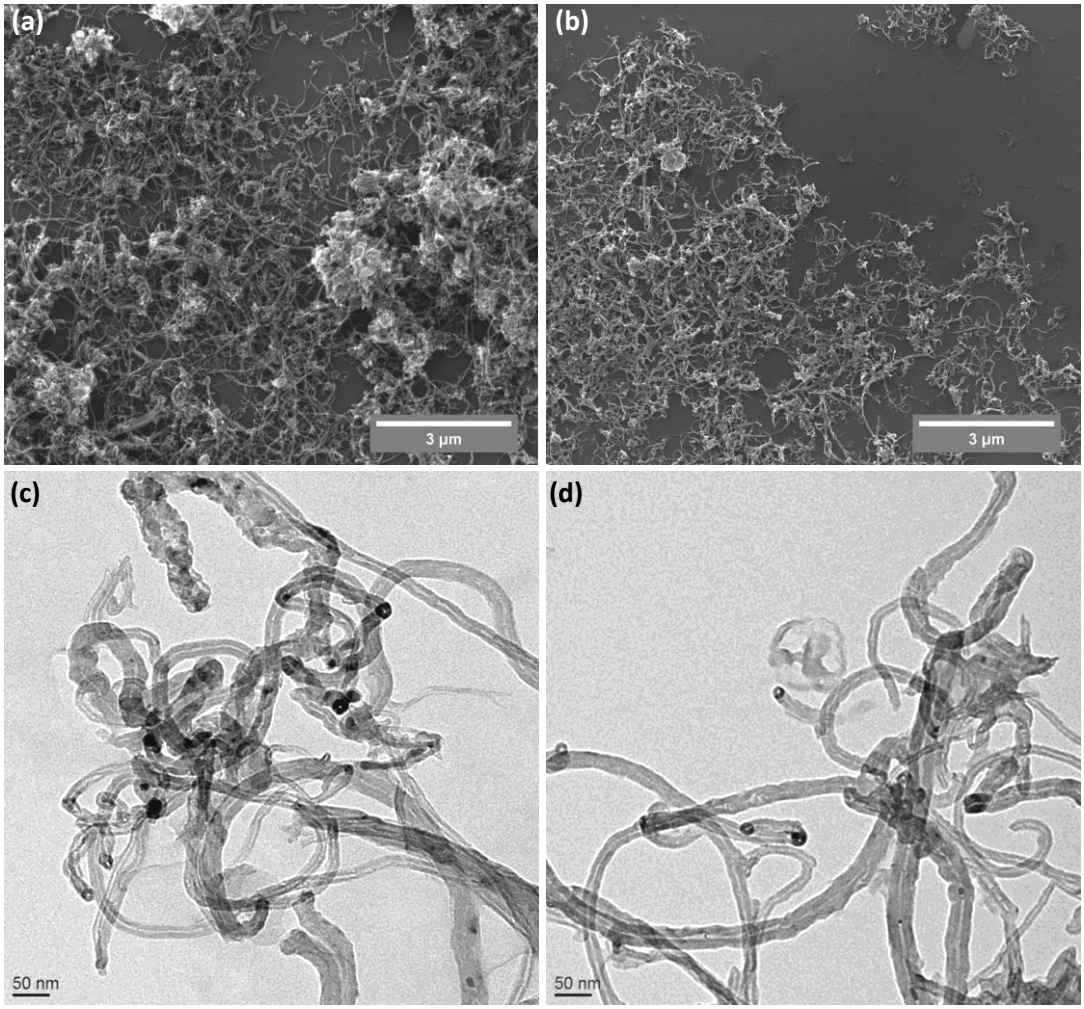

Fig. 4.3 SEM and TEM images of the carbon nanotubes: (a, c) raw MWNTs and (b, d) oxidized MWNTs.

FT-IR spectra of MWNTs in KBr tablet before and after oxidation are presented in Fig. 4.4a. Besides the peak at 1578 cm^{-1} which could be attributed to the vibration of carbon skeleton of the nanotubes [27], additional peaks appeared at around 3436, 1720 and 1213 cm^{-1} after acid treatment. These can be assigned to -OH, C=O, and C-C-O stretching present in carboxylic groups (-COOH), respectively [28], and their presence suggested the successful oxidation of MWNTs.

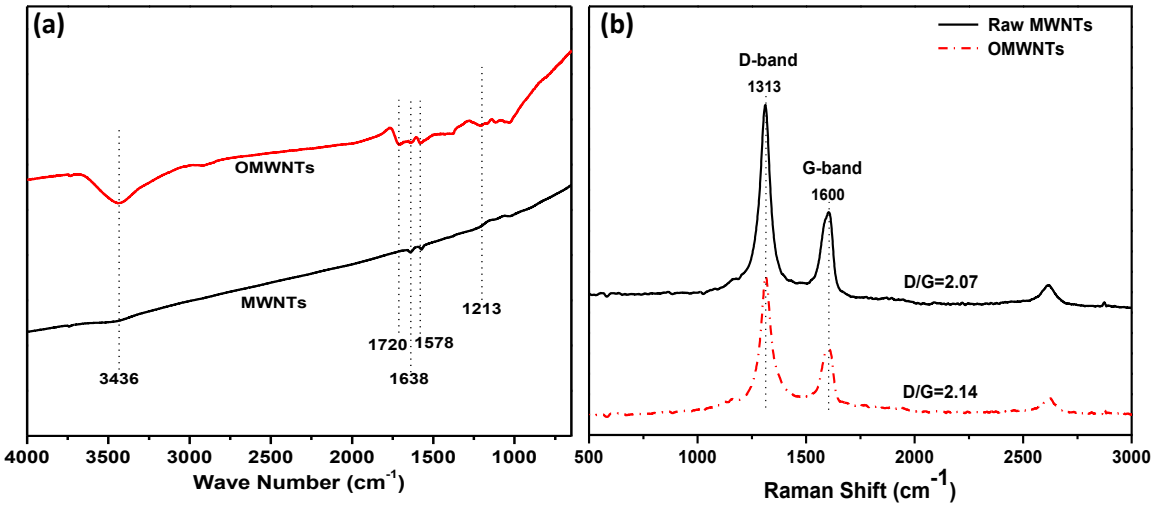

Fig. 4.4 Spectra of raw and oxidized MWNTs: (a) FT-IR; (b) Raman.

Raman scattering is a powerful technique to probe the changes of surface and structure of CNTs [29]. In the Raman spectra of MWNTs (Fig. 4.4b), two graphitic peaks could be observed. The peak at around 1600 cm^{-1} (G-band) corresponded to a splitting of the E_{2g} stretching mode of graphite, which has been assigned to the movement of two neighboring carbon atoms in opposite directions, characteristic of highly oriented pyrolitic graphite [30]. The peak at around 1313 cm^{-1} (D-band) could be assigned to the disordered graphite structure or sp^3-hybridised carbons of the nanotubes [28, 31]. Usually the relative degree of functionalisation or defects in the nanotubes could be evaluated by

the intensity ratio of the D-band to G-band (I_D/I_G). It can be seen that I_D/I_G of the OMWNTs (2.14) is larger than that of the raw MWNTs (2.07), which indicated more defects in crystal structure of OMWNTs than in that of raw MWNTs. These defects may be caused by the attacking of concentrated acid to the structure of nanotubes and the formation of oxygen-containing functional groups as identified by FT-IR spectra.

Same amounts (0.5 mg) of MWNTs and OMWNTs were dispersed in 10 mL of NMP and further sonicated for 5 min, and the dispersion status was examined afterwards in this study. As shown in Fig. 4.5, for the raw MWNTs, the nanotubes formed aggregations and settle down within several minutes; whereas, OMWNTs showed a good dispersion in the NMP solvent. This enhanced dispersion should facilitate the interaction between nanotubes and polymer chain and subsequently the dispersion inside the polymer matrix during the spinning process.

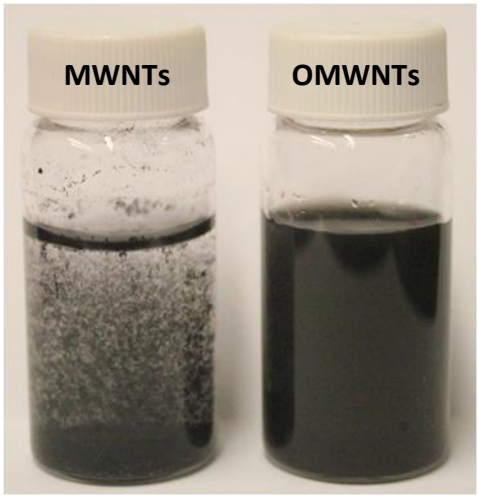

Fig. 4.5 Dispersion test of MWNTs in NMP (0.5 mg MWNTs/10 mL NMP).

4.3.2 Characteristics of hollow fiber membranes

As shown by Fig. 4.6, the original PSU membrane is white (Fig. 4.6a), whereas the incorporation of MWNTs resulted in a uniform dark gray tint of the membranes (Fig. 4.6b-f). With increasing filler content, the tint increased from gray to black. The uniformity of fiber colors indicated the existence of OMWNTs inside the membrane matrix and also suggested a good dispersion of these nanotubes. The significantly improved interfacial bonding between the nanotubes and polymer matrix upon the acid treatment was needed for the dispersion [1].

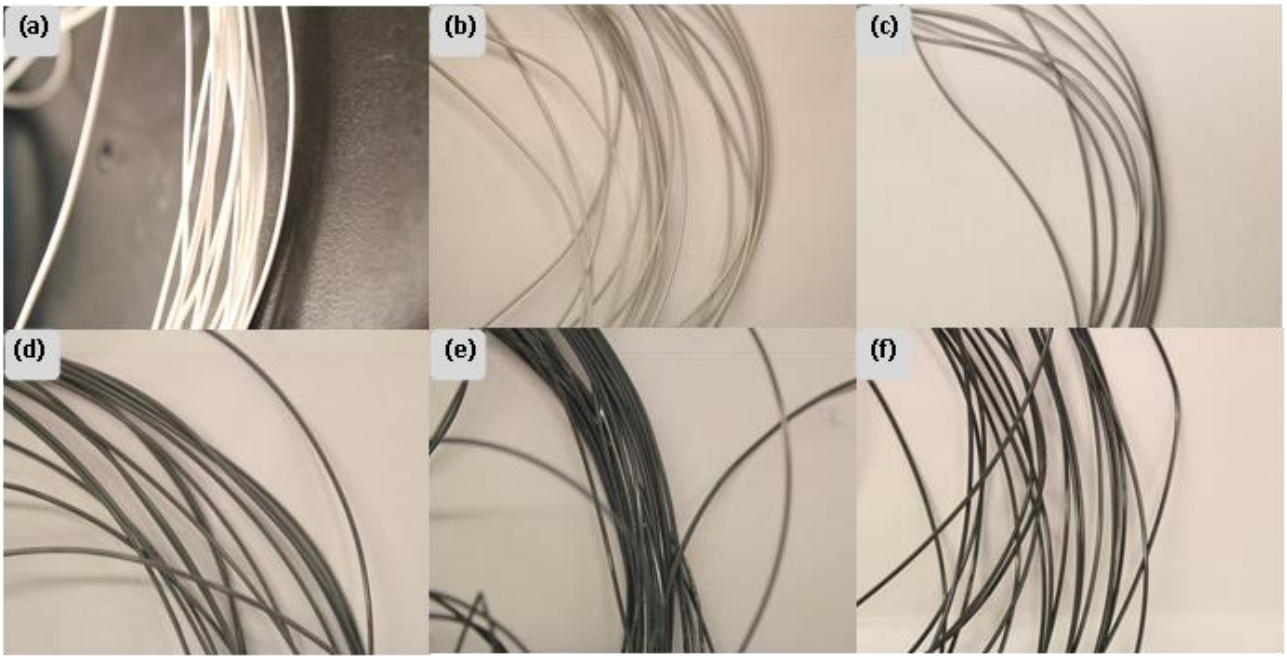

Fig. 4.6 Pictures of HFM18 with different OMWNTs content: (a) 0 wt%; (b) 0.1 wt%; (c) 0.25 wt%; (d) 0.5 wt%; (e) 0.75 wt% and (f) 1.0 wt%.

The ATR FT-IR spectra of membrane surfaces all showed similar profiles (figure was not shown). Peaks at 1585 $cm^{-1}$and 1488 cm^{-1} could be assigned to aromatic C-C stretching, 1325 cm^{-1} and 1298 cm^{-1} to the doublet from the asymmetric O=S=O stretching of sulfone group, 1245 cm^{-1} to the asymmetric C-O-C stretching of aryl ether

group and 1150 cm^{-1} to the symmetric O=S=O stretching of sulfone group [32, 33], which is consistent with the characteristic structure of PSU. The peak at around 1660 cm^{-1} corresponded to the characteristic peak of the secondary amide group of PVP [34], which might come from the residual PVP inside the membrane matrix. No other new peaks were observed after the incorporation of OMWNTs, which could be due to the relatively low concentration of fillers.

The cross-sectional images of pristine hollow fiber membranes without nanotubes are presented in Fig. 4.7. These fibers prepared with different PSU concentrations all showed uniform thickness. The outside diameter of the hollow fiber is around 950 μm. With increasing PSU concentration from 15 to 20%, the membrane thickness slightly increased from 90.5 to 92.3 and then to 96.0 μm. All these fibers consisted of finger-like voids extended from both inner and outer fiber surfaces to the near center of the fiber. This dual-layer structure is formed due to the use of water as the coagulant and bore fluid [35].

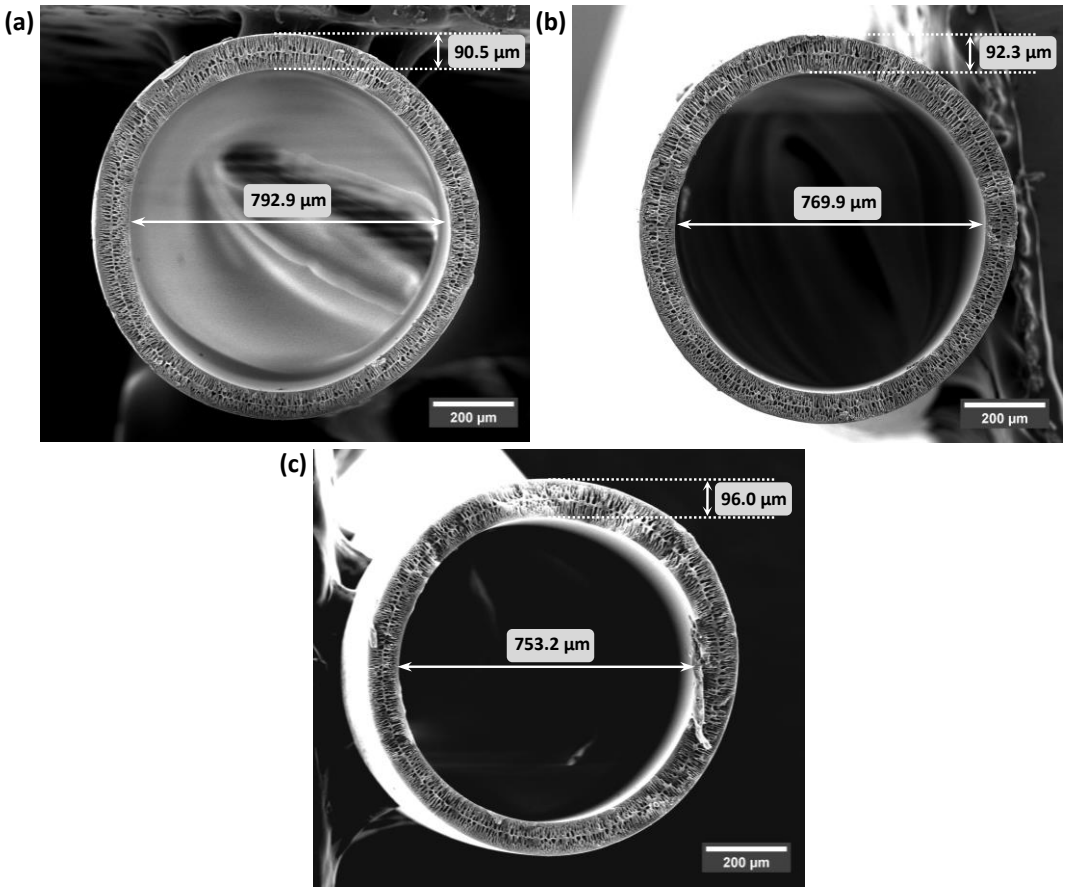

Fig. 4.7 Cross-sectional SEM images of hollow fiber membranes without fillers: (a) HFM15-0%; (b) HFM18-0%; (c) HFM20-0%.

Cross-sectional images at higher resolutions (Fig. 4.8) clearly showed the fingerlike macrovoids extending from both inner and outer surfaces, and an intermediate sponge-like layer. On both surfaces, a skin layer was formed on top of a porous substructure due to the instantaneous liquid-liquid demixing process [19]. There is no significant difference between these membrane samples. However, the intermediate sponge-like layer seems to increase with increasing PSU concentrations. The distribution of OMWNTs in the fibers could also be observed in the high resolution images (HFM15-1%H, HFM18-1%H and HFM20-1%H), as indicated by the white arrows. The diameter of nanotubes in the matrix

is similar to those observed in their pure form by SEM and TEM (Fig. 4.3). No obvious aggregates were observed in the cross-sectional image, which indicated the proper dispersion of OMWNTs. Similarly, the cross-sectional TEM images (Fig. 4.9a-c) also showed the good dispersion of OMWNTs inside the polymer matrix. No obvious aggregates were observed. The results as presented in Fig. 4.9(d-f) showed almost the same spectra (D-band and G-band) for different locations on the same membrane sample surface. So we would reasonably say that OMWNTs exist on membrane outside surface and there is no difference in the OMWNT dispersion on a scale larger than the spot size for Raman analysis, which is consistent with the uniformity of fiber colors. Other than the appearance of hydrophilic functional groups on OMWNTs, the existence of PVP inside the PSU matrix might have provided interfacial bonding between nanotubes and polymer matrix and facilitated the dispersion of OMWNTs [36].

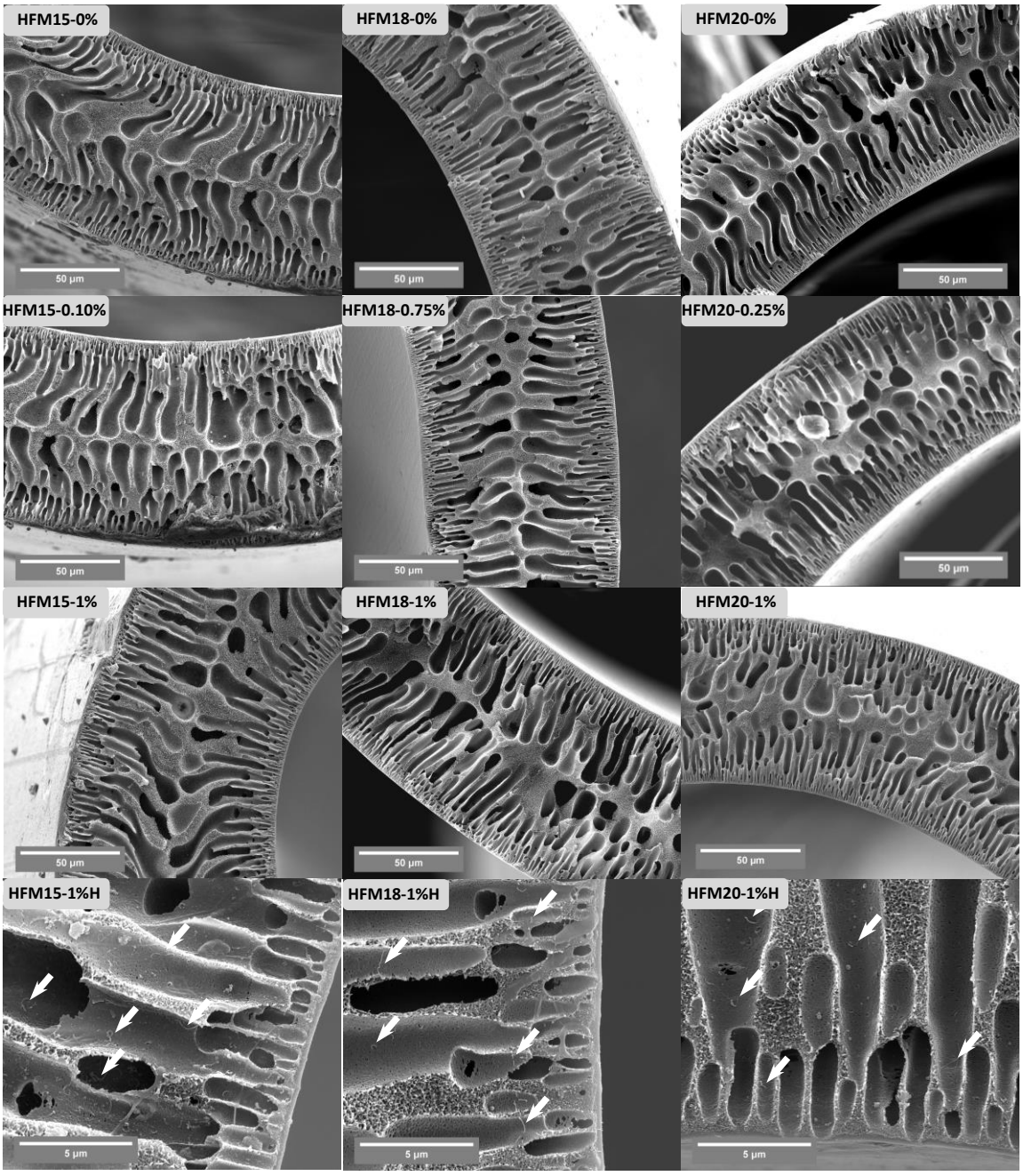

Fig. 4.8 Cross-sectional images of hollow fiber membranes

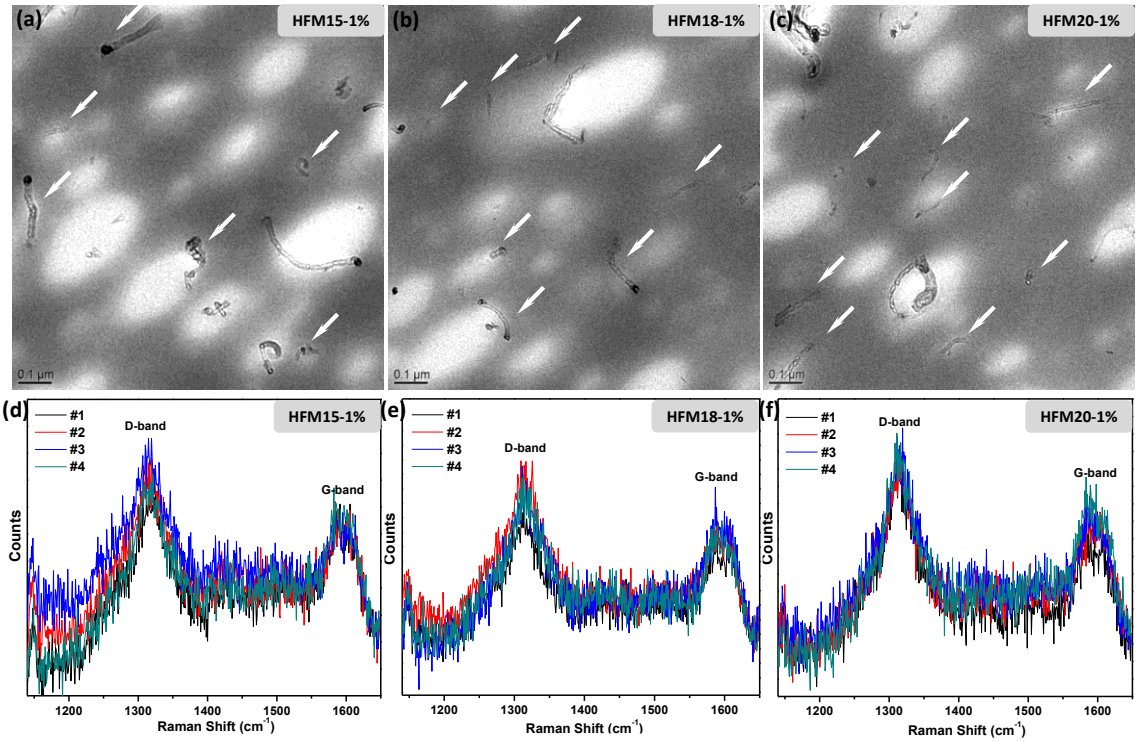

Fig. 4.9 TEM images of membrane cross-sections (a-c) and Raman spectra of membrane surfaces (d-f) (collected at four locations randomly selected on each membrane sample).

The outer surface morphologies of HFM18 membranes with different OMWNTs content are presented in Fig. 4.10. The outer surface of HFM18-0% was dense and no pores could be observed at a magnification of 100,000 (inset in Fig. 4.10a), so this membrane is considered a tight UF membrane [37]. After incorporation of nanotubes at an increasing concentration, the surface pore size increased firstly then decreased. Based on the calculation of ImageJ, the pore size is around 8.7 ± 3.2, 8.2 ± 2.8, 8.4 ± 2.5, 9.8 ± 3.4 and 4.4 ± 1.5 nm for 0.1, 0.25, 0.50, 0.75 and 1.0 wt%, respectively. Generally, the addition of hydrophilic substance in the dope solution leads to accelerated solvent and non-solvent exchange and thus encourages formation of a porous structure [38].

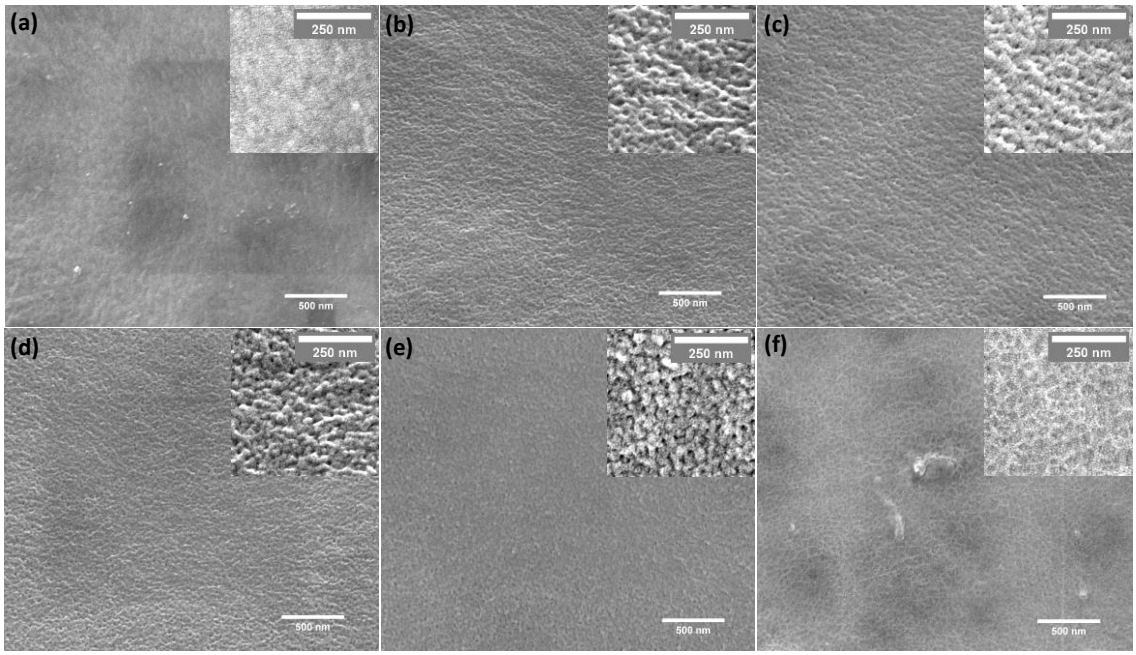

Fig. 4.10 Outside surface morphology of HFM18 with different OMWNTs content: (a) 0 wt%; (b) 0.1 wt%; (c) 0.25 wt%; (d) 0.5 wt%; (e) 0.75 wt% and (f) 1.0 wt%

The rheological behavior was estimated by measuring the viscosity of dope solutions and presented in Table 4.2. It is clear that viscosity of dope solution is mainly controlled by the polymer concentration. When polymer concentration increased from 15 to 20 wt%, the viscosity increased from 326.4 to 1401 cP. In comparison, while the viscosity of dope solution also increased with increasing OMWNTs concentration, but to a much lesser degree. For example, the viscosity of the dope solution containing 20 wt% PSU increased from 1401 to 1510 cP with increasing OMWNTs concentration from 0 to 1.0%. Similarly, the viscosity of dope solution with 15% PSU increased from 326.4 to 358.4 cP, and with 18 wt% PSU, increased from 825.6 to 896 cP. The increase in viscosity of the dope solution could be attributed to the large aspect ratio of nanotubes and the formation of a combined nanotube-polymer chain network [39, 40]. The higher solution viscosity indicates that kinetically, the overall diffusion between components in

the phase inversion system can be suppressed because of the increase in the rheological hindrance or a delayed exchange between solvent and non-solvent [2], which appeared to affect the characteristics of the resulting membranes and, hence, the membrane performance.

Table 4.2 Viscosity of dope solution (cP) with a shear rate of 13.2 sec^{-1} at 25 °C

PSU Concentration (wt%)	MWNTs Concentration (wt%)		
	0	0.5	1
15	326.4	343.5	358.4
18	825.6	876.8	896
20	1401	1478	1510

As shown in Fig. 4.11, the contact angle slightly decreased from about 69° to 57° as the concentration of OMWNTs was increased for HFM20. The other two membrane types showed similar decrease in contact angle, from 66° to 60° and 64° to 56°, respectively. Similar phenomenon was reported by Choi et al. [20] and was attributed to the migration of hydrophilic MWNTs to the membrane surface during the phase inversion process in water. The reduced contact angle indicated that the entrapped OMWNTs on the membrane could enhance hydrophilicity and thus mitigate membrane fouling caused by protein or other organic foulants [41, 42].

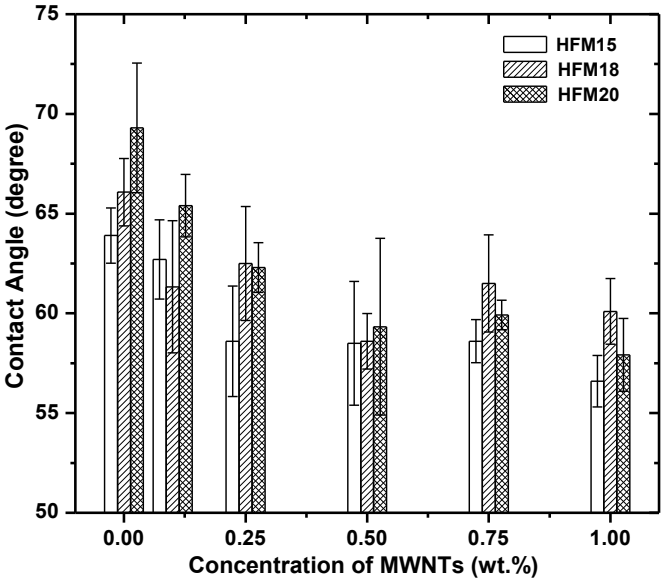

Fig. 4.11 Contact angles of nanocomposite membranes

4.3.3 Membrane performance

The membrane performances in terms of water flux and rejections of HA and PR, as well as relevant MWCO are presented in Fig. 4.12. The water flux first increased and then decreased with increasing OMWNTs concentration. To illustrate, the water flux of HFM15 increased from 36.1 ± 4.0 to 70.7 ± 1.8 L/m^{2}h and then decreased to 38.6 ± 1.0 L/m^{2}h when OMWNTs concentration increased from 0% to 0.1% and to 1.0%. The water flux of HFM18 increased from 24.8 ± 0.5 to 39.8 ± 0.4 L/m^{2}h and then decreased to 28.5 ± 1.5 L/m^{2}h. While the water flux of HFM20 increased from 14.1 ± 1.7 to 26.4 ± 0.5 L/m^{2}h and then decreased to 10.1 ± 0.9 L/m^{2}h. However, the transition thresholds are different. Generally, the pure water flux is related to the porosity, pore interconnection, surface pore size, and hydrophilic property of membrane [41]. The increase in surface pore size and hydrophilic property of membrane will promote the pure water flux. Meanwhile, the correlative MWCO (Fig. 4.11b, d, f) seems to have a good relationship with the pure water flux - high MWCO came with high water flux.

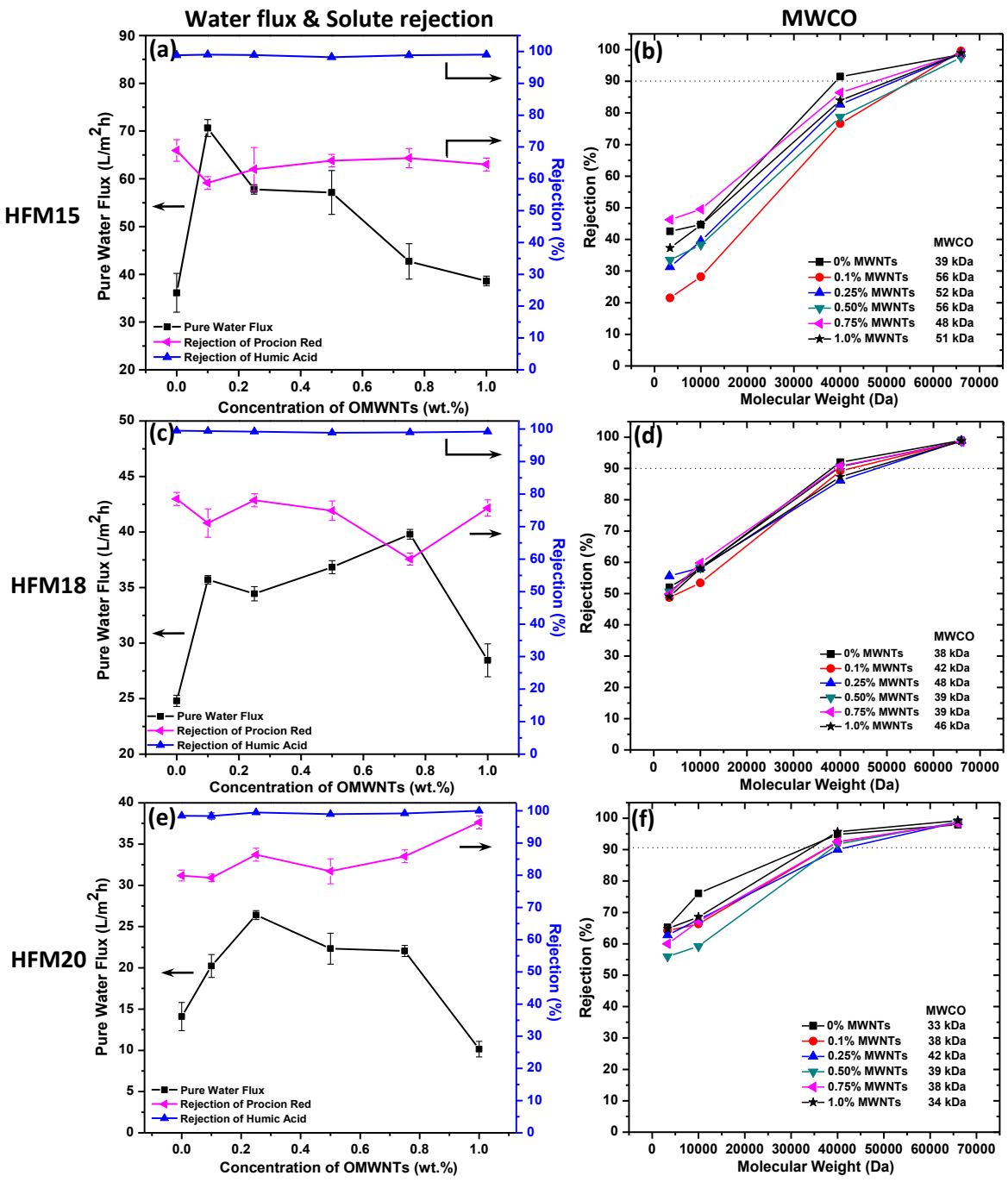

Fig. 4.12 Water fluxes, rejections and corresponding MWCO of HFM15 (a, b), HFM18 (c, d), and HFM20 (e, f).

Notably, the convex shape of flux change for HFM18 matched well with the change of surface pore size. The surface pore size increased to 9.8 ± 3.4 nm and then decreased

to 4.4 ± 1.5 nm in response to an increase of OMWNTs concentration to 0.75% and then to 1.0%. Such convex relationships between water flux and content of materials possessed non-solvent property such as PVP or TiO_2 have been reported in the literatures [43, 44]. It was proposed that thermodynamic immiscibility induced by the addition of PVP or TiO_2 could lead to the enhanced phase separation, while the viscosity increase induced by the addition of PVP or TiO_2 could hinder molecular diffusion. At low loading of PVP or TiO_2, enhancement of demixing could outweigh the hindered diffusion, leading to a more porous and permeable membrane. With further increase in loading and subsequently viscosity increase, diffusion delay could overcome the acceleration of phase separation. Under this delayed demixing condition, the top layer will be dense and thick with low porosity and low degree of pore interconnectivity due to the high concentration of the polymer solution at the onset of demixing [45]. Meanwhile the formation of macrovoid in the sublayer also could be suppressed [43]. As a result, fabricated membranes with low porosity and permeability are expected. Considering the effect of OMWNTs on hydrophilicity and viscosity, it could influence PSU membrane performance through a similar mechanism. The initial increase and then decrease in the pore size could be caused by the combined effect of lowered thermodynamic stability and increased viscosity of the dope solutions (presented in Table 4.2) [20].

During this process, the rejection of HA is almost constant (above 98%) and the rejection of PR changed a little bit. Additionally, there seems to have a trade-off relationship between the water flux and the rejection of PR. The average molecular weight of the Aldrich humic acid as used in this study is larger than 50 kDa [46], so it is difficult for the HA molecules to permeate through the membrane. Besides, HA is

strongly negatively charged at a pH greater than 4.7 [47] due to the deprotonation of carboxylic and phenolic functional groups [48]. At pH 5.8, negatively charged PSU membrane [49] would reject the HA due to the electrostatic repulsion between the negatively charged HA and the membrane surface. These two combined effects made it possible to remove HA almost completely by using our HFM no matter with CNTs or not. For PR with a molecular weight of 615 Dalton, the size exclusion would be less important. However, it has a low pK_a value of 2.5 [50], which results in predominantly negatively charged membrane through two dissociated sulphonate groups [51] in the pH range studied. So the electrostatic repulsion between the negatively charged PR and the membrane surface could lead to the relatively high rejection of PR, which is around 65%, 75% and 85% for HFM15, HFM18 and HFM20, respectively.

After comparing the performances among the three types (HFM15, HFM18 and HFM20), it can be seen that increasing PSU concentration in the dope solution from 15 to 20 wt% reduced the pure water flux and also the MWCO. Using pristine membranes as examples, the pure water flux decreased from 36.1 ± 4.0 L/m^2h to 24.8 ± 0.5 L/m^2h, and then to14.1 ± 1.7 L/m^2h with PSU concentration increasing from 15 to 20 wt%. At the same time, the MWCO decreased from 39 kDa to 38 kDa and then to 33 kDa. In other words, the membrane sample becomes denser and less permeable with the increase in polymer concentration. This is consistent with our general understanding that the addition of more polymers to the dope solution increases its viscosity and lifts the precipitation path, thus promote more selective but less productive membranes [45, 52]. These flux losses are the result of thicker and denser skins and transition layers.

4.3.4 BSA fouling tests

The water flux profiles of membranes during BSA fouling tests are shown in Fig. 4.13. The ratios of final flux to their initial values are also presented as percentage in the same figure. After feeding with BSA solution, water fluxes decreased gradually with time for all membranes. The adsorption of BSA on the membrane surface and the formation of cake layer during the protein solution permeation [42] could explain the observed decrease in the water flux. Notably, except for HFM20-1.0%, all other membrane samples containing OMWNTs showed a higher initial water flux than their pristine membranes. This result is consistent with the previous pure water flux tests and further confirms the positive effects of CNTs on membrane permeability. Moreover, those CNTs-containing membranes also showed a higher ratio of final flux to initial flux. For example, the ratios for pristine membranes with different PSU contents are 61.9%, 67.1% and 57.1%, respectively, which are consistently lower than the ratios of membranes containing nanotubes prepared under respective PSU content (Fig. 4.14).

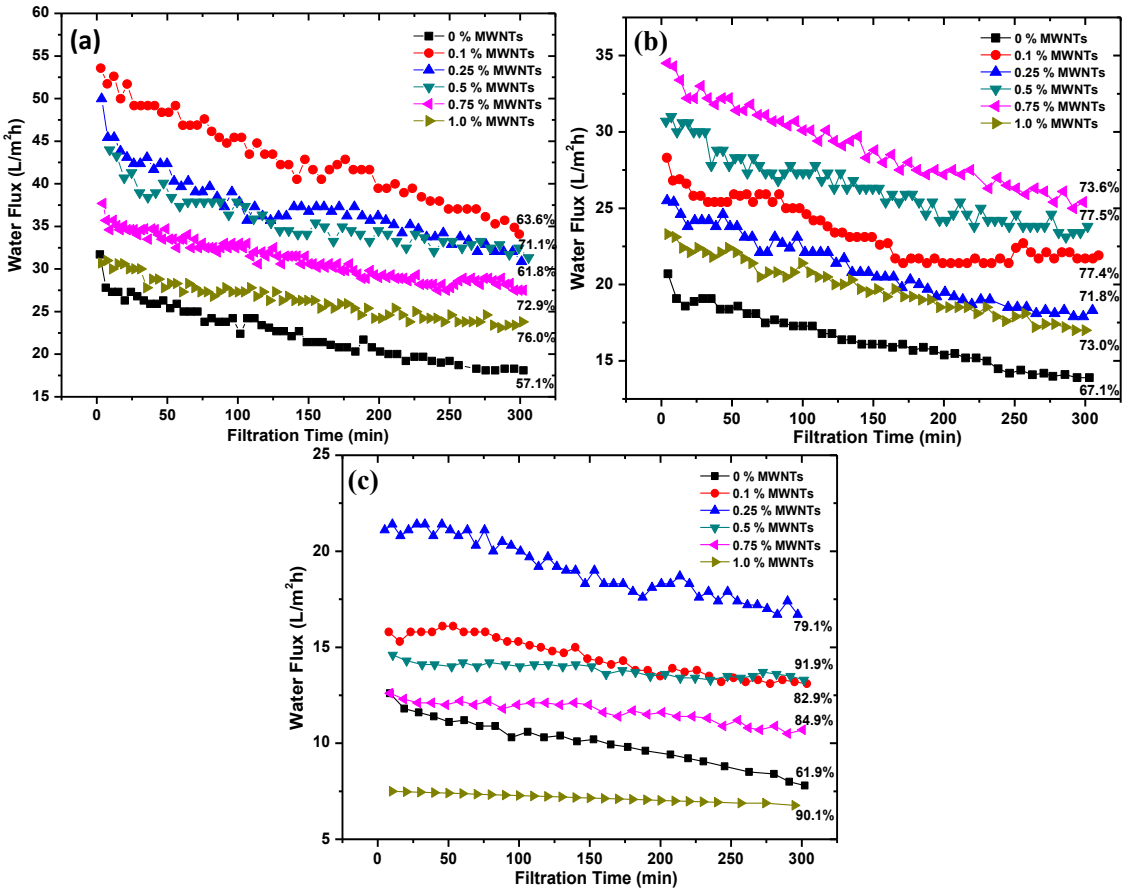

Fig. 4.13 Fouling behavior of HFM15 (a), HFM18 (b), and HFM20 (c) with filtration of BSA solution (1000 mg/L, pH~7.4, prepared with phosphate-buffered saline solution) at a TMP of 10 psi for 5 h.

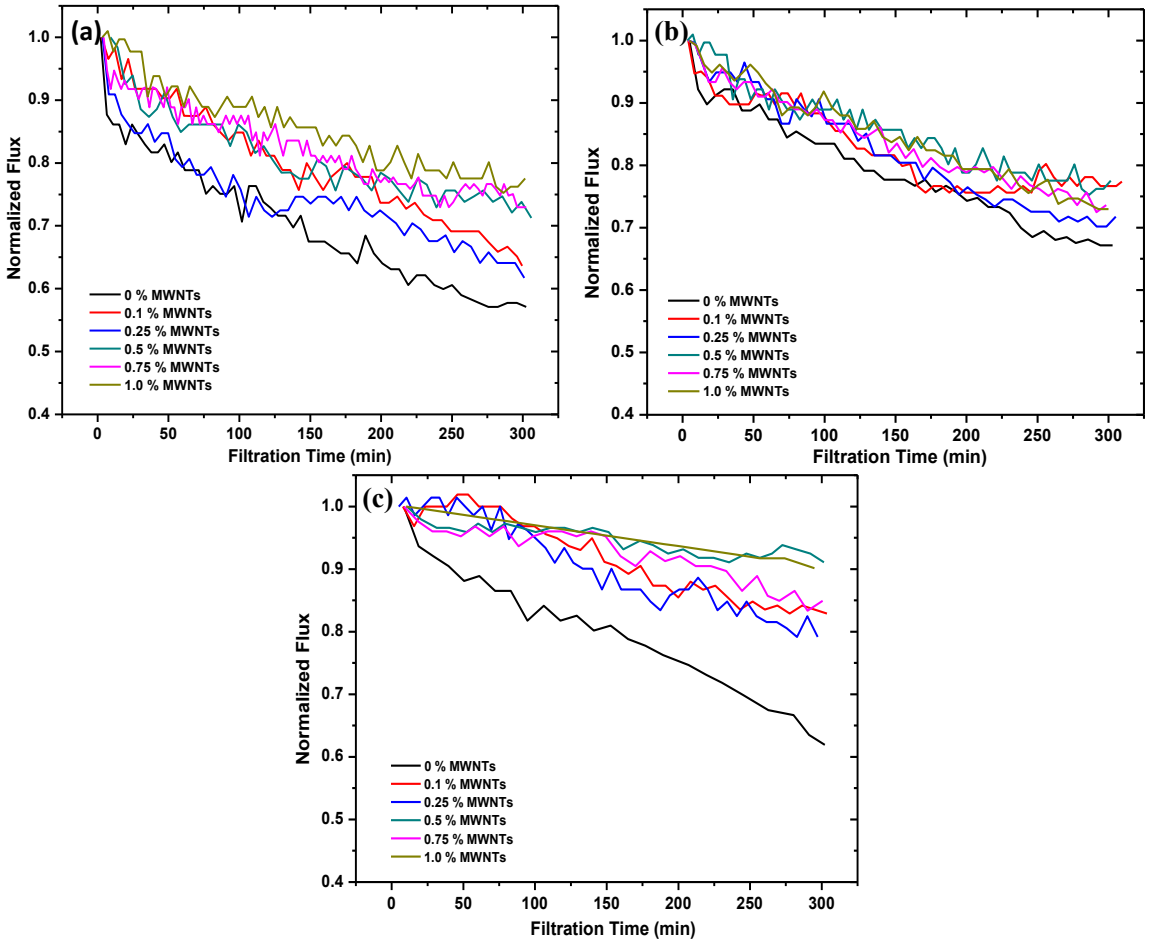

Fig. 4.14 Normalized fluxes of HFM15 (a), HFM18 (b), and HFM20 (c) in the fouling behavior test.

The degree of flux decline is usually indicative of the membrane fouling extent [53]. The less flux decline for membranes containing OMWNTs indicated that the nanocomposite membranes had an improved antifouling property for BSA. This could be due to the increased hydrophilicity of the membrane surface. Similarly for flat sheet PSU membranes containing MWNTs, Qiu et al. [13] found that introducing MWNTs reduced the adsorption of BSA on the membrane surface, thus the membranes could be used when it is necessary to avoid membrane fouling by protein adsorption.

4.4 Conclusions

This study has demonstrated that hollow fiber membranes containing CNTs can be fabricated following its purification and oxidation in a mixed acid. The incorporation of OMWNTs resulted in membranes with a uniform dark gray tint. The water contact angle of the nanocomposite membrane slightly decreased with increasing filler concentrations, which indicated the improved membrane surface hydrophilicity. The membrane surface showed a convex shape of pore size change with increasing OMWNTs concentration, which could be caused by the combined effect of lowered thermodynamic stability and increased viscosity of the dope solution introduced by the addition of hydrophilic nanotubes. Results of membrane performance tests indicated that at three different PSU concentrations (15, 18, 20 wt%), pure water flux of all membranes showed similar characteristics, with increasing filler concentrations, the flux first increased and then gradually decreased. This result on the water flux was consistent with the surface pore size measured. The optimized nanocomposite membranes showed a significant increase in pure water flux (60% to 100%) while maintaining the similar capability for solute rejection. In addition, the fouling resistance of the membrane to protein was enhanced as tested using BSA as the model foulant.

Acknowledgments

We gratefully acknowledge Dr. Mengshi Lin and Zhong Zhang in the Department of Food Science and Dr. Suchismita Guha and Danish Adil in the Department of Physics and Astronomy, all at University of Missouri (MU), for providing us access to the Raman spectroscopic instruments and analytical assistance. We also thank Professor Qingsong

Yu in the Department of Mechanical & Aerospace Engineering at MU for providing us access to the video contact angle measurement system.

References

[1] M.T. Byrne, Y.K. Guin'Ko, Recent advances in research on carbon nanotube - polymer composites, Advanced Materials, 22 (2010) 1672-1688.

[2] Z. Spitalsky, D. Tasis, K. Papagelis, C. Galiotis, Carbon nanotube-polymer composites: Chemistry, processing, mechanical and electrical properties, Progress in Polymer Science (Oxford), 35 (2010) 357-401.

[3] Y. Zhai, Y. Dou, D. Zhao, P.F. Fulvio, R.T. Mayes, S. Dai, Carbon materials for chemical capacitive energy storage, Advanced Materials, 23 (2011) 4828-4850.

[4] M. Scarselli, P. Castrucci, M. De Crescenzi, Electronic and optoelectronic nano-devices based on carbon nanotubes, Journal of Physics Condensed Matter, 24 (2012).

[5] P. Avouris, Z. Chen, V. Perebeinos, Carbon-based electronics, Nature Nanotechnology, 2 (2007) 605-615.

[6] D.W.H. Fam, A. Palaniappan, A.I.Y. Tok, B. Liedberg, S.M. Moochhala, A review on technological aspects influencing commercialization of carbon nanotube sensors, Sensors and Actuators, B: Chemical, 157 (2011) 1-7.

[7] T. Yamashita, K. Yamashita, H. Nabeshi, T. Yoshikawa, Y. Yoshioka, S.I. Tsunoda, Y. Tsutsumi, Carbon nanomaterials: Efficacy and safety for nanomedicine, Materials, 5 (2012) 350-363.

[8] Z. Liu, S. Tabakman, K. Welsher, H. Dai, Carbon nanotubes in biology and medicine: In vitro and in vivo detection, imaging and drug delivery, Nano Research, 2 (2009) 85-120.

[9] A. Kalra, S. Garde, G. Hummer, Osmotic water transport through carbon nanotube membranes, Proceedings of the National Academy of Sciences of the United States of America, 100 (2003) 10175-10180.

[10] H. Ma, K. Yoon, L. Rong, M. Shokralla, A. Kopot, X. Wang, D. Fang, B.S. Hsiao, B. Chu, Thin-film nanofibrous composite ultrafiltration membranes based on polyvinyl alcohol barrier layer containing directional water channels, Industrial and Engineering Chemistry Research, 49 (2010) 11978-11984.

[11] A. Tiraferri, C.D. Vecitis, M. Elimelech, Covalent binding of single-walled carbon nanotubes to polyamide membranes for antimicrobial surface properties, ACS Applied Materials and Interfaces, 3 (2011) 2869-2877.

[12] L. Zhanga, G.Z. Shia, S. Qiua, L.H. Cheng, H.L. Chen, Preparation of high-flux thin film nanocomposite reverse osmosis membranes by incorporating functionalized multi-walled carbon nanotubes, Desalination and Water Treatment, 34 (2011) 19-24.

[13] S. Qiu, L. Wu, X. Pan, L. Zhang, H. Chen, C. Gao, Preparation and properties of

functionalized carbon nanotube/PSF blend ultrafiltration membranes, Journal of Membrane Science, 342 (2009) 165-172.

[14] O.k. Park, N.H. Kim, K.t. Lau, J.H. Lee, Effect of surface treatment with potassium persulfate on dispersion stability of multi-walled carbon nanotubes, Materials Letters, 64 (2010) 718-721.

[15] P.S. Goh, B.C. Ng, A.F. Ismail, M. Aziz, Y. Hayashi, Pre-treatment of multi-walled carbon nanotubes for polyetherimide mixed matrix hollow fiber membranes, Journal of Colloid and Interface Science, (2012).

[16] S. Banerjee, T. Hemraj-Benny, S.S. Wong, Covalent surface chemistry of single-walled carbon nanotubes, Advanced Materials, 17 (2005) 17-29.

[17] K. Balasubramanian, M. Burghard, Chemically functionalized carbon nanotubes, Small, 1 (2005) 180-192.

[18] Z.L. Xu, F.A. Qusay, Polyethersulfone (PES) hollow fiber ultrafiltration membranes prepared by PES/non-solvent/NMP solution, Journal of Membrane Science, 233 (2004) 101-111.

[19] T.-S. Chung, J.-J. Qin, J. Gu, Effect of shear rate within the spinneret on morphology, separation performance and mechanical properties of ultrafiltration polyethersulfone hollow fiber membranes, Chemical Engineering Science, 55 (2000) 1077-1091.

[20] J.H. Choi, J. Jegal, W.N. Kim, Modification of performances of various membranes using MWNTs as a modifier, Macromolecular Symposia, 249-250 (2007) 610-617.

[21] Z. Wang, J. Ma, The role of nonsolvent in-diffusion velocity in determining polymeric membrane morphology, Desalination, 286 (2012) 69-79.

[22] L.Y. Jiang, T.S. Chung, C. Cao, Z. Huang, S. Kulprathipanja, Fundamental understanding of nano-sized zeolite distribution in the formation of the mixed matrix single- and dual-layer asymmetric hollow fiber membranes, Journal of Membrane Science, 252 (2005) 89-100.

[23] S.S. Madaeni, A. Rahimpour, Effect of type of solvent and non-solvents on morphology and performance of polysulfone and polyethersulfone ultrafiltration membranes for milk concentration, Polymers for Advanced Technologies, 16 (2005) 717-724.

[24] A.L. Ahmad, M. Sarif, S. Ismail, Development of an integrally skinned ultrafiltration membrane for wastewater treatment: Effect of different formulations of PSf/NMP/PVP on flux and rejection, Desalination, 179 (2005) 257-263.

[25] D.Y. Kang, H.M. Tong, J. Zang, R.P. Choudhury, D.S. Sholl, H.W. Beckham, C.W. Jones, S. Nair, Single-walled aluminosilicate nanotube/poly(vinyl alcohol) nanocomposite membranes, ACS Applied Materials and Interfaces, 4 (2012) 965-976.

[26] J. Yin, E.-S. Kim, J. Yang, B. Deng, Fabrication of a novel thin-film nanocomposite (TFN) membrane containing MCM-41 silica nanoparticles (NPs) for water purification, Journal of Membrane Science, 423–424 (2012) 238-246.

[27] W. Zhao, M. Li, Z. Zhang, H.X. Peng, EMI shielding effectiveness of silver nanoparticle-decorated multi-walled carbon nanotube sheets, International Journal of Smart and Nano

Materials, 1 (2010) 249-260.

[28] X. Jiang, J. Gu, X. Bai, L. Lin, Y. Zhang, The influence of acid treatment on multi-walled carbon nanotubes, Pigment and Resin Technology, 38 (2009) 165-173.

[29] W. Li, Y. Bai, Y. Zhang, M. Sun, R. Cheng, X. Xu, Y. Chen, Y. Mo, Effect of hydroxyl radical on the structure of multi-walled carbon nanotubes, Synthetic Metals, 155 (2005) 509-515.

[30] C. Velasco-Santos, A.L. Martínez-Hernández, V.M. Castaño, Silanization of Carbon Nanotubes: Surface Modification and Polymer Nanocomposites, 2011.

[31] A.M. Rao, P.C. Eklund, S. Bandow, A. Thess, R.E. Smalley, Evidence for charge transfer in doped carbon nanotube bundles from raman scattering, Nature, 388 (1997) 257-259.

[32] B.J.A. Tarboush, D. Rana, T. Matsuura, H.A. Arafat, R.M. Narbaitz, Preparation of thin-film-composite polyamide membranes for desalination using novel hydrophilic surface modifying macromolecules, Journal of Membrane Science, 325 (2008) 166-175.

[33] H. Deng, Y. Xu, Q. Chen, X. Wei, B. Zhu, High flux positively charged nanofiltration membranes prepared by UV-initiated graft polymerization of methacrylatoethyl trimethyl ammonium chloride (DMC) onto polysulfone membranes, Journal of Membrane Science, 366 (2011) 363-372.

[34] A.K. Ghosh, E.M.V. Hoek, Impacts of support membrane structure and chemistry on polyamide-polysulfone interfacial composite membranes, Journal of Membrane Science, 336 (2009) 140-148.

[35] J.J. Qin, J. Gu, T.S. Chung, Effect of wet and dry-jet wet spinning on the shear-induced orientation during the formation of ultrafiltration hollow fiber membranes, Journal of Membrane Science, 182 (2001) 57-75.

[36] L. Brunet, D.Y. Lyon, K. Zodrow, J.C. Rouch, B. Caussat, P. Serp, J.C. Remigy, M.R. Wiesner, P.J.J. Alvarez, Properties of membranes containing semi-dispersed carbon nanotubes, Environmental Engineering Science, 25 (2008) 565-575.

[37] N.A.A. Hamid, A.F. Ismail, T. Matsuura, A.W. Zularisam, W.J. Lau, E. Yuliwati, M.S. Abdullah, Morphological and separation performance study of polysulfone/titanium dioxide (PSF/TiO 2) ultrafiltration membranes for humic acid removal, Desalination, 273 (2011) 85-92.

[38] M. Mulder, Basic Principles of Membrane Technology, Kluwer Academic Publishers, Dordrecht, 1991.

[39] P. Pötschke, T.D. Fornes, D.R. Paul, Rheological behavior of multiwalled carbon nanotube/polycarbonate composites, Polymer, 43 (2002) 3247-3255.

[40] M. Abdel-Goad, P. Pötschke, Rheological characterization of melt processed polycarbonate-multiwalled carbon nanotube composites, Journal of Non-Newtonian Fluid Mechanics, 128 (2005) 2-6.

[41] W.Z. Lang, Z.L. Xu, H. Yang, W. Tong, Preparation and characterization of PVDF-PFSA blend hollow fiber UF membrane, Journal of Membrane Science, 288 (2007) 123-131.

[42] J.H. Li, Y.Y. Xu, L.P. Zhu, J.H. Wang, C.H. Du, Fabrication and characterization of a novel

TiO_2 nanoparticle self-assembly membrane with improved fouling resistance, Journal of Membrane Science, 326 (2009) 659-666.

[43] K.W. Lee, B.K. Seo, S.T. Nam, M.J. Han, Trade-off between thermodynamic enhancement and kinetic hindrance during phase inversion in the preparation of polysulfone membranes, Desalination, 159 (2003) 289-296.

[44] M.J. Han, S.T. Nam, Thermodynamic and rheological variation in polysulfone solution by PVP and its effect in the preparation of phase inversion membrane, Journal of Membrane Science, 202 (2002) 55-61.

[45] P. Van De Witte, P.J. Dijkstra, J.W.A. Van Den Berg, J. Feijen, Phase separation processes in polymer solutions in relation to membrane formation, Journal of Membrane Science, 117 (1996) 1-31.

[46] S. Hong, M. Elimelech, Chemical and physical aspects of natural organic matter (NOM) fouling of nanofiltration membranes, Journal of Membrane Science, 132 (1997) 159-181.

[47] F.J. Stevenson, Humus Chemistry: Genesis, Composition, Reactions, John Wiley & Sons, New York, 1982.

[48] Y. Furukawa, J.L. Watkins, J. Kim, K.J. Curry, R.H. Bennett, Aggregation of montmorillonite and organic matter in aqueous media containing artificial seawater, Geochemical Transactions, 10 (2009).

[49] A.W. Zularisam, A.F. Ismail, M.R. Salim, M. Sakinah, O. Hiroaki, Fabrication, fouling and foulant analyses of asymmetric polysulfone (PSF) ultrafiltration membrane fouled with natural organic matter (NOM) source waters, Journal of Membrane Science, 299 (2007) 97-113.

[50] A.R. Binupriya, M. Sathishkumar, S.H. Jung, S.H. Song, S.I. Yun, Bokbunja wine industry waste as precursor material for carbonization and its utilization for the removal of procion red MX-5B from aqueous solutions, Clean - Soil, Air, Water, 36 (2008) 879-886.

[51] A.R. Binupriya, M. Sathishkumar, C.S. Ku, S.I. Yun, Biosorption of Procion Red MX 5B by Bacillus subtilis and its extracellular polysaccharide: Effect of immobilization, Clean - Soil, Air, Water, 38 (2010) 775-780.

[52] N. Ali, H. Sofiah, A. Asmadi, A. Endut, Preparation and characterization of a polysulfone ultrafiltration membrane for bovine serum albumin separation: Effect of polymer concentration, Desalination and Water Treatment, 32 (2011) 248-255.

[53] Y. Hao, A. Moriya, T. Maruyama, Y. Ohmukai, H. Matsuyama, Effect of metal ions on humic acid fouling of hollow fiber ultrafiltration membrane, Journal of Membrane Science, 376 (2011) 247-253.

Support Information

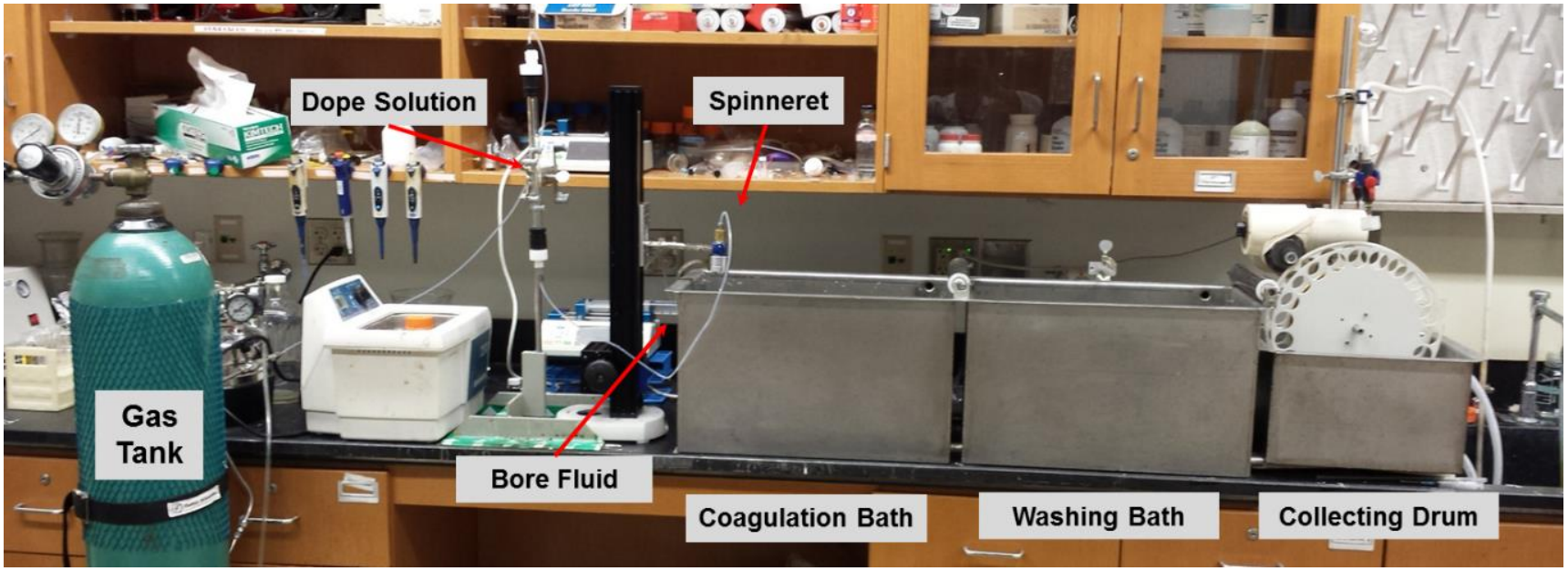

Fig. 4.1s A custom-designed single-head spinning machine

CHAPTER FIVE

Poly(vinylene fluoride) (PVDF)/nitrogen doped TiO_2 (N-TiO_2) nanocomposite hollow fiber membranes (HFMs) with advanced antifouling properties under visible light irradiation

Abstract

Nitrogen doped TiO_2 (N-TiO_2), a hydrophilic, visible light active photocatalyst, was applied to fabricate poly(vinylene fluoride) (PVDF)/ N-TiO_2 nanocomposite hollow fiber membranes (HFMs) through phase inversion method to improve filtration efficiency and antifouling property. The membranes were characterized by scanning electron microscopy (SEM), attenuated total reflection Fourier transform infrared (ATR FT-IR) spectroscopy, contact angle, UV-Vis absorbance, water uptake and molecular weight cut off (MWCO), and their performances were evaluated based on the water permeability, humic acid (HA) rejection and antifouling property. The resulting membrane showed brown color and an improved hydrophilicity, especially under light irradiation. Compared to original PVDF and PVDF/P25 membrane, nanocomposite membranes containing N-TiO_2 nanoparticles (NPs) showed clear photocatalytic activities under the visible light irradiation. In addition, membrane performance assessments indicated that PVDF/N-TiO_2 membranes possessed enhanced water flux, comparable HA rejection (above 96%), and improved fouling resistance when compared to the original PVDF membrane. These results have demonstrated that there is a great potential to use the methodology established here for developing membrane with an improved water permeability and superior antifouling properties, based on photodegradation process and photoinduced hydrophilicity enhancement driven by solar light as a renewable source of energy.

Keywords: Nitrogen doped TiO_2; PVDF; Nanocomposite membrane; Photocatalysis; Hydrophilicity; Antifouling

5.1 Introduction

The pioneering paper of Fujishima and Honda [1] on water splitting paved the way to tremendous researches and studies of titanium dioxide (TiO_2). Now, TiO_2 has been widely used for water splitting, water treatment, air purification and self-cleaning of surfaces because of its unique photocatalytic properties, stability, commercial availability, and ease of preparation [2, 3]. In correlation with increasing awareness to environmental issues, TiO_2 is considered to be an ideal choice as catalyst for water treatment due to the high oxidation power, photo-induced hydrophilicity, long-term photostability, high transparency in the visible range, good thermal and chemical stability, and non-toxicity [4]. However, the main technical barriers that hinder its commercialisation remained on the requirement of high energy input (UV light) to implement photodegradation and post-recovery of the catalyst particles after water treatment [5].

As a result of its relatively large band gap of 3.2 eV, TiO_2 (anatase) can only be activated by UV light which has a wavelength shorter than 380 nm [6]. So TiO_2 itself can only take advantage of 3-4% of the solar energy that reaches the earth [7]. Hence, many attempts have been devoted to prepare TiO_2 photocatalyst which can be activated under visible light with reasonable efficiency, such as dye sensitization [8, 9], noble metal deposition [10, 11], metal or non-metal doping [6, 12, 13]. Since the discovery of N-doped TiO_2 with a visible light absorption by Asahi et al. [14], great attention has been given to modify the electronic band gap of TiO_2 by doping method. Various elements (N [15, 16], F [17], S [18, 19], Fe [20], Co [21], Cr [22], Cu [23], Mn [24], and etc.) have been studied to enhance photocatalytic performance of TiO_2 in the visible region.

Compared to the other nonmetal elemental doping, N-doped TiO_2 materials exhibit a significant photocatalytic activity under visible light irradiation, probably because N 2*p* states mix with O 2*p* states, due to the fact that their energies are very close [14, 25].

Many researchers coupled TiO_2 photocatalysis with membrane separation to solve the post-recovery issue. For example, Xi and Geissen [26] reported the separation of TiO_2 from water by cross-flow microfiltration (MF) within wastewater treatment by photocatalysis using slurry reactor systems. In their study, the separation efficiency was strongly affected by cross-flow velocity, transmembrane pressure (TMP), feed concentration, pH of suspension and ionic strength. Le-Clech et al. [27] reported that a hybrid photocatalysis-PVDF MF membrane process was effective as a polishing treatment of surface water containing low concentration of natural organic matters. During the process, the membrane could totally reject the TiO_2 slurry particles and separate them from the treated water.

Due to the hydrophilic properties of TiO_2, the incorporation of this type of NPs into the membrane structure could enhance the composite material affinity to the water and hence the membrane water permeation and fouling resistance [28, 29]. So combining TiO_2's unique properties with membrane technology through integrating TiO_2 with membrane seems to be a great opportunity for advanced water treatment. This integrating technology not only keeps the characteristics and capacity of these two technologies, but also produces some synergistic effects to overcome the drawbacks of the single technology [30]. Firstly, the pollutants could be oxidized by the photocatalysis, while the membranes show the capability not only to retain the photocatalyst but also to partially reject organic species by controlling the residence time in the reacting system. That is to

say the membrane also works as a selective barrier for the targeted molecules, thus this technology could enhance the photocatalytic efficiency and achieve excellent effluent quality. Secondly, the integrating technology could solve or mitigate the problem of flux decline associated with membrane fouling [26]. Because TiO_2 particles on the membrane surface not only increase membrane hydrophilicity but also create photocatalytic property, which prevents the formation of cake layer and blocking of membrane pores. Thereby membrane life could be extended.

Generally, there are two main approaches for the fabrication of TiO_2 nanocomposite membranes: (1) depositing NPs onto membrane surface and (2) blending the NPs into the membrane.

In the depositing approach, TiO_2 NPs are coated or grafted on membrane surface. For example, Kuak et al. [31] and Kim et al. [32] prepared one kind of hybrid composite membrane by self-assembly of TiO_2 NPs through interaction with the COOH functional group of an aromatic polyamide thin-film layer. The membrane possessed excellent anti-bacterial effect on *E. coli* and good antifouling properties under UV light irradiation. Bae and Tak [33] immobilized the TiO_2 NPs on membrane surface by dipping method to increase the surface hydrophilicity for the filtration of mixed liquor from a membrane bioreactor (MBR). The results showed that membrane fouling was considerably mitigated though the flux still declined to some extent.

In the blending approach, TiO_2 NPs are dispersed in a casting solution and then membranes are cast by phase inversion method which was widely used for the preparation of polymeric membranes. For example, Bae and Tak [34] entrapped TiO_2

NPs into polymeric membrane to mitigate fouling of active sludge filtration. Wu et al. [35] prepared Polyethersulfone (PES)/TiO_2 composite membranes which showed enhanced hydrophilicity, thermal stability, mechanical strength and antifouling ability. TGA and mechanical strength analyses also indicated good compatibility between polymers and TiO_2 NPs. To avoid agglomerations and also to improve the stability of particles in the casting solution, Razmjou et al. [36] modified Degussa P25 TiO_2 NPs by a combination of chemical and mechanical methods for fabricating ultrafiltration (UF) membranes. The incorporation of modified NPs into PES UF membranes showed a significant improvement in fouling resistance and the increase in hydrophilicity was the most likely reason for improvement in antifouling performance. Compare to depositing approach the blending approach is simpler since the particles are added to the casting solution. Furthermore, coating of membranes can lead to some significant undesirable changes in membrane permeability due to pore narrowing or plugging and the potential delamination of coating layer is also a concern [36].

Here, we propose to synthesize nitrogen-doped TiO_2 NPs and then use blending approach to fabricate PVDF/N-TiO_2 nanocomposite HFMs which could be activated by visible light. Considering the existence of light irradiation and oxidation environment during the filtration process, PVDF was selected as membrane material due to its superior mechanical, chemical, and thermal stabilities, as well as outstanding antioxidation, corrosion resistance, and membrane-forming properties [37, 38]. By this way, hydrophilicity and photocatalytic function of TiO_2 could be introduced into the membrane system. Enhanced water permeability and fouling resistance are expected.

5.2 Materials and methods

5.2.1 Materials

During the synthesis of N-TiO_2 NPs, tetrabutyl titanate ($Ti(OBu)_4$, 97%, Aldrich) was used as titania precursor and ammonia aqueous solution (28 - 30%, Aldrich) was used as nitrogen source. PVDF with an average molecular weight (Mw) of 180 kDa was obtained from Sigma-Aldrich and dried for 3 h at 120 ℃ before usage. The 1-Methyl-2-pyrrolidinone (NMP, 99.5%, Aldrich) was selected as solvent. And polyvinylpyrrolidone (PVP, Aldrich) with average Mw of 10 kDa was used as porogen. All other chemicals were obtained from Sigma-Aldrich and were of ACS reagent grade. The reference titania (Degussa P25) was obtained from Degussa Corporation, Germany. Deionized water (DI) produced by Millipore DI system (Synergy 185, 18.2 MΩ·cm) was used for solution preparation and filtration study.

5.2.2 Synthesis and characterization of N-TiO_2 NPs

A method modified from literature [39] was used here to synthesis N-TiO_2 NPs. Briefly, a 10 ml ammonia aqueous solution was added dropwise into 20 ml $Ti(OBu)_4$ solution at room temperature under stirring to carry out hydrolysis. After continuously stirring for 10 min, the precursor was dried in an oven at 120 ℃ for 2 h. Finally, the TiO_2 precursor was calcinated at 400 ℃ for 1 h to obtain N-TiO_2 NPs, where the color of sample powder changed from white to brown.

Morphology and particle size of NPs were examined by SEM (Quanta FEG 600, FEI Company, Hillsboro, OR) and TEM (JEM 1400, JEOL Ltd., Peabody, MA). SEM specimen was prepared by dropping NPs-ethanol mixture suspension onto a silicon

wafer. After complete drying at room temperature, the specimen was coated with platinum by a sputter coater (K575x, Emitech Ltd., Kent, England) at 20 mA for 60 s. TEM samples were prepared by dropping the same suspension onto carbon coated copper grid and drying at the room temperature.

5.2.3 Spinning of hollow fiber membranes

The PVDF/N-TiO_2 nanocomposite HFMs were fabricated by the phase inversion method on a custom-designed single-head spinning machine based on our previous work [40]. To make dope solution, a certain amount of N-TiO_2 was dispersed in NMP solvent and sonicated for 1 h to achieve good dispersion. And then PVP was added into the mixture and stirred for 30 min. Finally, PVDF was added and stirred for 6 h at 50 ℃ to form dope solution. The dope solution was kept overnight for degassing prior to use.

The collected fibers were rinsed in the DI water at room temperature for at least 24 h to remove the residual solvent, and then immersed in a 25 wt% glycerol aqueous solution for another 24 h before drying in the ambient environment. Experimental parameters of spinning process were listed in Table 5.1. The membranes containing various amount of N-TiO_2 were labeled as PVDF/NT-x, where x stands for the concentration of NPs. For example, if a membrane sample possessed 2.5 wt% N-TiO_2, this membrane was named PVDF/NT-2.5.

Table 5.1 Spinning conditions of PVDF HFMs

Parameter	Condition
Spinneret OD/ID	1.0 mm/0.6 mm
Spinneret temperature (℃)	25
Dope solution	PVDF/PVP/NMP
Concentration (wt%)	16/5/79
Dope solution flow rate	1.0
Bore fluid composition	DI water
Bore fluid flow rate (mL/min)	0.8
Range of air-gap distance (cm)	0
Coagulant	Tap water
Coagulant temperature (℃)	25
Washing bath	Tap water
Washing bath temperature (℃)	25
Take-up speed (cm/min)	360

5.2.4 Photocatalytic properties of N-TiO_2 NPs and HFMs

A 300 W xenon lamp was used as the light source with a 400 nm glass filter to cutoff the UV light. In each run, 50 ml Methyl Orange (MO) aqueous solution (10 mg/L) with 25 mg sample powders was loaded in a glass container and stirred with a magnetic stirrer under 100 rpm. After ultrasonication for 5 min and stirring for 10 min, the light was turned on to initiate the reaction. Another light source with four full spectrum fluorescent lights (32W, Philips F32T8) was used to simulate sunlight to evaluate the photocatalytic properties of N-TiO_2 NPs. During the test, temperature of the solution was maintained at 23 ± 1 ℃. For HFM, membranes with length of 300 cm was cut into small pieces and mixed with 50 ml MO solution (10 mg/L) in a glass container for 24 h at dark condition. And then the light was turned on to initiate the reaction. Temperature of the solution was also maintained at 23 ± 1 ℃.

The spectrum of light source was recorded by a spectrometer (PC2000, Ocean Optics, Dunedin, FL) with a resolution of 1.5 nm and an entrance slit of 25 μm and

presented in Fig.5.1s. Furthermore, the light power was analysed by a calorimeter (Astral^{TM} AC5000, Scientech, Boulder, CO) connected to a Scientech power meter (Astral^{TM} AA30) under the same condition of photocatalytic reaction.

5.2.5 Membrane characterization and performance assessment

Membrane surface and cross-section were characterized by SEM on Quanta FEG 600. The sample of membrane surface was obtained by drying a piece of membrane at room temperature, while the cross-section was obtained by freeze-fracturing of the membranes in the liquid nitrogen. These specimens were coated with platinum at 20 mA for 60 s prior to imaging. Hydrophilicity of membrane surface was determined by measuring the pure water contact angle based on the sessile drop method. A video contact angle system (VCA-2500 XE, AST products, Billerica, MA) was employed to perform the test. At least eight stabilized contact angles from different sites of each sample were obtained to calculate the average contact angle and standard deviation. The functional groups of membrane surface were identified by Fourier transform infrared (FT-IR) spectroscopy on Nicolet 4700 FT-IR (Thermo Electron Corp., Waltham, MA). All spectra included the wave numbers from 500 to 4000 cm^{-1} with 128 scans at a resolution of 1.0 cm^{-1}. Membrane samples were also subjected to an UV-Vis absorbance characterization using a UV-Vis recording spectrophotometer (UV2401PC, Shimadzu Corp., Japan) from 190 to 900 nm and a clean PVDF membrane was used as the reference sample.

A low pressure cross-flow filtration system modified from our previous work [40] was used to evaluate pure water flux, solute rejection, molecular weight cut off (MWCO), and fouling resistance of the membranes. The membrane module made with quartz tube

was sealed by epoxy resin, with an effective membrane area of around 10 cm^2. A schematic diagram of the filtration system is shown in Fig. 5.1.

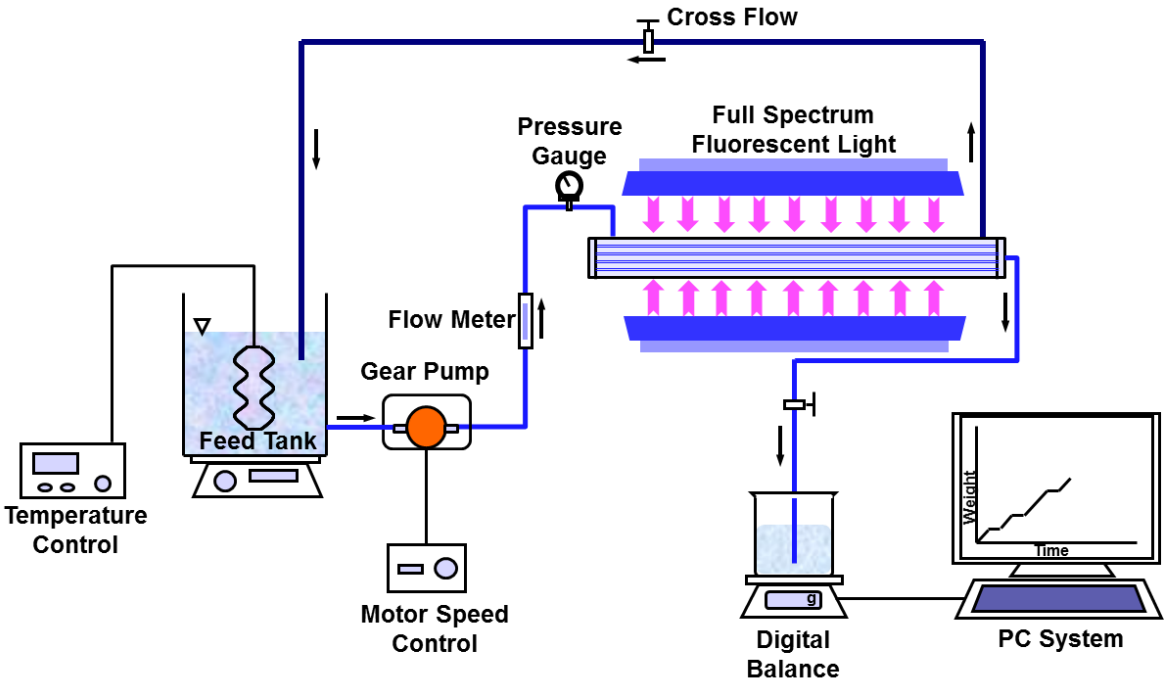

Fig. 5.1 Schematic diagram of the hollow fiber membrane filtration system

Prior to test, each membrane was compressed by DI water at a constant TMP of 6 psi for 3 h. Pure water flux was measured by weighing the permeate water as a function of time, and recorded by a LabVIEW automated system (National Instruments LabVIEW 8.2 with Ohaus digital balance). After the flux test, feed solution containing 20 mg/L of humic acid (HA, prefiltered with a 0.45 μm filter, Aldrich) was filtrated and solute concentrations of feed and permeate solutions were measured using a UV-visible spectrophotometer (Lambda 25, PerkinElmer, Waltham, MA) at a wavelength of 254 nm. Three light irradiation conditions were applied here: dark, visible light (F32T8 fluorescent lights, 10.9 mW/cm^2, Philips), UV light (602654 LPHO, 13.1 mW/cm^2, Trojan Technologies, Canada). Light irradiation was implemented 30 min prior to the HA

filtration tests and maintained until the end of tests. During the tests, HA solution was first filtrated for 180 min (Cycle 1), then feed solution was changed to DI water and filtrated for 30 min (Wash). After wash, HA solution was feed again for another 180 min (Cycle 2) and followed by DI water wash for 30 min. The flux and rejection was calculated with Equation (1) and Equation (2), respectively:

$$J = \frac{V_p}{A \cdot t} \tag{1}$$

$$R = \left(1 - \frac{C_p}{C_f}\right) \times 100 \tag{2}$$

where, J is the water flux (L/m^{2}h), V_p the permeate volume (L), A the membrane area (m^2) and t the treatment time (h). R is the rejection ratio and C_p and C_f are the concentrations of permeate and feed solution, respectively.

MWCO values of membranes were evaluated by determining the rejections of PVP (10, 40 and 360 kDa), BSA (67 kDa) or Poly(ethylene oxide) (PEO, 100 kDa) under a solution concentration of 1000 mg/L. The MWCO of a particular membrane was defined as the molecular weight of the solute which had a 90% rejection. The concentrations of PEO and PVP were measured by a TOC analyzer (TOC-5000, Shimadzu Corp., Japan), while the concentrations of BSA were determined on a UV-visible spectrophotometer at 280 nm.

5.3 Results and discussion

5.3.1 Characterization and photocatalytic properties of synthesized N-TiO_2 NPs

Synthesized N-TiO_2 NPs showed an average particle size of around 50 nm (Fig. 5.2b) and a BET surface area of 197 m^2/g, which are consistent with results reported by Wang et al. [39]. N-TiO_2 NPs exhibited strong photocatalytic capability under visible light irradiation (436.9 mW/cm^2, Fig. 5.2c). It can degrade MO (10 mg/L) over 98% within 3 h. When using fluorescent light as the light source, it still can degrade MO (10 mg/L) around 85% within 6 h (18.3 mW/cm^2, Fig. 5.2d).

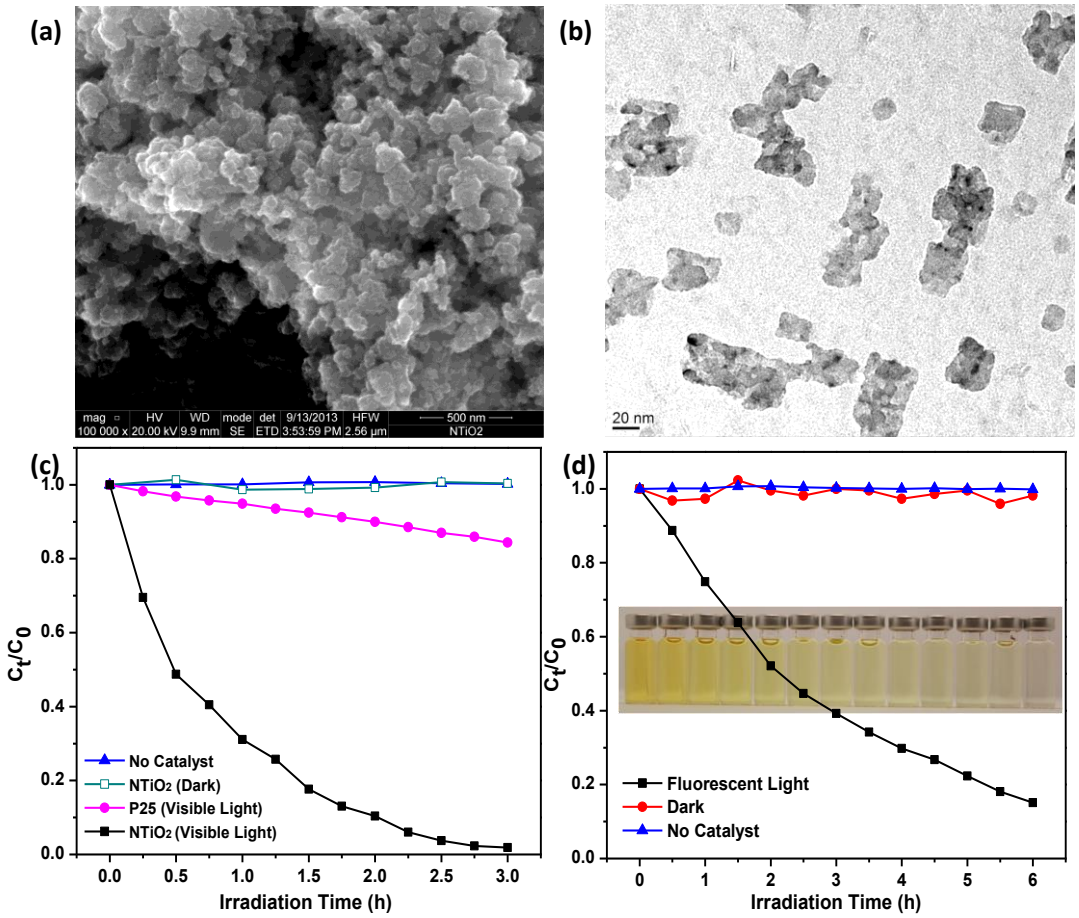

Fig. 5.2 Microscopic images and photocatalytic properties of N-TiO_2: (a) SEM image, (b) TEM image and photocatalytic activities under visible light irradiation (c) or under fluorescent light irradiation (d). For photocatalytic reaction, 25 mg N-TiO_2 was suspended in 50 mL MO solution containing MO of 10 mg/L.

5.3.2 Characterization of PVDF/N-TiO_2 membrane

As shown by Fig. 5.3(A1-D1), the original PVDF membrane showed white color, whereas the incorporation of N-TiO_2 NPs resulted in a uniform brown tint of the membranes. The brown color increased with increasing loading concentration. The uniformity of membrane colors indicated the existence of N-TiO_2 NPs inside the membrane matrix and also suggested a good dispersion of these materials. The SEM images (Fig. 5.3(A2-D2)) showed that all membranes had an outside diameter of around 900 μm, and some particles could be observed on the surfaces of nanocomposite membranes (Fig. 5.3(A3-D3)). Higher magnification images were also inserted in the upper right corner of A3-D3 to reveal the surface pore size change.

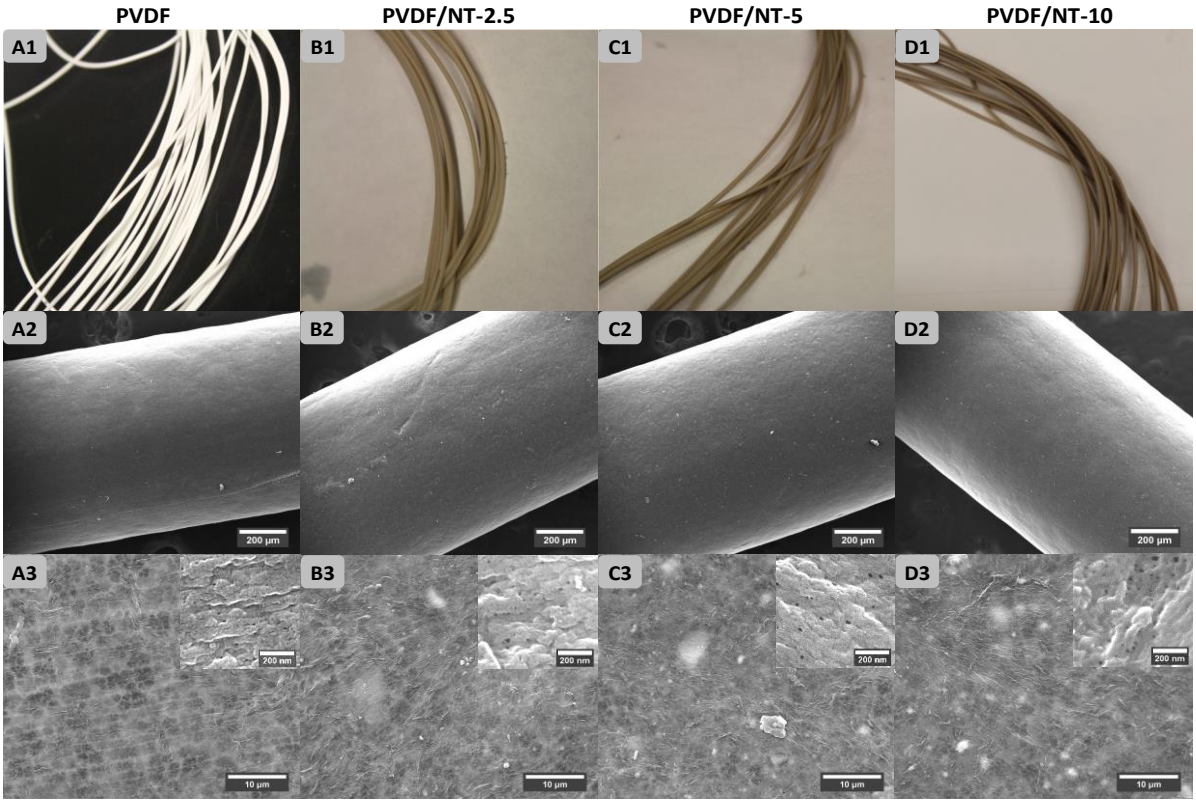

Fig. 5.3 Digital photos and SEM images of PVDF/N-TiO_2 membranes: (A1-D1) Digital photos, (A2-D2) SEM images with magnification of 200×, (A3-D3) SEM images with magnification of 5000×. Higher magnification images were inserted in the upper right corner of A3-D3 to reveal the surface pore size.

EDX mapping scanning spectra of PVDF/NT-5 membrane corresponding to carbon (C), nitrogen (N), fluorine (F), and titanium (Ti) elements, respectively, are shown in Fig. 5.4. Except the C and F elements from PVDF, Ti and N elements were also detected and showed uniform distribution along the membrane cross-section, indicating the successful incorporation of N-TiO_2 NPs inside polymer matrix. The distribution of TiO_2 on membrane surface was also analyzed and presented in Fig. 5.2s. The result further demonstrated the well distribution of N-TiO_2 NPs on PVDF/NT-5 membrane surface. The actual amount of NPs incorporated inside the polymer matrix was further evaluated by burning the membrane under 800 ℃ for 2 h inside a muffle furnace with exposure to atmosphere and weighing the residue. The results showed that the NPs concentration were 0.15 ±0.32%, 1.67 ±0.09%, 3.78 ±0.16% and 6.77 ±0.24% for PVDF, PVDF/NT-2.5, PVDF/NT-5 and PVDF/NT-10, respectively, indicating that most of the input NPs remained inside the membrane matrix after the phase inversion and washing processes.

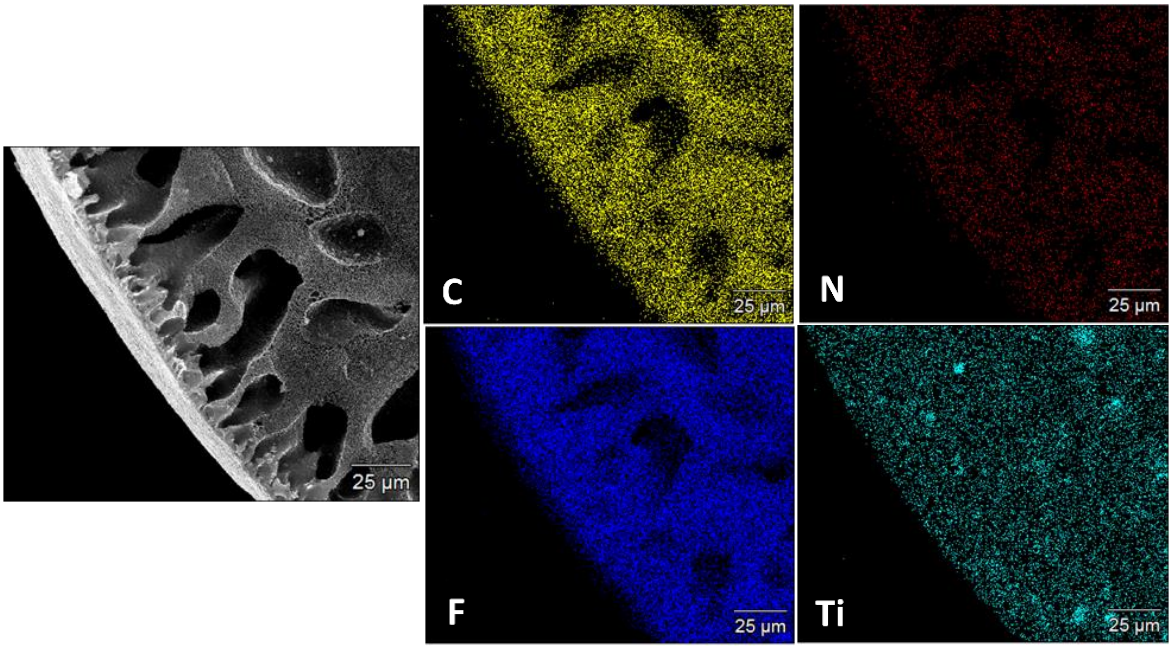

Fig. 5.4 SEM image and corresponding EDX mapping scanning spectra of PVDF/NT-5

The ATR FT-IR spectra of PVDF and PVDF/N-TiO_2 HFMs are shown in Fig. 5.5a. The strong absorption band at around 1180 cm^{-1} and 1402 cm^{-1} could be regarded as characteristic of CF_2 and CH_2 stretching mode, respectively in PVDF [41]. Meanwhile, the increased absorption band from the base line between 590 and 770 cm^{-1} could be attributed to the stretching vibration of Ti-O-Ti and Ti-O band [42], which indicated the existence of TiO_2 inside the membrane structure.

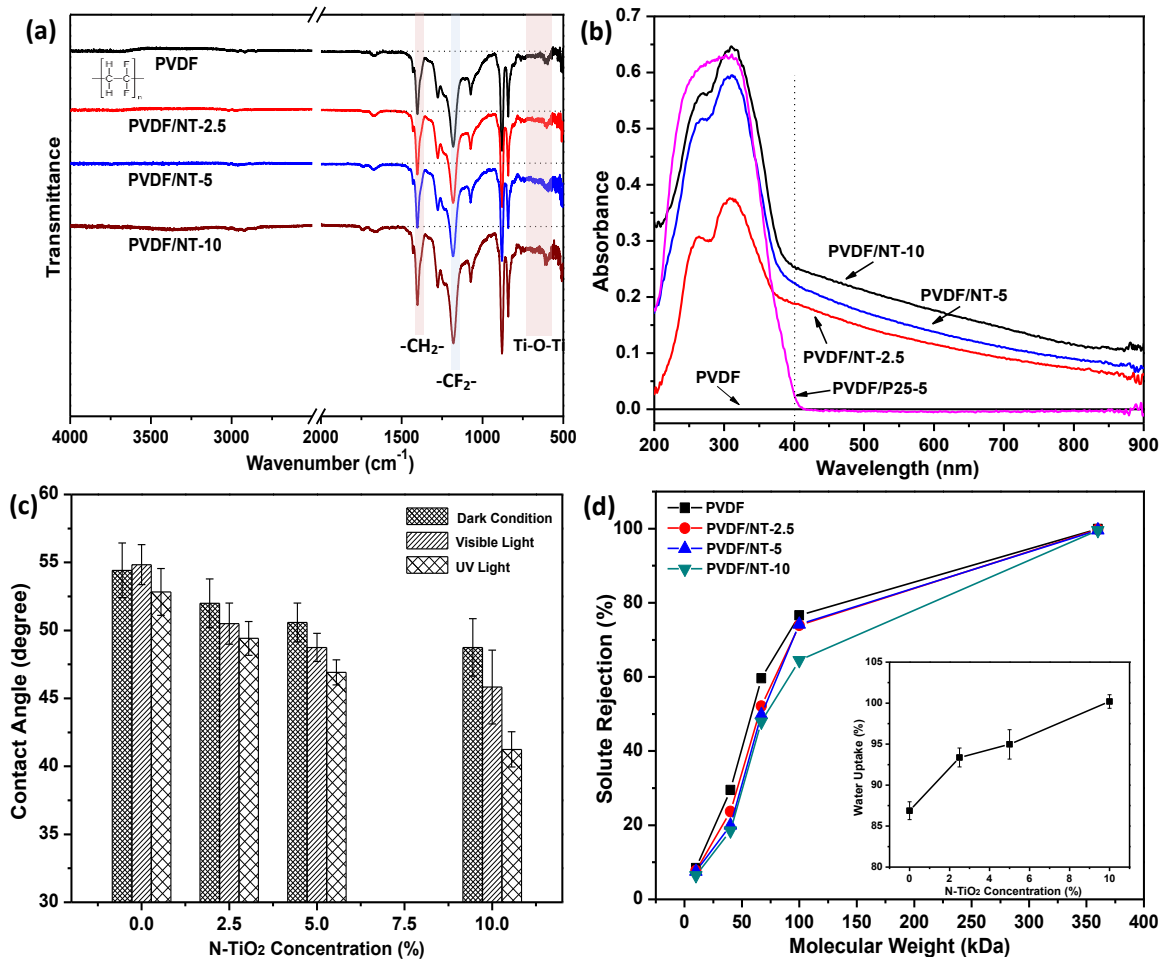

Fig. 5.5 Characterizations of PVDF/N-TiO_2 membranes: (a) ATR FT-IR, (b) UV-Vis absorbance, (c) Contact angle, and (d) MWCO and water uptake.

UV-Vis absorbances of membrane samples are presented in Fig. 5.5b. Except the strong absorbance in the UV range, the N-TiO_2 incorporated membrane also showed a clear absorbance in the visible range, which indicated the potential photocatalytic activity of the nanocomposite membrane under visible light irradiation. The absorbance also increased with increasing N-TiO_2 concentration, indicating more NPs located on top layer of membrane when increase loading concentration. As a comparison, membrane incorporated with 5% P25 NPs showed a clear absorbance in the UV range, while no obvious absorbance was observed in the visible range.

As presented in Fig. 5.5c, under dark condition, the contact angle of membranes decreased from $54.4 \pm 2.0°$ to $52.0 \pm 1.8°$, $50.6 \pm 1.4°$, and then to $48.9 \pm 2.1°$ with increasing NPs concentrations from 0 to 10%, which could be attributed to the hydrophilicity of TiO_2 located on membrane surface. Similarly, Yu et al. [38] and Rahimpour et al. [43] also observed the decrease of contact angle after blending TiO_2 NPs inside the polymeric membrane and attributed this change to the hydrophilicity of incorporated NPs. When irradiate membranes with visible light or even UV light for 30 min, the contact angle of nanocomposite membrane further decreased, although the change was not that significant.

Fig. 5.5d shows the results of water uptake and MWCO. The water uptake increased from $86.7 \pm 1.1\%$ to $100.2 \pm 0.8\%$ with increasing NPs loading from 0 to 10%. Meanwhile the MWCO increased after embedding NPs, where PVDF showed higher rejection regarding five tested molecules with different Mw (10, 40, 67, 100 and 360 kDa). With increasing NPs loading, solute rejections decreased, indicating membrane became more porous and loose. For example, the rejection for molecule (100 kDa)

decreased from 76.6 % for PVDF membrane to 64.5% for PVDF/NT-10. This is also consistent with the surface pore size presented previously in Fig. 3(A3-D3). When studied the effects of TiO_2 NPs on the surface chemistry, structure and fouling performance of PES UF membranes, Razmjou et al. [36] observed that after embedding 10-12.5% TiO_2 into PES matrix, the MWCO of membranes shifted from 100 kDa to around 240 kDa. It is believed that thermodynamic immiscibility induced by the addition of hydrophilic TiO_2 could lead to the enhanced phase separation, which could further lead to a more porous and permeable membrane.

5.3.3 Photocatalytic properties of PVDF/N-TiO_2 membrane

Photocatalytic properties of the nanocomposite membranes under visible light irradiation were also evaluated here (Fig. 5.6). N-TiO_2 incorporated membranes showed clear activities under the visible light irradiation. For PVDF/NT-10, a 79% removal rate of MO could be achieved within 16 h, whereas the PVDF/NT-2.5 and PVDF/NT-5 showed a removal rate of 49% and 64%, respectively, under the same irradiation condition. As comparison, original PVDF membrane showed no obvious effect on MO concentration, while membrane incorporated with 5% P25 showed a much lower removal rate of around 10%. These results indicated that incorporation of N-TiO_2 provided membranes with photocatalytic properties against organic materials under visible light irradiation.

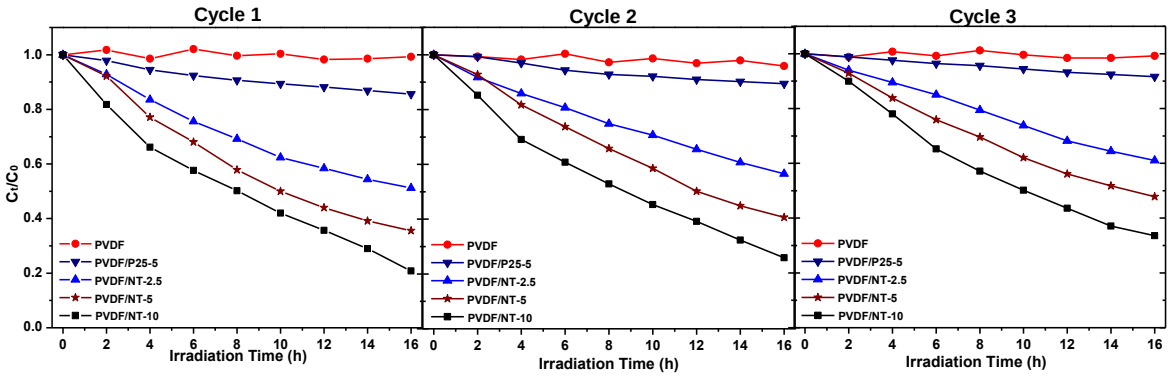

Fig. 5.6 Photocatalytic activities of PVDF/N-TiO_2 membranes under visible light irradiation. Membranes with length of 300 cm were cut into small pieces and suspended in 50 mL MO aqueous solution.

Further cycles were carried out to evaluate the stability of photocatalytic properties. During the subsequent cycles, the photocatalytic activities of nanocomposite membrane gradually decreased. In cycle 3, PVDF/NT-2.5, PVDF/NT-5 and PVDF/NT-10 showed a removal rate of 39%, 52% and 66%, respectively. The decreased photocatalytic activities could be attributed to the loss of N-TiO_2 NPs from membrane surface during the photodegradation process where mixing was implemented. However, the membranes still can maintain relatively high photocatalytic activities after three cycles of irradiation.

5.3.4 Membrane performance

The pure water fluxes of all membranes as a function of TMP are shown in Fig. 5.7a. The original PVDF membrane showed a water flux at 106 ± 4 L/m^2h under 6 psi. All other membranes showed higher pure water flux and the water flux gradually increased with increasing loading concentration. For example, under the same TMP of 6 psi, water fluxes were 144 ± 4, 155 ± 5 and 163 ± 6 L/m^2h for PVDF/NT-2.5, PVDF/NT-5 and PVDF/NT-10, respectively. This is consistent with contact angle, water uptake and

MWCO results, which could be caused by the increased surface hydrophilicity and porosity of membrane after embedding N-TiO_2 NPs.

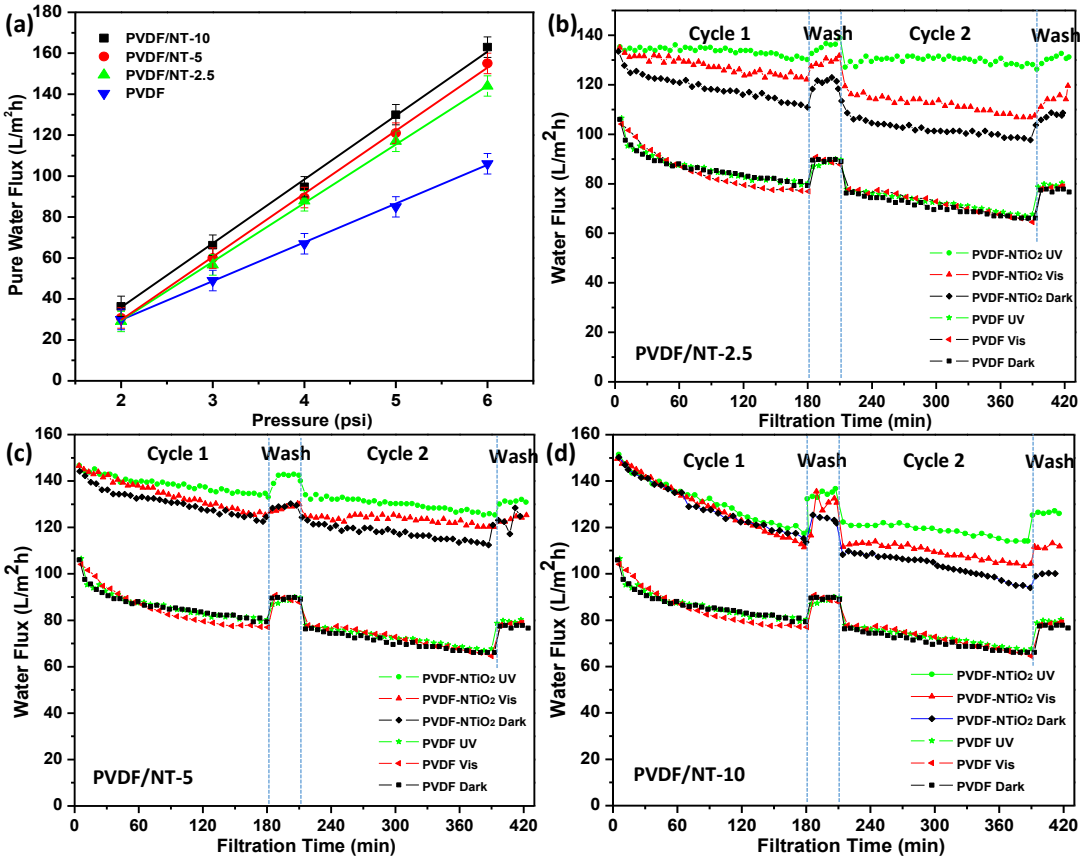

Fig. 5.7 Pure water flux (a) and fouling behaviors of membrane samples under various irradiation conditions: (b) PVDF/NT-2.5; (c) PVDF/NT-5; (d) PVDF/NT-10. Original PVDF membrane was used as a reference here. Fouling test conditions: concentration of HA feed solution was 20 mg/L; TMP was 6 psi; temperature was 23 ± 1 ℃.

Further experiments were carried out by using HA as the model foulant to evaluate the fouling behaviors of membrane samples under various irradiation conditions (dark, visible light or UV irradiation). During the test, all membrane samples with or without N-TiO_2 showed a good rejection to HA (above 96%). As presented in Fig. 5.7b, original PVDF membrane showed similar fouling behaviors with or without light irradiation,

whereas PVDF/NT-2.5 membrane showed improved fouling resistance under visible light irradiation, no matter in cycle one or cycle two. Once UV light was applied, the fouling resistance of membrane was further improved. Even under dark condition, N-TiO_2 incorporated membrane still showed higher water flux and fouling resistance than PVDF membrane, which could be attributed to the enhanced surface hydrophilicity provided by TiO_2 NPs. Same trend was also observed for PVDF/NT-5. Similar phenomenon was observed by Zhang et al. [44], who applied TiO_2 nanowire membrane for HA removal. They found the TMP of membrane increased slightly at the initial stage and then kept constant with UV irradiation, whereas, without of UV irradiation, TMP continuously increased and even sharply increased after 7 h of filtration. They attributed this phenomenon to the photocatalytic degradation of HA on membrane surface which activated by the UV irradiation.

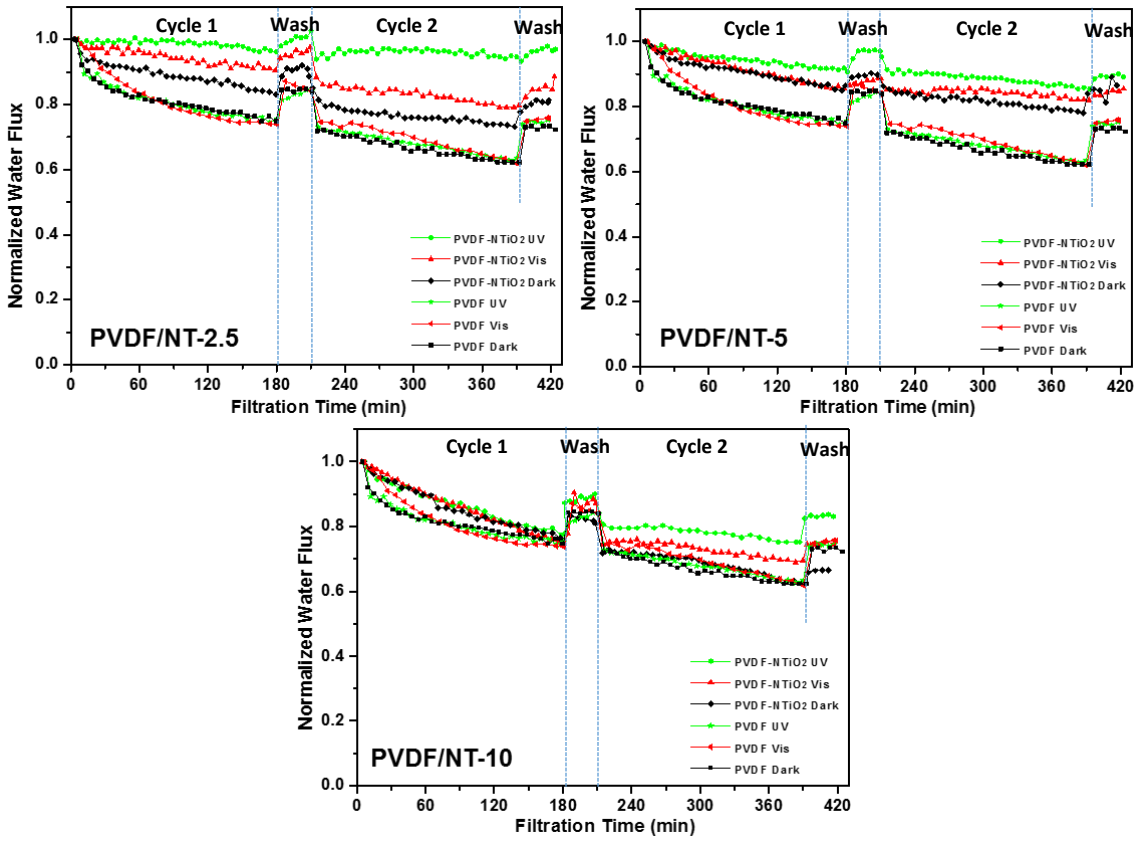

Fig. 5.8 Normalized water fluxes of membrane samples during the fouling behavior tests.

Interestingly, the first cycle of PVDF/NT-10 showed no obvious difference under different irradiation conditions. All fluxes decreased from around 150 L/m^{2}h to around 120 L/m^{2}h after 3 h filtration of HA solution. This phenomenon seemed to contradict with the expectation that higher surface hydrophilicity and higher photocatalytic activities of PVDF/NT-10 could lead to a superior fouling resistance. However, it could be explained by two reasons. First, because of the larger porosity and MWCO, HA could penetrate inside the membrane sublayer and lead to an internal fouling, where surface hydrophilicity and photocatalytic property may not work properly to mitigate flux decline. Second, the relatively higher water flux of PVDF/NT-10 made the accumulation of HA inside membrane faster, which further lead to a more serious flux decline. Once

the accumulation of foulant inside membrane structure narrowed membrane pores and made filtration process become surface sieving again, the superior surface hydrophilicity and photocatalytic capability may work to mitigate surface fouling again. That's why during the second cycle, membranes with UV and visible light irradiation began to show better antifouling behaviors than membrane under dark condition.

5.3.5 Mechanisms for the enhanced antifouling properties of PVDF/N-TiO_2 membranes

A conceptual representation of the proposed mechanisms for the enhanced antifouling properties of nanocomposite membrane is shown in Fig. 5.9. The hollow fiber membrane was surrounded by feed solution containing HA (presented as brown ball) with an outside-in configuration. The red balls located on membrane surface presented the incorporated N-TiO_2 NPs. The enhanced antifouling properties under light irradiation could be attributed to two possible reasons. One is the improved surface hydrophilicity, which could be provided both by the hydrophilic TiO_2 NPs and photoinduced hydrophilicity enhancement of TiO_2. In the second situation, water molecules could occupy photo-generated oxygen vacancies and produce adsorbed OH groups, leading to an enhanced surface hydrophilicity of TiO_2 [45, 46]. With an enhanced surface hydrophilicity, the adsorption of HA on membrane surface could be reduced, and those already deposited HA could be removed more easily by cross flow. This is consistent with the general strategy to mitigate UF membrane fouling by enhancing membrane surface hydrophilicity [47-49].

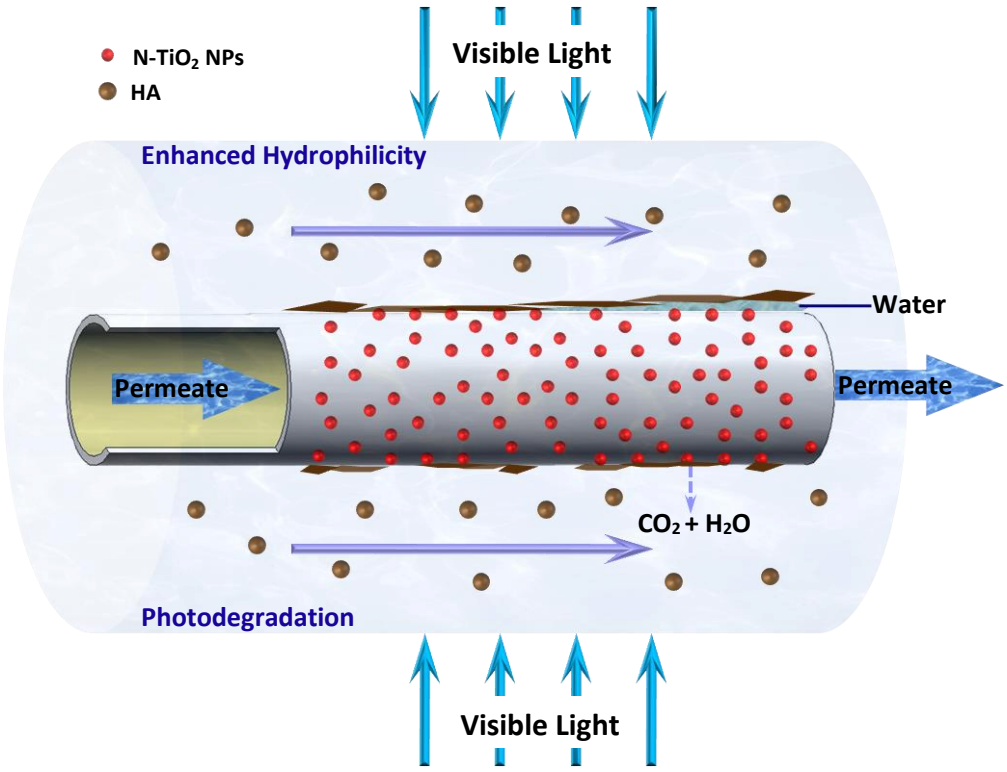

Fig. 5.9 Schematic illustration of hypothesized mechanisms of PVDF/N-TiO_2 nanocomposite HFMs with enhanced anti-fouling properties.

The other reason is the photodegradation process, which could decompose HA around the membrane surface by producing strong oxidant reagents such as hydroxyl radicals (OH) [6, 39, 43]. This phenomenon could mitigate the accumulation of HA on membrane surface, and then maintain relatively high flux compared to original PVDF membrane during the fouling test.

5.4 Challenges and opportunities

These results demonstrated that antifouling properties of PVDF/N-TiO_2 nanocomposite HFMs were clearly improved under light irradiation, especially under UV light. However, the enhancement and durability of those antifouling properties was still a big challenge if considering the practical application as the ultimate goal. Here, the

improvement of antifouling properties was limited by the amount, physicochemical properties of embedded TiO_2 and availability of suitable light. The amount of surface located TiO_2 determined the number of activated sites; the photocatalytic activities determined the efficiency of single spot; the interaction between TiO_2 and polymer matrix determined the stability of those surface located activated sites. It is conceivable that, with the power of chemical and material science, the antifouling properties of this novel membrane could be further improved. Here, several improvement strategies regarding above challenges are suggested as below.

More NPs could be blended into membrane casting solution to increase the amount of surface located TiO_2, however the percentage of TiO_2 in casting solution should have an upper bound basing on the criterion that no dramatic change or even damage of membrane structure (surface pore size, porosity et al.) occurs.

Plenty of research works about further improve photocatalytic efficiency of TiO_2 through doping, coupling, sensitization or hydrogenation are keeping coming out, such as N-F-codoped TiO_2 [50] and black hydrogenated TiO_2 [51], suggesting a good opportunity for the development of visible light activated nanocomposite membranes.

The interaction between TiO_2 and polymer matrix could be improved by modifying TiO_2 surface with certain agent, such as polyacrylic acid (PAA) [42] or silane coupling agents [52, 53]. However such modification should be well controlled to prevent it seriously blocking the contacts either between light and TiO_2 or between contaminates and generated strong oxidant reagents during the photodegradation process. At the same

time the modification agent should also be stable enough to tolerate the potential attack of oxidant reagents.

Although the enhanced water flux of nanocomposite membrane could offset some part of the pack-density decrease, how to design the membrane module to make most of membrane exposure to light irradiation and not sacrifice too much specific membrane area is still a question needs to be addressed. Accordingly, novel optical materials could be introduced into membrane module design and fabrication to bring in outside light source and expend the light availability inside the module. Moreover, besides sun light, energy efficient light source, such as light-emitting diode (LED), which possesses low power consumption, quick response time, flexibility, semi-permanent lifetime, and small footprint [50, 54], could be used inside the module for light irradiation.

5.5 Conclusions

In this study, N-TiO_2 NPs with visible light activity was applied to fabricate PVDF/N-TiO_2 nanocomposite HFMs through phase inversion method with blending approach. The resulting membrane showed brown color and an improved hydrophilicity, especially under light irradiation. Compared to the original PVDF and PVDF/P25-5 membrane, nanocomposite membranes containing N-TiO_2 NPs showed clear photocatalytic activities under the visible light irradiation. This is consistent with the UV-Vis absorbance results, where all N-TiO_2 incorporated membranes showed improved absorbance in the visible range besides the characteristic absorption peak of TiO_2 in the UV range. Membrane performance assessments indicated that PVDF/N-TiO_2 membranes possessed enhanced water flux, comparable HA rejection (above 96%), and improved fouling resistance when compared to the original PVDF membrane. These results have

demonstrated that there is a great potential to use the methodology established here for developing membrane with an improved water permeability and superior antifouling properties, based on photodegradation process and photoinduced hydrophilicity enhancement driven by solar light as a renewable source of energy. Its potential applications are mainly related to photodegradation & separation area, especially where light is available or even essential. It could be algae bioreactor, surface water treatment, wastewater treatment effluent polishing, photodegradation of organic contaminants under sun light irradiation and so on.

Acknowledgments

We gratefully acknowledge Professor Qingsong Yu in the Department of Mechanical & Aerospace Engineering at University of Missouri for providing us access to the video contact angle measurement system. We also thank Professor Ping Yu in Department of Physics and Astronomy at MU for providing us access to the light source analysis instruments (spectrometer and power meter) and analytical assistance.

References

[1] A. Fujishima, K. Honda, Electrochemical photolysis of water at a semiconductor electrode, Nature, 238 (1972) 37-38.

[2] A. Mills, S. Le Hunte, An overview of semiconductor photocatalysis, Journal of Photochemistry and Photobiology A: Chemistry, 108 (1997) 1-35.

[3] Y. Paz, Application of TiO_2 photocatalysis for air treatment: Patents' overview, Applied Catalysis B: Environmental, 99 (2010) 448-460.

[4] J. Yu, J.C. Yu, W. Ho, Z. Jiang, Effects of calcination temperature on the photocatalytic activity and photo-induced super-hydrophilicity of mesoporous TiO_2 thin films, New Journal of Chemistry, 26 (2002) 607-613.

[5] M.N. Chong, B. Jin, C.W.K. Chow, C. Saint, Recent developments in photocatalytic water treatment technology: A review, Water Research, 44 (2010) 2997-3027.

[6] X. Chen, S.S. Mao, Titanium dioxide nanomaterials: Synthesis, properties, modifications and applications, Chemical Reviews, 107 (2007) 2891-2959.

[7] S.K. Joung, T. Amemiya, M. Murabayashi, K. Itoh, Mechanistic studies of the photocatalytic oxidation of trichloroethylene with visible-light-driven N-doped TiO_2 photocatalysts, Chemistry - A European Journal, 12 (2006) 5526-5534.

[8] M.K. Nazeeruddin, P. Péchy, M. Grätzel, Efficient panchromatic sensitization of nanocrystalline TiO_2 films by a black dye based on a trithiocyanato-ruthenium complex, Chemical Communications, (1997) 1705-1706.

[9] K. Hara, Y. Tachibana, Y. Ohga, A. Shinpo, S. Suga, K. Sayama, H. Sugihara, H. Arakawa, Dye-sensitized nanocrystalline TiO_2 solar cells based on novel coumarin dyes, Solar Energy Materials and Solar Cells, 77 (2003) 89-103.

[10] M. Mrowetz, A. Villa, L. Prati, E. Selli, Effect of Au nanoparticles on TiO_2 in the photocatalytic degradation of an azo dye, Gold Bulletin, 40 (2007) 154-160.

[11] P. Sangpour, F. Hashemi, A.Z. Moshfegh, Photoenhanced degradation of methylene blue on cosputtered M:TiO_2 (M = Au, Ag, Cu) nanocomposite systems: A comparative study, Journal of Physical Chemistry C, 114 (2010) 13955-13961.

[12] N. Serpone, Is the band gap of pristine TiO_2 narrowed by anion- and cation-doping of titanium dioxide in second-generation photocatalysts?, Journal of Physical Chemistry B, 110 (2006) 24287-24293.

[13] A.W. Xu, Y. Gao, H.Q. Liu, The preparation, characterization, and their photocatalytic activities of rare-earth-doped TiO_2 nanoparticles, Journal of Catalysis, 207 (2002) 151-157.

[14] R. Asahi, T. Morikawa, T. Ohwaki, K. Aoki, Y. Taga, Visible-light photocatalysis in nitrogen-doped titanium oxides, Science, 293 (2001) 269-271.

[15] C. Di Valentin, E. Finazzi, G. Pacchioni, A. Selloni, S. Livraghi, M.C. Paganini, E. Giamello, N-doped TiO_2: Theory and experiment, Chemical Physics, 339 (2007) 44-56.

[16] T. Morikawa, R. Asahi, T. Ohwaki, K. Aoki, Y. Taga, Band-gap narrowing of titanium dioxide by nitrogen doping, Japanese Journal of Applied Physics, Part 2: Letters, 40 (2001) L561-L563.

[17] W. Ho, J.C. Yu, S. Lee, Synthesis of hierarchical nanoporous F-doped TiO_2 spheres with visible light photocatalytic activity, Chemical Communications, (2006) 1115-1117.

[18] T. Ohno, M. Akiyoshi, T. Umebayashi, K. Asai, T. Mitsui, M. Matsumura, Preparation of S-doped TiO_2 photocatalysts and their photocatalytic activities under visible light, Applied Catalysis A: General, 265 (2004) 115-121.

[19] T. Ohno, T. Mitsui, M. Matsumura, Photocatalytic activity of S-doped TiO_2 photocatalyst under visible light, Chemistry Letters, 32 (2003) 364-365.

[20] J. Yu, Q. Xiang, M. Zhou, Preparation, characterization and visible-light-driven photocatalytic activity of Fe-doped titania nanorods and first-principles study for electronic structures, Applied Catalysis B: Environmental, 90 (2009) 595-602.

[21] J. Choi, H. Park, M.R. Hoffmann, Effects of single metal-ion doping on the visible-light photoreactivity of TiO_2, Journal of Physical Chemistry C, 114 (2010) 783-792.

[22] J.M. Herrmann, J. Disdier, P. Pichat, Effect of chromium doping on the electrical and catalytic properties of powder titania under UV and visible illumination, Chemical Physics Letters, 108 (1984) 618-622.

[23] G. Colón, M. Maicu, M.C. Hidalgo, J.A. Navío, Cu-doped TiO_2 systems with improved photocatalytic activity, Applied Catalysis B: Environmental, 67 (2006) 41-51.

[24] L.G. Devi, S.G. Kumar, B.N. Murthy, N. Kottam, Influence of Mn2+ and Mo6+ dopants on the phase transformations of TiO_2 lattice and its photo catalytic activity under solar illumination, Catalysis Communications, 10 (2009) 794-798.

[25] A.B. Murphy, Does carbon doping of TiO_2 allow water splitting in visible light? Comments on "Nanotube enhanced photoresponse of carbon modified (CM)-n-TiO_2 for efficient water splitting", Solar Energy Materials and Solar Cells, 92 (2008) 363-367.

[26] W. Xi, S.U. Geissen, Separation of titanium dioxide from photocatalytically treated water by cross-flow microfiltration, Water Research, 35 (2001) 1256-1262.

[27] P. Le-Clech, E.K. Lee, V. Chen, Hybrid photocatalysis/membrane treatment for surface waters containing low concentrations of natural organic matters, Water Research, 40 (2006) 323-330.

[28] J. Kim, B. Van Der Bruggen, The use of nanoparticles in polymeric and ceramic membrane structures: Review of manufacturing procedures and performance improvement for water treatment, Environmental Pollution, 158 (2010) 2335-2349.

[29] A. Sotto, A. Boromand, R. Zhang, P. Luis, J.M. Arsuaga, J. Kim, B. Van der Bruggen, Effect of nanoparticle aggregation at low concentrations of TiO_2 on the hydrophilicity, morphology, and fouling resistance of PES-TiO_2 membranes, Journal of Colloid and Interface Science, 363 (2011) 540-550.

[30] Y.T. Xiao, S.S. Xu, Z.H. Li, X.H. An, L. Zhou, Y.L. Zhang, F.Q. Shiang, Progress of applied research on TiO_2 photocatalysis-membrane separation coupling technology in water and wastewater treatments, Chinese Science Bulletin, 55 (2010) 1345-1353.

[31] S.Y. Kwak, S.H. Kim, S.S. Kim, Hybrid organic/inorganic reverse osmosis (RO) membrane for bactericidal anti-fouling. 1. Preparation and characterization of TiO_2 nanoparticle self-assembled aromatic polyamide thin-film-composite (TFC) membrane, Environmental Science and Technology, 35 (2001) 2388-2394.

[32] S.H. Kim, S.-Y. Kwak, B.-H. Sohn, T.H. Park, Design of TiO_2 nanoparticle self-assembled aromatic polyamide thin-film-composite (TFC) membrane as an approach to solve biofouling problem, Journal of Membrane Science, 211 (2003) 157-165.

[33] T.-H. Bae, T.-M. Tak, Preparation of TiO_2 self-assembled polymeric nanocomposite membranes and examination of their fouling mitigation effects in a membrane bioreactor system, Journal of Membrane Science, 266 (2005) 1-5.

[34] T.-H. Bae, T.-M. Tak, Effect of TiO_2 nanoparticles on fouling mitigation of ultrafiltration membranes for activated sludge filtration, Journal of Membrane Science, 249 (2005) 1-8.

[35] G. Wu, S. Gan, L. Cui, Y. Xu, Preparation and characterization of PES/TiO_2 composite membranes, Applied Surface Science, 254 (2008) 7080-7086.

[36] A. Razmjou, J. Mansouri, V. Chen, The effects of mechanical and chemical modification of TiO_2 nanoparticles on the surface chemistry, structure and fouling performance of PES ultrafiltration membranes, Journal of Membrane Science, 378 (2011) 73-84.

[37] A.M. Kelly, S. T., Fabrication of composites, North-Holland, Amsterdam, 1983.

[38] L.Y. Yu, H.M. Shen, Z.L. Xu, PVDF-TiO_2 composite hollow fiber ultrafiltration membranes prepared by TiO_2 sol-gel method and blending method, Journal of Applied Polymer Science, 113 (2009) 1763-1772.

[39] Z. Wang, W. Cai, X. Hong, X. Zhao, F. Xu, C. Cai, Photocatalytic degradation of phenol in aqueous nitrogen-doped TiO_2 suspensions with various light sources, Applied Catalysis B: Environmental, 57 (2005) 223-231.

[40] J. Yin, G. Zhu, B. Deng, Multi-walled carbon nanotubes (MWNTs)/polysulfone (PSU) mixed matrix hollow fiber membranes for enhanced water treatment, Journal of Membrane Science, 437 (2013) 237-248.

[41] B. Deng, M. Yu, X. Yang, B. Zhang, L. Li, L. Xie, J. Li, X. Lu, Antifouling microfiltration membranes prepared from acrylic acid or methacrylic acid grafted poly(vinylidene fluoride) powder synthesized via pre-irradiation induced graft polymerization, Journal of Membrane Science, 350 (2010) 252-258.

[42] S.S. Madaeni, S. Zinadini, V. Vatanpour, A new approach to improve antifouling property of PVDF membrane using in situ polymerization of PAA functionalized TiO_2 nanoparticles, Journal of Membrane Science, 380 (2011) 155-162.

[43] A. Rahimpour, S.S. Madaeni, A.H. Taheri, Y. Mansourpanah, Coupling TiO_2 nanoparticles with UV irradiation for modification of polyethersulfone ultrafiltration membranes, Journal of Membrane Science, 313 (2008) 158-169.

[44] X. Zhang, A.J. Du, P. Lee, D.D. Sun, J.O. Leckie, TiO_2 nanowire membrane for concurrent filtration and photocatalytic oxidation of humic acid in water, Journal of Membrane Science, 313 (2008) 44-51.

[45] A. Fujishima, T.N. Rao, D.A. Tryk, Titanium dioxide photocatalysis, Journal of Photochemistry and Photobiology C: Photochemistry Reviews, 1 (2000) 1-21.

[46] R. Wang, K. Hashimoto, A. Fujishima, M. Chikuni, E. Kojima, A. Kitamura, M. Shimohigoshi, T. Watanabe, Light-induced amphiphilic surfaces, Nature, 388 (1997) 431-432.

[47] F. Liu, Y.-Y. Xu, B.-K. Zhu, F. Zhang, L.-P. Zhu, Preparation of hydrophilic and fouling resistant poly(vinylidene fluoride) hollow fiber membranes, Journal of Membrane Science, 345 (2009) 331-339.

[48] C. Jönsson, A.-S. Jönsson, Influence of the membrane material on the adsorptive fouling of ultrafiltration membranes, Journal of Membrane Science, 108 (1995) 79-87.

[49] E.R. Cornelissen, T. van den Boomgaard, H. Strathmann, Physicochemical aspects of polymer selection for ultrafiltration and microfiltration membranes, Colloids and Surfaces A: Physicochemical and Engineering Aspects, 138 (1998) 283-289.

[50] D. Li, H. Haneda, S. Hishita, N. Ohashi, Visible-light-driven N-F-codoped TiO_2 photocatalysts. 2. Optical characterization, photocatalysis, and potential application to air purification, Chemistry of Materials, 17 (2005) 2596-2602.

[51] X. Chen, L. Liu, P.Y. Yu, S.S. Mao, Increasing solar absorption for photocatalysis with black hydrogenated titanium dioxide nanocrystals, Science, 331 (2011) 746-750.

[52] A. Razmjou, A. Resosudarmo, R.L. Holmes, H. Li, J. Mansouri, V. Chen, The effect of modified TiO_2 nanoparticles on the polyethersulfone ultrafiltration hollow fiber membranes, Desalination, 287 (2012) 271-280.

[53] B. Rajaeian, A. Rahimpour, M.O. Tade, S. Liu, Fabrication and characterization of polyamide thin film nanocomposite (TFN) nanofiltration membrane impregnated with TiO_2 nanoparticles, Desalination, 313 (2013) 176-188.

[54] X. Wang, T.-T. Lim, Solvothermal synthesis of C–N codoped TiO_2 and photocatalytic evaluation for bisphenol A degradation using a visible-light irradiated LED photoreactor, Applied Catalysis B: Environmental, 100 (2010) 355-364.

Support Information

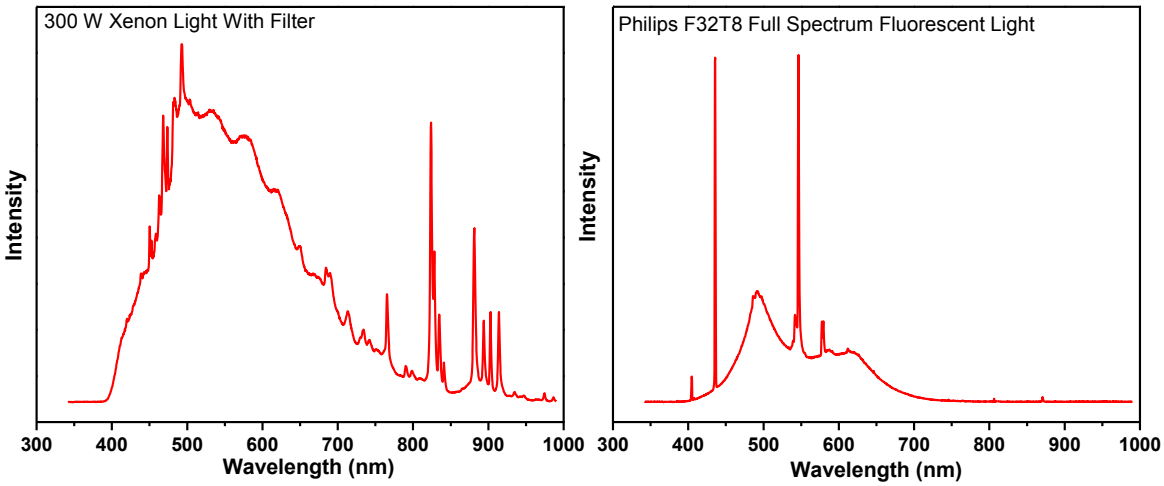

Fig. 5.1s Spectra of light sources for photocatalytic reactions

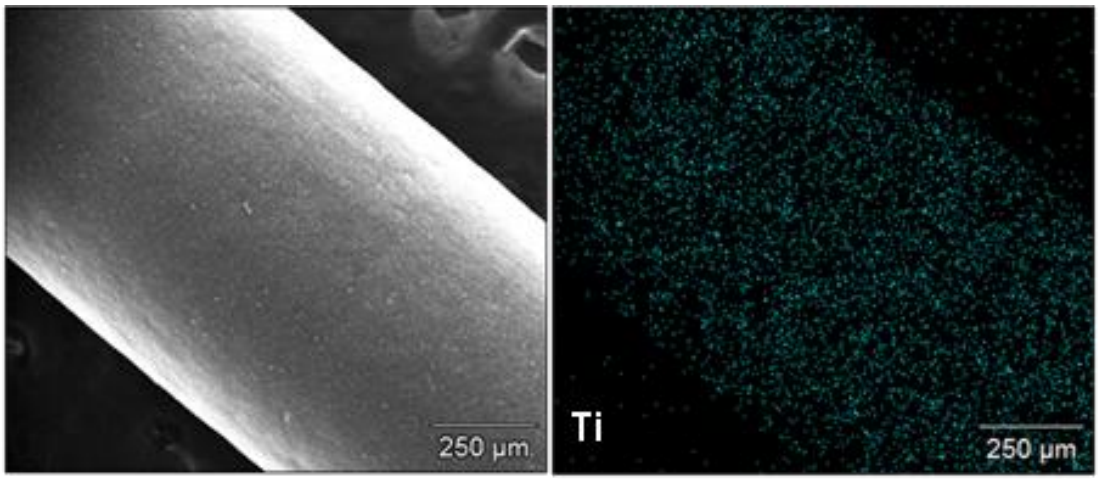

Fig. 5.2s EDX mapping scanning spectra of PVDF/NT-5 surface

CHAPTER SIX
Graphene oxide (GO) enhanced polyamide (PA) thin-film nanocomposite (TFN) membrane for water purification

Abstract

A thin-film nanocomposite (TFN) membrane containing graphene oxide (GO) nanosheets was prepared by the in-situ interfacial polymerization (IP) process. Aqueous *m*-phenylenediamine (MPD) and organic trimesoyl chloride (TMC)-GO mixture solutions were used in the IP process. GO nanosheets with multiple layer structure and an interlayer spacing around 0.83 nm were prepared and used as the fillers to fabricate the TFN membrane at concentrations ranging from 0 to 0.02 wt%. The membranes were characterized by scanning electron microscopy (SEM), transmission electron microscopy (TEM), atomic force microscopy (AFM), Raman spectroscopy and attenuated total reflection Fourier transform infrared (ATR FT-IR) spectroscopy, and their performances were evaluated based on the water permeability and salt rejection. Results indicated that the GO nanosheets dispersed well in polyamide (PA) thin-film layer and improved membrane performances under optimal concentrations. By increasing concentration of GO nanosheets, the permeate water flux increased from 39.0 $\pm$1.6 L/m^{2}h to 59.4 $\pm$0.4 L/m^{2}h, while rejections of NaCl and Na_2SO_4 slightly decreased from 95.7 $\pm$0.6% to 93.8 $\pm$0.6% and 98.1 $\pm$0.4% to 97.3 $\pm$0.3%, respectively. The interlayer spacing of GO nanosheets may work as channels for water migration and hence contributed to the water permeability enhancement.

Keywords: Graphene oxide; Polyamide; Thin-film nanocomposite; Interfacial polymerization; Desalination

6.1 Introduction

Graphene, a single-atom-thick sheet of hexagonally arrayed sp^2-bonded carbon atoms, is a two-dimensional (2D) macromolecule exhibiting extremely high specific surface area (2600 m^2/g) [1, 2]. Graphene exhibits extraordinary thermal, mechanical, and electrical properties, which are believed to be yielded by long-range π-conjugation inside its structure [3]. Recently, graphene has attracted both academic and industrial interest and has been explored for many applications including electronic device, polymer composite, catalyst, sensor, and membrane separation [4, 5].

In membrane separation area, graphene with controlled pores is believed to form the ultimate thin membrane for fluid or gas separation [6]. However, the scalable manufacturing of large monolayer graphene membranes with narrowly distributed subnanometer pores is still a big challenge [7]. Alternatively, strategies of preparing stacked graphene nanosheets or graphene-polymer nanocomposites have been explored to evaluate their potential applications in water purification area.

One strategy is to transfer or coat few-layered, ultrathin graphene derivatives, such as GO and reduced GO (rGO) on polymeric substrates [8-11]. The resultant membranes all showed promising filtration performance. For instance, Han et al. [9] prepared ultrathin graphene NF membrane atop a microfiltration (MF) membrane through vacuum filtration of rGO suspension. Similarly, stacked GO-TiO_2 membrane was prepared via vacuum filtration of GO-TiO_2 composite nanosheets by Xu et al. [11]. In order to improve the stability of stacked graphene membrane, Hu and Mi [8] prepared a membrane via layer-by-layer deposition of GO nanosheets onto a polydopamine coated polysulfone (PSU) substrate, where TMC was used as cross-linking agent. The resultant

membrane showed a very high water permeability and good rejection to Rhodamine-WT dye. However, the relatively weak stability of GO on membrane surface under water stream was still a challenge need to be addressed especially under cross-flow conditions.

The other strategy is to incorporate GO nanosheets into the polymeric matrix. Although pristine graphene is not compatible with organic polymers, GO sheets with bearing hydroxyl, epoxide, diols, ketones and carboxyls functional groups can alter the van der Walls interactions significantly and be more compatible with organic polymers [12]. In the past two years, several studies have been carried out to prepare GO-polymer nanocomposite membranes [13-17]. For example, Zhao et al. [15] incorporated isocyanate-treated GO (iGO) into PSU UF membrane and developed a nanocomposite membrane with enhanced hydrophilicity and fouling resistance. In the other study [13], nanocomposite PSU membranes containing SiO_2/GO hybrid nanosheets exhibited good overall properties in permeability, protein rejection, and fouling resistance. The synergistic effect of SiO_2/GO could be attributed to its high hydrophilicity as well as special sandwich structure which will facilitate its dispersion in the PSU matrix.

Additionally, during the oxidation process oxygen-containing functionalities will be introduced into the basal plane of GO [3, 18]. Then the increased hydrophilicity of GO could make the water molecules easily intercalate into the interlayer structure to generate an idea water channel [10]. Based on our previous study about mesoporous silica enhanced TFN membrane [19], those interlayer space inside GO may provide additional short paths for water stream through PA thin-film layer to generate a TFN membrane with enhanced water permeability.

Therefore, the primary objective of this study is to illustrate the potential application of GO nanosheets on TFN membrane preparation, and then develop a high performance TFN membrane. GO nanosheets will be prepared through modified Hummers' method, and then those nanosheet will be embedded into PA thin-film layer by in-situ IP process. The physicochemical properties of the GO nanosheets and TFN membranes will be evaluated by SEM, TEM, AFM, Raman Spectroscopy, ATR FT-IR spectroscopy, and contact angle. The membrane performances will be examined by water permeability and solute rejection based on different loadings of nanosheets.

6.2 Materials and methods

6.2.1 Materials

PSU (Mw = 35,000, Aldrich) pellets dissolved in *N*, *N*-dimethylformamide (DMF, 99.8%, Aldrich) were used as the casting solution to make the support layer. MPD (>99%, Aldrich) and TMC (>98.5%, Aldrich) were monomers used in the IP process. All chemicals were ACS reagents grade. Deionized (DI) water produced by Millipore DI system (Synergy 185, 18.2 MΩ·cm) was used for solution preparation and filtration study.

6.2.2 Preparation and characterization of GO

Graphene oxide (GO) was synthesized using modified Hummers' method [18] by reacting commercially graphite flake (Aldrich) with a mixture of H_2SO_4, $NaNO_3$, and $KMnO_4$. Briefly, H_2SO_4 solution was maintained under ice bath condition in order to make it reach a temperature lower than 4 ℃. $NaNO_3$ and graphite flakes were added into above H_2SO_4 solution with a continuous stirring for 2 h, then $KMnO_4$ was dosed slowly. The color

of the mixture solution gradually became dark green. Subsequently, ice bath was removed and pre-determined DI water was slowly added while keeping solution temperature at 35 ± 2 ℃. At this stage, the color of the reaction solution was changed to brown from dark green. After 1 h, the temperature of the reaction solution without stirring was raised and controlled at 95 ± 2 ℃ for 30 min. Finally, a certain amount of H_2O_2 was introduced into the mixture solution, a bright yellow GO solution was produced. The GO was centrifuged and washed with 5% HCl and DI water twice. A brown gel GO attained after acid washing and centrifugation was rinsed using ethanol (≥ 99.5%). GO sheet obtained by drying under 40 ℃ for 24 h in an oven was ground into a brown GO powder for later use.

The crystalline structures of synthesized GO nanosheets were analyzed by an X-ray powder diffractometer (XRD, Ultima IV, Rigaku Americas Corp., The Woodlands, TX). The samples were scanned from 5 °to 40 °(2θ) with a step size of 0.05 °and a count time of 1 s at each point. Morphology of nanosheets was examined by SEM (Quanta FEG 600, FEI Company, Hillsboro, OR) and TEM (JEM 1400, JEOL Ltd., Peabody, MA). SEM specimen was prepared by dropping GO-ethanol mixture solution onto a silicon wafer. After complete drying at room temperature, the specimen was coated with platinum by a sputter coater (K575x, Emitech Ltd., Kent, England) at 20 mA for 1 min to increase conductivity. TEM samples of NPs were prepared by dropping GO-ethanol mixture solution onto carbon coated copper grid and drying at the room temperature.

6.2.3 Preparation of PSU support layer and TFN membrane

The PSU support layer with a surface pore size of 23.2 ± 8.4 nm was fabricated by the phase inversion method follow our previous study [19]. Briefly, a 15 wt% PSU-DMF casting solution was stirred at 50 ℃ for 6 h, and kept overnight for degassing. The clear

solution was spread on a glass plate and casted by casting knife (EQ-Se-KTQ-150, MTI Corp., Richmond, CA) to approximately 100 μm of film thickness. Then, glass plate was immediately immersed into a DI water bath (25 ℃). The precipitated PSU support membrane was washed and stored in DI water at least 24 h until use.

For TFN membrane fabrication, the prepared PSU support layer was immersed in a 2.0 wt% MPD-water solution for 3 min. Excess solution on the surface was removed by a rubber roller. Next, the MPD saturated PSU support layer was soaked in a 0.15 wt% of TMC-hexane solution for 1 min, resulting in the formation of a PA thin-film layer. A series of GO-ethanol stock suspensions with different GO concentration were prepared by ultrasonication. And then, TMC-hexane solutions with GO concentrations varied from 0 to 0.02 wt% were prepared by spiking with GO-ethanol stock suspensions. Here, ethanol stock suspension was used to facilitate the dispersion of GO in hexane solution, and the final concentration of ethanol in hexane solution was around 0.5% (v/v). A complete mixing of GO in the hexane solution was achieved by ultrasonication for 30 min prior to the IP process. The TFN membranes were rinsed with pure hexane and cured at 80 ℃ in an oven for 5 min, and then stored in DI water at 5 ℃. The final products were named as GO-x, where x denoted the concentration of filler in TMC solution during the IP process. For example, TFN membrane prepared by 0.02 wt% GO TMC solution was named as GO-0.02.

6.2.4 TFN membrane characterization and performance assessment

SEM analysis of membrane surface was conducted using a piece of membrane dried at room temperature. The operational condition was identical with GO analysis described in the section of 6.2.2. To obtain the TEM cross-section, the membranes were embedded

in Epon resin (Eponate 12, Ted Pella, Inc., Redding, CA) and cut by Reichert-Jung Ultracut E ultramicrotome (Reichert, Inc. Depew, NY). The images were taken under 80 kV by using JEM 1400. Hydrophilicity of membrane was assessed based on the measurement of pure water contact angles. The video contact angle system (VCA-2500 XE, AST products, Billerica, MA) was employed to perform the sessile drop method. At least six stabilized contact angles from different sites of each sample were obtained to calculate average contact angle and standard deviation. The functional groups of membrane surface were identified by ATR FT-IR spectroscopy. Nicolet 4700 FT-IR (Thermo Electron Corporation, Waltham, MA) equipped with multi-reflection Smart Performer® ATR accessory was used for this analysis. All spectra included the wave numbers from 500 to 4000 cm^{-1} with 128 scans at a resolution of 2.0 cm^{-1}. Quantitative surface roughness of the membrane was analyzed by atomic force microscopy (AFM5500, Agilent Technologies, Inc. Santa Clara, CA) with tapping mode in air. A 9 × 9 μm of surface area was tested and the root mean square (RMS) roughness was recorded.

Membrane performance test was conducted following our previous study [19]. Briefly, a high pressure cross-flow filtration system (pressure range: 50-500 psi) with an effective membrane area of 9.6 cm^2 was used to evaluate water flux and solute rejection. Prior to test, each membrane was compressed by DI water at 300 psi for 3 h. Water flux was measured by the weight of the permeate water at a constant transmembrane pressure (TMP). The weight of the permeate water was recorded by a LabVIEW automated system (National Instruments LabVIEW 8.2 with Ohaus digital balance). After pure water flux test, salt solution (final concentration of 2,000 ppm of NaCl or Na_2SO_4) was

added and the conductivity of feed and permeate solutions was measured by a conductivity/TDS meter (HACH Company, Loveland, CO). The measurement was conducted at 25 ± 1 ℃, which was controlled by a water circulator (Isotemp 6200 R20F, Fisher Scientific, Inc., Pittsburgh, PA). The flux and rejection was calculated with equation (1) and equation (2), respectively.

$$J = \frac{V_p}{A \cdot t} \tag{1}$$

$$R = \left(1 - \frac{C_p}{C_f}\right) \times 100 \tag{2}$$

where J is the water flux (L/m^{2}h), V_p is the permeate volume (L), A is the membrane area (m^2) and t is the treatment time (h). R is the rejection ratio and C_p and C_f are the conductivities of permeate and feed solution, respectively.

6.3 Results and discussion

6.3.1 Characterization of GO

SEM and TEM images of prepared GO are presented in Fig. 6.1, where sheet structure are clearly observed. Typical wrinkle structures are also observed on GO nanosheets both from SEM and TEM images, which could be attributed to both intrinsic (thermal fluctuation) and extrinsic (i.e. defects, functionalization, and applied stresses) factors [20]. Based on these images, the size of nanosheets could be from 500 nm to several micrometers.

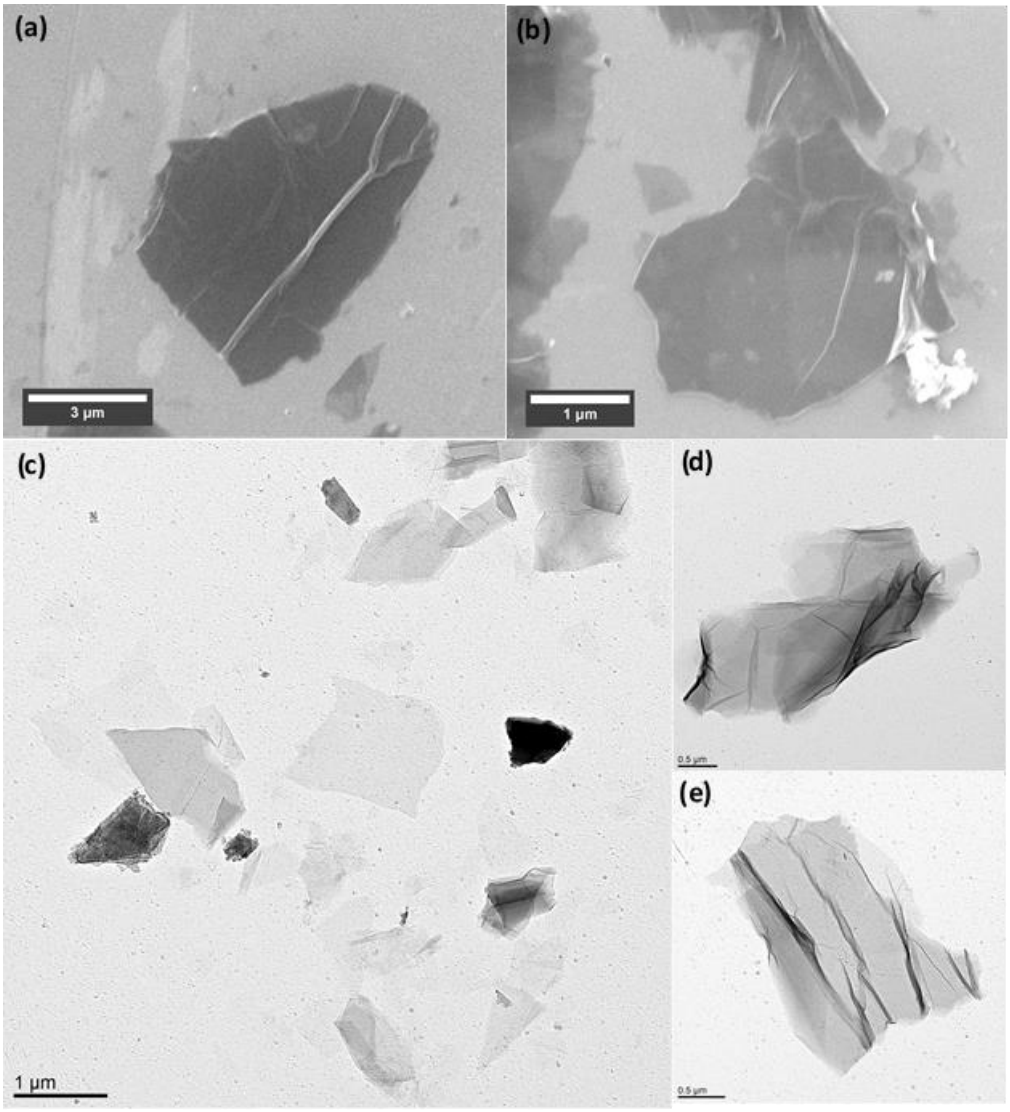

Fig. 6.1 SEM images (a, b) and TEM images (c-e) of prepared GO nanosheets.

Fig. 6.2 shows the XRD pattern of GO sample. A clear peak at around 11.66 ºwas observed, which was corresponded to a 0.83 nm d-space [21]. Accordingly, the characteristic (002) peak of graphite usually located at 2θ = 26.5 º, which implying an interlayer spacing of 0.34 nm [21-23]. The increased interlayer spacing after oxidation could be attributed to the hydrophilic property of oxygen functionalized GO, which made the water molecules easily intercalate into the interlayer structure [22].

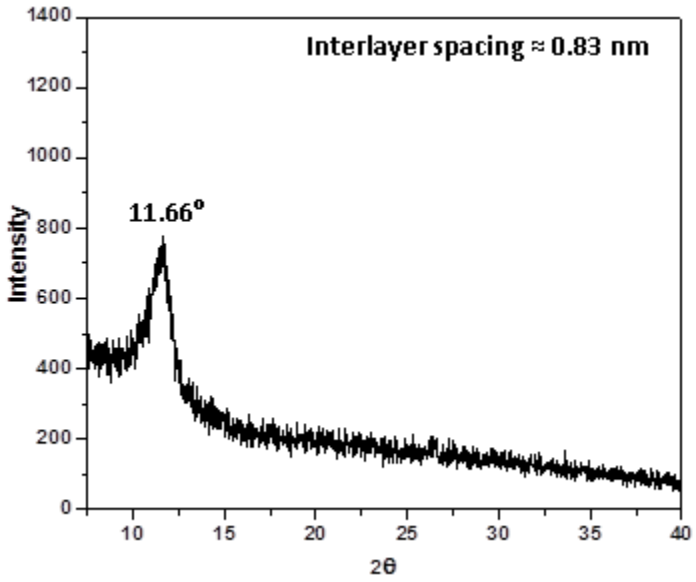

Fig. 6.2 X-ray diffraction pattern of GO sample

6.3.2 Characterization of GO-TFN membranes

The SEM images of membrane surfaces and TEM images of cross-sections are presented in Fig. 6.3. These membrane surfaces showed a typical leaf-like morphology due to the formation of PA thin-film layer. As presented in cross-sectional TEM images, all membranes had a PA thin-film layer with a thickness between 200 and 300 nm. The impregnation of GO nanosheets did not show significant effects on the overall morphology of PA layer in the tested concentration range. However, there shows some clusters on PA layer surface when the concentration of nanofiller goes high, especially under 0.02%. This could be caused by the aggregation of GO. As compared with our previous work [19], where silica NPs with a diameter of 100 nm were clearly observed inside the PA thin-film layer, the existence of GO nanosheets was not clearly presented in these TEM images probably due to their sheet structure with thickness of several nanometers. Accordingly, Raman spectroscopy was further used to verify the existence of GO inside thin-film layer.

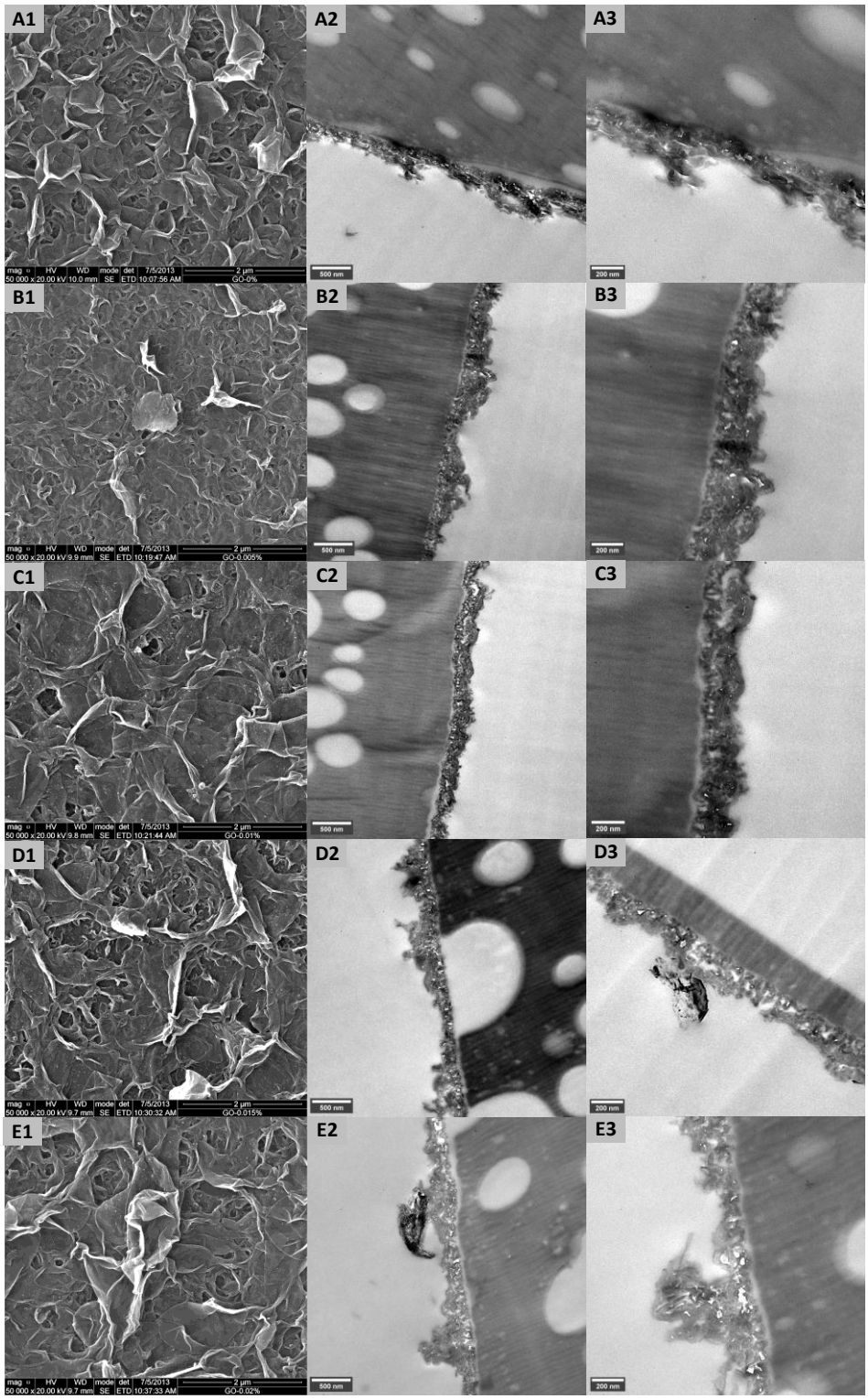

Fig. 6.3 SEM images of membrane surfaces (A1-E1) and TEM images of cross-sections (A2-E2 low magnification; A3-E3 high magnification). A (0%); B (0.005%); C (0.01%); D (0.015%); E (0.02%).

In the Raman spectra of GO (Fig. 6.4), two graphitic peaks could be observed. The peak at around 1590 cm^{-1} (G-band) corresponded to a splitting of the E_{2g} stretching mode of graphite, which has been assigned to the movement of two neighboring carbon atoms in opposite directions, characteristic of highly oriented pyrolitic graphite [30]. The peak at around 1350cm^{-1} (D-band) could be attributed to the disordered graphite structure or sp^3-hybridized carbons [24, 25], which reflecting the extent of defect.

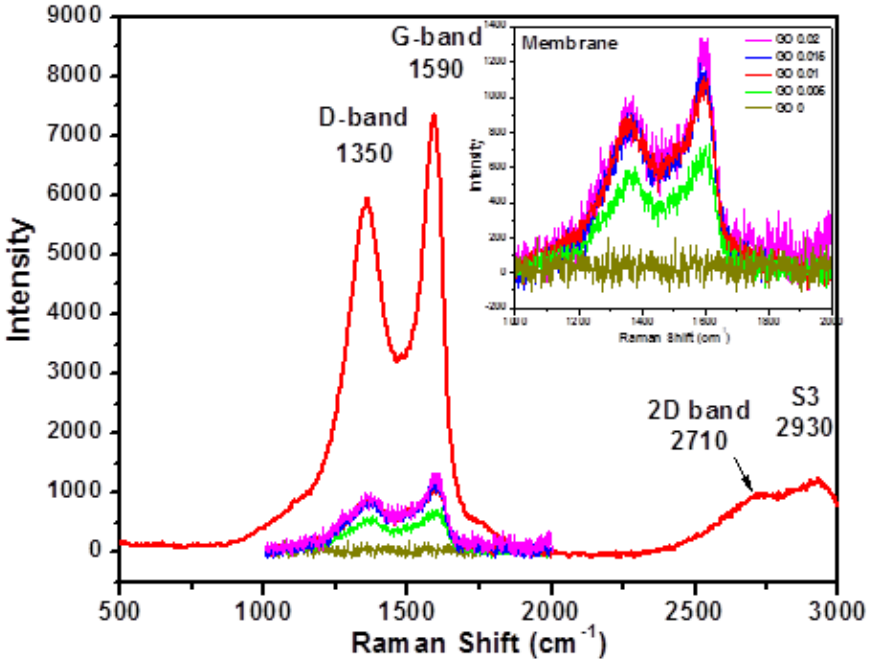

Fig. 6.4 Raman spectra of prepared GO and GO-TFN membranes. Enlarged spectra of TFN membranes were inserted in the upper right corner of this figure.

In addition, the 2D band around 2710 cm^{-1} as the second order of zone-boundary phonons was observed [26]. Furthermore, a S3 peak near 2930 cm^{-1} showed up which could be attributed to the lattice disorders and its number of Raman shift was roughly the combination of the G and D peaks.

In this case, the 2D band shifted to higher frequencies (2710 cm^{-1}) from the typical peak (2679 cm^{-1}) of single layer structure, indicating the possible multilayer structure of GO samples prepared here. This is consistent with the TEM images in Fig. 6.1. Similarly, Ferrari and et al. [25] found the 2D band could shift to higher frequencies and become broader with increasing layer number, especially with a layer number less than five. Graf and et al. [27] examined spatially resolved Raman spectra for single- and few-layer graphene, and also found the same phenomenon. In their case, the 2D band shifted 19.0 ± 1.5 cm^{-1} and 28 ± 2 cm^{-1} for 2-layer and 6-layer structure, respectively.

The Raman spectra of membrane surfaces were also collected and presented in Fig. 6.5. Original TFC membrane doesn't show any peak between 1000 and 2000 cm^{-1}. After incorporating GO, TFN membranes all show two peaks corresponding to the D-band and G-band of GO filler, which indicating the existence of GO in the top layer of membrane samples.

Surface functional groups of TFN membranes were identified by FT-IR spectroscopy and the results are presented in Fig. 6.5. Peaks at 1660 cm^{-1} (amide I, C=O stretching vibrations of amide), 1547 cm^{-1} (amide II, in-plane N–H bending and C–N stretching vibrations), 1610 cm^{-1} (N–H stretching of amide) and 1450 cm^{-1} (C=O stretching and O–H bending of carboxylic acid) were originated from the PA polymerization and consisted with amide functionalities [15, 24, 25]. The broad peak appearing at a wavenumber of 3300 cm^{-1} could be assigned as originating from stretching vibrations of O-H groups attached to the basal plane of graphite in graphene oxide. With increasing GO concentration, the intensity of this peak gradually increased possibly due to the increased amount of GO inside the membrane top layer.

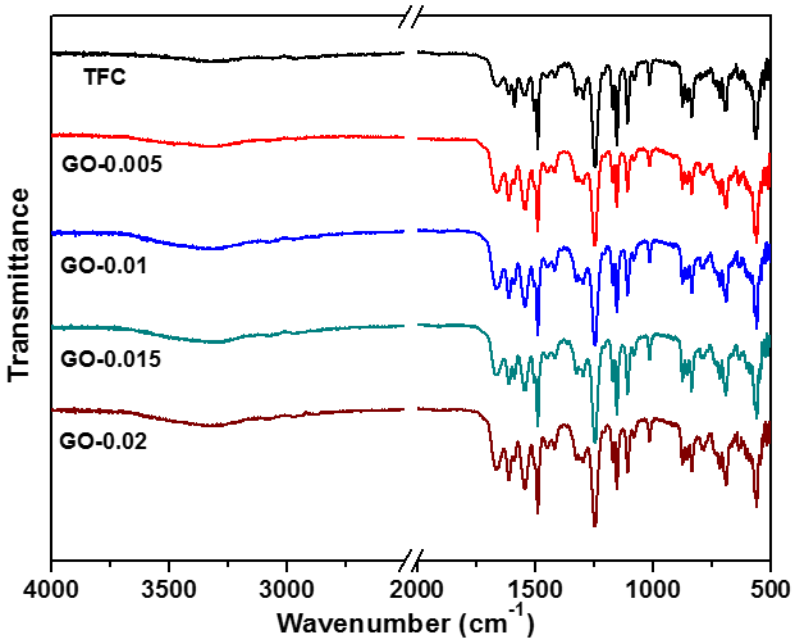

Fig. 6.5 ATR FT-IR spectra of TFN membranes

As presented in Fig. 6.6, the contact angle of TFN membranes slightly decreased from 60.4 ± 2.5 °to 55.4 ± 1.7 °with increasing GO concentration. This could be caused by some surface located GO material as well as the influenced IP reaction between MPD and TMC due to the existence of hydrophilic filler material. Meanwhile, the surface roughness were evaluated, where corresponding AFM images are illustrated in Fig. 6.7. The RMS value first increased and then decreased with change of GO loading. The surface morphology indicated in AFM images are consistent with the SEM images presented in Fig. 6.3. The initial decrease of roughness could be attributed to the interruption of GO nanosheets on the growth of leaf-like structure during the IP process. While the observed roughness increase in GO-0.02 could be caused by the surface-located clusters formed by aggregation of GO.

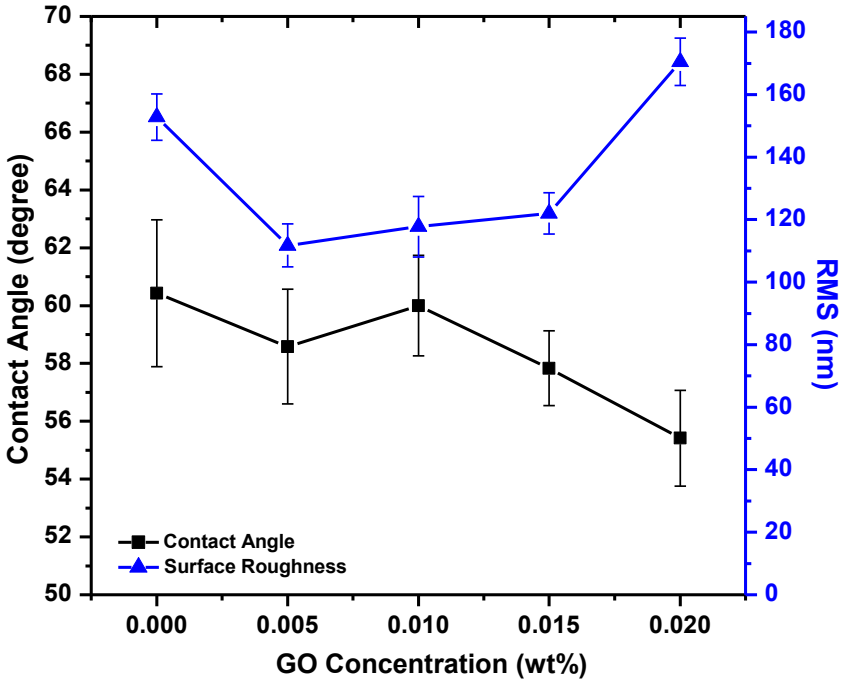

Fig. 6.6 Contact angle and surface roughness of membrane surface

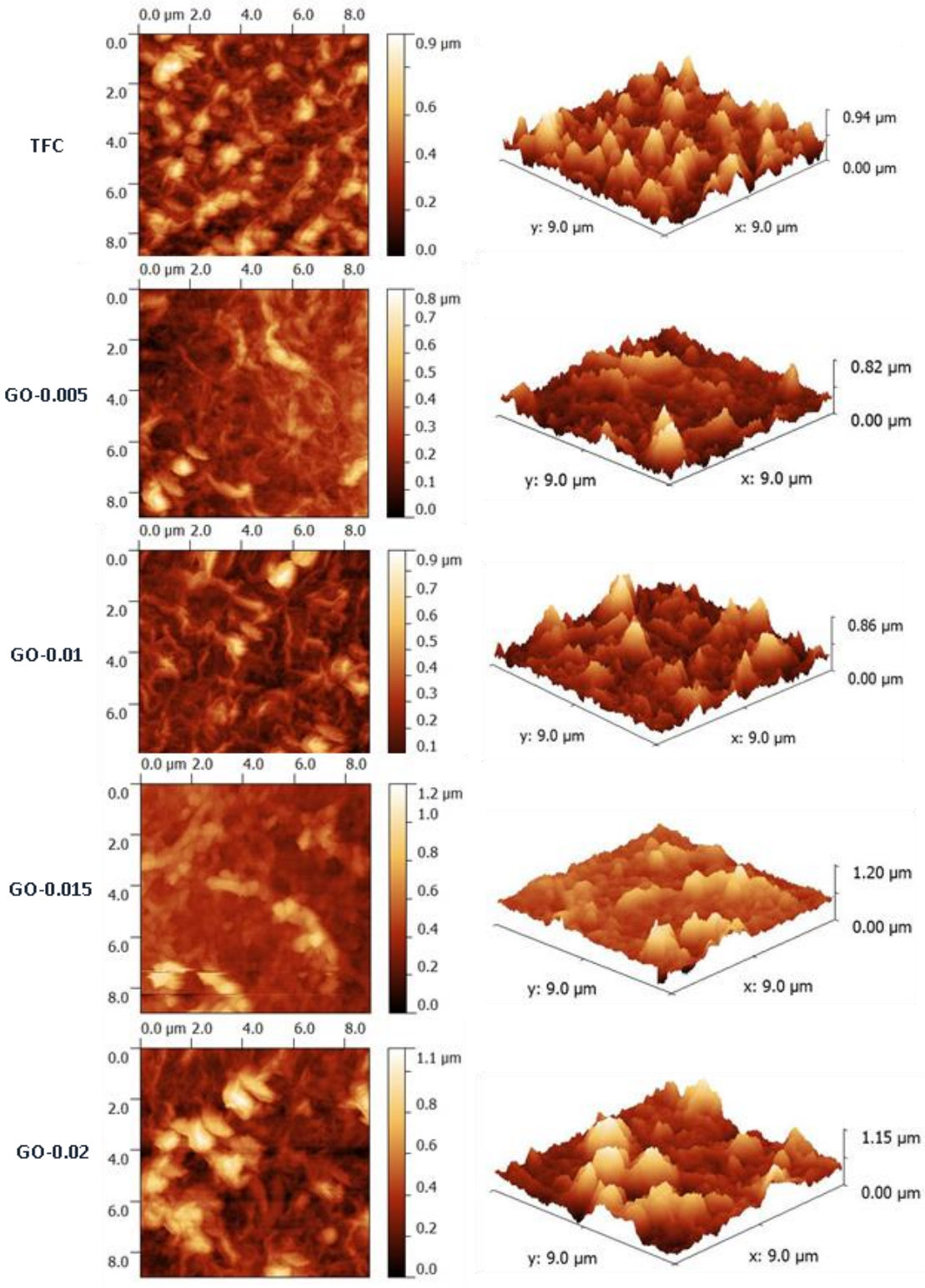

Fig. 6.7 AFM analysis of membrane surfaces

6.3.3 Performance of TFN membranes

Permeate flux and salt rejections are presented in Fig. 6.8. By increasing concentration of nanosheets, the permeate water flux increased from 39.0 ± 1.6 L/m^{2}h to 59.4 ± 0.4 L/m^{2}h, while rejections of NaCl and Na_2SO_4 slightly decreased from 95.7 ± 0.6% to 93.8 ± 0.6% and 98.1 ± 0.4% to 97.3 ± 0.3%, respectively.

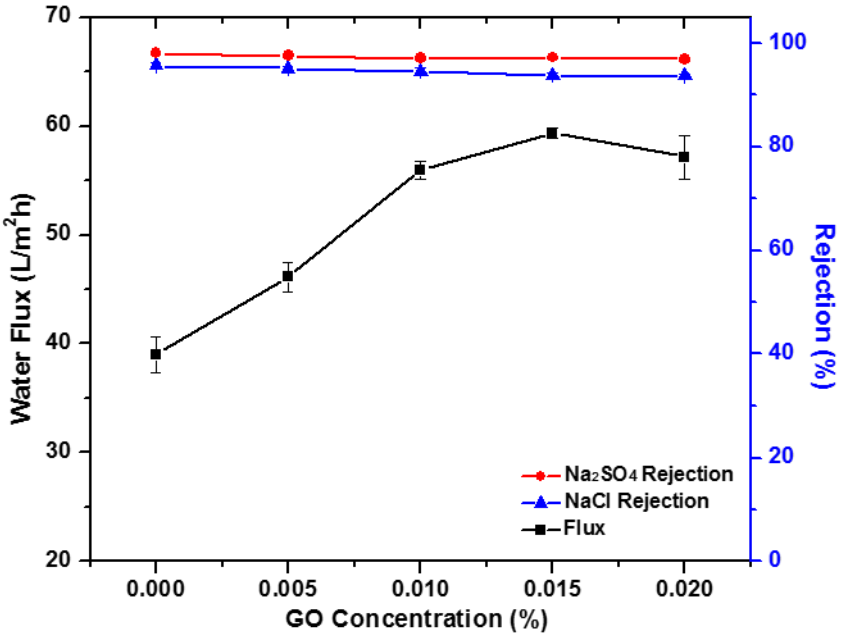

Fig. 6.8 Permeate flux and salt rejection of GO TFN membranes

During the filtration process, the slightly increased surface hydrophilicity will facilitate the solubilization of water molecules on membrane surface, thus improve water permeability [28]. Furthermore, similarly to our previous study about mesoporous silica enhanced TFN membrane [19], those interlayer space inside GO nanosheets may provide additional short paths for water stream through PA thin-film layer (Fig. 6.9). This is consistent with other researchers' strategy to prepare water channel membranes by using stacked GO layers, where the interlayer space of GO layers could be further adjusted to fit proposed applications. With increasing filler concentration, more water channels were

introduced into the dense barrier layer, resulting in an increased water flux. The level off or even decrease of permeability enhancement was observed when GO concentration was higher than 0.015%. It could be attributed to the aggregation of nanofillers at high concentrationF, which can influence the absolute number and distribution of resulting water channels. This phenomenon was also observed in other studies of TFN membranes including our own works [19, 29]. However, the critical concentrations on these studies were diverse, which could be caused by the different properties and morphologies of corresponding nanofillers.

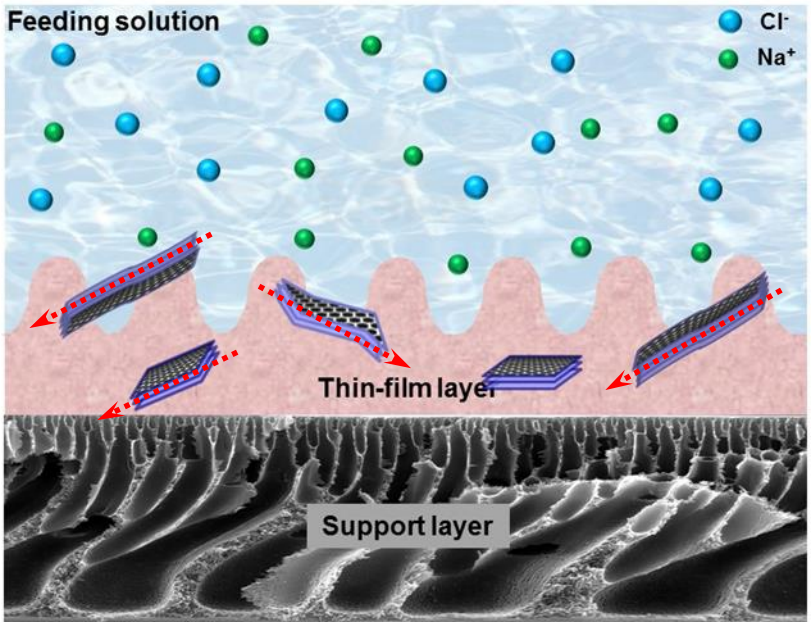

Fig. 6.9 Schematic illustration of hypothesized mechanism of GO TFN membrane

As a typical RO membrane, a higher rejection of Na_2SO_4 than that of NaCl was observed, which could be caused by the higher negative charge and larger size of hydrated SO_4^{2-} ions. Compared to TFN membrane containing MCM-41 NPs which can maintain essentially the same salt rejection as pristine TFC membrane, GO-TFN membrane showed a slightly decreased salt rejection after incorporating GO nanosheets.

This phenomenon could be attributed to the different particle size and structure of nanofillers used in these two studies. MCM-41 NPs has a particle size around 100 nm which can well fit the thickness of PA thin-film layer and may not ruin the integrity of this layer. As a two-dimensional material, GO nanosheets has a thickness around several nanometers determined by layer numbers and relatively large sheet size (500 nm to 2 μm). During the IP process, some nanosheets may have affected the integrity of PA thin-film layer and generate some defects.

6.4 Conclusions

A novel TFN membrane containing GO nanosheets was prepared by the in-situ IP process. GO nanosheets with multiple-layer structure and an interlayer spacing around 0.83 nm were prepared and used as the fillers to fabricate the TFN membrane at concentrations ranging from 0 to 0.02 wt%. Results indicated that the GO nanosheets dispersed well in PA thin-film layer and improved membrane performances under optimal concentrations. By increasing concentration of GO nanosheets, membrane hydrophilicity increased. At the same time, the permeate water flux increased from 39.0 ± 1.6 L/m^{2}h to 59.4 ± 0.4 L/m^{2}h, while rejections of NaCl and Na_2SO_4 slightly decreased from 95.7 ± 0.6% to 93.8 ± 0.6% and 98.1 ± 0.4% to 97.3 ± 0.3%, respectively. The interlayer spacing of GO nanosheets may work as channels for water migration and hence contributed to the water permeability enhancement. Optimizing incorporation conditions further for the membrane preparation could result in membranes with even higher water permeability and high salt rejection.

Acknowledgement

We gratefully acknowledge Zach Robert Thacker and Professor Patrick Pinhero in Department of Chemical Engineering at University of Missouri for providing us access to the AFM instrument and analytical assistance. We also thank Professor Qingsong Yu in the Department of Mechanical & Aerospace Engineering at MU for providing us access to the video contact angle measurement system.

Reference

[1] H. Kim, A.A. Abdala, C.W. MacOsko, Graphene/polymer nanocomposites, Macromolecules, 43 (2010) 6515-6530.

[2] B.M. Yoo, H.J. Shin, H.W. Yoon, H.B. Park, Graphene and graphene oxide and their uses in barrier polymers, Journal of Applied Polymer Science, 131 (2014).

[3] M.J. Allen, V.C. Tung, R.B. Kaner, Honeycomb carbon: A review of graphene, Chemical Reviews, 110 (2010) 132-145.

[4] C.N.R. Rao, A.K. Sood, K.S. Subrahmanyam, A. Govindaraj, Graphene: The new two-dimensional nanomaterial, Angewandte Chemie - International Edition, 48 (2009) 7752-7777.

[5] W. Choi, I. Lahiri, R. Seelaboyina, Y.S. Kang, Synthesis of graphene and its applications: A review, Critical Reviews in Solid State and Materials Sciences, 35 (2010) 52-71.

[6] V. Berry, Impermeability of graphene and its applications, Carbon, 62 (2013) 1-10.

[7] E.N. Wang, R. Karnik, Water desalination: Graphene cleans up water, Nature nanotechnology, 7 (2012) 552-554.

[8] M. Hu, B. Mi, Enabling graphene oxide nanosheets as water separation membranes, Environmental Science and Technology, 47 (2013) 3715-3723.

[9] Y. Han, Z. Xu, C. Gao, Ultrathin graphene nanofiltration membrane for water purification, Advanced Functional Materials, 23 (2013) 3693-3700.

[10] R.K. Joshi, P. Carbone, F.C. Wang, V.G. Kravets, Y. Su, I.V. Grigorieva, H.A. Wu, A.K. Geim, R.R. Nair, Precise and ultrafast molecular sieving through graphene oxide membranes, Science, 343 (2014) 752-754.

[11] C. Xu, A. Cui, Y. Xu, X. Fu, Graphene oxide-TiO_2 composite filtration membranes and their potential application for water purification, Carbon, 62 (2013) 465-471.

[12] T. Kuilla, S. Bhadra, D. Yao, N.H. Kim, S. Bose, J.H. Lee, Recent advances in graphene based polymer composites, Progress in Polymer Science (Oxford), 35 (2010) 1350-1375.

[13] H. Wu, B. Tang, P. Wu, Development of novel SiO_2-GO nanohybrid/polysulfone membrane with enhanced performance, Journal of Membrane Science, 451 (2014) 94-102.

[14] B.M. Ganesh, A.M. Isloor, A.F. Ismail, Enhanced hydrophilicity and salt rejection study of graphene oxide-polysulfone mixed matrix membrane, Desalination, 313 (2013) 199-207.

[15] H. Zhao, L. Wu, Z. Zhou, L. Zhang, H. Chen, Improving the antifouling property of polysulfone ultrafiltration membrane by incorporation of isocyanate-treated graphene oxide, Physical Chemistry Chemical Physics, 15 (2013) 9084-9092.

[16] C.A. Crock, A.R. Rogensues, W. Shan, V.V. Tarabara, Polymer nanocomposites with graphene-based hierarchical fillers as materials for multifunctional water treatment membranes, Water Research, 47 (2013) 3984-3996.

[17] S. Zinadini, A.A. Zinatizadeh, M. Rahimi, V. Vatanpour, H. Zangeneh, Preparation of a novel antifouling mixed matrix PES membrane by embedding graphene oxide nanoplates, Journal of Membrane Science, 453 (2014) 292-301.

[18] W.S. Hummers, R.E. Offeman, Preparation of Graphitic Oxide, Journal of the American Chemical Society, 80 (1958) 1339-1339.

[19] J. Yin, E.S. Kim, J. Yang, B. Deng, Fabrication of a novel thin-film nanocomposite (TFN) membrane containing MCM-41 silica nanoparticles (NPs) for water purification, Journal of Membrane Science, 423-424 (2012) 238-246.

[20] X. Shen, X. Lin, N. Yousefi, J. Jia, J.K. Kim, Wrinkling in graphene sheets and graphene oxide papers, Carbon, 66 (2014) 84-92.

[21] L. Shao, X. Cheng, Z. Wang, J. Ma, Z. Guo, Tuning the performance of polypyrrole-based solvent-resistant composite nanofiltration membranes by optimizing polymerization conditions and incorporating graphene oxide, Journal of Membrane Science, 452 (2014) 82-89.

[22] A.R. Kumarasinghe, L. Samaranayake, F. Bondino, E. Magnano, N. Kottegoda, E. Carlino, U.N. Ratnayake, A.A.P. De Alwis, V. Karunaratne, G.A.J. Amaratunga, Self-assembled multilayer graphene oxide membrane and carbon nanotubes synthesized using a rare form of natural graphite, Journal of Physical Chemistry C, 117 (2013) 9507-9519.

[23] H.C. Schniepp, J.-L. Li, M.J. McAllister, H. Sai, M. Herrera-Alonso, D.H. Adamson, R.K. Prud'homme, R. Car, D.A. Saville, I.A. Aksay, Functionalized Single Graphene Sheets Derived from Splitting Graphite Oxide, The Journal of Physical Chemistry B, 110 (2006) 8535-8539.

[24] V.C. Tung, M.J. Allen, Y. Yang, R.B. Kaner, High-throughput solution processing of large-scale graphene, Nat Nano, 4 (2009) 25-29.

[25] A.C. Ferrari, J.C. Meyer, V. Scardaci, C. Casiraghi, M. Lazzeri, F. Mauri, S. Piscanec, D. Jiang, K.S. Novoselov, S. Roth, A.K. Geim, Raman Spectrum of Graphene and Graphene Layers, Physical Review Letters, 97 (2006) 187401.

[26] G. Jiang, Z. Lin, C. Chen, L. Zhu, Q. Chang, N. Wang, W. Wei, H. Tang, TiO_2 nanoparticles assembled on graphene oxide nanosheets with high photocatalytic activity for removal of pollutants, Carbon, 49 (2011) 2693-2701.

[27] D. Graf, F. Molitor, K. Ensslin, C. Stampfer, A. Jungen, C. Hierold, L. Wirtz, Spatially Resolved Raman Spectroscopy of Single- and Few-Layer Graphene, Nano Letters, 7 (2007) 238-242.

[28] I.J. Roh, A.R. Greenberg, V.P. Khare, Synthesis and characterization of interfacially polymerized polyamide thin films, Desalination, 191 (2006) 279-290.

[29] E.-S. Kim, B. Deng, Fabrication of polyamide thin-film nano-composite (PA-TFN) membrane with hydrophilized ordered mesoporous carbon (H-OMC) for water purifications, Journal of Membrane Science, 375 (2011) 46-54.

Conclusions and Future Work

7.1 Conclusions

In this project, novel nanocomposite membranes with enhanced separation performance were developed for water and wastewater treatment. First, both flat-sheet and hollow fiber membrane fabrication systems were set up for the nanocomposite membrane preparation. Then, to improve membrane performance, nanomaterials with different components (inorganic or organic), structures (porous or nonporous), functionalities (inert, antimicrobial activity, or photocatalytic activity) were incorporated into polymeric membranes based on proposed applications. Several nanomaterials, including mesoporous silica, carbon nanotubes or graphene oxide, were applied to study their effects on membrane structure and physicochemical properties. Biocidal nanomaterial, AgNPs, was used to improve membrane's anti-biofouling capability. While photocatalytic nanomaterial, nitrogen doped TiO_2 with visible light activity, was applied to improve membrane's antifouling properties. In the following, the significant results of this work are summarized.

A novel mesoporous silica NPs (MCM-41) enhanced TFN membrane was first prepared by an in situ IP process using aqueous MPD and organic TMC-NPs mixture solutions. A good dispersion of MCM-41 NPs occurred in the PA thin-film layer. With an increasing concentration of MCM-41 NPs, the membrane hydrophilicity, roughness and zeta potential all increased. The resulting increase in the permeate water flux was 63.5% while the salt rejections were maintained essentially the same. Compared with S-TFN membranes, the M-TFN membranes showed enhanced permeability, suggesting that a

short flow path through the hydrophilic porous structure of MCM-41 NPs had played an important role in water permeation. This fundamental understanding will help screen and develop new advanced TFN membranes in general.

With the vision of the importance of porous structure inside nanofiller, GO nanosheets which have a multiple layer structure and an interlayer spacing around 0.83 nm were prepared and their potential application on TFN membrane preparation was evaluated. By increasing concentration of the GO nanosheets, hydrophilicity of the TFN membrane increased. At the same time, the permeate water flux increased by 52.3%, while rejections of NaCl and Na_2SO_4 slightly decreased. The interlayer spacing of GO nanosheets may work as channels for water migration and hence contributed to the water permeability enhancement.

A covalent bonding method was developed to attach AgNPs onto the surface of PA TFC membrane with cysteamine as a bridging agent. The modified membranes showed good stability for the immobilized AgNPs and excellent antibacterial properties, while maintained a good water flux and salt rejection. The results demonstrated that chemically immobilizing AgNPs onto membrane surface could be an effective approach to reduce membrane biofouling.

After incorporating OMWNTs into PSU HFMs, the surface hydrophilicity of the resulting nanocomposite membrane increased. Meanwhile, the membrane surface showed a convex shape of pore size change with increasing filler concentration, which could be caused by the combined effect of lowered thermodynamic stability and increased viscosity of the dope solution introduced by the addition of the hydrophilic carbon

nanotubes. The optimized nanocomposite membranes showed a significant increase in pure water flux (60% to 100%) while maintaining the similar capability for solute rejection. In addition, the fouling resistance of the membrane to protein was enhanced as tested using BSA as the model foulant.

Following the similar blending approach used in PSU/OMWNTs membrane preparation, N-TiO_2 NPs with visible light activity was applied to fabricate PVDF/N-TiO_2 nanocomposite HFMs. The resulting membranes showed an improved hydrophilicity and clear photocatalytic activities under the visible light irradiation. They also possessed enhanced water flux, comparable HA rejection (above 96%), and improved fouling resistance when compared to the original PVDF membrane. These results have demonstrated that there is a great potential to use the established methodology for developing membranes with an improved water permeability and superior antifouling properties, based on photodegradation process and photoinduced hydrophilicity enhancement driven by solar light as a renewable source of energy.

In conclusion, nanocomposite membranes were promising to mitigate or even overcome the intrinsic challenges of current polymeric membranes on the market. The incorporation of nanomaterials with conventional membrane polymers could not only tune structure and physicochemical properties (e.g. hydrophilicity, porosity, charge density, thermal, and mechanical stability) of membranes, but also introduce unique functionalities (e.g. antibacterial property and photocatalytic capability) into the membranes. Overall, nanocomposite provides polymeric membrane design a new dimension, which could lead to the next generation of high performance membranes.

7.2 Future work

This work stimulated us to make the following suggestions for future research.

7.2.1 Investigating the effects of physicochemical properties and structures of nanofiller on membrane performance

Although hydrophilic and porous nanofillers have been demonstrated to be good candidates for high performance membrane preparation, no fundamental understandings were developed to systematically reflect the effects of nanomaterials on membrane structures and correlate them to the membrane performance changes. The specific contributions of surface hydrophilicity, pore size, charge density and membrane porosity to membrane performance are still unclear.

More quantitative and qualitative studies are needed in this area. In our lab, we are continuously exploring these relationships by controlling the surface hydrophilicity as well as pore size of nanofiller which are important to the membrane performance.

7.2.2 Improving the dispersion of nanomaterials inside polymeric membranes

Aggregation is a common problem for nanomaterials. Considering the importance of making nanofillers homogeneously dispersed inside the polymer matrix to the final enhancement of membrane properties, research is needed to further improve the dispersion of nanofillers by modifying nanofiller surface or optimizing embedding process. In addition, there is no comprehensive model to describe the dispersion of nanofillers inside membranes. Information of concentration, diffusivity in aqueous or organic solution, hydrodynamics, and surface reaction kinetics all need to be examined to perform this complex simulation.

7.2.3 Investigating the interaction between nanofillers and polymeric materials and further studying the stability of nanofillers inside membrane structure

The compatibility of nanofillers with polymer will determine both the optimal performance enhancement and the stability of nanofillers within the host polymer. These two factors are critical to optimize the loading concentration and durability of nanocomposite membranes. Further research is needed to develop desirable nanofillers with good polymer compatibility either by designing novel fillers based on material science or introducing polymer compatible functional groups to the surface of common fillers. In addition, considering the potentially harmful effects of leached nanomaterials to the environment, nanomaterial leakage and its environmental toxicity need to be systematically evaluated.

7.2.4 Exploring the commercial values of nanocomposite membranes

It is expected that using the advanced high performance nanocomposite membranes will result in lower energy consumption in the membrane filtration systems. However, the practical applications of nanocomposite membranes are still at their initial stages. It is very important to develop a cost-effective method for scale up in terms of nanomaterial preparation and membrane fabrication, and monitor membranes' long-term stability under practical application conditions. Those studies should be implemented on a case by case basis fully considering the environment and the attributes of the system. Using antimicrobial membrane as an example, while it has demonstrated resistance to membrane biofouling, for long-term application, the loss of antimicrobial activity due to the depletion of biocidal agents or insufficient contact between bacteria and biocide caused by other foulants need to be evaluated. How to effectively attach biocidal agents

onto membrane and control their release should be a future research direction. For commercial applications, there is a need to consider cost-effectiveness of attaching biocidal agents onto a membrane and recharging them as needed.

VITA

On December 26th, 1983, Jun Yin was born in a small town located in Kunshan, China. He received his Bachelor's and Master's degrees from Nanjing University with a major in Environmental Engineering on June 2006 and March 2009, respectively.

He has over 9 years research experience related to environmental engineering including nanomaterial synthesis and modification, membrane separation, membrane fabrication and modification, photocatalysis, heavy metal removal, and oil spill treatment.

His PhD research topic is "Fabrication and modification of nanocomposite membranes for enhanced water purification", which focuses on applying nanotechnology into polymeric membrane design to improve membrane performance in terms of water permeability, solute rejection, and fouling resistance to further improve energy efficiency and cost effectiveness of membrane separation process.